

Correlation Effects in 2-Dimensional Electron Systems - Composite Fermions and Electron Liquid Crystals

**Von der Fakultät für Mathematik und Physik der Universität Stuttgart zur
Erlangung der Würde eines Doktors der Naturwissenschaften
(Dr. rer. nat.) genehmigte Abhandlung**

vorgelegt von

JÖRN GÖRES

aus Hilden, Deutschland

Hauptberichter:	Prof. Dr. K. v. KLITZING
Mitberichter:	Prof. Dr. T. PFAU
Tag der Einreichung:	03. 06. 2004
Tag der mündlichen Prüfung:	28. 09. 2004

**MAX-PLANCK-INSTITUT FÜR FESTKÖRPERFORSCHUNG
STUTTGART, 2004**

Contents

Symbols, Constants, and Abbreviations	6
1 Introduction	11
2 Fundamentals	15
2.1 Two-dimensional electron systems	15
2.1.1 Low-field magnetoresistance	16
2.1.2 Energy spectrum in a quantizing magnetic field	18
2.1.3 Integer Quantum Hall Effect (IQHE)	20
2.1.4 Landauer-Büttiker formalism	21
2.1.5 Fractional Quantum Hall Effect (FQHE)	23
2.1.6 Higher Landau levels	24
2.1.7 Aharonov-Bohm effect	26
2.2 Composite Fermions	27
2.2.1 Chern-Simons transformation	28
2.2.2 Mean field approximation	28
2.2.3 Beyond mean field - the RPA approximation	30
2.2.4 The FQHE revisited - The IQHE of Composite Fermions	31
2.2.5 Composite Fermions at filling fraction $\nu = 3/2$	32
2.2.6 Composite Fermions in higher Landau levels	34
2.3 Correlated phases in higher Landau levels	35
2.3.1 Charge Density Wave (CDW) picture	36
2.3.2 Electron Liquid Crystal (ELC) picture	41

3	Ballistic Transport	47
3.1	Quantum Point Contacts (QPCs)	47
3.2	Ballistic electron transport	50
3.3	Ballistic Composite Fermion transport	52
3.3.1	QPC voltage dependence	53
3.3.2	Temperature dependence	56
3.3.3	Filling factor $\nu = 3/2$	58
4	Phase coherent Transport	61
4.1	Antidot geometry	61
4.2	Trapped classical orbits	62
4.3	Aharonov-Bohm oscillations	64
4.3.1	Temperature dependence	66
4.3.2	Phase dislocations	70
5	Correlated phases in the $N = 2$ Landau level	73
5.1	Resistance around $\nu = 9/2$	73
5.1.1	van-der-Pauw geometry	74
5.1.2	Hall-bar geometry	77
5.2	Differential resistance around $\nu = 9/2$	80
5.2.1	'easy-axis' configuration - AC/DC currents along $[110]$ -axis	81
5.2.2	'hard-axis' configuration - AC/DC currents along $[1\bar{1}0]$ -axis	83
5.2.3	'mixed-axis' configuration - AC/DC currents along different axes	90
5.2.4	Temperature dependence	93
5.2.5	Discussion	96
6	Conclusions	105
	Deutsche Zusammenfassung	113
A	Sample fabrication	123
A.1	Heterostructures	123
A.2	Optical lithography	123
A.2.1	Mesa etch	124
A.2.2	Ohmic contacts	126

A.2.3	Gate connections	128
A.2.4	Pads and e-beam alignment marks	129
A.3	Electron-beam lithography	130
A.3.1	Surface gates	130
A.3.2	Air-bridge gates	131
B	Ultra-low temperature probe	135
B.1	Cooling of the 2DES	135
B.2	RF-heating	137
B.3	RF-filter	137
B.3.1	Room temperature π -filter	137
B.3.2	RC-filter at 1K-Pot	138
B.3.3	Strip-line filter at base temperature	138
B.3.4	Ag/Si Faraday-shield	139
B.4	Sintered Ag-heat exchangers	140
	Bibliography	141
	Acknowledgements	147
	Curriculum Vitae	151

Symbols, Constants, and Abbreviations

Symbols

\mathbf{a}	Chern-Simons vector potential.
\mathbf{A}	vector potential.
A	contact area.
A	area enclosed by electron paths.
A_{AD}	antidot area.
b	Chern-Simons magnetic field.
Δb	fluctuations of Chern-Simons magnetic field.
B, \mathbf{B}	magnetic field.
ΔB	Aharonov-Bohm oscillation period.
B_{eff}	effective magnetic field for Composite Fermions.
B_ν	magnetic field at filling factor ν .
C	capacitance.
d	wire diameter.
d	length of QPC constriction.
D	internal Luttinger liquid interaction parameter.
\bar{D}	interaction parameter between neighboring Luttinger liquids.
D_0	constant 2-dimensional density of states at $B = 0$.
$D(E)$	density of states.
D_i	width of regions with $\nu_{\text{N}}^{\text{loc}} = i$.
Δ_e / Δ_h	activation energy for electron/hole bubble phase.
e^*	quasi-particle charge.
E, \mathbf{E}	electric field.
E	energy.
ΔE	energy spread.
E_{corr}	correlated phase (pseudo-)gap energy.
E_{F}	Fermi energy.
E_{n}	energy eigenvalues of harmonic oscillator.
E_{Z}	Zeeman energy.

ϵ	total electron energy.
ϵ_z^0	lowest subband energy of 2DES.
$\delta\epsilon$	energy level spacing from size quantization.
f	frequency.
F_L	Lorentz force.
φ	phase of electron wavefunction.
$\Delta\varphi$	phase shift.
Φ	magnetic flux.
$\Phi(x, y)$	energy eigenfunctions of electrons in a quantizing magnetic field.
\tilde{g}	smooth part of conductance.
δg	oscillatory part of conductance.
G	two-point conductance.
$\tilde{G} = G/(e^2/h)$	normalized two-point conductance.
H_n	Hermite polynomial of order n .
I_{AC}	AC probe current.
I_{inj}	current through injector QPC.
I_p	current flowing through terminal p .
j, \mathbf{j}	current density.
k, k_x, k_y	electron wavevector.
k_F	Fermi wavevector.
l	transport mean free path.
l_B	magnetic length.
l_φ	inelastic mean free path.
L	sample length.
L	orbit length.
L	distance between QPCs.
L_{th}	thermal length.
λ_F	Fermi wavelength.
λ_{CDW}	CDW modulation period.
$\lambda_{Lutt.}$	charge-density fluctuation period of Luttinger liquid.
m_{CF}^*	effective Composite Fermion mass.
μ	mobility.
μ^{CF}	Composite Fermion mobility.
$\mu_{ch.}$	chemical potential.
n	electron density.
Δn	electron density variation.
n_{bulk}	bulk electron density.
n_{gate}	electron density underneath gate.
n_{CF}	Composite Fermion density.

n_F	Fermi-distribution function.
N	Landau level index.
N	number of transverse modes.
N_e	number of electrons.
N_L	Landau level degeneracy.
ν	filling factor.
ν_{bulk}	bulk filling factor.
ν_{eff}	effective filling factor of Composite Fermions.
ν_{gate}	filling factor underneath gate.
ν_N	filling factor of highest occupied Landau level.
ν_N^{loc}	local ν_N .
ν_N^{theo}	theoretically predicted ν_N .
ν_{QPC}	filling factor in QPC constriction.
ω_c	cyclotron frequency.
\hat{p}	canonical momentum operator.
$P_{\text{el-diff}}$	cooling power by electron diffusion.
$P_{\text{el-ph}}$	cooling power by electron-phonon scattering.
Ψ_{CF}	Composite Fermion wavefunction.
Ψ_{el}	electron wavefunction.
Ψ_{MR}	Moore-Read wavefunction.
\dot{Q}	heat flux.
$\mathbf{r}_i, \mathbf{r}_j, \mathbf{r}_k,$	particle coordinates.
R	reflection coefficient.
R_t	transfer resistance.
ΔR_0	ballistic peak resistance at $T = 0$.
ΔR_{peak}	ballistic peak resistance.
R_c	cyclotron radius.
R_c^{CF}	Composite Fermion cyclotron radius.
R_K	Kapitza resistance.
R_{xx}, R_{xy}	longitudinal and Hall resistance.
ρ	resistivity tensor.
ρ^{CS}	Chern-Simons contribution to resistivity at $\nu = 1/2$.
$\rho_{xx}, \rho_{yy}, \rho_{xy}, \rho_{yx}$	resistivity tensor components.
$\sigma_{xx}, \sigma_{yy}, \sigma_{xy}, \sigma_{yx}$	conductivity tensor components.
T	temperature.
ΔT	temperature difference.
T_0	characteristic decay temperature.
T_{base}	base temperature of dilution refrigerator.
T_c	critical temperature.

T_d	total transmission through device.
T_e, T_{2DES}	temperature of 2DES.
T_{GaAs}	temperature of GaAs crystal lattice.
T_{leads}	temperature of electrons in the metal leads.
T_n	transmission of n th edge channel.
T_{pq}	transmission probability from terminal q to terminal p .
τ	transport scattering time.
τ^{CF}	Composite Fermion transport scattering time.
τ_{CFCF}	Composite Fermion-Composite Fermion scattering rate.
τ_{ee}	electron-electron scattering rate.
τ_i	scattering time across regions with $\nu_N^{loc} = i$.
$\Delta\theta$	phase fluctuation parameter.
V	Coulomb interaction potential.
V_{AC}	AC probe voltage.
V_{AD}	antidot gate voltage.
V_{coll}	voltage across collector QPC.
V_p	voltage at terminal p .
V_{QPC}	QPC gates voltage.
V_{sg}	side gate voltage.
v	electron velocity.
v_d	drift velocity.
v_F	Fermi velocity.
W	sample width.
W_c	width of QPC constriction.
χ_ν	electron wavefunction at filling factor ν .
ΔY	shape fluctuation parameter.
$\hat{\mathbf{z}}$	unit vector in z -direction.
z_i, z_j	coordinates in complex notation.

Constants

$e = -1.6021917 \cdot 10^{-19} \text{ C}$	electron charge.
$e^2/h = 1/R_K = 0.3874045 \cdot 10^{-6} \Omega^{-1}$	conductance quantum.
$\Phi_0 = h/e = 2.41797 \text{ Tm}^2$	magnetic flux quantum.
$g_S = 1, 2$	spin degeneracy.
$g^* = -0.44$	effective Landé-factor of electrons in bulk GaAs.
$h = 6.626196 \cdot 10^{-34} \text{ Js}$	Planck constant.
$\hbar = h/2\pi$	reduced Planck constant.
$m_0 = 9.109558 \cdot 10^{-31} \text{ kg}$	electron mass.
$m^* = 0.067m_0$	effective electron mass in bulk GaAs.
$\mu_B = 9.274096 \text{ JT}^{-1}$	Bohr magneton.
$R_K = 25812.807 \Omega$	v. Klitzing constant.

Abbreviations

2DES	two-dimensional electron system.
AD	antidot.
a.u.	arbitrary units.
CDW	Charge Density Wave
CF	Composite Fermion.
ELC	Electron Liquid Crystal.
FQHE	Fractional Quantum Hall Effect.
IQHE	Integer Quantum Hall Effect.
QPC	Quantum Point Contact.
RIQHE	Reentrant Integer Quantum Hall Effect.
MBE	Molecular Beam Epitaxy.
sg	side gate.
vdP	van der Pauw.

Chapter 1

Introduction

Ever since the discovery of the Integer Quantum Hall Effect (IQHE) by K. von Klitzing *et al.* in 1980 [1], semiconductor electron systems confined to two dimensions (2DES) have been an extremely fascinating playground for experimental and theoretical condensed matter physics alike.

Experimentally, progress has been achieved mainly through a continuous improvement of the sample quality. In state of the art samples, electrons travel approximately $200\ \mu\text{m}$ in the 2DES plane without suffering any scattering. This amounts to an increase of about three orders of magnitude as compared to samples used in early experiments. The progress in sample quality in conjunction with the ability to carry out sensitive electronic measurements in high magnetic fields ($B \approx 10\ \text{T}$) at ever lower temperatures ($T \approx 10\ \text{mK}$) have led to a panoply of exciting discoveries in the 2DES during the last 24 years.

These discoveries have triggered intense theoretical efforts to unravel the fundamental processes and principles involved. In the early years of research on 2DES, non-interacting, single particle models were mostly sufficient to describe the observed phenomena. The discovery of the Fractional Quantum Hall Effect (FQHE) in 1982 by Tsui *et al.* [2] and its explanation by Laughlin [3] brought the importance of electron-electron correlation effects into focus. Correlations turn out to often dominate the physics of clean 2DES subjected to a strong perpendicular magnetic field, because the kinetic degrees of freedom are effectively frozen out. Soon, it also became clear that deep insights into the subtleties of quantum field theory have to be invoked to improve our understanding of the rich physics in this field. For example, the precise resistance quantization within the IQHE has been accounted for by Laughlin based on a gauge invariance argument [4].

Up to this day, the complicated collective phenomena that arise from electron correlations remain a challenging subject of research throughout physics. This thesis mainly deals with two prominent examples of correlation phenomena in 2DES, namely Composite Fermions and Electron Liquid Crystal phases. We briefly introduce both in the next paragraphs.

In 1989, in an attempt to account in an intuitive fashion for the FQH-states observed in experiments, J. Jain introduced the concept of Composite Fermions [5]. These are quasi-particles each assembled from one electron and two elementary magnetic flux quanta. Within this framework, the FQHE of electrons is naturally understood as the IQHE of Composite Fermions. It was shown by Halperin, Lee, and Read in 1993 that Composite Fermions exist independently of the IQHE and behave as weakly interacting particles subjected to an effective magnetic field which is substantially reduced from the external magnetic field [6].

Guided by the analogy with electron systems at low magnetic fields, one can devise mesoscopic transport experiments for Composite Fermions. The outcome of such experiments would have never been predictable without resorting to Composite Fermions.

The Composite Fermion concept is fascinating also from a general field theoretical viewpoint. By means of a well defined mathematical transformation, a strongly interacting system is recast into a weakly interacting one. The transformed system is much easier to deal with quantitatively and also makes the problem intuitively accessible. Hence, it seems to depend on our viewpoint how complicated an interacting system looks like. An important question comes to our mind in this context: Is it just a lucky coincidence that such a simplifying transformation exists in the case of 2-dimensional electrons in high magnetic fields? Or does such a transformation exist for any strongly interacting system? We will briefly comment on this question in our conclusions.

In our thesis, we mainly study the particle-like behavior of Composite Fermions in transport through well defined and tunable geometries. These experiments were motivated by the question of how far the limits of the Composite Fermion picture can be pushed. Ultimately, the fascinating question poses whether it is also possible to observe wave-like properties of Composite Fermions. As an important first step towards this goal, we study special device geometries which show pronounced interference signatures for electrons at low magnetic fields. In the concluding chapter, we briefly discuss the remaining difficulties for the observation of Composite Fermion interference effects.

At intermediate magnetic fields, outside the realm of the FQHE observed at high fields, electron correlations lead to qualitatively new experimental signatures, namely strongly anisotropic transport and a reentrant IQHE (RIQHE). Only as recently as 1999, with the advent of extremely high quality samples, these phenomena were independently revealed by Lilly *et al.* and Du *et al.* [7, 8].

Qualitatively, the effects can be explained within a scheme that was put forward by Koulakov *et al.* and also Moessner and Chalker in 1996, prior to the experimental observations [9, 10]. These groups had independently predicted an instability of the 2DES towards the formation of long range ordered electron density modulations. The modulation is triggered by a competition between repulsive and attractive interaction components, and it bears a strong similarity to the

charge modulation in conventional Charge Density Wave (CDW) conductors [11]. Depending on the morphology of the charge density modulation of the 2DES, one distinguishes between anisotropic stripe phases and isotropic bubble phases. Transitions between the different types of phases are induced by simply tuning the applied magnetic field. The bubble phase in the CDW picture is the many-electron analogue of the well known Wigner crystal [12]. There single electrons form a triangular lattice because of their mutual Coulomb repulsion, whereas in the bubble phase, the lattice sites are occupied by a collection of two or more electrons instead.

A more sophisticated model was introduced by Fradkin and Kivelson [13] who noted the importance of quantum fluctuations for a realistic description of the correlated phases. The resulting phase diagram is very similar to that of classical molecular liquid crystals [14]. Therefore, the model is known as the Electron Liquid Crystal (ELC) picture. Similar long range ordered phases are common in a variety of physical and chemical systems, like for example thin magnetic films and ferrofluids [15]. In all cases, the phases can be traced back to competing repulsive and attractive interaction forces. In the case of the Coulomb interaction in an electronic system, the ELC picture is also discussed in the context of high- T_c superconductors where correlated phases are thought to be responsible for the onset of superconductivity [16].

In our own study of the ELC phases in high quality 2DES, we use offset currents to induce a non-equilibrium situation within the sample and destabilize the correlated phases in a very controlled way. This provides us with an additional parameter which we use to investigate the ELC phases in more detail. In the concluding chapter, we will point out new insights into ELC phases gained from our observations and the interesting new questions they pose.

The remainder of this thesis is organized into the following chapters:

- **Chapter 2** Fundamental concepts are discussed which are necessary to understand our own experimental results presented in later chapters. We first introduce the Integer- and the Fractional Quantum Hall Effects, and the Aharonov-Bohm interference effect. A second section covers Composite Fermions, their particle-like behavior and their role in understanding the FQHE. Finally, we turn our attention to the correlated phases which appear at intermediate magnetic fields and discuss the CDW as well as the ELC picture.
- **Chapter 3** After introducing experiments that probe ballistic transport of electrons at low magnetic fields, we repeat similar experiments for Composite Fermions. The particle-like behavior of Composite Fermions is investigated and emphasized. Differences to electrons are pointed out.
- **Chapter 4** Electron transport in tunable antidot geometries is studied. After describing experiments which rely on the classical, particle-like behavior of electrons, we turn our attention to interference effects which emerge at low temperatures in these geometries.
- **Chapter 5** Experiments investigating the transport properties in the CDW/ELC phase

regime are presented. First, resistance measurements in two different geometries are covered. The remainder of the chapter discusses differential resistance measurements in the same geometries in great detail.

- **Chapter 6** We draw conclusions from our experimental results and show their relevance for understanding Composite Fermion transport at high magnetic fields as well as the Electron Liquid Crystal phases at intermediate fields. We finish this chapter with an outlook on further work.
- **Appendix A** Sample fabrication steps for the various devices, studied throughout this document, are discussed.
- **Appendix B** General considerations for cooling a 2DES are addressed. The design of the ultra-low temperature probe, which has been crucial for our experimental results, is then discussed in detail.

We believe that an improved understanding of the properties of Composite Fermions and Electron Liquid Crystal phases will not only contribute to the field of electron correlations in semiconductor 2DES. Likely, it will also have an impact on related areas of physics like high- T_c superconductivity, the physics of ultra-cold atoms in optical lattices, quantum phase transitions, and quantum field theory in general.

Chapter 2

Fundamentals

2.1 Two-dimensional electron systems

In a two-dimensional electron system (2DES), the electron motion is restricted to a plane with the help of a suitable confinement potential [17]. In this work, we will exclusively discuss 2DES formed at the interface of modulation-doped Gallium-Arsenide/Aluminium-Gallium-Arsenide heterostructures and grown with Molecular Beam Epitaxy (MBE) [18, 19]. The semiconductors $GaAs$ and $Al_xGa_{1-x}As$ have almost identical lattice constants and can be grown on top of each other with relatively little strain at the interfaces. This results in mono-crystalline layered systems. A simplified sketch of a typical heterostructure used in our experiments together with the corresponding band-structure is shown in Figure 2.1. The Si-doping is adjusted such that at low temperatures electrons only occupy the lowest energy state of the triangular potential well. Therefore the electron motion is quenched in the z -direction and the total energy of each electron is given by

$$\varepsilon(k_x, k_y) = \frac{\hbar^2}{2m^*}(k_x^2 + k_y^2) + \varepsilon_z^0, \quad (2.1)$$

where k_i is the electron wavevector in i -direction, ε_z^0 is the energy of the lowest subband, and m^* is the effective mass of conduction band electrons. In $GaAs/Al_xGa_{1-x}As$ heterostructures m^* is essentially the effective mass of bulk GaAs ($m_{GaAs}^* \approx 0.066 m_0$) since the electron wavefunction is mainly localized within the GaAs layer. Because of the two-dimensional parabolic energy dispersion $\varepsilon(k_x, k_y)$, one obtains a constant density of states

$$D_0 = \frac{dn}{dE} = \frac{g_s m^*}{2\pi\hbar^2}, \quad (2.2)$$

with $g_s = \{1, 2\}$ indicating the spin degeneracy. This also relates the Fermi-energy E_F to the electron density n in a straightforward way

$$E_F = \frac{\pi\hbar^2}{m^*}n, \quad (2.3)$$

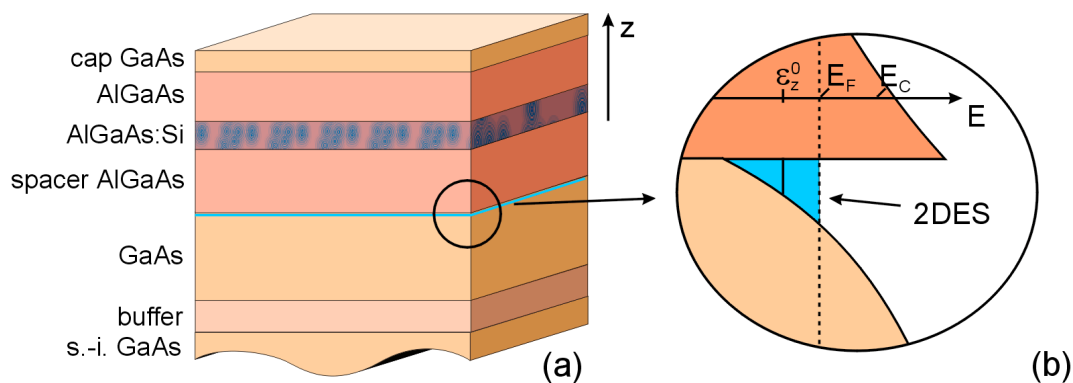


Figure 2.1: (a) Typical heterostructure. A semi-insulating GaAs layer is first overgrown by a buffer layer to provide an atomically smooth surface for the following layers. The 2DES forms at the interface between the lowest GaAs layer and the spacer AlGaAs layer (circle). The spacer separates the Si dopants from the 2DES to minimize residual scattering. The heterostructure is capped by a GaAs layer to prevent the AlGaAs from oxidizing. (b) Schematic view of the energy band structure at the interface between the undoped GaAs and AlGaAs layers. Electrons fill up a narrow triangular potential well near the interface, so that their motion is restricted to the plane near the interface.

and defines the Fermi-wavevector

$$k_F = \frac{2\pi}{\lambda_F} = \sqrt{2\pi n}, \quad (2.4)$$

where λ_F is the Fermi-wavelength, typically of the order of 60 nm for our samples.

2.1.1 Low-field magnetoresistance

Resistivity measurements in weak magnetic fields are used to characterize the transport properties of semiconductor 2DESs. The components of the resistivity tensor

$$\rho = \begin{bmatrix} \rho_{xx} & \rho_{xy} \\ \rho_{yx} & \rho_{yy} \end{bmatrix}, \quad (2.5)$$

which connect the local electric field \mathbf{E} to the current density \mathbf{j} , are typically determined in a Hall-bar measurement setup (Fig. 2.2). At low magnetic fields, i.e. when the quantization of the energy spectrum can be neglected, the Drude-model [20] accounts well for the transport properties of a 2DES. In this simple model, electrons with an effective mass m^* receive momentum from an external electric field \mathbf{E} and a magnetic field \mathbf{B} and lose momentum through elastic scattering events with the static disorder potential resulting in the steady state condition

$$\left[\frac{d\mathbf{p}}{dt} \right]_{\text{scattering}} = \left[\frac{d\mathbf{p}}{dt} \right]_{\text{field}} \iff \frac{m^* \mathbf{v}_d}{\tau} = e [\mathbf{E} + \mathbf{v}_d \times \mathbf{B}], \quad (2.6)$$

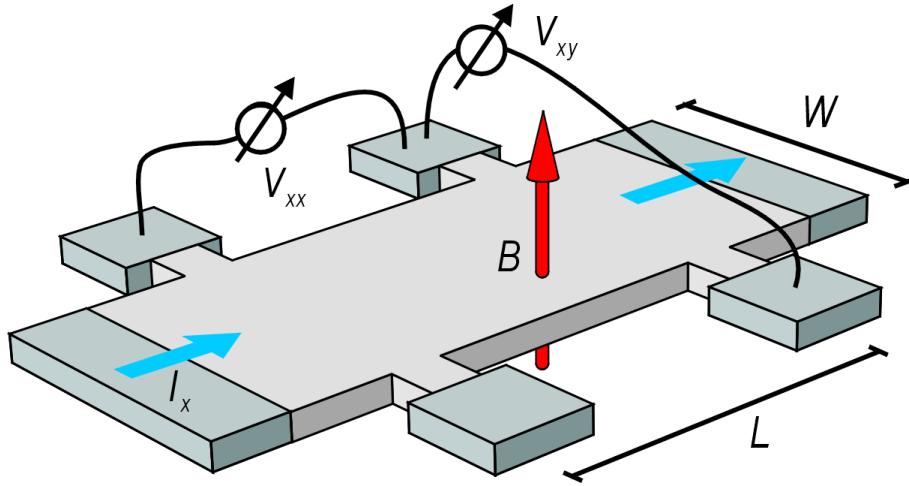


Figure 2.2: Hall-bar measurement setup. The longitudinal voltage V_{xx} and Hall voltage V_{xy} are measured when a current I_x is driven through the sample. The components of the resistivity tensor 2.5 follow from $\rho_{xy} = V_{xy}/I_x$ and $\rho_{xx} = (W/L) \cdot V_{xx}/I_x$, where W/L is the geometry factor. The magnetic field B is applied perpendicular to the 2DES.

where \mathbf{v}_d is the drift velocity and τ the transport scattering time. Together with the definition of the current density $\mathbf{j} = en\mathbf{v}_d$ and Ohm's law $\mathbf{E} = \rho\mathbf{j}$, this yields

$$\rho_{xx} = \frac{m^*}{ne^2\tau} = \frac{1}{n|e|\mu}, \quad (2.7)$$

$$\rho_{xy} = \frac{B}{|e|n}. \quad (2.8)$$

Within the Drude-model the diagonal resistivity ρ_{xx} is independent of the external magnetic field and is related to the electron mobility μ . The mobility is the ratio between the drift velocity and the external electric field

$$\mu = \frac{|\mathbf{v}_d|}{|\mathbf{E}|} = \frac{|e|\tau}{m^*}. \quad (2.9)$$

The electron mobility is generally used as a measure of the sample quality, since it is related to the transport mean free path, i.e. the distance an electron at the Fermi edge travels between successive backscattering events. The transport mean free path follows from $l = v_F\tau$, with $v_F = \sqrt{2E_F/m^*}$ the Fermi velocity. The classical Hall-resistivity ρ_{xy} does not depend on the scattering time and increases linearly with magnetic field. It offers a convenient way to determine the carrier concentration n of the electron system.

2.1.2 Energy spectrum in a quantizing magnetic field

The Drude-model fails when the magnetic field becomes so strong that it quantizes the energy spectrum. In a fully quantum mechanical treatment, which neglects scattering processes and also the electron spin, a 2DES subjected to an external magnetic field $\mathbf{B} = \nabla \times \mathbf{A}$ can be described by a time-independent Schrödinger equation. In the Landau gauge $\mathbf{A} = (-By, 0, 0)$, it takes on the form

$$\frac{1}{2m^*} \left[(\hat{p}_x - eBy)^2 + \hat{p}_y^2 \right] \Phi(x, y) = E_n \Phi(x, y), \quad (2.10)$$

with the canonical momentum operators \hat{p}_i . The eigenfunctions $\Phi(x, y)$ consist of a plane wave in x -direction with wave vector k_x and a bound harmonic oscillator state in y -direction

$$\Phi(x, y) = e^{ik_x x} \cdot H_n \left(\frac{y - y_0}{l_B} \right) \exp \left[-\frac{(y - y_0)^2}{2l_B^2} \right], \quad (2.11)$$

where H_n is the n th Hermite polynomial. The bound state wavefunctions are centered around $y_0 = -l_B^2 k_x$ and have an extent $R_c^n = l_B \sqrt{2n + 1}$ in y -direction. The magnetic length $l_B = \sqrt{\hbar/|e|B}$ is a new scale introduced by the magnetic field. The energy eigenvalues E_n are those of an harmonic oscillator

$$E_n = (n + 1/2)\hbar\omega_c, \quad n = 0, 1, 2, \dots \quad (2.12)$$

with the cyclotron frequency

$$\omega_c = \frac{eB}{m^*}. \quad (2.13)$$

The extend R_c^n of the wavefunction is identical with the radius of the classical circular motion of an electron with energy E_n revolving with the cyclotron frequency ω_c . The discrete energy levels are referred to as Landau levels. Since the Landau level energy E_n does not depend on the center position of the wavefunction parameterized by k_y , each Landau level consists of the same number N_L of energetically degenerate states

$$N_L = \frac{L_y}{\Delta y_0} = \frac{L_x L_y}{2\pi l_B^2} = \frac{B L_x L_y}{h/|e|} = \frac{\Phi}{\Phi_0}. \quad (2.14)$$

Here Δy_0 is the distance between neighboring states in y -direction and L_i is the characteristic size of the sample in i -direction. The last identity clarifies that N_L is also the number of magnetic flux quanta penetrating the sample. In summary, in the presence of a magnetic field, electrons fill up a discrete set of Landau levels with energy E_n separated by the cyclotron gap $\hbar\omega_c$. Each Landau level may host exactly N_L electrons. The ratio between the number of electrons N_e and the number of states available in each Landau level N_L is referred to as the filling factor

$$\nu = \frac{N_e}{N_L} = \frac{hn}{|e|B}. \quad (2.15)$$

When ν takes on integer values n it means that n Landau levels are completely filled with electrons and the others are empty. The chemical potential μ_{ch} , i.e. the energy required to add an additional electron to the system, experiences a jump of size $\hbar\omega_c$ at integer filling factors (Fig. 2.3 (a)). In a more realistic model, scattering processes broaden the Landau levels and disorder in the sample gives rise to localized states that do not contribute to electronic transport (Fig. 2.3 (b)) [21]. In this situation, when the magnetic field is varied, the chemical potential gradually moves through the localized states between the Landau levels instead of directly jumping from one Landau level to the next as in the ideal case.

In our treatment, we have neglected the electron spin because it does not play an important role in our later considerations. We will shortly mention it at this point, mainly to avoid confusion with the nomenclature in the literature. Electrons with spin subjected to a magnetic field acquire an additional Zeeman energy shift

$$E_Z = \pm \frac{1}{2} g^* \mu_B B, \quad (2.16)$$

where $\mu_B = 57.884 \mu\text{eV}/\text{T}$ is the Bohr magneton and $g^* = -0.44$ is the Landé g -factor of electrons in bulk GaAs. The g -factor for electrons in a 2DES can be considerably enhanced [22] but we will neglect this complication here. The sign of the energy shift depends on the orientation of the electron spin. Each Landau level therefore splits into two levels, one for each spin orientation. In the definition of the filling factor (eq. 2.15), we assumed one electron

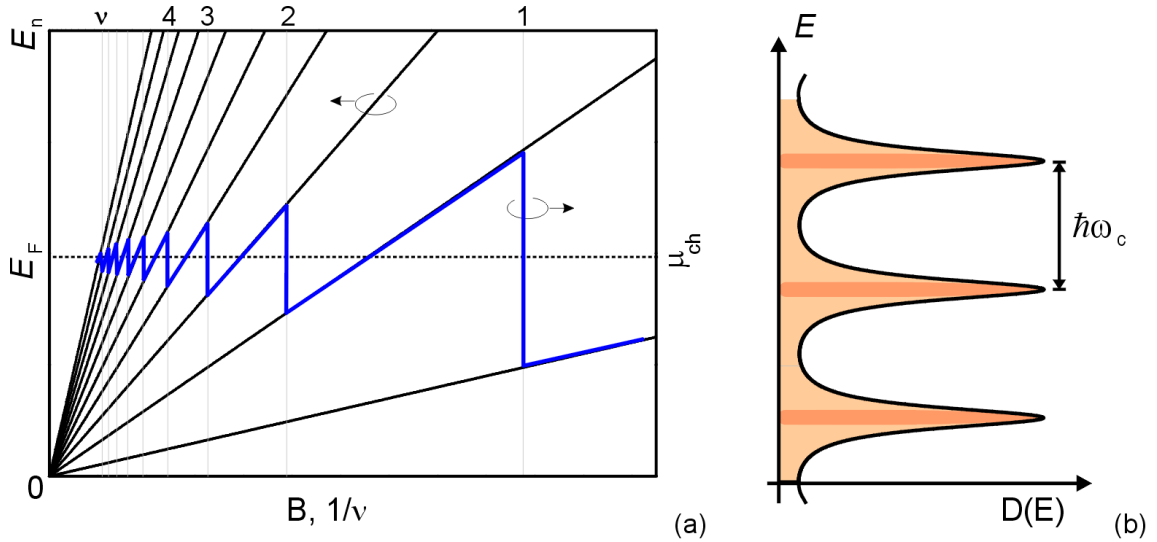


Figure 2.3: (a) Chemical potential μ and Landau level energy E_n (eq. 2.12) as a function of the magnetic field (The spin degeneracy is ignored for simplicity). (b) Density of states at high magnetic field. Landau levels are broadened by scattering processes. Only extended states in the center of each Landau level (dark orange) contribute to electronic transport whereas localized states (light orange) do not.

Landau level	filling factor range	electron correlation effect	section
$N = 0, \uparrow \text{ and } \downarrow$	$0 \leq \nu \leq 2$	FQHE, CFs	2.1.5, 2.2
$N = 1, \uparrow \text{ and } \downarrow$	$2 \leq \nu \leq 4$	CF pairing, FQHE	2.1.5, 2.1.6, 2.2.6
$N \geq 2$	$4 \leq \nu \leq \infty$	CDW states	2.3

Table 2.1: Landau level index N , the corresponding filling factor ranges and the observed electron correlation effects. Each effect is discussed in the listed sections.

for each state within a Landau level. This counting argument and therefore equation 2.15 still hold true when we include spin. When referring to the $N = 0$ Landau level we mean the two lowest spin split energy levels, i.e. $N = (0, \uparrow)$ and $N = (0, \downarrow)$. To avoid confusion, we have listed the relationship between Landau level index N and the corresponding filling factor range in table 2.1. The index N determines which electron correlation phenomena govern the transport properties of the 2DES.

2.1.3 Integer Quantum Hall Effect (IQHE)

In a self-consistent Born approximation (SCBA), the longitudinal resistivity is connected with the density of states at the Fermi energy according to $\rho_{xx} \sim D(E_F)^2$ [17]. At low magnetic fields, the density of states and thus the longitudinal resistance are constant. This is the regime where the Drude picture holds (cf. section 2.1.1). At intermediate fields, when the cyclotron gap exceeds the Landau level broadening, the density of states starts to oscillate as a function of the energy. Accordingly, the longitudinal resistivity displays the so called Shubnikov-deHaas oscillations (Fig. 2.4) when the magnetic field is varied [23]. The resistivity takes on a minimum at integer filling factors $\nu = 1, 2, 3, \dots$. The minima become true zeros (i.e. $\rho_{xx} \rightarrow 0$) at still higher magnetic fields. This indicates that scattering processes disappear at these points, and hence, electronic transport becomes dissipationless. Transport stays dissipationless for a finite range of magnetic fields as long as the chemical potential moves through the localized states. It turns out that in the same magnetic field range the Hall-resistivity stays quantized with very high accuracy to the value of the nearest integer filling factor i

$$\rho_{xy} = \frac{h}{ie^2}, \quad i = 1, 2, 3, \dots \quad (2.17)$$

The dissipationless transport together with the quantization of the Hall-resistivity over a range of magnetic fields constitutes the famous Integer Quantum Hall Effect (IQHE) [1, 24]. The existence of a mobility gap at the Fermi level together with topological arguments give a beautiful

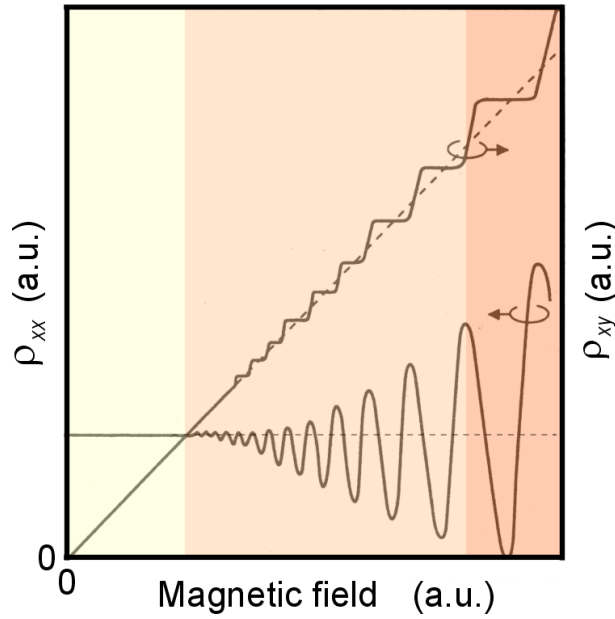


Figure 2.4: Resistivity tensor components ρ_{xx} and ρ_{xy} of a 2DES in a perpendicular magnetic field. In the low magnetic field regime (yellow), the classical Drude picture holds. At intermediate fields (light orange), Shubnikov-deHaas oscillations reflect the modification of the density of states by the magnetic field. Finally, in the high field regime (dark orange) dissipationless longitudinal transport and exactly quantized Hall-resistivity are the fingerprints of the IQHE.

explanation for the astonishing accuracy¹ and sturdiness of the IQHE in finite size samples [4]. Still, a complete and rigorous microscopic derivation of the effect using only local quantities (i.e. valid for an infinite sample) has yet to be found.

2.1.4 Landauer-Büttiker formalism

In many cases, the experimentally relevant resistances of a multi-terminal conductor (like a Hall-bar) can be determined by an approach originally put forward by Landauer and Büttiker [26]. It treats voltage and current terminals on an equal footing and describes electronic transport in terms of transmission probabilities between different terminals [27]. A current I_p flowing through terminal p is expressed as a function of the voltage difference $V_p - V_q$ with respect to all other terminals q of the sample

$$I_p = \frac{2e^2}{h} \sum_q T_{qp} [V_p - V_q] . \quad (2.18)$$

¹Since 1990, a fixed value of $R_{K-90} = 25812.807 \Omega$ for the v. Klitzing constant $R_K = h/e^2$ defines the resistance standard [25].

The transmission coefficients T_{qp} describe the probability of scattering an electron from terminal p to terminal q and take on values between 0 and 1. Each fully transmitting channel ($T = 1$) contributes a quantum $2e^2/h$ to the conductance. The Landauer-Büttiker formalism has been especially useful in the framework of the IQHE because of vanishing backscattering and the importance of the sample edges in this regime. The confinement potential bents upward the Landau levels towards the edges of the sample. Hence, Landau levels which lie below the Fermi energy in the bulk will cross the Fermi energy near the edges and form one dimensional edge channels with low energy excitations of the electronic system which is in equilibrium with the contact reservoirs. The current carrying channels ideally run parallel to the sample boundary (Fig. 2.5). The gradient of the confinement potential at the edges determines the direction of the electron velocity. Electrons in edge channels on opposite sides of the sample move in reversed directions. Each channel contributes exactly $2e^2/h$ to the total conductance because of a special relation between the electron velocity v and its density of states in a one dimensional channel

$$dn/dE = 1/hv . \quad (2.19)$$

Dissipationless transport and the quantization of the Hall resistance then follow very intuitively. Dissipation only occurs when electrons loose energy via backscattering processes. Because of the chiral nature of the edge channels and the large distance between edge channels of opposite current direction, backscattering and therefore dissipation are strongly suppressed. Hence, edge channels form equipotential lines and the voltage between two terminals connected to the same edge channels will always be zero. At the same time, each edge channels contributes exactly

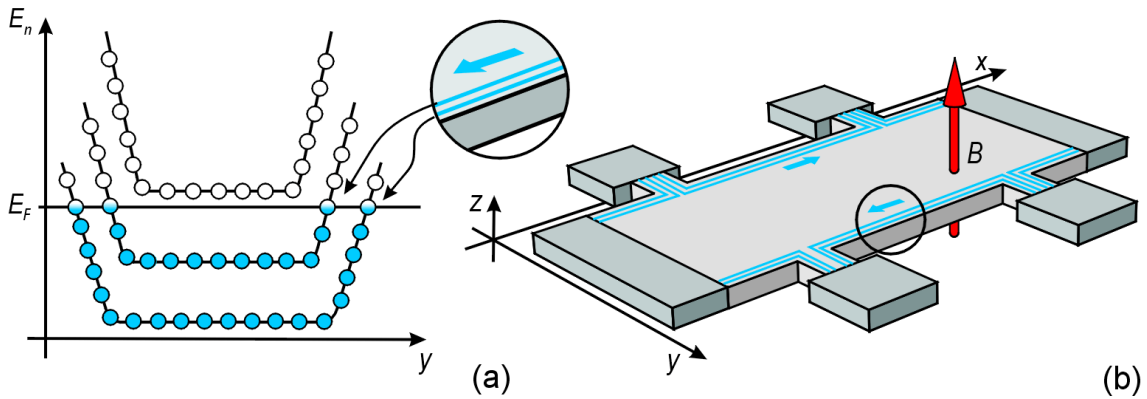


Figure 2.5: Landauer-Büttiker edge channel picture for bulk filling factor $\nu = 2$. (a) Landau level energies increase towards the edges of the sample because of the confinement potential. Partially occupied Landau levels (blue/white) exist whenever a filled level (blue) crosses the Fermi energy. (b) One-dimensional current carrying edge-channels exist at the positions of the partially filled Landau levels (circle).

one conductance quantum to the total conductance. Therefore, the Hall resistance is precisely quantized because it effectively measures the electrochemical potential difference between edge channels on opposite sides of the sample.

2.1.5 Fractional Quantum Hall Effect (FQHE)

The hallmarks of the Quantum Hall Effect, namely quantized Hall resistance and vanishing longitudinal resistance, are not restricted to integer filling factors (Fig. 2.6). In high mobility samples, they also appear at fractional filling factors $\nu = p/q$, where p, q are integers and q is odd [2, 28, 29]. This originally came as a big surprise because in the single particle picture explaining the IQHE no excitation gap is expected when Landau levels are only partially filled. In the Fractional Quantum Hall Effect (FQHE), electron-electron correlations mediated by the Coulomb interaction are responsible for the existence of the gap at the Fermi energy. In partially filled Landau levels, the number of electronic states exceeds the number of electrons to fill them and the ground state is therefore highly degenerate. Ample numerical and analytical evidence suggests that the Coulomb repulsion lifts this degeneracy and opens up an excitation gap [30]. Laughlin proposed a fermionic many-body ground state wavefunction for the most pronounced

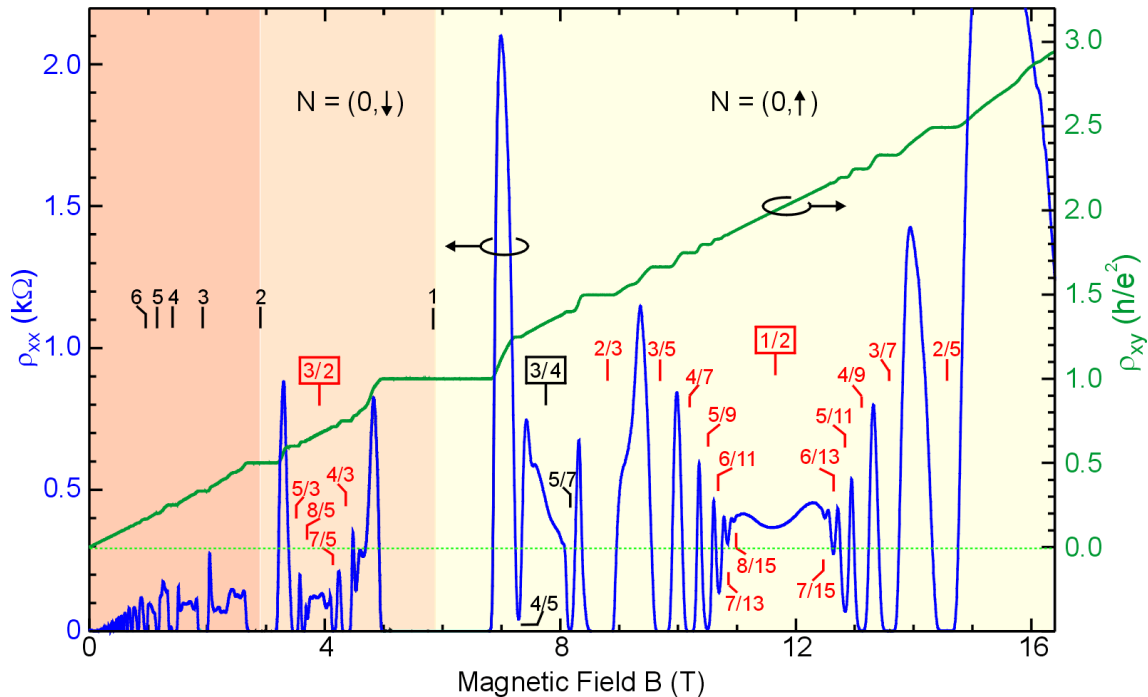


Figure 2.6: Longitudinal and Hall resistivity components for a high mobility 2DES sample at $T = 50$ mK. The FQHE appears mainly in the lowest Landau level $N = (0, \uparrow)$ and $N = (0, \downarrow)$ (yellow and light orange) at filling factors which converge towards half filling ($\nu = 1/2$ and $3/2$).

FQHE state at $\nu = 1/q$ of the form [3]

$$\chi_{(1/q)} = \prod_{i < j} \left(\frac{z_i - z_j}{l_B} \right)^q \exp \left[-\frac{1}{4} \sum_i \frac{|z_i|^2}{l_B^2} \right], \quad (2.20)$$

where $z_i = x_i + iy_i$ are the electron positions in complex notation. The wavefunction describes a homogeneous incompressible state in the lowest Landau level in which electrons optimally avoid each other to reduce the overall energy of the system. The lowest energy excitations are quasiparticles with charge $e^* = e/q$ and the excitation gap scales with the strength of the electron-electron interaction energy. The Laughlin wavefunction has an almost complete overlap with exact numerical wavefunctions obtained for systems with a small number of electrons. It can be shown to be the true ground state for the fractions $\nu = 1/q$. The explanation of the exact quantization and the finite extent of the Hall-plateaus and resistance minima in the FQHE is analogous to that for the IQHE (section 2.1.3) if electrons are replaced by Laughlin quasiparticles.

The Laughlin wavefunction also explains the FQHE at filling factors $\nu = 1 - 1/q$ by using electron-hole symmetry arguments [31]. The FQHE at other fractions such as $\nu = 3/5$ has originally been interpreted using a hierarchical scheme that involves Laughlin states recursively built from Laughlin quasiparticles instead of electrons [32]. This scheme produces very complicated wavefunctions and can not explain the relative strength of the FQHE states born out in experiment. More recently, the FQHE has been very elegantly rephrased in terms of new particles called Composite Fermions. These fascinating quasi-particles will be introduced in detail in section 2.2.

Since the FQHE appears at high magnetic fields, the early treatments always assumed the 2DES to be spin polarized. Meanwhile, it has become evident that many nontrivial effects in the regime of the FQHE originate from the electron spin (i.e. spin polarized-unpolarized phase transitions). We do not wish to enter this vastly growing field at this point, because it is not relevant to our work.

2.1.6 Higher Landau levels

Does the picture of the QHE survive as one moves to higher Landau levels ($N \geq 1$)? Naively, one would expect a repetition of the physics taking place in the lowest Landau level. This is indeed the case for the IQHE. It develops even when ten or more Landau levels are occupied. At still higher filling factors, the effect breaks down because disorder and temperature broadening of the levels become comparable to the cyclotron splitting, and the relevant gaps at the Fermi energy close. The situation is different for the FQHE. Already in the second Landau level ($N = 1$), unusual fractions appear at half filling that are in conflict with the orthodox theory of the FQHE. In the third or higher Landau levels ($N \geq 2$), the FQHE has never been observed.

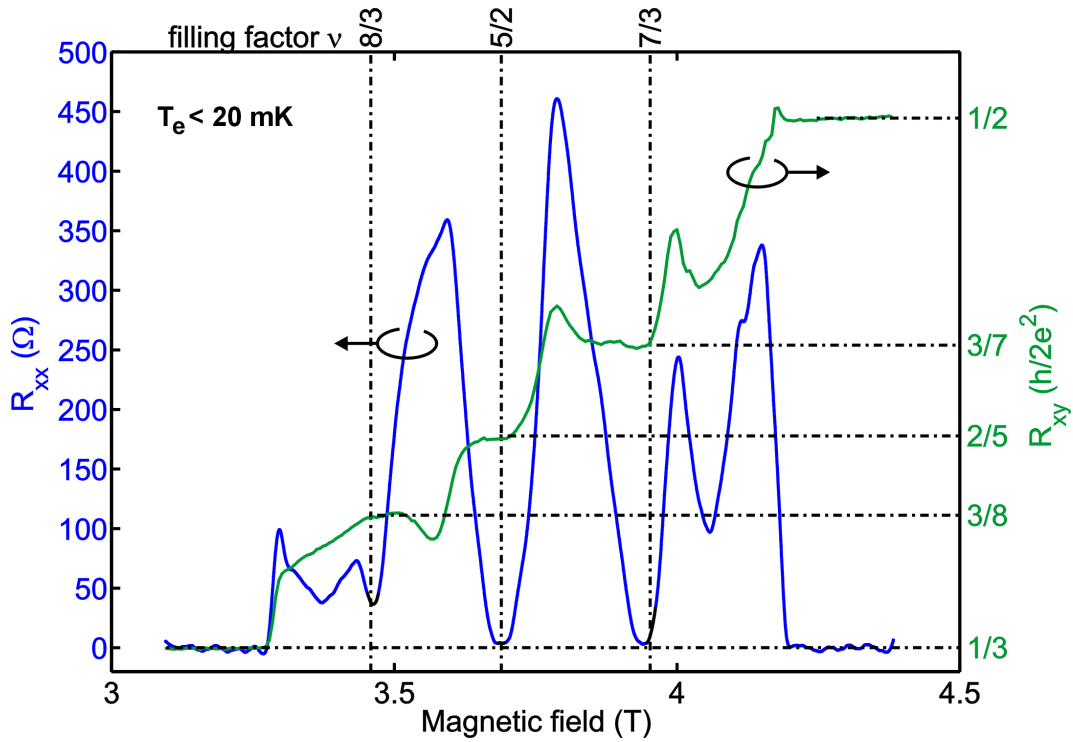


Figure 2.7: FQHE states in the first excited Landau level ($N = (1, \uparrow)$) around filling factor $5/2$. The fractions $7/3 = 2 + 1/3$ and $8/3 = 2 + 2/3$ are expected from the orthodox theory of the FQHE. The Quantum Hall state at the even denominator fraction $5/2$ is unexpected and can be explained by proposing a pairing mechanism for Composite Fermions (sec. 2.2.6).

FQHE states at $5/2$ and $7/2$

The apparent rule that the FQHE occurs only at fractions with odd denominator is deeply linked to the Fermi statistics of the constituent particles, namely electrons [33]. It therefore came as a great surprise that in the second lowest Landau level ($N = (1, \uparrow \text{ and } \downarrow)$) a FQHE state at $\nu = 5/2$ (Fig. 2.7) and $\nu = 7/2$ occurs [34, 35]. The apparent contradiction can be resolved if one postulates bosonic quasiparticles for these fractions. Initially, these quasiparticles were thought to consist of spin-singlet pairs of electrons [36]. This notion seemed to be corroborated by experiments where the FQHE state is destroyed in tilted magnetic fields [37]. The currently most favored explanation for this state is p-wave pairing of Composite Fermions (see sec. 2.2.6).

The Quantum Hall state at $\nu = 5/2$ is extremely fragile, with an activation energy gap of only $\Delta_{5/2} \approx 100$ mK for an electron density of $n = 2.3 \cdot 10^{15} \text{ m}^{-2}$ [35]. The proof of an exact quantization of this state has only been possible with the advent of very high mobility samples ($\mu \geq 1000 \text{ m}^2/\text{Vs}$) and very low electron temperatures ($T_e < 20$ mK) in recent years [35]. Our own results in figure 2.7 demonstrate that we are able to meet these requirements with the

ultra-low temperature probe (see Appendix B) that has been designed in the course of this PhD work.

Stripe and bubble phases

In higher Landau levels ($N \geq 2$) the FQHE has never been observed. Instead, the competition between repulsive and attractive Coulomb interaction components gives rise to completely new ground states with fragile long range ordered electronic phases. These so called stripe and bubble phases will be introduced in depth in section 2.3.

2.1.7 Aharonov-Bohm effect

A charged particle subjected to a magnetic vector-potential experiences a phase shift of its wavefunction that depends on the path along which the particle moves [38]. The wavefunction transforms according to

$$\Psi' = \Psi e^{-i\varphi} = \Psi \exp \left[-\frac{ie}{\hbar} \int_C \mathbf{A} \cdot d\mathbf{x} \right], \quad (2.21)$$

where C parameterizes the particle's path. Nontrivial phase shifts arise when the space of possible paths is not simply connected. e.g. in a ring (Fig. 2.8). Then, the total phase shift acquired is simply

$$\Delta\varphi = \frac{e}{\hbar} \Phi = 2\pi \frac{\Phi}{\phi_0}, \quad (2.22)$$

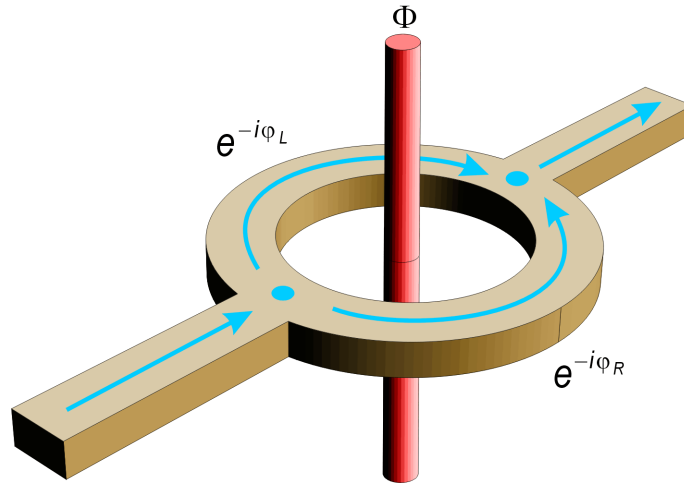


Figure 2.8: Aharonov-Bohm effect. Charged particles (blue) passing a magnetic flux line of strength Φ (red) on different sides acquire phase shifts φ_L and φ_R such that $\Delta\varphi = \varphi_L - \varphi_R = 2\pi\Phi/\phi_0$.

where Φ is the magnetic flux enclosed by the trajectories in the ring. Since the phase of the wavefunction is only defined modulo 2π , every physical quantity will be periodic in the external flux with a period of $\phi_0 = h/e$. By altering the phase of the wave-function, the enclosed flux has a measurable impact on the particle even though the flux is not actually "seen" by the particle, i.e. no classical electromagnetic forces act on it. The Aharonov-Bohm effect is truly quantum mechanical since it relies on the wavelike properties of each particle. It is also a topological effect since it depends on the particle's path and the structure of space, and it is especially important in low dimensional systems that are penetrated by a magnetic field.

2.2 Composite Fermions

In section 2.1.5 we have shortly introduced the FQHE. It shows the same hallmarks as the IQHE, i.e. vanishing longitudinal resistance and quantization of the Hall resistance. Still, the IQHE is understood in a picture of non-interacting electrons whereas the FQHE arises purely from many-body Coulomb interaction effects. In 1989, J. Jain introduced fascinating new quasiparticles called Composite Fermions which allow us to understand the FQHE in terms of the IQHE of these quasiparticles. It turns out that the concept of Composite Fermions is relevant beyond the FQHE, especially around filling factor $\nu = 1/2$. It is deeply rooted to particles statistics and two-dimensional quantum field theory.

For topological reasons, in two-dimensional systems the familiar concepts of Bose and Fermi statistics can be generalized to that of anyons obeying fractional statistics [39,40]. Moreover, using the idea of statistical transmutability, particle statistics can be changed at will without influencing the physical properties of the underlying system. Transmutation of statistics is implemented at the level of local quantum field theory by a universal construction, the so called Chern-Simons transformation [39]. Here, singular gauge fields are artificially introduced and interact with the constituent particles. Equivalently, this can be seen as attaching statistical flux tubes to the particles resulting in transformed composite particles [41]. At first glance, it seems that introducing additional fields or flux tubes into the problem will not lead to any simplifications. However, certain approximations propose themselves naturally in the composite particle representation that are not at all evident in the original one.

If an even number of flux tubes (each of unit strength ϕ_0) is attached to every electron in a 2DES, the resulting composite particles again obey Fermi statistics, i.e. they are Composite Fermions. Specifically, we will discuss the case where two statistical flux tubes are attached to each electron and the system is at filling factor $\nu = 1/2$. Then, the average of the statistical flux exactly cancels the external magnetic flux [6]. Thus, if fluctuations of the gauge field are ignored, the original situation of electrons in high magnetic field is greatly simplified to one of Composite Fermions at zero magnetic field.

2.2.1 Chern-Simons transformation

We start with a two dimensional interacting electron system in a uniform external magnetic field $\mathbf{B} = \nabla \times \mathbf{A}$. Additionally, we assume that the field is high enough such that the system is fully spin polarized and hence the spin degree of freedom can be neglected. The composite particle wavefunction Ψ_{CF} arises from a unitary transformation of the electron wavefunction Ψ_{el}

$$\Psi_{\text{CF}}(\mathbf{r}_i) = \prod_{i < j} \left(\frac{z_i - z_j}{|z_i - z_j|} \right)^{\tilde{\phi}} \Psi_{\text{el}}(\mathbf{r}_i), \quad (2.23)$$

where $\tilde{\phi} = 2m$ is an even number. Then, Ψ_{CF} also obeys Fermi statistics and thus we are dealing with Composite Fermions. In general, $\tilde{\phi}$ could be any number resulting also in bosons or anyons but we will not consider those cases here. From now on, we will only consider the case $m \equiv 1$. As a result of this singular gauge transformation, we have to adjust the Hamiltonian accordingly

$$H = \sum_j \frac{1}{2m^*} [\mathbf{p}_j - e\mathbf{A}(\mathbf{r}_j) - \mathbf{a}(\mathbf{r}_j)]^2 + V. \quad (2.24)$$

where V is the Coulomb interaction potential and $\mathbf{a}(\mathbf{r})$ is the Chern-Simons vector potential of the form

$$\mathbf{a}(\mathbf{r}) = \frac{-2\phi_0}{2\pi} \sum_{k \neq j} \frac{\hat{\mathbf{z}} \times (\mathbf{r}_j - \mathbf{r}_k)}{|\mathbf{r}_j - \mathbf{r}_k|^2}. \quad (2.25)$$

This results in a fictitious, singular magnetic field

$$\mathbf{b} = \nabla \times \mathbf{a} = -2\phi_0 \hat{\mathbf{z}} \sum_{j \neq k} \delta(\mathbf{r}_j - \mathbf{r}_k), \quad (2.26)$$

that is only nonzero at the positions of the electrons.

2.2.2 Mean field approximation

The merits of the Chern-Simons transformation become obvious when the Composite Fermion system is analyzed on a mean-field level, i.e. when the fictitious, singular magnetic flux tubes (eq. 2.26) are smeared out into a homogenous magnetic field

$$\langle b \rangle = b - \delta b = -2\phi_0 n, \quad (2.27)$$

and the Coulomb interaction is neglected.² The Chern-Simons flux has been chosen to be in the opposite direction of the external magnetic field so that the residual effective magnetic field B_{eff} seen by the Composite Fermions is given by

$$B_{\text{eff}} = B - 2\phi_0 n. \quad (2.28)$$

²With hindsight, this is justified because most of the electronic correlations induced by the Coulomb interaction are accounted for by the introduction of statistical flux tubes [6].

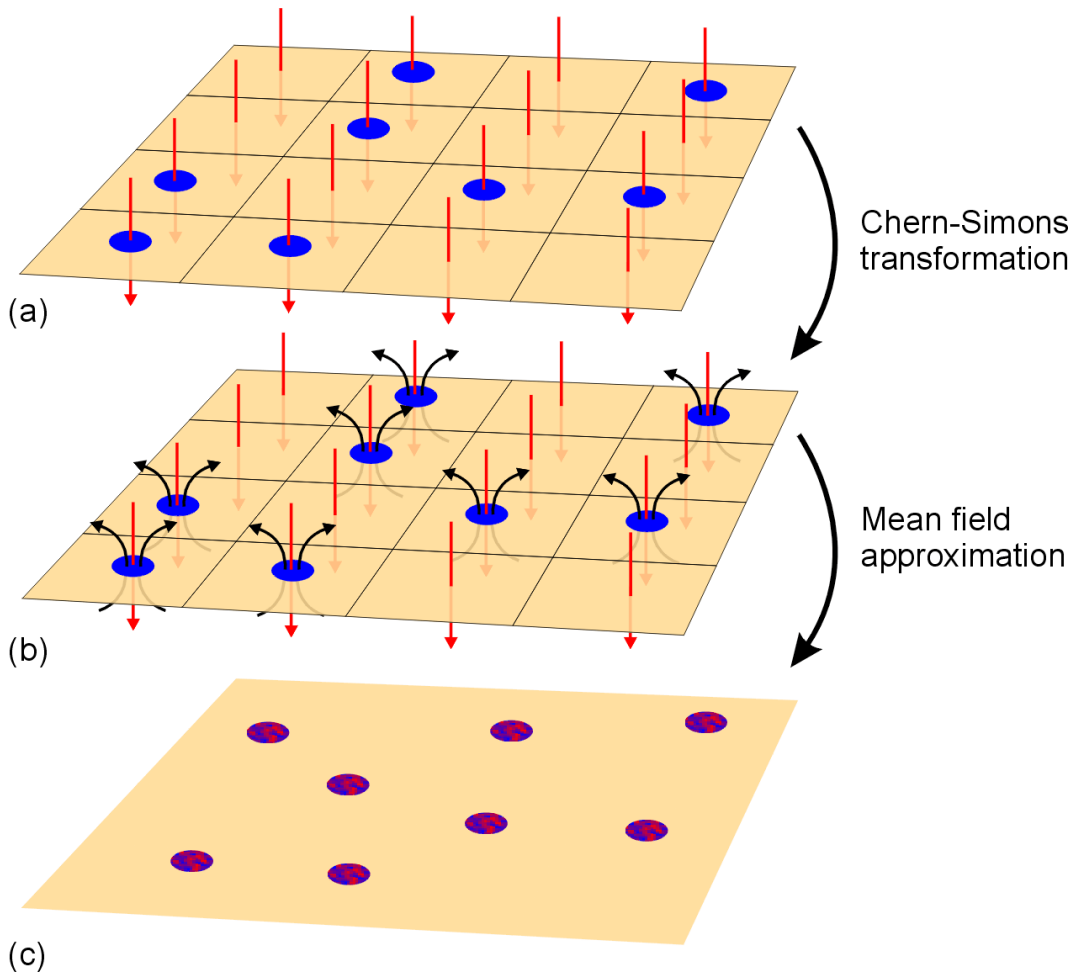


Figure 2.9: Composite Fermion picture. (a) The external magnetic field creates one electronic state (squares) for each flux quantum (red arrow) through the sample. At $\nu = 1/2$, half of the states are occupied by electrons (blue). (b) The Chern-Simons transformation attaches two statistical flux tubes (black arrows) to each electron. (c) In the mean field approximation, the external flux and the statistical flux cancel. The system then consists of weakly interacting Composite Fermions without an effective magnetic field ($B_{\text{eff}} = 0$).

Taken literally, this result has astonishing implications. A system of electrons in an external magnetic field can be transformed into a system of Composite Fermions that is subjected to a reduced effective magnetic field.

Strikingly, when the external magnetic field is adjusted to the filling factor $\nu = 1/2$ the effective magnetic field experienced by the Composite Fermions vanishes. The ground state of this Fermi system at $B_{\text{eff}} = 0$ will be a metallic Fermi sea filled up to the Fermi-wavevector

$$k_{\text{F}}^{(1/2)} = \sqrt{4\pi n}. \quad (2.29)$$

The additional factor of $\sqrt{2}$ over the electron case (eq. 2.4) arises from a simple counting argument because the system is assumed to be spin polarized. Accordingly, at finite but small effective magnetic fields Composite Fermions should follow semi-classical cyclotron trajectories with a radius

$$R_c^{\text{CF}} = \frac{\hbar k_F^{(1/2)}}{|e|B_{\text{eff}}}. \quad (2.30)$$

These two predictions, the existence of a Fermi surface for the Composite Fermion liquid and the relevance of the effective cyclotron radius, have been verified by experiments for $\nu = 1/2$ [42, 43, 44] and will be discussed further in chapter 3.

2.2.3 Beyond mean field - the RPA approximation

Very profound predictions concerning the behavior of 2DES around $\nu = 1/2$ are already obtained at the mean field level of the Composite Fermion picture (eqs. 2.28 - 2.30). However, many questions remain unsolved at this level of approximation. For example, why is the Hall resistivity $\rho_{xy} = h/2e^2$ at this filling factor and not zero as it should be for a metallic system at zero magnetic field. To solve these issues, it is important to take fluctuations of the gauge field δb into account (see eq. 2.27). This is done in the framework of the RPA or time-dependent Hartree approximation [6]. Since the derivations are rather cumbersome and not very illuminating for our discussion, we will just state the most important results and fit them into an intuitive picture of Composite Fermion transport.

The resistivity tensor for electrons directly at $\nu = 1/2$ can be written as a sum of two components that result from Composite Fermion theory at the RPA level [6]

$$\rho = \rho^{\text{CS}} + \rho^{\text{CF}}. \quad (2.31)$$

The first contribution originates from the Chern-Simons gauge field term in the Hamiltonian (eq. 2.24)

$$\rho^{\text{CS}} = \frac{4\pi\hbar}{e^2} \begin{pmatrix} 0 & -1 \\ 1 & 0 \end{pmatrix}, \quad (2.32)$$

and is responsible for the value of the Hall resistance at $B_{\text{eff}} = 0$. This term can be motivated by a hand-waving argument. For each electron, two flux tubes connected to it have to be moved through the sample. According to Faraday's law $V = -d\Phi/dt$, this leads to a transverse resistance

$$R_{xy} = \frac{d\Phi}{dQ} = \frac{2\Phi_0}{e} = \frac{2h}{e^2}, \quad (2.33)$$

where Q is the total charge. Therefore, although we are dealing with a metallic system of Composite Fermions at vanishing B_{eff} , the Hall resistivity is finite because Composite Fermions by definition carry magnetic flux tubes around with them. The second term in equation 2.31

$$\rho^{\text{CF}} = \rho_0^{\text{CF}} \begin{pmatrix} 1 & 0 \\ 0 & 1 \end{pmatrix}, \quad (2.34)$$

is the resistivity of a Fermi system with contributions from impurity scattering as well as scattering induced by gauge field fluctuations. The latter are a qualitatively new ingredient when dealing with Composite Fermion transport. Small density fluctuations Δn translate via equation 2.28 into substantial effective magnetic fields ΔB_{eff} . These magnetic fluctuations provide strong scattering centers. Assuming that gauge field contributions can be absorbed into a modified transport scattering time τ^{CF} , one may cast the longitudinal resistivity in the Drude form similar to equation 2.7

$$\rho_0^{\text{CF}} = \frac{m_{\text{CF}}^*}{ne^2\tau^{\text{CF}}} = \frac{1}{n|e|\mu^{\text{CF}}} . \quad (2.35)$$

From an experimental point of view, it is most convenient to use the last term of the equation since it does not include the effective mass m_{CF}^* of Composite Fermions. There is still considerable debate about the value of this effective mass exactly at $\nu = 1/2$, although recent experiments indicate that it is roughly an order of magnitude higher than the effective electron mass at zero magnetic field, i.e. $m_{\text{CF}}^* \approx 10m^*$ [45]. Using eq. 2.35, one can experimentally determine the mobility of Composite Fermions by measuring the longitudinal resistivity directly at $\nu = 1/2$, i.e. at $B_{\text{eff}} = 0$. This mobility turns out to be about two orders of magnitude lower when compared to that of electrons at $B = 0$. Taking into account the increased effective Composite Fermion mass, the scattering time τ^{CF} is at least one order of magnitude smaller than the one for electrons at zero field. Evidently then, scattering by gauge field fluctuations is an effective mechanism and must be taken into account when quantifying Composite Fermion transport.

2.2.4 The FQHE revisited - The IQHE of Composite Fermions

In analogy to the electronic case, the energy spectrum of a Composite Fermion system subjected to a non-zero effective magnetic field should consist of discrete Landau levels. Accordingly, it should display the IQHE effect near integer effective filling factors

$$\nu_{\text{eff}} = \frac{n\phi_0}{B_{\text{eff}}} = \pm 1, 2, 3, \dots . \quad (2.36)$$

These are related to the electronic filling factor (eq. 2.15) via

$$\nu = \frac{|\nu_{\text{eff}}|}{2\nu_{\text{eff}} \pm 1} . \quad (2.37)$$

Strikingly, the IQHE of Composite Fermions occurs at exactly those positions where the FQHE for electrons occur. Indeed, the FQHE effect of electrons, which is purely driven by electron-electron interactions is a manifestation of single-particle physics on the level of Composite Fermions [46]. The close connection between the FQHE of electrons and IQHE of Composite Fermions can be seen also from a closer look at the wavefunctions. For example, the electronic wavefunction for the IQHE state at $\nu = 1$ reads [47]

$$\chi_1 = \prod_{i < j} \left(\frac{z_j - z_k}{l_B} \right) \exp \left[-\frac{1}{4} \sum_i \frac{|z_i|^2}{l_B^2} \right] . \quad (2.38)$$

Performing a Chern-Simons transformation (eq. 2.23) with index $\tilde{\phi} = q - 1$ yields the equation

$$\chi_{(1/q)} = \prod_{i < j} \left(\frac{z_j - z_k}{|z_j - z_k|} \right)^q \exp \left[-\frac{1}{4} \sum_i \frac{|z_i|^2}{l_B^2} \right]. \quad (2.39)$$

This resembles Laughlin's famous wavefunction for the FQHE state at $\nu = 1/q$ (eq. 2.20). The difference in the prefactor is eliminated if one includes higher order terms that appear in the RPA approximation [48].

We have learned in section 2.1.5 that Laughlin quasi-particles at $\nu = 1/q$ possess a fractional charge $e^* = e(1 - 2\nu) = e/q$.³ On the other hand, Composite Fermions are quasi-particles with charge e subjected to an effective magnetic field $B_{\text{eff}} = B - 2n\Phi_0 = B(1 - 2\nu)$. No contradiction arises here because the expression $eB_{\text{eff}} = eB(1 - 2\nu) = e^*B$ remains the same in both pictures.

To summarize, the FQHE can be very elegantly rephrased as the IQHE of Composite Fermions. This notion not only explains most of the observed fractions and their relative strength, it also shows how a strongly interacting system can be recast into a weakly interacting one.

2.2.5 Composite Fermions at filling fraction $\nu = 3/2$

At filling factor $\nu = 3/2$, the spin up branch of the lowest Landau level ($N = (0, \uparrow)$) is completely filled with electrons, whereas the spin down branch ($N = (0, \downarrow)$) is only half filled. All electrons in the partly filled branch can be converted into Composite Fermions whereas the other electrons remain normal, i.e. they are not dressed with flux tubes (Fig. 2.10). Therefore, the situation is largely equivalent to the one at $\nu = 1/2$ with a few differences that are related to the reduced Composite Fermion density which now also depends on the external magnetic field [6, 50]. The effective magnetic field is

$$B_{\text{eff}}^{(3/2)} = B - 2\Phi_0 n_{\text{CF}}, \quad (2.40)$$

where the total carrier density n in eq. 2.28 has been replaced by the Composite Fermion density n_{CF} . Using the constraint $n = n_e + n_{\text{CF}}$, with n_e being the density of normal electrons, the last equation can be expressed in terms of the magnetic field $B_\nu = n\Phi_0/\nu$ exactly at $\nu = 3/2$

$$B_{\text{eff}}^{(3/2)} = 3(B - B_{3/2}), \quad (2.41)$$

where we have also used $n_e = B/\Phi_0$ because of the completely filled lowest Landau level. The effective magnetic field is zero at $\nu = 3/2$ and its scale is stretched by a factor of 3 as compared to the case at $\nu = 1/2$. Since the Composite Fermion density changes with the external magnetic field, the Fermi wave vector depends on the filling factor

$$k_{\text{F}}^{(3/2)} = \sqrt{4\pi n_{\text{CF}}} = \sqrt{\frac{\nu - 1}{\nu}} k_{\text{F}}^{(1/2)}. \quad (2.42)$$

³This was originally shown for $q = 3, 5, \dots$. However, the picture has been extended to that of dipolar quasi-particles where q can be any number, e.g. $q = 2$ [49].

The conductivity tensor exactly at filling factor $\nu = 3/2$ is the sum of the tensor for a full Landau level and a half filled one

$$\sigma^{(3/2)} = \begin{pmatrix} 0 & 1 \\ -1 & 0 \end{pmatrix} \frac{e^2}{h} + \begin{pmatrix} \sigma_{xx}^{(1/2)} & e^2/2h \\ -e^2/2h & \sigma_{xx}^{(1/2)} \end{pmatrix} = \begin{pmatrix} \sigma_{xx}^{(1/2)} & 3e^2/2h \\ -3e^2/2h & \sigma_{xx}^{(1/2)} \end{pmatrix}, \quad (2.43)$$

where $\sigma_{xx}^{(1/2)}$ is the electronic σ_{xx} at $\nu = 1/2$ which is related to the resistivities at the same filling factor by

$$\sigma_{xx}^{(1/2)} = \frac{\rho_{xx}^{(1/2)}}{(\rho_{xx}^{(1/2)})^2 + (\rho_{xy}^{(1/2)})^2} \approx \frac{\rho_{xx}^{(1/2)}}{(2h/e^2)^2}. \quad (2.44)$$

Here we used $\rho_{xx}^{(1/2)} \ll \rho_{xy}^{(1/2)} = 2h/e^2$. The longitudinal resistivity $\rho_{xx}^{(3/2)}$ at $\nu = 3/2$ follows from inversion of the above conductivity tensor

$$\rho_{xx}^{(3/2)} = \frac{\sigma_{xx}^{(1/2)}}{(\sigma_{xx}^{(1/2)})^2 + (3e^2/2h)^2} \approx \frac{\rho_{xx}^{(1/2)}}{9}. \quad (2.45)$$

Then the mobility of Composite Fermions in the upper half filled Landau level is

$$\mu^{\text{CF}} = \frac{1}{\rho_{xx}^{(1/2)} n_{\text{CF}} e} = \frac{1}{3\rho_{xx}^{(3/2)} n e}. \quad (2.46)$$

If we assume that the mobility of Composite Fermions at $\nu = 1/2$ and $\nu = 3/2$ is the same, then the longitudinal resistivity at $\nu = 3/2$ should be reduced by a factor of three compared to that at $\nu = 1/2$. This is indeed true to a very good approximation in high quality samples (Fig. 2.6).

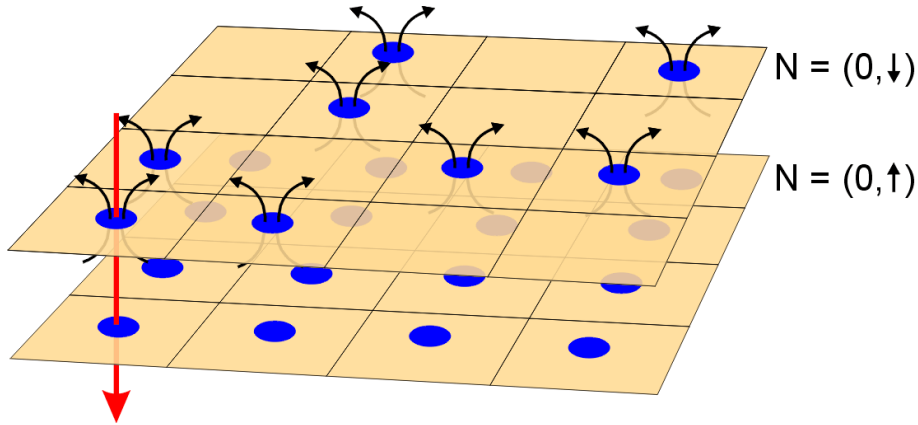


Figure 2.10: Electron system at filling factor $\nu = 3/2$. The spin up branch of the lowest Landau level ($N = (0, \uparrow)$) is fully occupied with normal electrons, whereas the spin down branch ($N = (0, \downarrow)$) is half filled with Composite Fermions. The statistical flux (black arrows) of the Composite Fermions completely cancels the external magnetic field (red arrow - only one is depicted for clarity - see Fig. 2.9) on the mean field level.

2.2.6 Composite Fermions in higher Landau levels

The powerfulness of the CF picture in the lowest Landau level is based on the observation that CFs can be treated as non-interacting particles to a very good approximation. This means that electron-electron correlations induced by the Coulomb interaction are well incorporated into the CF wavefunction (eq. 2.23). In a sense, the Coulomb interaction is replaced by the effect of statistical flux tubes that induce very similar correlations.

In higher Landau levels, the short range repulsive part of the Coulomb interaction is weakened by virtual excitations involving the completely filled lower levels [51].⁴ The flux attachment procedure is the same as in the lowest Landau level, and therefore one expects that the Coulomb interaction will not be completely cancelled by it. Instead, the Coulomb interaction will be overscreened and a residual attractive interaction between Composite Fermions results. In the $N = 1$ Landau level, the weak attractive interaction allows Composite Fermions to form pairs that behave as bosons and then condense into their ground state at low temperatures.⁵ This is the reason why a Quantum Hall state is possible at half filled Landau level $\nu = 5/2$ and $\nu = 7/2$. The rule that only odd denominators are allowed just holds for fermions. It is

⁴Equivalently speaking, the electron wavefunctions - compared at the same magnetic field values - are more spread out towards higher Landau levels (compare section 2.3.1).

⁵The situation in superconductors where phonon mediated effective electron-electron attraction leads to boson (Cooper pair) condensation is very analogous.

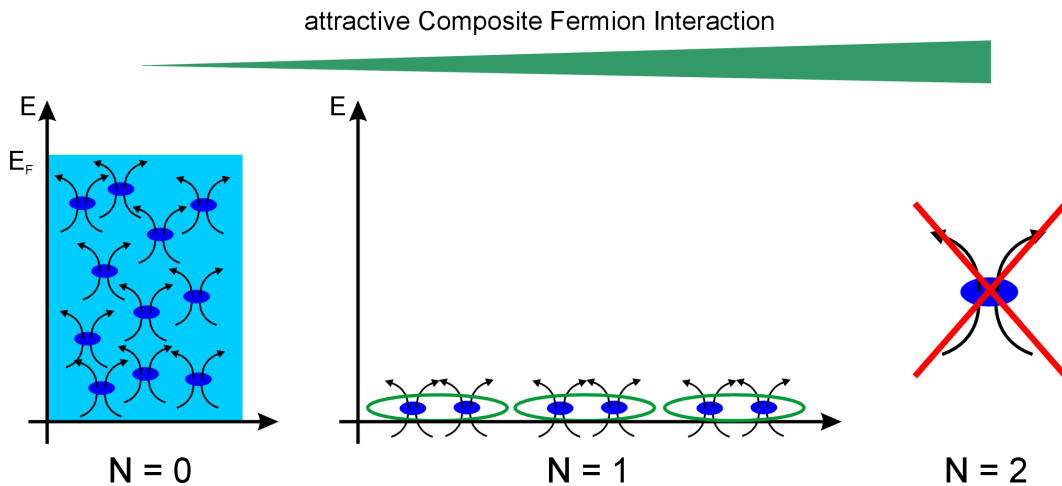


Figure 2.11: Because the Coulomb interaction becomes weaker in higher Landau levels, the flux tube attachment overscreens the Coulomb interaction and leads to an effective attractive interaction between CFs. Whereas in the lowest Landau level, CF fill up a Fermi sea, they form pairs in the next Landau level and thus condense into a ground state like bosons. In the $N = 2$ Landau level, the attraction is so strong that the CF picture presumably loses its meaning.

currently believed that the ground state at the half filled $N = 1$ Landau level is the Moore-Read state

$$\Psi_{\text{MR}} = \text{Pf} \frac{1}{z_i - z_j} \chi_{(1/2)}, \quad (2.47)$$

with $\chi_{(1/2)}$ being the Laughlin wavefunction (eq. 2.39) for $q = 2$ and the Pfaffian Pf is a special antisymmetrisation operator [51]. The wavefunction describes p-wave pairing of Composite Fermions [51]. The state has a very peculiar nature and is under strong investigation since it is thought to have quasiparticles with nonabelian statistics. The experimental implications of this peculiar statistics of the quasiparticles have not been resolved. In the $N = 2$ Landau level, the residual attractive interaction between Composite Fermions is so strong that the validity of the Composite Fermions picture itself is questionable. Instead, correlation effects in this Landau Level are usually described in the CDW-picture of electrons (sec. 2.3.1). Whether the competition of long range Coulomb repulsion and short range attraction that leads to the formation of CDW-like states can be also formulated in the framework of Composite Fermions is still an open question.

2.3 Correlated phases in higher Landau levels

Electron correlations in the two lowest Landau levels ($N = 0, 1$) give rise to the FQHE. However, they manifest themselves in a qualitatively different way in higher Landau levels ($N \geq 2$). There, the existence of completely filled lower Landau levels modifies the balance between the long range, repulsive part and the short ranged, attractive part of the Coulomb interaction. As a consequence, it is energetically favorable for the electron system to break up into regions of integer filling factors. Within these regions, the topmost Landau level is either completely filled with electrons or completely empty. Regions of the same filling factor arrange themselves into long range ordered patterns with a symmetry which depends on the average filling factor. Similar examples of self-organization arising from the competition of attractive and repulsive forces on different length scales are known from other areas of physics like magnetic thin films and ferrofluids [15]. The separation of the system into regions of distinct filling factors within the bulk of the sample also brings about a modulation of the electron density. This has led to the formulation of the Charge Density Wave (CDW) picture of electron correlations in higher Landau levels. In early years, self consistent Hartree-Fock calculations suggested that charge-density-wave (CDW)-like states would be the ground states of a 2DES in strong magnetic fields [52]. With the discovery of the FQHE, this notion was discarded because it turned out that Laughlin states (eq. 2.20) have the lowest energy. However, in the third and higher Landau levels ($N \geq 2$) no FQHE states have ever been observed. Numerical calculations show that slight differences in the electron-electron interaction in these Landau levels favor the CDW-like states and lead to qualitatively different magnetotransport behavior [10,9,53]. Because the formation energies for the CDW-like states are extremely small, they only exist at very low temperatures

($T < 150$ mK) and in very high mobility samples ($\mu \geq 1 \cdot 10^7$ cm²/Vs).

Recently the CDW-picture has been extended. When quantum fluctuations are properly taken into account, a more sophisticated picture arises, referred to as the Electron Liquid Crystal (ELC) picture [13]. It bears a strong similarity to the description of ordinary, classical liquid crystal systems [14].

Within the framework of the very intuitive CDW picture, we discuss the different correlated phases together with their experimental signatures. Afterwards, we present the more realistic ELC picture.

2.3.1 Charge Density Wave (CDW) picture

In order to understand the effect of the competition between the repulsive and the attractive part of the Coulomb interaction on an intuitive level, we should consider the shape of the wavefunction for electrons in higher Landau levels. In the symmetric gauge, they resemble rings with a size determined by the cyclotron radius R_c and a width given by the magnetic length l_B (Fig. 2.12(b)) [10]. This picture of extended rings becomes more exact for $N \gg 1$ because $R_c = \sqrt{2N+1} l_B$, however, it is already a good approximation at $N = 2$. The direct part of the Coulomb interaction between two electrons depends on the overlap of the electron density distributions (i.e. of the rings), whereas the exchange part depends on the distance between the center coordinates of the wavefunctions. For this reason, it is energetically favorable for the wavefunction centers to arrange into clusters, with a distance between neighboring clusters on the order of the cyclotron radius. This maximizes the attractive exchange interaction, while at the same time, the repulsive direct interaction increases only slightly, since rings in adjacent clusters overlap almost as much as rings within the same cluster (Fig. 2.12(c)). Since the position of the wavefunction centers determines the local filling factor ν_N^{loc} , one can think of the electron system as breaking up into clusters with either a completely filled ($\nu_N^{\text{loc}} = 1$) or a completely empty ($\nu_N^{\text{loc}} = 0$) topmost Landau level (Fig. 2.12(a)). The relative abundance of each type of cluster depends on the average filling factor of the topmost Landau level $\nu_N = \nu - [\nu]$ where $[\nu]$ is the greatest integer less than ν . Although the local filling factor is strongly modulated, the extended shape of a wavefunction produces only a weak modulation of the average electron density (Fig. 2.12(a)). The states are referred to as Charge Density Wave (CDW) phases in analogy to similar density modulations in other materials [10, 9]. Depending on the average filling factor ν_N of the topmost Landau level, the CDW states have different long range spatial symmetries induced by the repulsive part of the interaction forces (Fig. 2.12(d)). One distinguishes between anisotropic stripe phases and isotropic bubble or Wigner crystal phases. In each phase, the characteristic length scale, i.e. the distance between adjacent bubbles or stripes, is [10]

$$\lambda_{\text{CDW}} \approx \frac{2\pi R_c}{2.4}. \quad (2.48)$$

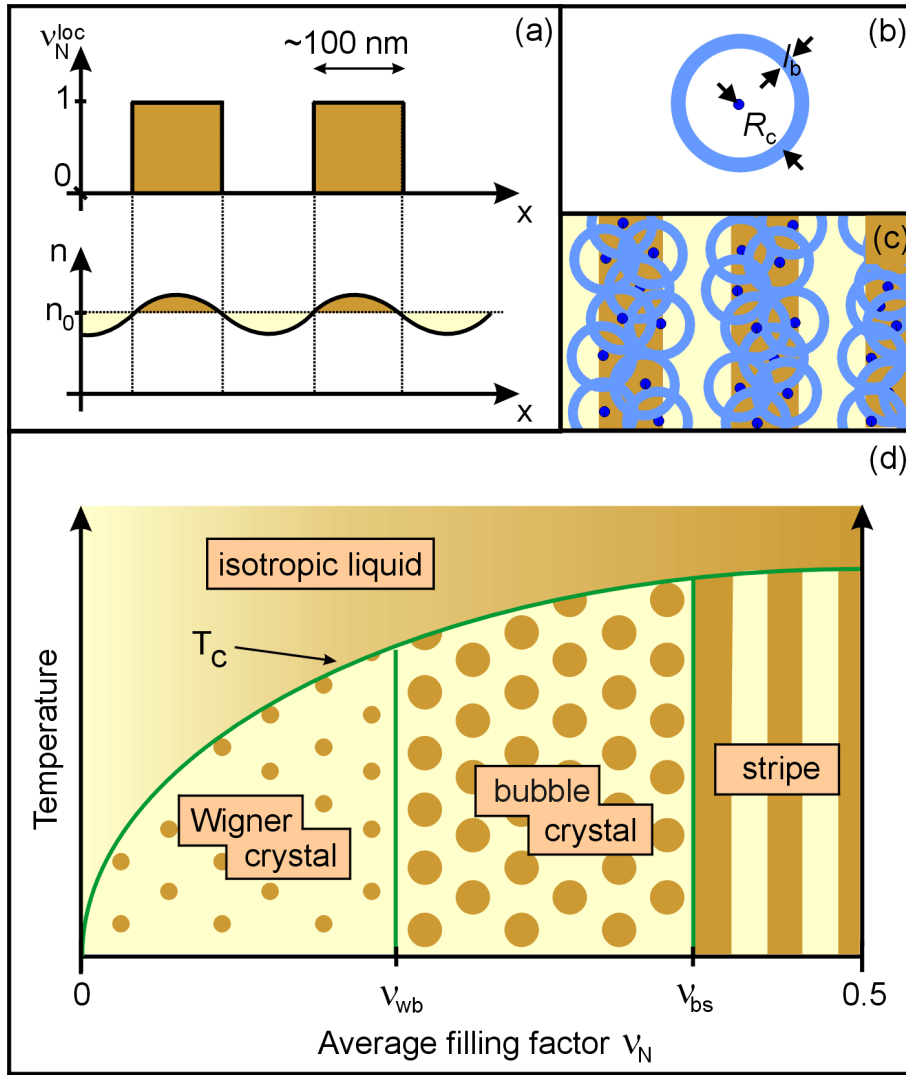


Figure 2.12: (a) Modulation of the local filling factor ν_N^{loc} (top) and the electron density n (bottom) of the topmost Landau level within the CDW phases. (b) Ringlike shape of the electron wavefunction in higher Landau levels ($N \geq 2$). (c) Electrons cluster into long range ordered patterns (e.g. stripes). Still, electron density variations are small because of the extended nature of the electron wavefunctions. (d) Approximate phase diagram for the $N = 2$ Landau level according to the CDW picture. Phases consist of domains with integer local filling factors. Light areas correspond to $\nu_N^{\text{loc}} = 0$ and dark ones to $\nu_N^{\text{loc}} = 1$. The ordered CDW phases break down into an isotropic liquid phase above a critical temperature T_c .

For a typical sample density, $n = 2 \cdot 10^{15} \text{ m}^{-2}$, around filling factor $\nu = 9/2$, this amounts to $\lambda_{\text{CDW}} \approx 100 \text{ nm}$.

Near half filling, $\nu_N \approx 0.5$, the ground state is an anisotropic stripe phase. Towards lower

fillings, first an isotropic 2-electron bubble phase⁶ appears, followed by a Wigner crystal phase, both with a triangular symmetry. Above a critical transition temperature T_c , the correlated CDW phases cease to exist and give way to an ordinary, isotropic electron liquid. So far, the best prediction for the position of the phase boundaries at $T = 0$ comes from the density matrix renormalization group (DMRG) method [53]. We discuss each phase separately in the next three sections.

Stripe phase

The anisotropic stripe phase is predicted to be stable near the half filled Landau level, i.e. in the filling factor range $0.4 < \nu_N^{\text{theo}} < 0.6$ [53, 10]. In this phase, electrons cluster into parallel stripes of alternating integer filling factor which have a distance of λ_{CDW} to each other. In the simplest picture, perfectly parallel stripes extend throughout the sample. The stripes consist of regions of alternating filling factors (e.g. $\nu = 4$ and $\nu = 5$) and the width of the stripes is on the

⁶Hartree-Fock calculations also predict a 3-electron bubble phase in the $N = 2$ Landau level. There is no sign of this phase, though, in more sophisticated approximations [53] as well as experiments.

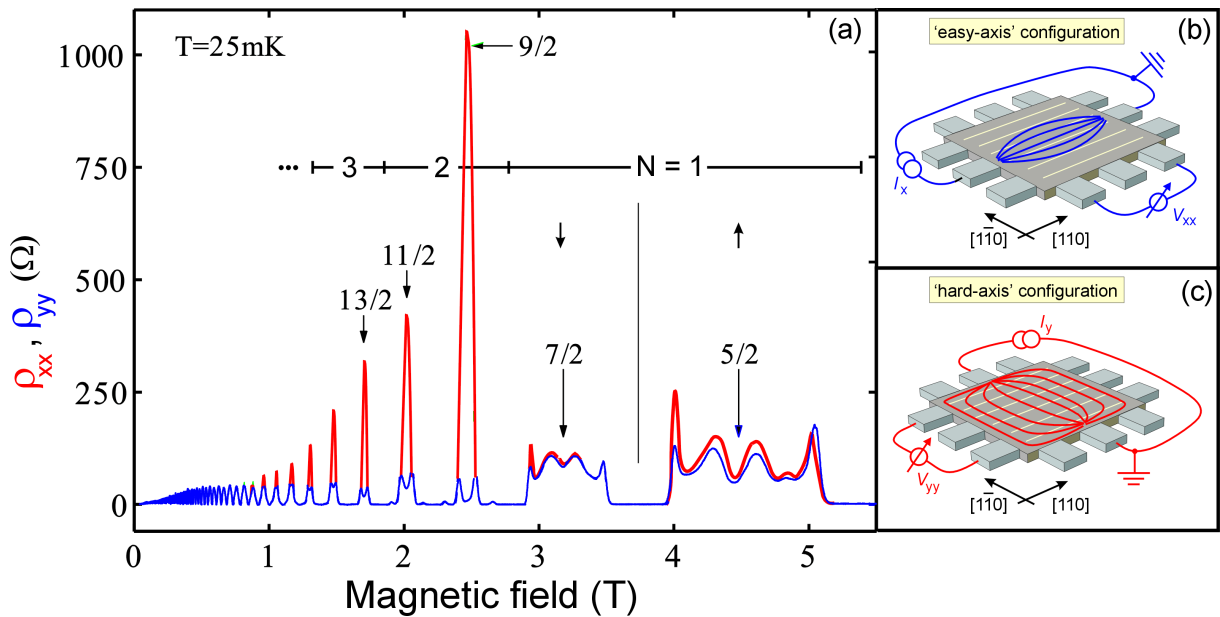


Figure 2.13: Anisotropic transport in higher Landau levels ($N \geq 2$). When the current is directed perpendicular to the stripes (red - 'hard-axis' configuration (c)), a huge resistance peak occurs around half filled Landau levels (e.g. $\nu = 9/2$). In the perpendicular current direction (blue - 'easy-axis' configuration (c)), a pronounced minimum is observed instead. No anisotropy is visible in the $N = 1$ Landau level. Data from [7].

order of 100 nm for typical sample densities [10].⁷

The most striking experimental signature of the stripe phase is the large anisotropy which shows up in the longitudinal resistance [54, 35]. If the current is directed along the stripes, the resistance is very low, whereas for current directed in the perpendicular direction, a huge resistance maximum occurs (Fig. 2.13). Because of current channeling [55], resistance anisotropies in square samples can be as high as $R_{xx}/R_{yy} \approx 3500$, whereas they are substantially smaller (≈ 10) for conventional Hall-bars [56]. The resistance anisotropy increases with decreasing temperature. Nevertheless, the maximum resistance seems to saturate at a value close to $R_{xx} \approx 1300 \Omega$ at the lowest temperatures. The mechanism that aligns the stripes with a certain crystal direction is still unclear [57].⁸ It has been shown that the stripe direction can be influenced with a magnetic field component pointing parallel to the 2DES [59, 56]. For the usual samples, the stripes orient themselves perpendicular to the field direction at sufficiently high in-plane magnetic fields. This has been confirmed theoretically [60].

Bubble phase

Further away from half filling, the ground state is the 2-electron bubble phase which is believed to be isotropic [10]. The bubble phase is theoretically predicted to be stabilized in the filling factor regime $0.25 < \nu_N^{\text{theo}} < 0.36$ [53]. It is thought to consist of islands (bubbles) of one filling factor $\nu = m$ immersed in a background of a neighboring filling factor $\nu = m \pm 1$. The bubbles form a long range ordered triangular crystal with a lattice constant λ_{CDW} . Therefore, the bubble phase is the many particle analogue of the famous Wigner crystal [12] (see next section). Weak long range disorder is sufficient to localize the bubble crystal at low temperatures giving rise to an insulating phase in which the longitudinal resistance vanishes and the Hall resistance is quantized. Unlike for the FQHE though, the Hall resistance is quantized to the value of the nearest integer filling factor (Fig.2.14). The bubble phase can only be distinguished from the neighboring IQHE because both regimes are separated by a narrow range of magnetic fields in which the longitudinal resistance is non-zero. For this reason, the quantization effect in the bubble phase is dubbed the Reentrant Integer Quantum Hall Effect (RIQHE). In analogy to the ordinary IQHE, where single electrons are localized by a short range disorder potential, the RIQHE is explained as collective pinning of a bubble crystal by weak long range disorder.

Non-equilibrium transport measurements have further supported the existence of a bubble phase. When a high DC current bias is applied to the sample in the bubble phase regime, the RIQHE suddenly breaks down in a hysteretic way [54]. This is thought to be an indication of a first order depinning transition of the bubble crystal. At sufficiently high bias, the bubble

⁷The charge for each electron is smeared out over a similar scale and therefore the overall charge modulation in the stripe state is only of the order of 15%. To be precise one should therefore speak of a filling-factor-wave state instead of a CDW state.

⁸At the usual 2DES densities ($n \approx 1 - 2 \cdot 10^{15} \text{ m}^{-2}$), the stripes are always aligned along the [110] crystal axis. Above $n \approx 2.9 \cdot 10^{15} \text{ m}^{-2}$, the stripes may rotate into the [1 $\bar{1}$ 0] direction [58].

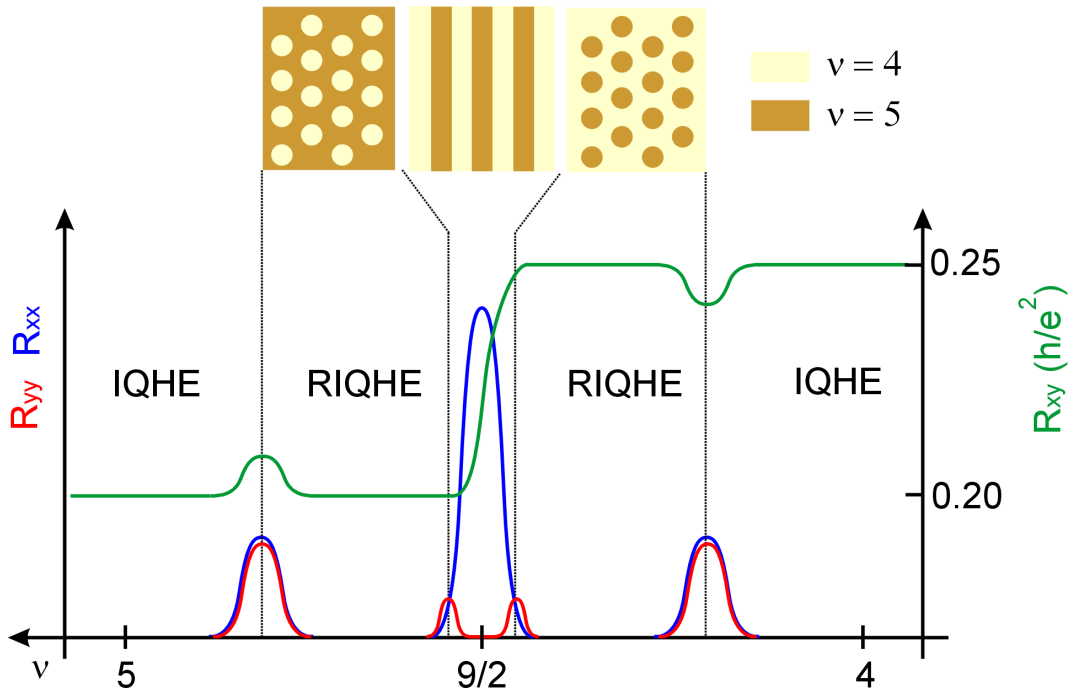


Figure 2.14: Schematic behavior of the longitudinal and Hall resistance around filling factor $\nu = 9/2$. The anisotropic stripe phase is located close to the half filled Landau level. On each side of the stripe phase, the isotropic bubble phase is stabilized. Pinning of the bubbles leads to the RIQHE (see text) where the Hall resistance is quantized to the adjacent IQHE value.

crystal is free to slide over the disorder potential, thereby inducing dissipation. At the same time, narrow band, high frequency noise is observed [61]. It is identified with the washboard noise known from other CDW systems [11].⁹ Although the non-equilibrium breakdown measurements strongly support the bubble phase picture, they have to be treated with caution. The applied currents are high enough to induce Joule heating and other unwanted nonlinear effects. We will return to this question when we discuss our own experimental results in chapter 5.

The bubble phase in the $N = 2$ Landau level has also been identified by microwave measurements [62]. In these experiments, the bubble phase is observed over a range of filling factors ($0.20 < \nu_N < 0.38$) and it is found to be most stable around $\nu_N \approx 0.25$.

Wigner crystal phase

The Wigner crystal phase is predicted to appear at low electron densities of the partially filled Landau level, i.e. $\nu_N^{\text{theo}} < 0.25$ [53]. In this isotropic phase, a triangular crystal lattice with

⁹An unresolved issue here is the observed frequency which is much too low to be explained by conventional models.

long range order forms with one electron per lattice site. The Wigner crystal phase in higher Landau levels is believed to be identical to the one found in the $N = (0, \uparrow)$ Landau level at filling factors $\nu < 0.2$ [63]. The lowest energy modes are collective excitations of the electrons around their equilibrium positions. These magnetophonon modes are the analogue to phonons in real crystals. They are pinned, i.e. localized, even by weak long range disorder in the sample. Here, 'weak' refers to a disorder strength that is not strong enough to disrupt the crystalline order at small length scales.¹⁰ The localized modes are referred to as pinning modes, observable in microwave experiments. For small excitations, electrons in a pinned Wigner crystal are immobile and thus the phase will be an insulator. Theory predicts the Wigner crystal to be stable all the way down to the empty Landau level, i.e. $\nu_N = 0$. However, calculations so far neglect the effects of disorder. In realistic samples, disorder disrupts the Wigner crystal and therefore destroys the electron correlations. This becomes most significant at the lowest densities within the Landau level where one therefore expects the IQHE to be the ground state instead of the correlated Wigner crystal. In this scenario, the boundary between the IQHE and the Wigner crystal phase move towards zero filling as the disorder potential is turned off.

The experimental evidence for a Wigner crystal phase in the lowest, i.e. $N = (0, \uparrow)$, Landau level is substantial. There, photoluminescence, microwave as well as transport measurements have confirmed its existence [63, 64]. Very recently, Wigner crystallization has also been observed by microwave excitation of its pinning mode in the $N = 1$ Landau level around $\nu = 3$ [65] and in the $N = 2$ Landau level around $\nu = 4$ [66]. To our knowledge, Wigner crystal formation in the $N = 2$ Landau level has not been observed in any transport measurements.

2.3.2 Electron Liquid Crystal (ELC) picture

In a more sophisticated theoretical description of the $N = 2$ Landau level, quantum fluctuations are taken into account. This leads to the Electron Liquid Crystal (ELC) picture for electron correlations in higher Landau levels [13]. ELC phases are the quantum mechanical analogue of classical liquid crystals. They are predicted to be a generic feature of strongly correlated fermionic systems with Coulomb-like interactions. For instance, the theory of ELC phases in high Landau levels has a strong similarity to that of fluctuating, metallic stripes in doped Mott insulators [16]. We introduce the concept of ELC phases closely following Fradkin and Kivelson [13].

We start with a configuration that resembles the CDW stripe phase introduced in the previous section and then discuss the modifications arising from quantum fluctuations. Stripe-shaped regions of alternating integer local filling factor $\nu_N^{\text{loc}} = 1$ and $\nu_N^{\text{loc}} = 0$ are directed along the x-axis (Fig. 2.15(a)). Within these regions, the Hall conductance is quantized to the values $2Ne^2/h$ and $2(N + 1)e^2/h$, respectively. Initially, we assume that this configuration is stable

¹⁰However, it may disrupt the long range order. In that case, the phase rather resembles a polycrystal with independent regions of crystalline order.

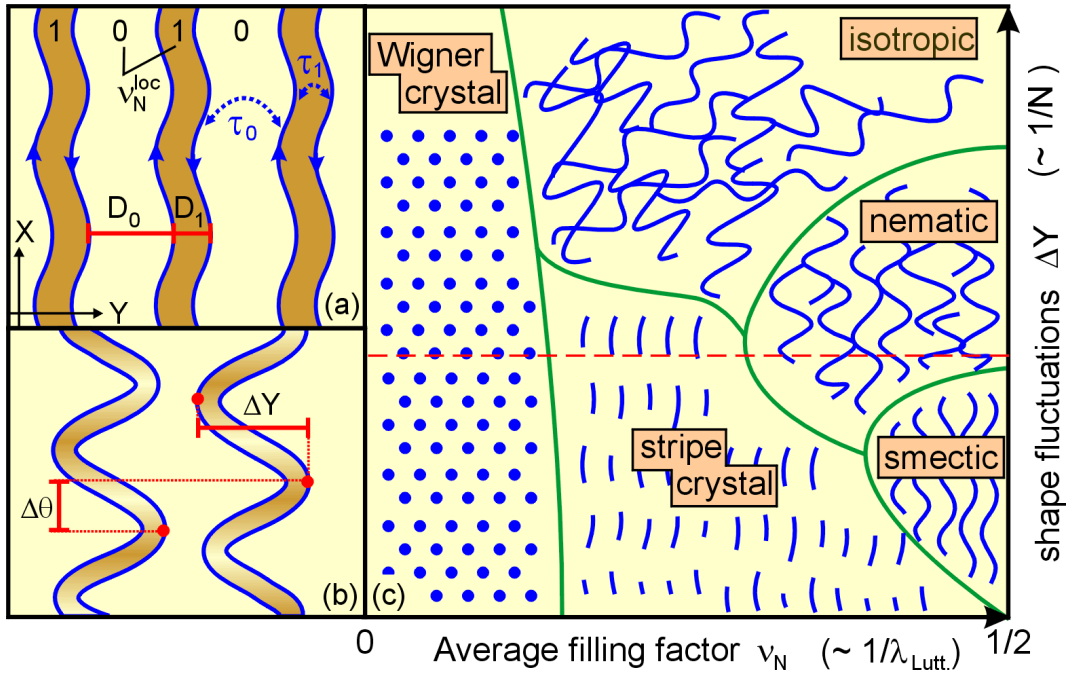


Figure 2.15: (a) Self consistent, chiral edge states (blue) form at the boundaries between regions with $\nu_N^{\text{loc}} = 1$ and $\nu_N^{\text{loc}} = 0$. The regions have respective widths of D_1 and D_0 which depend on the average filling factor (eq. 2.49). Tunneling between the edge states is parameterized by scattering times τ_0 and τ_1 , respectively. (b) Quantum fluctuations of paired edge states: (i) Transverse shape modulations with amplitude ΔY . (ii) Phase shift $\Delta\theta$ between charge modulation of adjacent edge pairs (Luttinger liquids). (c) ELC phase diagram at $T = 0$ as a function of the quantum fluctuation strength ΔY and the average filling factor ν_N . The red horizontal line indicates the region of the phase diagram relevant in the $N = 2$ Landau level. The diagram is based on [13].

within the whole filling factor range of the topmost Landau level ($\nu_N = 0 \dots 1$). Only the widths of the regions are variable and depend on the filling factor according to

$$\nu_N = \frac{D_1}{D_0 + D_1}, \quad (2.49)$$

where D_i is the width of regions with local filling factor $\nu_N^{\text{loc}} = i$. The sum of the widths $D_0 + D_1 = \lambda_{\text{CDW}}$ is given by the period of the local filling factor modulation which follows from equation 2.48. Hence, at filling $\nu_N = 1/2$ both kinds of regions have the same width ($D_0 = D_1$), whereas away from half filling, the width of one type of region increases at the expense of the other type.

In the Büttiker picture of the QHE (section 2.1.4), gapless, i.e. conducting, edge states occur at the boundaries of any two regions with differently quantized Hall resistance. Therefore,

one also expects such metallic-like edge states between the incompressible regions in the ELC phases (Fig. 2.15 (a)).¹¹ Equivalent to the case of the IQHE, edge state electrons on opposite sides of a quantized region have opposite velocities, i.e. they constitute a chiral electron liquid.

However, there are important differences between the edge states at the boundaries of a Quantum Hall-device and the internal edge states of the ELC phases. In the case of the IQHE, the edge states are generated by the confinement potential at the boundaries of the sample, whereas the ELC edge states form self-consistently driven by the Coulomb interaction. This gives rise to a new class of low-energy excitations, related to fluctuations of the edge shape. The deformations are parameterized by a length ΔY which specifies how much a conducting edge curls up into the y-direction (Fig. 2.15 (b)). Without fluctuations, $\Delta Y = 0$, and the edges run perfectly straight along the x-direction. In this limit, the ELC picture corresponds to the CDW picture of the last section.

Another difference is that in the IQHE, the edges of opposite chirality are usually far apart from each other, and thus their mutual interaction can be neglected. This is not the case for the ELC edge states which have a distance of the order of the cyclotron radius only. Close to the half filled Landau level, the interactions between the edge states can be parameterized by two scattering times τ_0 and τ_1 across empty and filled regions, respectively (Fig. 2.15(a)). For general filling factors, the complex problem of edge interactions is greatly simplified in an elegant, field-theoretical description. Everywhere, except exactly at half filling, each edge state has a nearest neighbor of opposite chirality at a distance D and another neighbor further away at a distance \bar{D} (see Fig. 2.15(a) for the case $\nu_N < 1/2$, i.e. $D = D_1 < D_0 = \bar{D}$). It is advantageous to pair up nearest neighbor edge states and represent each pair as a single non-chiral Luttinger liquid.¹² The internal interaction parameter of the Luttinger liquid is derived from the distance D between the edge state pair that forms this liquid.

In summary, we are left with conducting Luttinger liquids (with internal interaction parameter D) which interact with neighboring Luttinger liquids (parameterized by \bar{D}). The Luttinger liquids display charge-density fluctuations along their extended axis (the x-axis in our case) with a characteristic period given by their internal interaction parameter (and thus D) according to

$$\lambda_{\text{Lutt.}} = \frac{4\pi l_B^2}{D}. \quad (2.50)$$

Therefore, using equation 2.49, the period of the charge density fluctuations $\lambda_{\text{Lutt.}}$ depends directly on the average filling factor. The interaction between adjacent Luttinger liquids locks their respective charge-density fluctuations to each other such that the whole system of interacting Luttinger liquids becomes unstable, leading to crystallization.

The ELC phase diagram at $T = 0$ is shown in Figure 2.15(c). The symmetry of the phases

¹¹Similar to the CDW case, this picture becomes exact for $l_B \ll \lambda_{\text{CDW}} \approx 2.6R_c$, i.e. $N \gg 1$. Still, it should be a reasonable approximation already at $N = 2$.

¹²Luttinger liquids are one-dimensional, strongly correlated electron liquids which are described by an internal interaction parameter.

is symbolized by blue lines which represent the interacting, conducting Luttinger liquids. The phase diagram is shown as a function of the filling factor ν_N and of the shape fluctuation strength ΔY . The magnitude of the shape fluctuations increases along the y-axis. Generally, it is expected that shape fluctuations are strong in the lowest Landau level and weaken towards higher Landau levels. In a sense, the electron system behaves more classically in higher Landau levels, and the y-axis can be symbolically labelled by the Landau level index like $1/N$. Along the x-axis, the filling factor of the topmost Landau level ν_N is plotted. As mentioned above, an increasing filling factor leads to a decreasing period $\lambda_{\text{Lutt.}}$ of the charge density fluctuations within the Luttinger liquids.

In the following, we will discuss the different ELC phases separately including their phase boundaries, the effect of finite temperature, and also the implications for transport experiments within the different phases.

smectic phase

The smectic phase strongly resembles the CDW stripe phase from Hartree-Fock theory described in section 2.3.1. It breaks the translational symmetry in the y-direction and also the rotational symmetry. However, there are small, but important differences. In the smectic phase, the perfectly oriented stripes of the CDW stripe phase are slightly disturbed by small shape fluctuations. Small in this context means $\Delta Y \ll \lambda_{\text{CDW}}$. The shape fluctuations actually stabilize the smectic phase against crystal formation away from exactly half filling of the Landau level, because they induce a phase difference $\Delta\theta$ between the charge fluctuations on adjacent Luttinger liquid stripes (see below). The smectic phase is compressible, and therefore the Hall conductance is not quantized and varies continuously with the filling factor.

Within the smectic phase, the theory of coupled Luttinger liquids [67] provides predictions for the conductivities

$$\begin{aligned}\sigma_{xx} &= \frac{e^2}{h} \frac{\lambda_{\text{CDW}}}{v_F(\tau_0 + \tau_1)}, \\ \sigma_{yy} &= \frac{e^2}{h} \frac{v_F \tau_0 \tau_1}{\lambda_{\text{CDW}}(\tau_0 + \tau_1)}, \\ \sigma_{xy} &= \frac{e^2}{h} \left([\nu] + \frac{\tau_1}{\tau_0 + \tau_1} \right),\end{aligned}\tag{2.51}$$

where v_F is the Fermi velocity, λ_{CDW} the CDW period (eq. 2.48), and τ_i are the scattering times introduced above (see Fig. 2.15(a)). From particle-hole symmetry, one expects $\tau_0 = \tau_1$ at exactly half filling of the Landau level ($\nu_N = 0.5$). Here, equations 2.52 reduce to the important parameter free prediction

$$\begin{aligned}\sigma_{xx}\sigma_{yy} &= (e^2/2h)^2, \\ \sigma_{xy} &= \frac{e^2}{h} ([\nu] + 1/2).\end{aligned}\tag{2.52}$$

Therefore, the Hall resistivity at half filling is reduced from the classical value $\rho_{xy} = (h/e^2)/([\nu] + 1/2)$ to

$$\rho_{xy} = \frac{\sigma_{xy}}{\sigma_{xx}\sigma_{yy} + \sigma_{xy}^2} = \frac{h}{e^2} \frac{2[\nu] + 1}{([\nu] + 1)^2 + [\nu^2]}. \quad (2.53)$$

Although the above prediction is valid only for $\nu_N = 0.5$, we can infer from this that the transition between the Hall plateaus (and probably also the maximum in the longitudinal resistance) should be shifted from half filling to slightly higher magnetic fields (i.e. to $\nu_N < 0.5$).

nematic phase

The nematic phase evolves from the smectic one when the size of the transverse fluctuations becomes large enough so that neighboring conducting stripes start to touch, i.e. when $\Delta Y \approx \lambda_{CDW}$. From this point on, dislocations of the perfect stripe pattern may occur where two stripes merge or a single one terminates. Thus, in the nematic phase long range stripe order is destroyed and only short range order survives. For this reason, the nematic phase is translationally invariant in both crystal directions but the rotational symmetry is still broken. A generalization of the theory for the smectic phase shows that equations 2.52 and 2.53 are also valid in the nematic phase [68]. Recently, tilted magnetic field studies have supported the notion that it is indeed the nematic phase and not the smectic phase which is stabilized around filling factor $\nu_N = 0.5$ [69, 70].

stripe crystal phase

Charge-density fluctuations of adjacent Luttinger liquids are locked in phase because of their mutual interactions. This triggers an enhancement of the fluctuations until the Luttinger liquids break up into disconnected smaller pieces along their extended axis. An insulating stripe crystal forms, since current cannot longer flow between the stripe pieces. At the lowest temperatures, this crystal phase is a true insulator. Since only the topmost Landau level is insulating, one expects $\sigma_{xx} = \sigma_{yy} = 0$ but $\sigma_{xy} = ie^2/h$, where i is the number of the nearest integer filling factor. This is the same behavior as expected from the CDW bubble phase, and it also explains the RIQHE at intermediate filling factors $0.2 < \nu_N < 0.4$. Unlike the isotropic CDW bubble phase, the ELC stripe crystal phase is anisotropic. This difference is difficult to address by transport experiments since both phases are insulating. So far, the only indication for an isotropic insulating state comes from microwave experiments [65]. They seem to indicate, that excitation of pinning modes in this regime does not depend on the polarization of the microwave radiation. In our opinion, however, the question whether an isotropic or anisotropic crystal forms has not been convincingly answered up to date.

The stripe crystal phase is stable over the whole range of filling factors as long as the shape fluctuations are negligible ($\Delta Y \approx 0$, bottom part of Fig. 2.15(c)). As the shape fluctuations

increase, a phase difference $\Delta\theta$ is induced between the charge density fluctuations on neighboring Luttinger liquids (Fig. 2.15(b)). When this phase difference reaches a critical value, adjacent Luttinger liquids are effectively independent and hence remain conducting. In this case, the smectic or nematic phase is stabilized. Obviously, shape fluctuations produce larger phase shifts when the period of the charge density modulations $\lambda_{\text{Lutt.}}$ is small. Therefore, stabilization of the conducting phases takes place close to the half filled Landau level for small shape fluctuation strengths, and it moves towards lower filling factors for increasing strength.

isotropic liquid

All phases discussed above will turn into a isotropic liquid phase as soon as the shape fluctuations become sufficiently strong. Here, the stripes have no preferred direction anymore, and translational as well as rotational symmetries are restored. Therefore, all transport coefficients should be isotropic. Some local stripe correlations might still exist in the isotropic liquid phase for some range of fluctuation strengths, but they will vanish if the strength increases beyond a certain point.

Wigner crystal phase

The Wigner crystal phase develops from the stripe crystal phase at low filling factors ν_N . In this regime, the period $\lambda_{\text{Lutt.}}$ of the charge fluctuations along the stripes becomes so small that the stripe pieces left over after crystallization are only composed of a single electron. This phase is identical to the CDW Wigner crystal.

Chapter 3

Ballistic Transport

In this chapter, we investigate ballistic transport of electrons and of Composite Fermions. We show that Composite Fermions behave as ordinary particles and can be studied in well defined and tunable geometries. After we introduce Quantum Point Contacts (QPCs) at low and high magnetic fields, we look at straight ballistic electron transport in a two QPC geometry. The remainder of the chapter discusses straight ballistic transport of Composite Fermions.

3.1 Quantum Point Contacts (QPCs)

One of the most important building blocks of mesoscopic transport experiments is the Quantum Point Contact (QPC) [71]. QPCs are short and narrow constrictions in a 2DES with a width W_c of the order of the Fermi wavelength λ_F (Fig. 3.1 (b)). Because of the resulting size quantization, electrons occupy only a finite number of transverse modes in the constriction. The conductance through a QPC is quantized to

$$G = \frac{2e^2}{h} N, \quad (3.1)$$

where N is the number of transverse modes which can be estimated from $N = \text{Int}[k_F W_c / \pi]$. Experimentally, QPCs are realized by means of metallic lateral surface gates (Fig. 3.1(b)). When a negative voltage V_{QPC} is applied to the gates, a constriction in the underlying 2DES is formed since electrons are repelled from underneath the gates. The width of the constriction decreases as the QPC voltage is made more negative, and fewer and fewer transverse modes are occupied in the constriction. This results in a stepwise decrease of the conductance according to equation 3.1.

As a specific example, we now discuss a lithographically defined QPC-device (for fabrication details see Appendix A). Its 2-point conductance is shown in Figure 3.1(a) as a function of the voltage V_{QPC} applied simultaneously to both gates. At small negative voltages ($V_{\text{QPC}} > -0.45$ V), the QPC is not well defined because the 2DES underneath the gates is

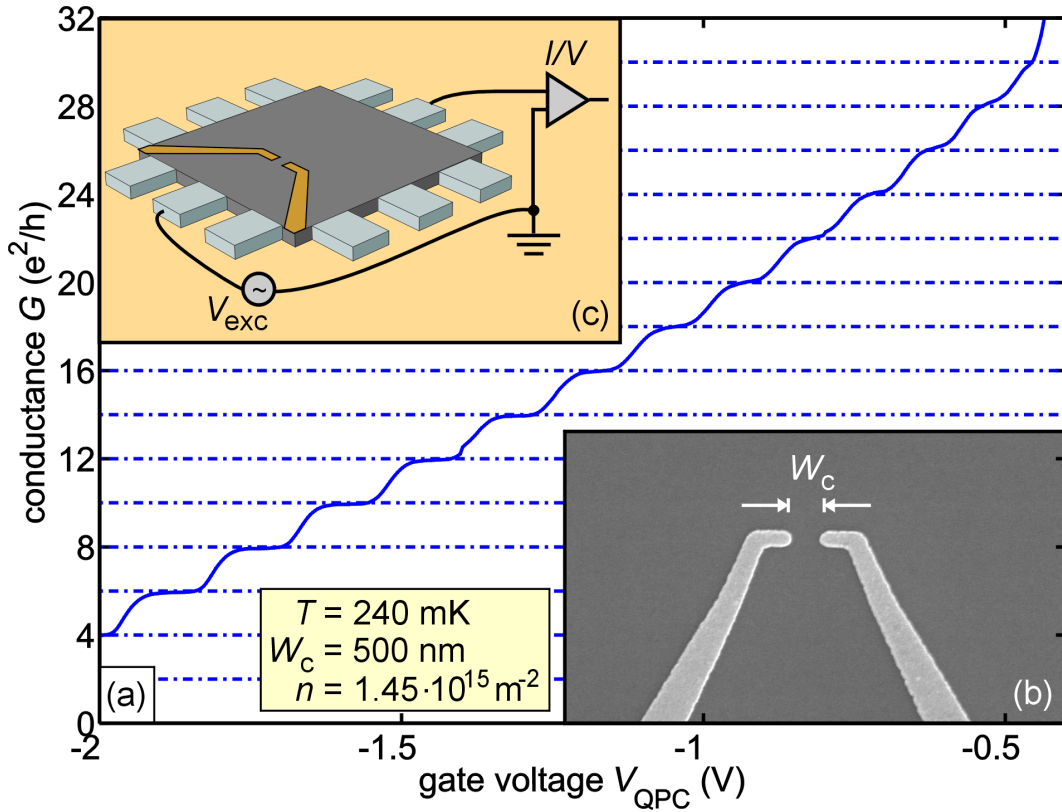


Figure 3.1: (a) Conductance G of a Quantum Point Contact as a function of the voltage V_{QPC} applied to the gates. (b) Electron-microscopic image of the metallic surface gates (light gray) used to define a QPC of lithographic width W_c . (c) Measurement configuration for the 2-terminal conductance G . The triangle labelled with I/V symbolizes a current amplifier.

not fully depleted. At $V_{\text{QPC}} \approx -0.45 \text{ V}$, the number of occupied transverse modes is $N = 15$, and it decreases down to $N = 2$ at the biggest negative voltage $V_{\text{QPC}} = -2 \text{ V}$. The QPC conductance can not be reduced to zero because leakage currents start to appear between the gates and the 2DES at still higher gate voltages ($V_{\text{QPC}} < -2 \text{ V}$). From equation 3.1, we can estimate that the width of the constriction decreases from $W_c \approx 490 \text{ nm}$ to $W_c \approx 65 \text{ nm}$ for the voltage range shown in figure 3.1. The largest width corresponds nicely to the lithographically defined gate opening of $W_c = 500 \text{ nm}$.

At non-zero magnetic fields, when the cyclotron radius becomes smaller than the width of the constriction, i.e. $2R_c \leq W_c$, the number of conducting modes in the QPC is not related to its dimensions anymore. Instead, it is given by the number of occupied Landau levels in the constriction [72]. The quantization of the QPC conductance is then a manifestation of the Quantum Hall Effect in the constriction. In the Büttiker picture of the Quantum Hall Effect (sec. 2.1.4), the 2-terminal conductance through the QPC is determined by the number of edge

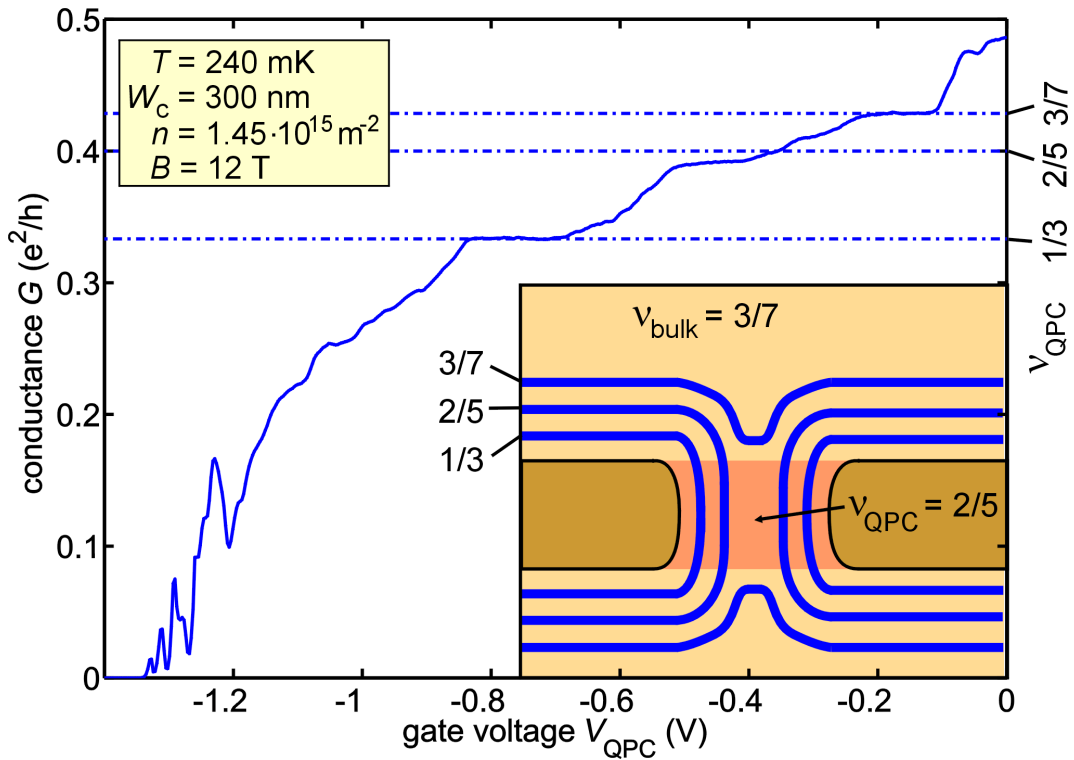


Figure 3.2: QPC conductance at high magnetic field ($\nu \approx 1/2$ in the bulk 2DES). Conductance plateaus occur whenever the density in the QPC is reduced, so that a fractional filling factor ν_{QPC} occurs within the constriction. In the Büttiker picture, the conductance is determined via eq. 3.2 by the type of edge channels traversing the QPC (e.g., inset for $\tilde{G} = 2/5$).

channels that traverse it

$$\tilde{G} \equiv G/(e^2/h) = \sum_n T_n(\nu_n - \nu_{n-1}) = \nu_{\text{QPC}}, \quad (3.2)$$

where \tilde{G} is conductance in units of e^2/h , T_n is the transmission coefficient for the n th edge channel, and the sum runs over all filling factors smaller or equal to the filling factor ν_{QPC} in the QPC. For the last identity we have assumed $T_n = 1$, i.e. perfect transmission, for all edge channels which traverse the QPC. The identity is obvious for the IQHE regime, where $\nu_n - \nu_{n-1} \equiv 1$, but it is equally valid for the FQHE regime [73]. Figure 3.2 shows the conductance through a QPC at a magnetic field of 12 T. The bulk filling factor, far away from the QPC gates, is slightly below $\nu \approx 1/2$. Hence, the 2-terminal conductance without any voltage applied to the QPC is close to $\tilde{G} \approx 0.5$, because it is just the inverse of the 2-terminal Hall resistance in this case. Since the filling factor ν_{QPC} in the QPC can only be smaller than the one in the bulk, we do not expect to observe any signs of the IQHE. Instead, conductance plateaus occur whenever the density in the QPC is reduced such that a FQHE state develops

in the QPC. For example, this means that $\tilde{G} = 2/5$ when the region within the constriction is at filling factor $\nu_{\text{QPC}} = 2/5$ (inset Fig. 3.2), i.e. at a gate voltage of $V_{\text{QPC}} \approx -0.4$ V. Conductance plateaus occur at $\tilde{G} = 1/3, 2/5,$ and $3/7$, as expected from the Büttiker picture according to equation 3.2. Strikingly, the first conductance plateau at $\tilde{G} = 3/7$ already occurs at a voltage $V_{\text{QPC}} \approx -0.15$ V. This voltage is only 33% of the one required to deplete the 2DES underneath the gates at zero magnetic field (compare Fig. 3.1). Hence, in a strong magnetic field a slight reduction of the density underneath the gates is already sufficient to define the QPC. This behavior can be explained, if we look at the relative density change $\Delta n/n_{\text{bulk}}$ necessary to reduce the filling factor underneath the gates from the bulk value ν_{bulk} to the value ν_{gate}

$$\frac{n_{\text{bulk}} - n_{\text{gate}}}{n_{\text{bulk}}} = \frac{\Delta n}{n_{\text{bulk}}} = 1 - \frac{\nu_{\text{gate}}}{\nu_{\text{bulk}}}. \quad (3.3)$$

If a filling factor of $\nu_{\text{gate}} = 1/3$ is reached, transport underneath the gates will be definitely suppressed because a QH state forms in this region. This situation arises exactly when $\Delta n/n_{\text{bulk}} = 33\%$, and therefore, the gate voltage V_{QPC} at which the QPC is defined should be reduced by the same factor.

We can also infer from Figure 3.2 that resonance-like features are observed in the conductance at large negative gate voltages $V_{\text{QPC}} < -1.1$ V. This phenomenon is present at a very low density inside the QPC constriction, shortly before the QPC closes and the conductance vanishes. In this regime, transport takes place via tunneling through localized states in the constriction [74].

3.2 Ballistic electron transport

An experimental setup which measures the nonlocal transfer resistance (for the setup, see Fig. 3.4(b)) between two opposing QPCs (inset Fig. 3.3) is sensitive to straight ballistic transport of electrons [75]. A well defined current I_{inj} is applied across the injector QPC, and the voltage V_{coll} is detected across the collector QPC. Both quantities determine the transfer resistance $R_t = V_{\text{coll}}/I_{\text{inj}}$. At zero magnetic field and for sufficiently high mobility, electrons travel ballistically on straight paths between the QPCs thereby raising the potential at the collector and contributing to R_t around zero magnetic field. In the presence of a magnetic field, electrons are deflected from straight trajectories like classical point charges as a result of the Lorentz force

$$\mathbf{F}_L = -e\mathbf{v}_F \times \mathbf{B}. \quad (3.4)$$

This quickly reduces the transfer resistance, so that it tends to zero at a sufficiently high magnetic field (≈ 0.2 T in Fig. 3.3). A peak in the transfer resistance around $B = 0$ is therefore an unequivocal sign of ballistic electron transport between the QPCs. In our device, ballistic transport is detected over distances of $L = 1 \mu\text{m}$. This is not surprising since the electron mean free path in our 2DES ($\mu \approx 10 \cdot 10^6 \text{ cm}^2/\text{Vs}$) should be around $l \approx 75 \mu\text{m}$ (eq. 2.9). In

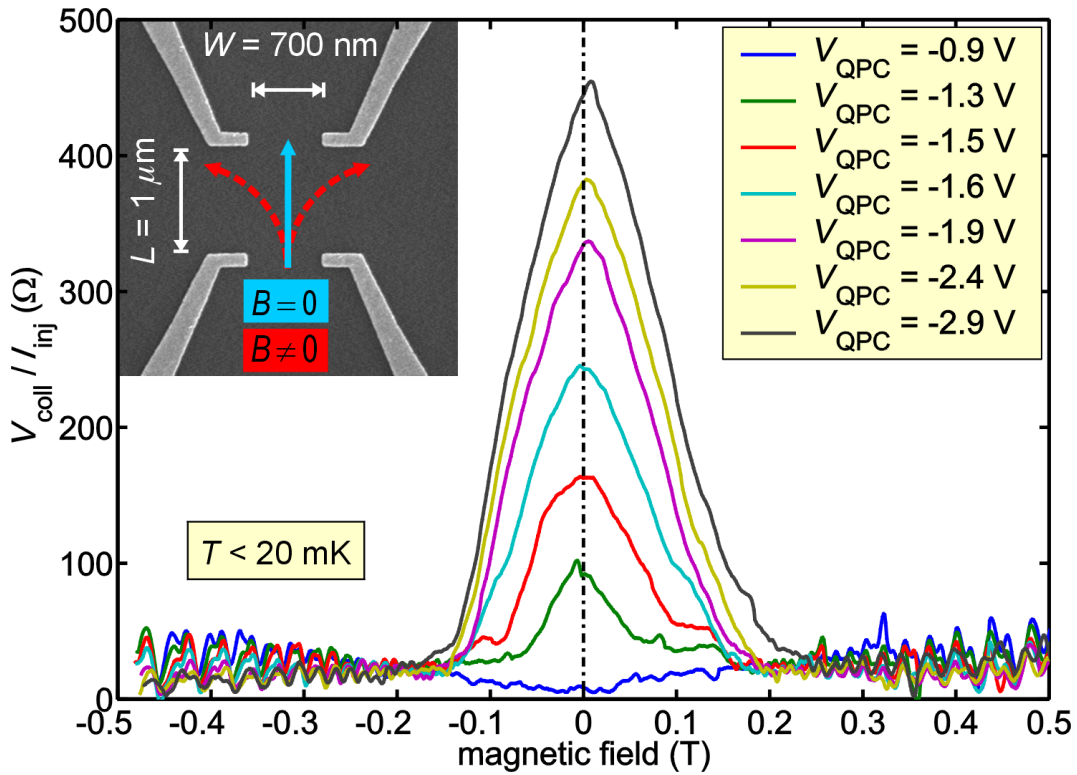


Figure 3.3: Ballistic transfer resistance peak around zero magnetic field. It arises from electrons travelling ballistically between the QPCs. The peak is enhanced when the QPC constrictions are made smaller by applying higher negative voltages to the gates. The inset shows an SEM image of the device along with its dimensions.

principle, one could even determine the opening angle of the electron beam that is emitted from the injector QPC by analyzing the maximum value and the shape of the transfer resistance peak around zero magnetic field [75]. For reasons which will become clear only in the next section, the experiment shown in figure 3.3 deploys rather wide QPCs ($W_c = 700$ nm). Therefore, there are many transverse modes in each constriction for the gate voltages shown. The 2-point conductance (compare Fig. 3.1) would not show any plateaus in this voltage regime. The ballistic resistance peak increases as V_{QPC} is made more negative, mostly because the voltage drop V_{coll} is inversely proportional to the conductance of the collector QPC.

Figure 3.4 shows that, at higher magnetic fields ($B > 0.2$ T), the transfer resistance R_t resembles the usual longitudinal resistance R_{xx} trace, and Shubnikov-deHaas as well as Quantum Hall features develop. In our experiments, we have used two different measurement configurations (Fig. 3.4(b) and (c)). The green curve in Figure 3.4(a) was taken using the configuration in Fig. 3.4(b). Here, the transfer resistance of the ballistic peak around $B = 0$ has the same sign as the magneto-resistance features at higher magnetic fields. On the other hand, in the

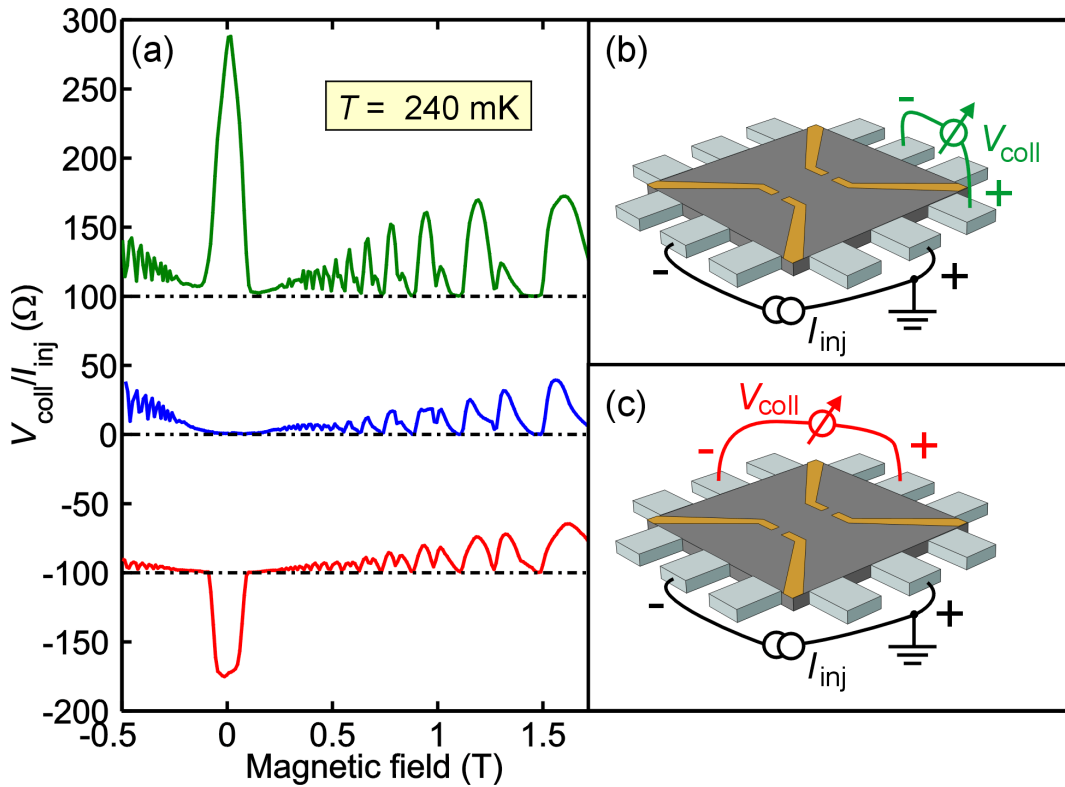


Figure 3.4: (a) Ballistic transfer resistance peak and magneto-resistance for two different measurement configurations. For configuration (b), the ballistic resistance peak has the same sign as the other magneto-resistance features (green curve in (a)), whereas for configuration (c), it has the opposite one (red curve). For comparison, a resistance trace is shown (blue) when the QPCs are not defined.

configuration used to obtain the red curve and illustrated in Fig. 3.4(c), the ballistic peak has flipped its sign while the other features have not. The sign of the ballistic peak depends on the polarity of the voltage probe which is connected to the collector QPC, whereas the sign of the other magneto-resistance features depends on the orientation of the voltage probes with respect to the current direction. This configuration dependence is very useful if one wants to distinguish ballistic transport from other magneto-resistance effects. We will return to this point when we discuss ballistic transport of Composite Fermions at $\nu = 3/2$ in section 3.3.3.

3.3 Ballistic Composite Fermion transport

The double-QPC geometry, introduced in the last section, is sensitive to straight ballistic motion of charge carriers between the QPCs. This type of transport takes place for electrons *only* around $B = 0$. At higher magnetic fields, the Lorentz force deflects electrons away from the collector,

and no ballistic transfer occurs.

The Composite Fermion picture which was introduced in section 2.2 implies that Composite Fermions behave like ordinary charged particles subjected to an effective magnetic field $B_{\text{eff}} = B - 2\Phi_0 n$ (eq. 2.28). Accordingly, also the Lorentz force for Composite Fermions depends on the effective field, and hence, Composite Fermions are predicted to move along straight trajectories at $B_{\text{eff}} = 0$, i.e. $\nu = 1/2$.

3.3.1 QPC voltage dependence

This prediction is indeed verified in Figure 3.5 where we measure the transfer resistance up to high magnetic fields ($B \approx 17$ T) in the device we introduced in the previous section. For slightly positive voltages (red trace), the usual shallow minimum occurs at filling factor $\nu = 1/2$. When the gate voltage V_{QPC} is made more negative, the ballistic transport peak for

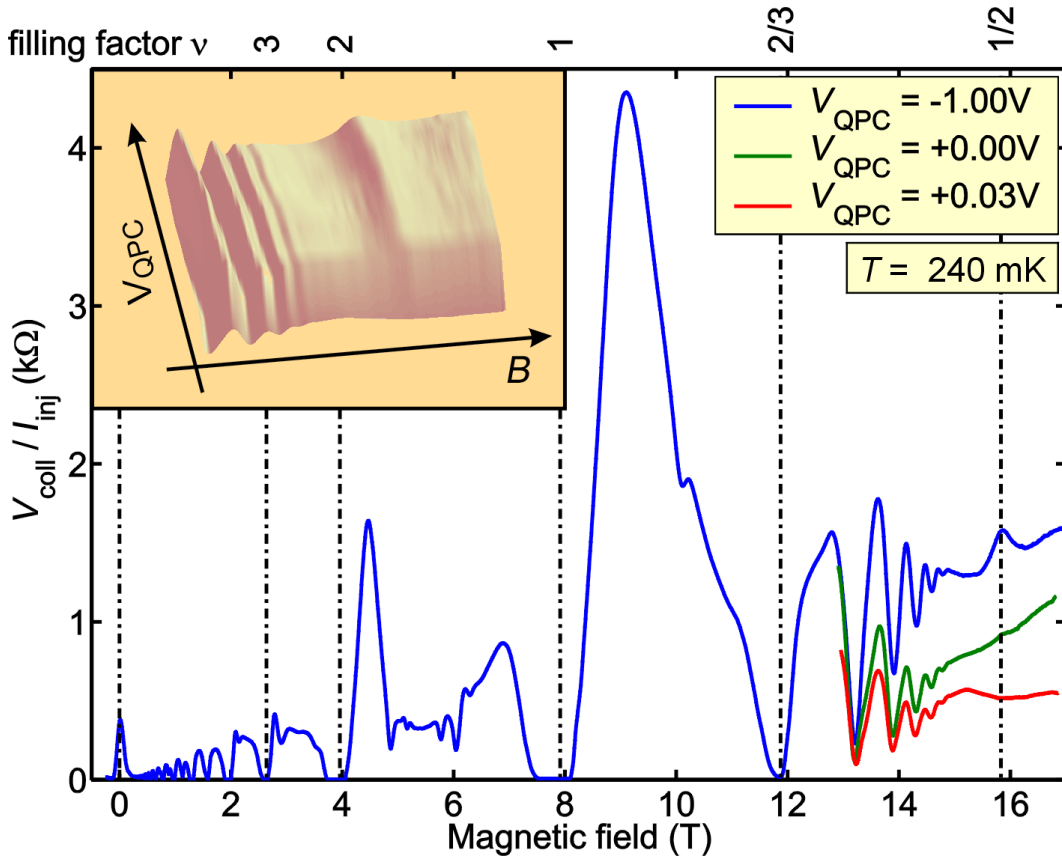


Figure 3.5: Transfer resistance in the two-QPC geometry (Fig. 3.4(b)) up to high magnetic fields. When the QPCs are defined (blue trace), a distinct peak at $\nu = 1/2$ indicates ballistic transport of Composite Fermions. The inset shows the gradual evolution of the ballistic peak with the applied QPC voltage.

Composite Fermions gradually appears at this filling (green and blue trace). It is truly remarkable that straight ballistic motion of charge carriers is observed over a distance of $1 \mu\text{m}$ at a magnetic field of $B = 16 \text{ T}$. At this field, the cyclotron radius of electrons is less than 5 nm . This shows the predictive power of the Composite Fermion picture. To our knowledge, it is impossible to explain the transfer resistance peak at filling $\nu = 1/2$ if one relies solely on the non-interacting electron picture. In section 2.35, we stated that the Composite Fermion mobility μ^{CF} is typically about two orders of magnitude lower than the electron mobility μ , and hence, the mean free path of Composite Fermions should be reduced by the same factor. We expect ballistic transport of Composite Fermions over distances of about $l^{\text{CF}} \approx 750 \text{ nm}$ and have chosen the distance between the QPCs accordingly.

In most cooldowns of the device, the position of the Composite Fermion ballistic resistance peak on the magnetic field scale turns out to shift with the applied QPC gate voltage. This effect does not happen with electrons at $B = 0$. It is a manifestation of the intimate relationship

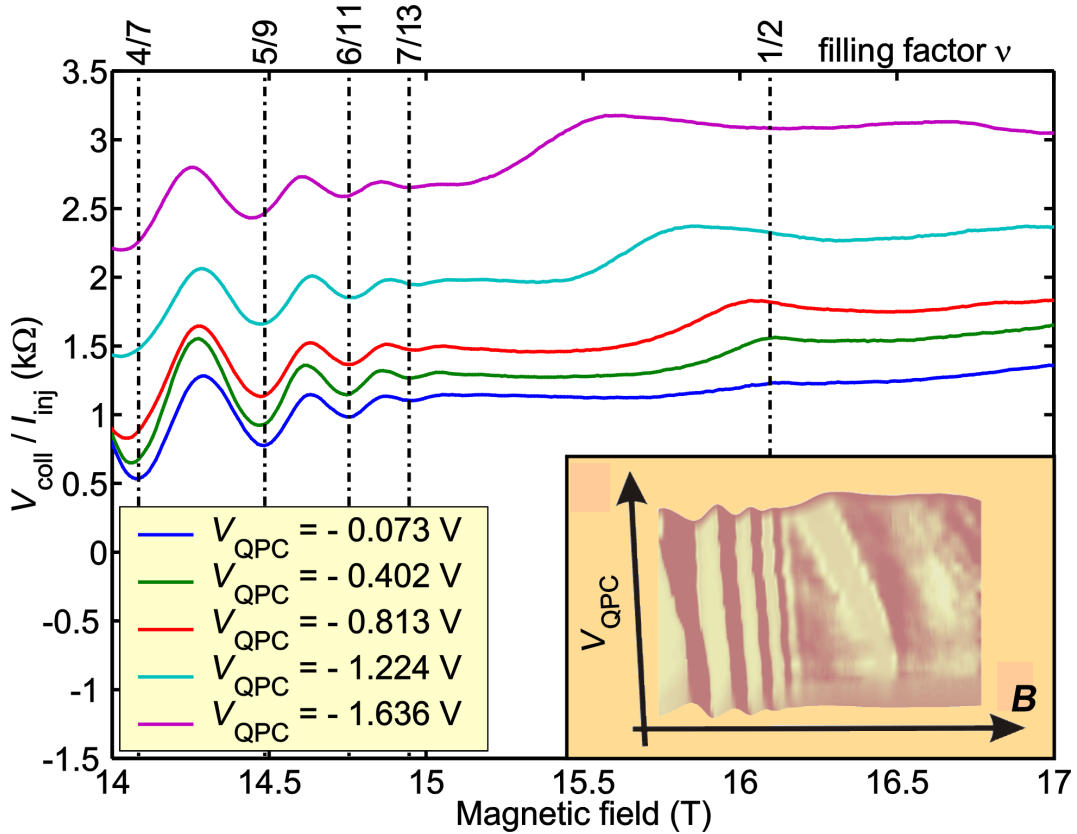


Figure 3.6: Composite Fermion ballistic transfer resistance peak at $T = 240 \text{ mK}$. For increasingly negative gate voltages V_{QPC} , the ballistic peak shifts towards lower magnetic fields. This indicates a reduced charge carrier density inside the QPC constriction.

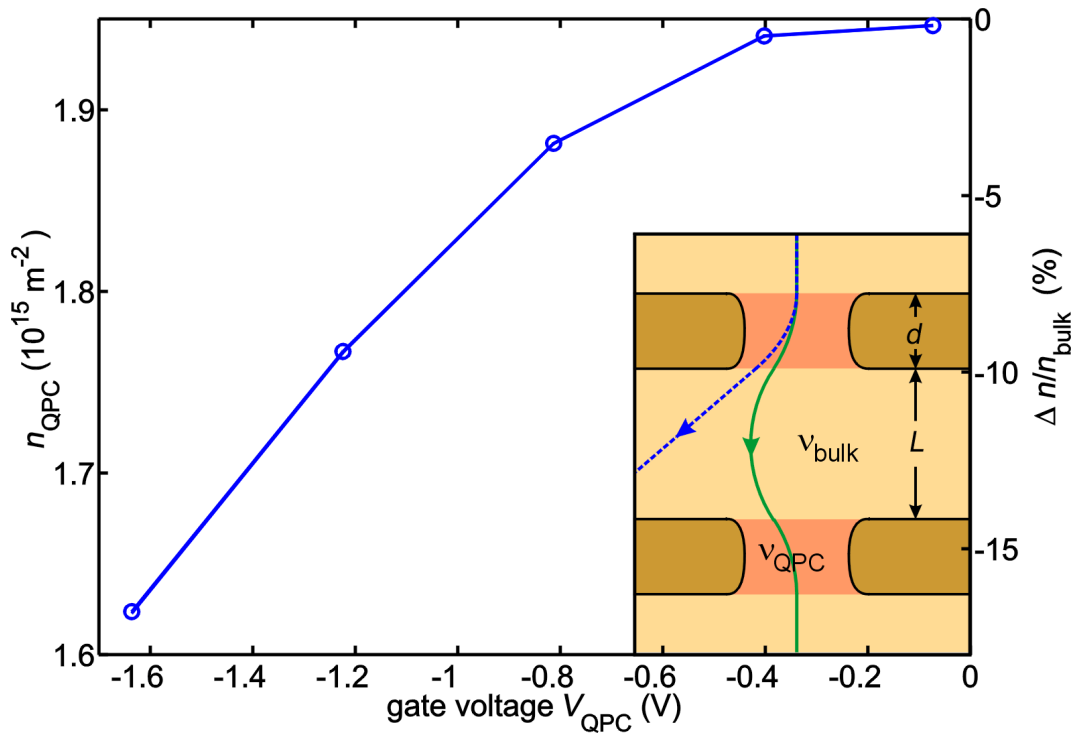


Figure 3.7: Change of the maximum electron density in the QPC n_{QPC} with the gate voltage V_{QPC} extracted from the data of Figure 3.6. The inset shows how Composite Fermions are deflected by a reduced density in the constrictions when $\nu_{\text{bulk}} = 1/2$ (blue) and how this can be compensated for by choosing an appropriate, smaller external magnetic field $\nu_{\text{bulk}} > 1/2 > \nu_{\text{QPC}}$ (green).

between external magnetic field and charge carrier density for Composite Fermions reflected in equation 2.28. Figure 3.6 shows the change in the position of the ballistic transfer resistance peak as the voltage on the QPCs is made more negative. At the same time, the features arising from the Quantum Hall Effect remain fixed in position. This originates from the fact that Quantum Hall features are sensitive mainly to the unaltered bulk electron density, whereas the ballistic peak strongly depends on the density Composite Fermions encounter on their path between the QPCs. To illustrate this point, we assume that the density within a QPC drops below the bulk value. When the external magnetic field is set to $\nu = 1/2$, Composite Fermions will experience a vanishing field $B_{\text{eff}} = 0$ and move on a straight line everywhere except inside the QPCs (blue line, inset Fig. 3.7). There, they will be deflected to the side, because the reduced density produces a non-zero effective magnetic field. Consequently, the Composite Fermions miss the collector. To compensate for the deflection inside the QPC, the external magnetic field has to be slightly decreased, so that the effective field is negative in the bulk, but still remains positive in the QPCs. Under these circumstances, Composite Fermions in the bulk and in the QPCs will be deflected in opposite directions. When the external magnetic field is tuned to

the right value, these deflections will compensate each other and Composite Fermions succeed to travel ballistically from injector to collector (green line, inset Fig. 3.7). Simple geometric considerations yield the identity

$$\frac{L/2}{d} = \frac{R_{\text{bulk}}}{R_{\text{QPC}}}, \quad (3.5)$$

where d is the length of the constrictions, L is the distance between the QPCs, and $R_{\text{bulk}}, R_{\text{QPC}}$ are the cyclotron radii of Composite Fermions in the bulk and inside the constrictions, respectively. From the position of the ballistic Composite Fermion peak and the device dimensions, the quantity R_{QPC} can be determined and in turn the density change in the QPCs (Fig. 3.7).

The last paragraph illustrates that, in order to observe the Composite Fermion ballistic peak, it is necessary to keep the density reduction in the constrictions below $\Delta n_{\text{QPC}} \approx 20\%$. Otherwise, the shift of the ballistic peak towards lower magnetic fields would be so large that it would overlap with FQHE features. It turns out, that the density reduction inside the constriction is quite substantial around $\nu = 1/2$. To alleviate this effect, we chose rather wide QPCs ($W_c = 500 - 700$ nm) for our experiments. Also, it turned out that it is necessary to illuminate our samples with a red LED in order to observe the ballistic transfer resistance peak for Composite Fermions. Under illumination AlGaAs based heterostructures exhibit the persistent photo-conductance effect. It increases the carrier density, as well as the mobility in such heterostructures. A higher mobility improves the Composite Fermion mean free path, and thus facilitates the observation of ballistic effects. Even more importantly, the sample illumination leads to a sharper confinement potential, and hence, the density reduction within the constriction is kept small. It has previously been reported that the persistent photo-conductance effect sharpens the confinement potential near the mesa edges [76], but it remains unclear why it should have a similar effect on QPC constrictions which are defined by lateral surface gates. One plausible reason may be that the persistent photoconductance-effect induces a weakly conducting parallel layer of electrons in the dopant region of the AlGaAs barrier close to the 2DES, which partially screens the electrostatic potential of the metallic surface gates. Effectively, the surface gates are moved closer to the 2DES and the confinement potential is sharpened. The idea of screening by a parallel conducting layer is supported by the observation that it is necessary to apply a higher negative voltage to define the QPCs after illumination than prior to it.

3.3.2 Temperature dependence

The temperature dependence of the Composite Fermion ballistic transfer resistance peak at $\nu = 1/2$ additionally confirms that this peak arises from a ballistic effect (Fig. 3.8). The resistance peak is considerably less sensitive to temperature than the surrounding resistance oscillations that arise from the Composite Fermion IQHE (i.e. the electron FQHE). The visibility of these oscillations depends on the size of the gap between quantized Composite Fermion Landau levels as compared to thermal broadening. Conversely, the appearance of the ballistic peak depends only on a well defined Composite Fermion Fermi surface and a sufficiently long mean free

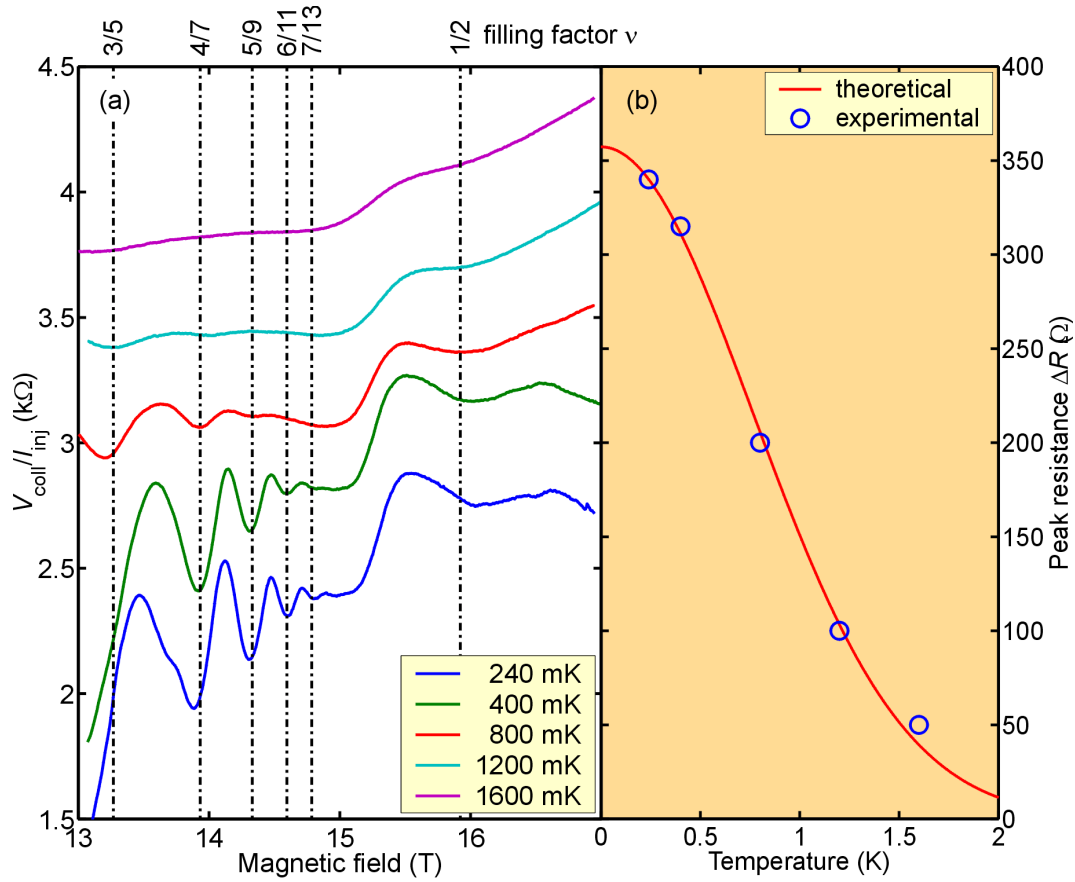


Figure 3.8: (a) Temperature dependence of the ballistic transfer resistance peak near $\nu = 1/2$. The ballistic peak is shifted towards lower magnetic field because the density within the QPC is reduced (see last section). (b) The suppression of the ballistic peak ΔR_{peak} can be explained by assuming a temperature dependent Composite Fermion - Composite Fermion scattering rate τ_{cfcf} (eq. 3.6).

path. In this sense, the Composite Fermion IQHE is a manifestation of a quantum mechanical effect, and the ballistic peak is a ‘classical’ effect at the level of Composite Fermions. This is analogous to the behavior of electrons at $B = 0$, where the classical, ballistic peak is more robust against a temperature increase than the Quantum Hall states at higher filling factors [77]. The temperature dependence of the ballistic peak resistance ΔR_{peak} (Fig. 3.8) can be well parameterized by

$$\Delta R_{\text{peak}} = R_0 e^{-(T/T_0)^2}, \quad (3.6)$$

where R_0 is the peak resistance at $T = 0$, and T_0 is a characteristic decay temperature. This functional dependence follows if one assumes a temperature dependent Composite Fermion - Composite Fermion scattering rate of the form $1/\tau_{\text{CFCF}} \propto T^2$ as well as an exponential dependence of the peak resistance on the inverse scattering time $\Delta R_{\text{peak}} \propto \exp(-1/\tau_{\text{CFCF}})$

[77]. In the case of electrons around $B = 0$, a similar temperature dependence for the electron-electron scattering rate is predicted, $1/\tau_{ee} \propto T^2 \ln(T)$ [78].¹ From the fit of equation 3.6 to our data shown in Figure 3.8 we obtain $T_0 = 1.08$ K.

3.3.3 Filling factor $\nu = 3/2$

The Composite Fermion picture can also be invoked to understand experimental observations in the magnetic field regime around filling factor $\nu = 3/2$ (compare section 2.2.5). At this filling, the lowest $N = (0, \uparrow)$ spin resolved Landau level is completely filled with electrons whereas the upper $N = (0, \downarrow)$ spin branch is only half filled. Only the electrons in the partially filled $N = (0, \downarrow)$ level are transformed into Composite Fermions. Since the degeneracy of each Landau level is modified upon changing ν , the Composite Fermion density depends on the external

¹This equation also fits the data very well. Since it requires an additional parameter, we have used the simpler dependence (eq. 3.6).

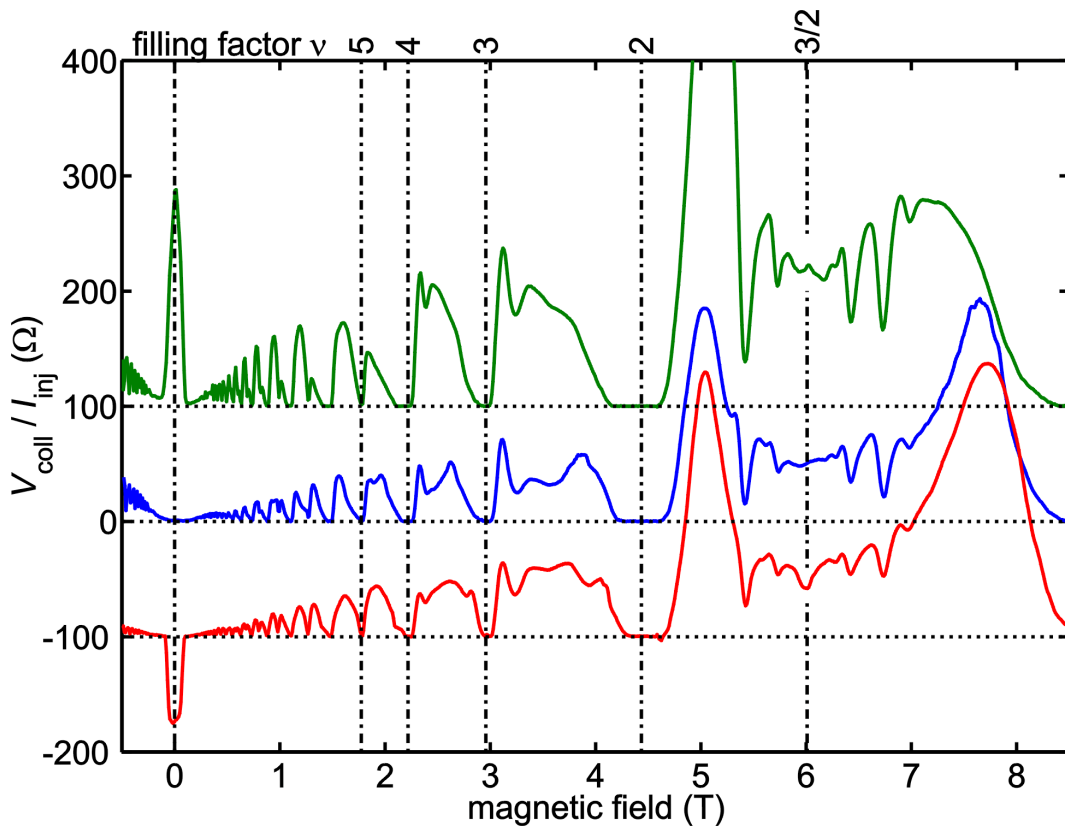


Figure 3.9: Ballistic Composite Fermion transport around $\nu = 3/2$ at $T = 240$ mK. The measurement configurations for the differently colored traces are the same as in Figure 3.4. The weak resistance feature at $\nu = 3/2$ changes its sign in the same way as the electron peak at $B = 0$. This confirms its ballistic origin.

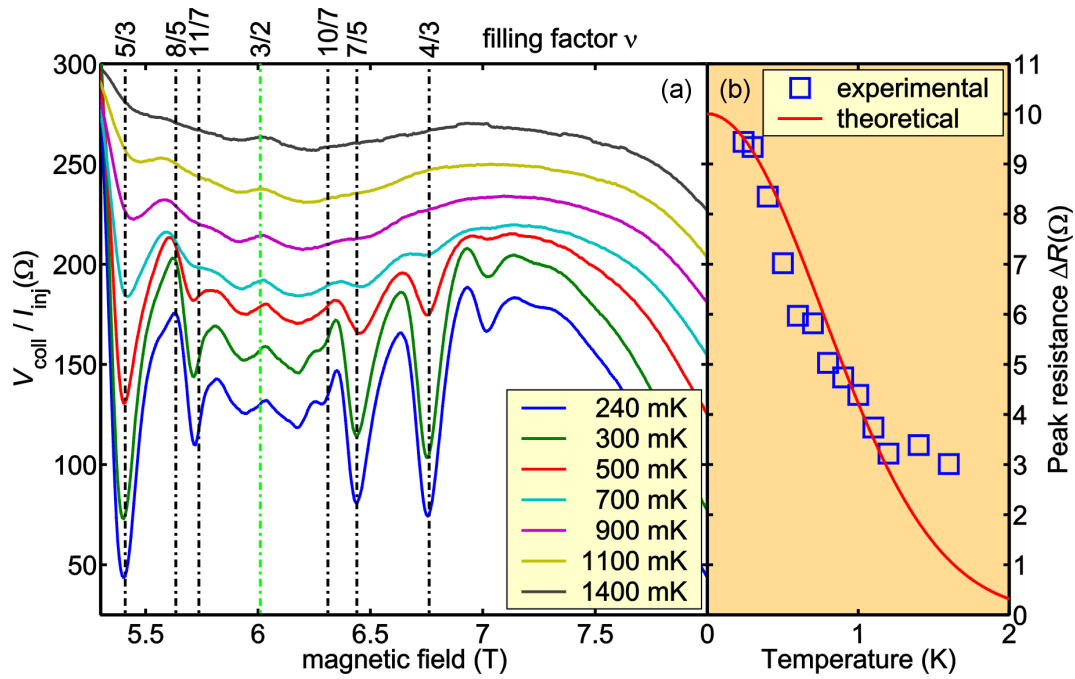


Figure 3.10: (a) Temperature dependence of the ballistic transport peak at $\nu = 3/2$ (compare Fig. 3.8). (b) The suppression of the resistance peak height is compared with the result of eq. 3.6 (red lines), using the same parameter $T_0 = 1.08$ K that was obtained from the fit shown in Fig. 3.8 at $\nu = 1/2$.

magnetic field. For this reason, the effective magnetic field $B_{\text{eff}}^{(3/2)} = 3(B - B_{3/2})$ increases three times faster than the external magnetic field away from $\nu = 3/2$ (eq. 2.41). Thus, all magneto-resistance features related to Composite Fermions are closer together on the external magnetic field axis. It is therefore more difficult to distinguish the ballistic transfer resistance peak from features that originate from the FQHE. We circumvent interpretation difficulties by exploiting the dependence of the relative sign between the ballistic peak and the QHE features on the measurement configuration as explained in Figure 3.4. We show in Figure 3.9 that the resistance feature observed at $\nu = 3/2$ changes its sign in the same way as the ballistic electron peak at $B = 0$. This clearly verifies that the resistance feature arises from ballistic transport of Composite Fermions at $\nu = 3/2$. The same figure also shows that the ballistic peak vanishes when no voltage is applied to the QPC gates (blue trace). In fact, the peak at $\nu = 3/2$ gradually develops as the gate voltage is made more negative (data not shown).

The ballistic transport peak at $\nu = 3/2$ survives up to temperatures higher than 1400 mK (Fig. 3.10(a)). Similar to the situation at $\nu = 1/2$, the surrounding FQHE features already disappear at considerably lower temperatures, emphasizing the ‘classical’ character of the ballistic transfer resistance feature. At $\nu = 3/2$, the extraction of the resistance peak height as a function of temperature (Fig. 3.10(b)) is difficult since the peak is rather small and not very

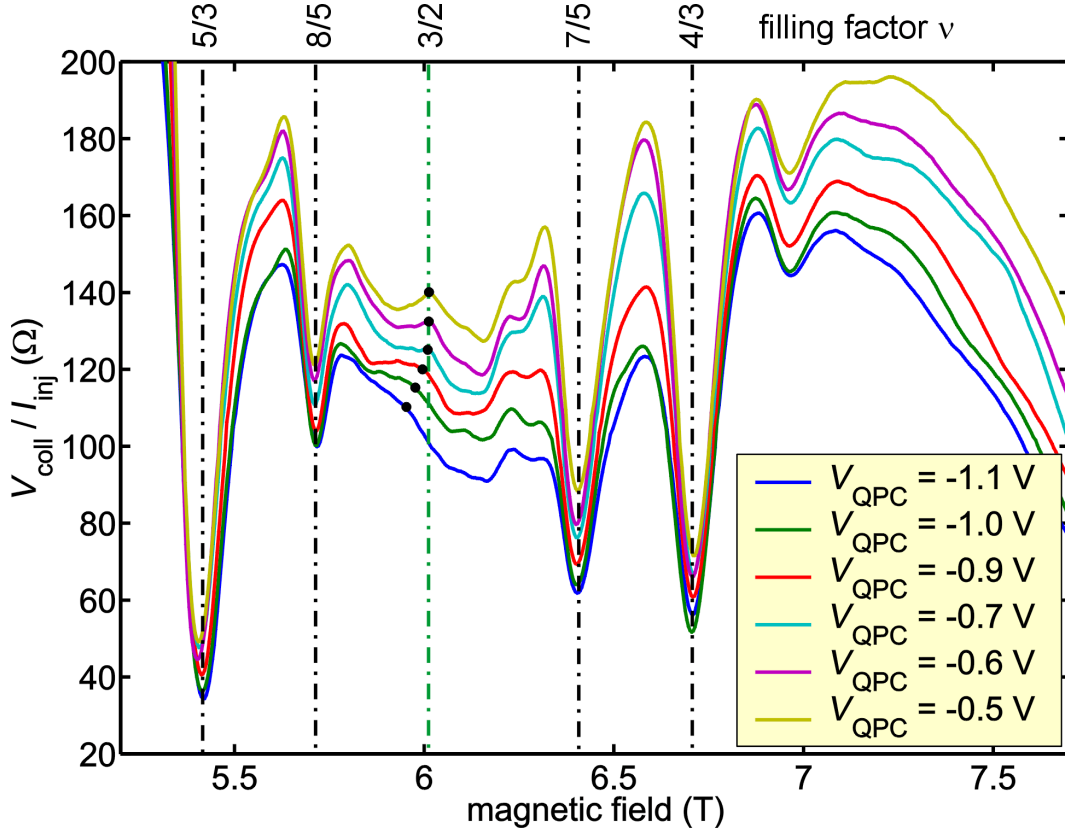


Figure 3.11: Ballistic transport peak at $\nu = 3/2$ as a function of the voltage applied to the QPCs. With increasingly negative V_{QPC} the ballistic peak shifts towards negative magnetic fields as a result of the duality between the Composite Fermion density and the external magnetic field. The temperature is $T = 240$ mK.

well separated from the QHE features at lower temperatures. Still, we fit the resistance peak height with equation 3.6, where we choose $T_0 = 1.08$ K, identical to the value obtained from the temperature dependence at $\nu = 1/2$ (Fig. 3.8). Although the fit is not very accurate, the same temperature scale appears relevant for the suppression of the resistance peak at $\nu = 3/2$ and $\nu = 1/2$. This observation suggests similar scattering mechanisms for Composite Fermions at these two filling factors.

As for $\nu = 1/2$, the ballistic peak at $\nu = 3/2$ shifts to lower magnetic fields whenever the voltage on the QPCs is made more negative (Fig. 3.11). In order to compensate for the deflection of Composite Fermions within the QPCs, the external magnetic field has to be reduced (compare Fig. 3.7).

Chapter 4

Phase coherent Transport

This chapter is devoted to transport in mesoscopic devices that contain a tunable antidot: an area that is depleted from electrons but surrounded by the 2DES from all sides. After introducing the specifics of this device geometry, we first look at classical orbits of electrons around the antidot. The main section then discusses phase coherent transport in the devices and its explanation in the framework of the Aharonov-Bohm effect. The temperature dependence of the interference effect is treated extensively, and the section is concluded with a short introduction to interesting topological defects in the interference pattern referred to as phase dislocations.

4.1 Antidot geometry

The devices used for the experiments in the following sections have been fabricated using a 2DES with a mobility of $\mu = 1 \times 10^6 \text{ cm}^2/\text{Vs}$ and a density of about $n = 2.1 \times 10^{15} \text{ m}^{-2}$. Central to the geometry is a gated antidot (Fig. 4.1) with a lithographic area of $A_{\text{AD}} \approx 0.32 \text{ }\mu\text{m}^2$. Electrons are electrostatically repelled from underneath the antidot by applying a negative voltage V_{AD} . Hence, a tunable potential hill is created within the 2DES. It extends above the Fermi energy for sufficiently large negative gate voltages and effectively forms a hole in the 2DES. This is a necessary condition to observe the Aharonov-Bohm effect. The antidot is located in a constriction of the 2DES that is formed by a negative voltage V_{sg} on the side gates (Fig. 4.1). The device can be regarded as two parallel Quantum Point Contacts (QPCs - see section 3.1) that are independently tunable. The antidot is electrically contacted using an air-bridge gate technique [79].¹ Although technologically challenging, the electrical connection of the antidot is necessary to adjust the electric potential of the antidot gate and thus make the device fully tunable.

¹The devices have been fabricated by Y. Feng, National Research Council, Ottawa, Canada. In the later stage of this work, we employed a similar air-bridge gating technique that we describe in Appendix A.3.2.

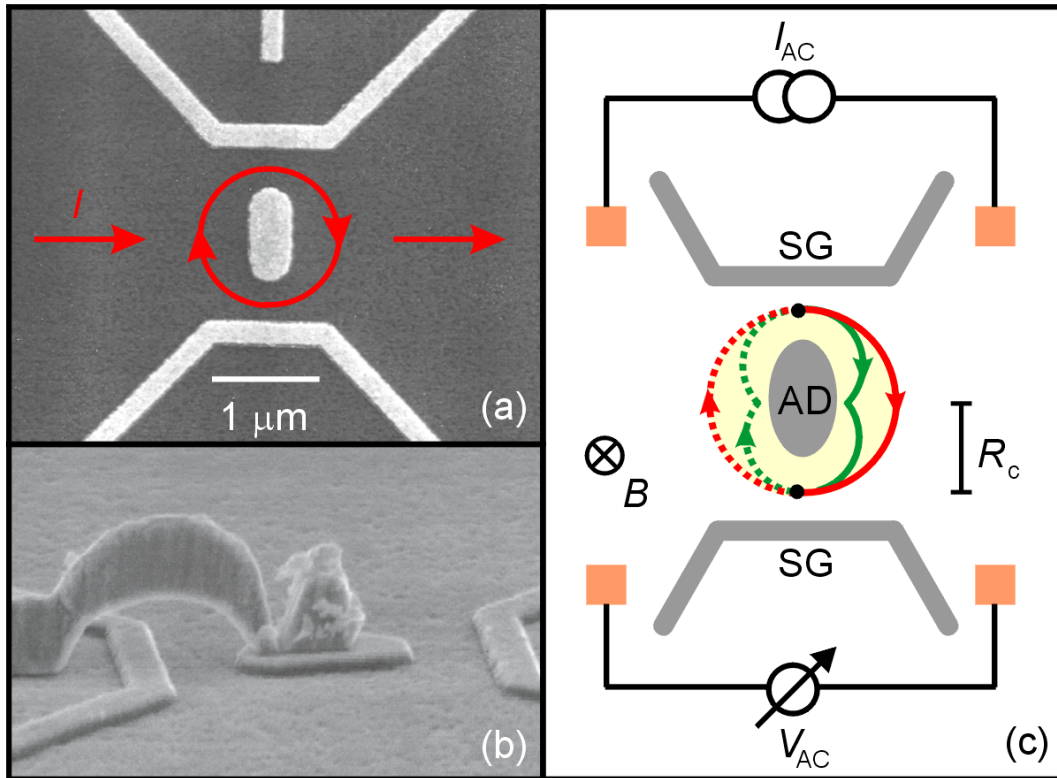


Figure 4.1: (a) Electron micrograph of the antidot device geometry. The light regions are the metallic gates that are used to deplete the 2DES underneath. (b) The central antidot is electrically connected via a metallic air-bridge [79]. (c) Schematic drawing of the device geometry and the measurement setup. The circular (red) and peanut shaped (green) orbits around the antidot (AD) are shown. The side gates (SG) define a narrow channel when a negative voltage V_{sg} is applied to them.

4.2 Trapped classical orbits

Applying a negative voltage to the side gates as well as the antidot defines two parallel QPCs that are individually tunable. We have confirmed the existence of each QPC by recording its conductance quantization in multiples of $2e^2/h$ (compare section 3.1). A measurement of the low field four-terminal resistance at $T = 1.2$ K is shown in Figure 4.2. Both QPCs have been adjusted so that only one transverse mode is occupied in each of them resulting in a total resistance close to $R = 1/(2e^2/h + 2e^2/h) \approx 6.5\text{k}\Omega$ at zero magnetic field. The negative magneto-resistance in the regime between $B = 0$ T and $B = 0.1$ T results from the mismatch between the number of transverse magnetic modes in the constrictions and in the wide part of the 2DES far away from the constrictions [80].

At slightly higher magnetic fields, resonance-like structures appear in the resistance. They

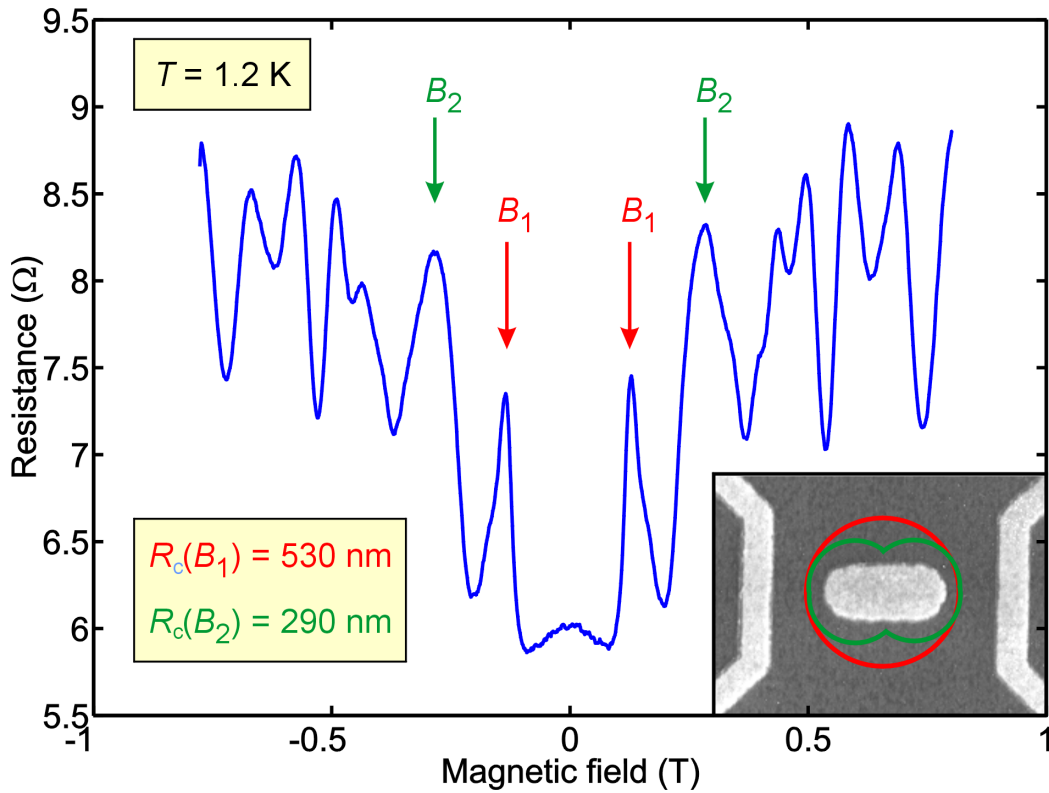


Figure 4.2: Magneto-resistance at $T = 1.2$ K. The resistance maxima, labelled with arrows, arise from trapping orbits of electrons around the elliptical antidot (shown in the inset with correct scale). The most simple orbits are circular- (red) and peanut-shaped (green). The peanut-shaped orbit includes a specular reflection from the antidot. From the magnetic field position B_1 and B_2 of the maxima, it is possible to extract the curvature of the specific orbits.

occur whenever electrons are trapped into orbits around the antidot by the magnetic field-induced Lorentz force [81]. Trapped electrons do not contribute to the transport since they effectively do not traverse the device. This leads to an increase in the resistance at the magnetic field values that support stable orbits around the antidot. The radius of the most simple, circular trapping orbit (inset Fig. 4.2) can be extracted from the magnetic field position of the first resonance via $R_c(B_1) = \hbar k_F / e B_1$. From $B_1 = 0.132$ T, we obtain $R_c(B_1) = 575$ nm which is in good agreement with the device dimensions. It has been shown by simulations that an elliptical antidot, akin to the one used in the experiment, favors well-defined trapping resonances of the resistance as a function of the magnetic field [82]. The resistance peak at roughly twice the field of the primary trapping peak, i.e. at $B_2 = 0.286$ T $\approx 2B_1$, is ascribed to an orbit that includes an additional specular reflection off the antidot boundary (inset Fig. 4.2). At even higher fields and in certain regimes of gate voltage, the resonance pattern is more complicated. It would require detailed simulations to identify each structure with a particular orbit of electrons around

the antidot.

4.3 Aharonov-Bohm oscillations

At low temperatures ($T = 50$ mK), one observes quasiperiodic oscillations of the magneto-resistance, superposed on the general features that arise from magnetic trapping (Figure 4.3). Quantum mechanics prescribes that electrons pick up an additional phase when they encircle the antidot. The phase is proportional to the magnetic flux penetrating the area enclosed by the electrons' path (see section 2.1.7). Constructive or destructive interference occurs between those electrons encircling the antidot and those simply passing by. This causes oscillations in the resistance as a function of the external magnetic field - the well known Aharonov-Bohm

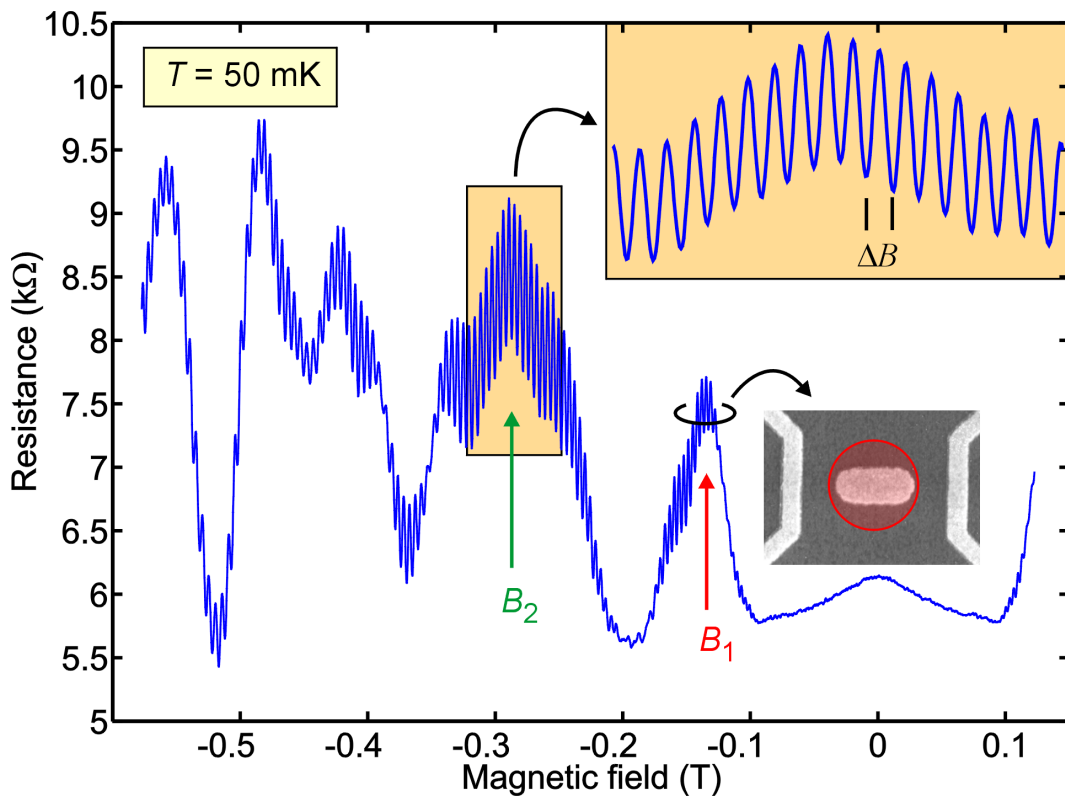


Figure 4.3: Magneto-resistance at $T = 50$ mK. The QPC gate voltage settings are very similar but not identical to the ones in Figure 4.2. Aharonov-Bohm oscillations start to appear around a magnetic field B_1 corresponding to the circular trapping orbit (small inset). A closeup (top inset) shows the quasi-periodicity of the oscillations. From the local period ΔB , one can infer the area enclosed by the orbit.

effect.² The area A enclosed by the electrons' path can be determined from the period ΔB of the Aharonov-Bohm oscillations: $A = \Phi_0/\Delta B$. A period of $\Delta B_1 = 3.6$ mT and $\Delta B_2 = 4.3$ mT has been extracted in the magnetic field regime of the circular and peanut-shaped trapping orbits, respectively. The corresponding circular areas have radii of $R(\Delta B_1) = \sqrt{A_1/\pi} = 600$ nm and $R(\Delta B_2) = 550$ nm. These values agree well with the device dimensions and also with the dimensions extracted from the magnetic field position of the respective trapping peaks (Fig. 4.2).

For a detailed analysis of the Aharonov-Bohm interference effect in our device, it is useful to separate the quasi-periodic oscillations from the smoothly varying background. The conductance³ $G = 1/R$ can be written as

$$G = \tilde{g} + \delta g \quad (4.1)$$

where \tilde{g} is the smoothly varying part and δg the oscillatory part of the conductance. We extract \tilde{g} from our data by means of a Savitzky-Golay smoothing technique [83]. This technique has an advantage over other smoothing techniques because it preserves the amplitude of the extracted oscillatory part of the data if the parameters are chosen carefully. The resulting \tilde{g} for the measurement of Figure 4.3 is shown in Figure 4.4(b). The oscillatory part δg is obtained by subtracting the smooth part \tilde{g} from the total conductance (Fig. 4.4(a)). The quality of the separation can be judged by noticing that the extracted oscillatory part of the conductance has a baseline of zero, and the smoothed part shows no remnants of the oscillations.

From the oscillatory part δg of the conductance, we can now extract the periodicity ΔB of the Aharonov-Bohm oscillations as a function of the magnetic field (Fig. 4.4(c)). The periodicity monotonically increases from low to high magnetic fields. This general trend reflects the fact that the trapped orbits shrink as the magnetic field is increased. At $B \approx 0.2$ T, where the orbit type changes from circular to peanut-shaped, the periodicity behavior shows a kink. The area of the peanut-shaped orbit depends more strongly on the cyclotron radius than the circular orbit since it essentially consists of two adjacent circles. Therefore, the periodicity will increase faster in the regime of the peanut-shaped orbit which is indeed observed. Beyond $B \approx 0.4$ T, the periodicity starts to level off, and it saturates at a value of $\Delta B = 4.9$ mT. The saturation of the periodicity is expected since the area enclosed by the electron orbit can not decrease below the size of the antidot. The area extracted from the saturation value, ΔB ($A_{\min} \approx 0.84 \mu\text{m}^2$), is substantially larger than the lithographic antidot gate area (see above). The electrostatic potential of the antidot gate will be blurred out at the position of the 2DES because of its distance from the surface. Hence, the area in which the 2DES is depleted will certainly be bigger than

²To be precise, the effect that we describe here differs from the historic Aharonov-Bohm effect [38]. The electrons are not only subjected to a magnetic vector potential but they directly feel the magnetic field. Additionally, the electron orbits are only stable in a suitable magnetic field interval, unlike in the historic case. However, the terminology is often used in a wider sense.

³The four-terminal measurement is effectively a two-terminal measurement as far as the device is concerned. Then, the conductance is just the reciprocal of the resistance.

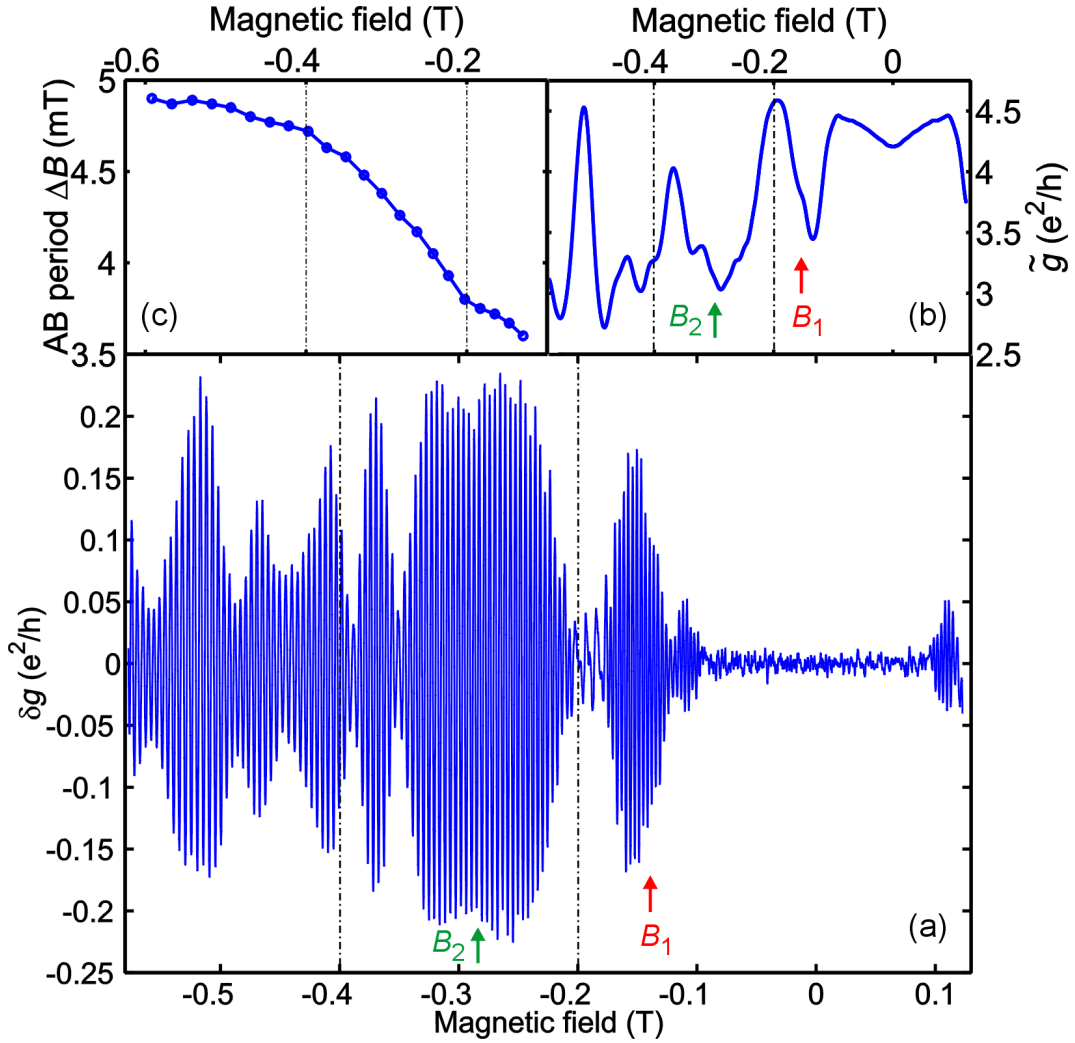


Figure 4.4: (a) Aharonov-Bohm contribution δg of the conductance through the device at a fixed gate voltage setting extracted from a measurement at $T = 50$ mK by a digital filtering technique (see text). (b) Smoothly varying part \tilde{g} of the conductance from the same measurement. (c) Aharonov-Bohm period extracted from (a) as a function of the magnetic field.

the antidot gate size.

4.3.1 Temperature dependence

The Aharonov-Bohm oscillations in the antidot device depend very sensitively on the temperature, and they completely vanish above $T \approx 700$ mK (Fig. 4.6). This reduction of the interference effect can be understood as a thermally induced phase averaging effect [84]. Since electrons have energies within a window of the order of $\Delta E = k_B T$ around the Fermi en-

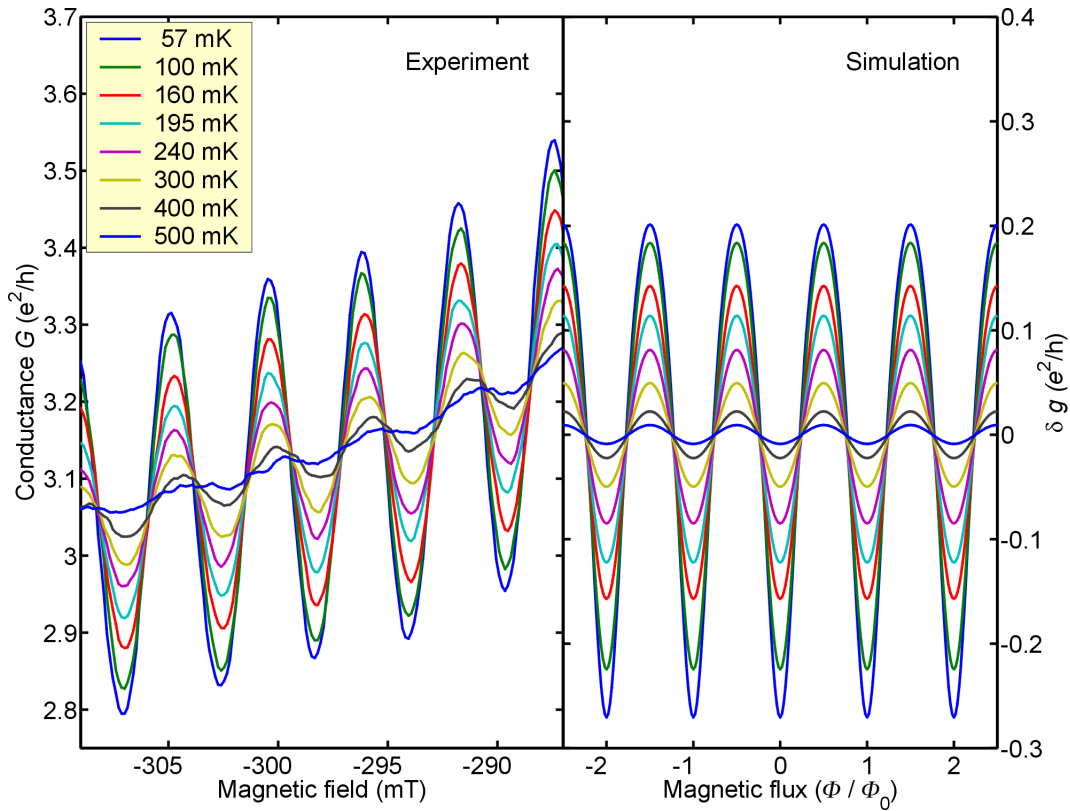


Figure 4.5: Measured conductance G (left) at different temperatures in the regime of the peanut shaped orbit (see Fig. 4.2). The simulation (right) shows the conductance oscillations δg , obtained from the model described in the text, for the parameters $T_0 = 85$ mK and $R = 0.82$ at the same temperatures.

ergy, they will experience a spread in their respective dynamical phases over time according to $\Delta\varphi \approx \Delta E \cdot t/\hbar$. If the temperature is high enough, so that $\Delta\varphi > \pi/2$ within the time the electrons spend in the device, destructive interference occurs between electrons with different energies, and the oscillations vanish. The condition given above can be rephrased in terms of the thermal length [85]

$$L_{\text{th}} = \frac{\hbar v_F}{k_B T}. \quad (4.2)$$

In this terminology, the interference effect becomes suppressed when the thermal length becomes shorter than the typical orbit length.

Here, we will address the effect of phase averaging from an essentially equivalent viewpoint. To simulate the interference effect, we assume a simple model for the transmission of electrons through the antidot device (Fig. 4.6(b),(c)). Electrons, moving through the constrictions of the device, have a certain, small probability $R \ll 1$ to tunnel on and off the closed orbit that encircles the antidot. For simplicity, we have chosen this probability to be the same in each constriction. The resulting energy dependent transmission coefficient for electrons passing

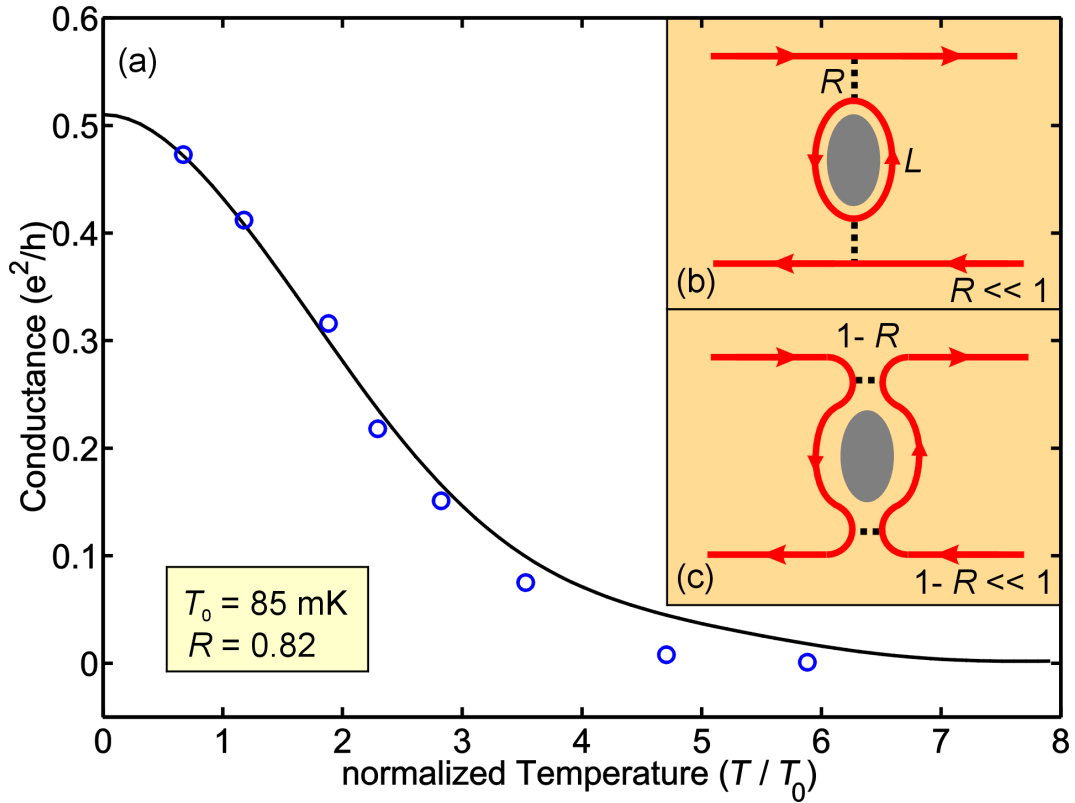


Figure 4.6: (a) Temperature dependence of the Aharonov-Bohm oscillation amplitude (circles) extracted from the data shown in Fig. 4.5. The solid line represents the theoretical prediction from the model described in the text. The given values for T_0 and R result in the best fit. In two limiting cases, the electrons orbiting the antidot are either weakly (b) or strongly (c) coupled to the electrons passing by.

through the device is [85]

$$T_d(\epsilon) = 1 - \frac{R^2}{1 + (1 - R)^2 - 2(1 - R) \cos 2\pi(\epsilon/\Delta\epsilon + \Phi/\Phi_0)}. \quad (4.3)$$

Here, Φ is the magnetic flux through the area of the closed orbit, and $\Delta\epsilon$ is the level spacing arising from the size quantization of this orbit.⁴ In the low magnetic field regime, the circular orbit around the antidot is completely determined by the applied magnetic field. Similar to the case of Shubnikov-deHaas oscillations, the energy spectrum of the antidot orbit is quantized with a level spacing

$$\Delta\epsilon = \hbar\omega_c. \quad (4.4)$$

⁴The same values for $\Delta\epsilon$ are valid for all tunnel couplings R , although strictly speaking, there is no closed orbit around the antidot for $R \approx 1$ [85]. See insets in Figure 4.6 for the two limiting cases $R \ll 1$ and $(1 - R) \ll 1$.

Using $\omega_c = v_F/R_c = 2\pi\hbar k_F/m^*L$, the energy spacing can be written as a function of the length of the cyclotron orbit L

$$\Delta\epsilon = \frac{2\pi\hbar^2 k_F}{m^*L}. \quad (4.5)$$

This expression is advantageous when dealing with non-circular orbits, since they are not completely described by the magnetic field value where they occur but rather by the orbit length L . The exact same expression can be obtained if one uses the Bohr-Sommerfeld quantization rule for non-interacting electrons with linear dispersion in a ring of length L . The quantization condition $L = 2\pi/\Delta k$, together with the linear dispersion relation $\Delta\epsilon/\Delta k = \hbar v_F$, directly gives the desired result. The temperature dependent conductance follows from the Landauer-Büttiker formalism

$$G(\mu^{\text{ch}}) = -\frac{e^2}{h} \int d\epsilon \frac{\partial n_F}{\partial \epsilon} T_d(\mu^{\text{ch}} + \epsilon), \quad (4.6)$$

where μ^{ch} is the (mean) electrochemical potential and n_F denotes the Fermi-distribution function [86]. Using

$$\frac{\partial n_F}{\partial \epsilon} = \frac{1}{4kT \cosh^2(\epsilon/2kT)}, \quad (4.7)$$

the conductance can be numerically evaluated. An analytical expression is obtained in the strong coupling limit ($R \approx 1$) [85, 87]

$$G = \tilde{g} + \delta g \cos 2\pi \left(\frac{\mu^{\text{ch}}}{\Delta\epsilon} + \frac{\Phi}{\Phi_0} \right). \quad (4.8)$$

Here

$$\tilde{g} = 2(1 - R) \frac{e^2}{h}, \quad (4.9)$$

is the constant part of the conductance, and the oscillating part has a prefactor

$$\delta g = -2(1 - R) \frac{e^2}{h} \frac{T/T_0}{\sinh T/T_0}, \quad (4.10)$$

where $k_B T_0 = \Delta\epsilon/2\pi^2$ is the temperature scale set by the level spacing. Note that the linewidth is temperature-independent and that the temperature scale is reduced by a factor $2\pi^2$ over a naive estimate of separated, Fermi-Dirac broadened levels. This can be traced back to the cosine dependence of the transmission on the electron energy.

From the period of the Aharonov-Bohm oscillations on the second focusing resistance peak, where the temperature dependence has been recorded, one can directly extract the area enclosed by the orbit producing this peak by means of $A = \phi_0/\Delta B$. If the orbit were circular, its length would be $L = 2\pi \times 550$ nm. The real orbit length is somewhat longer because of the specular reflection off the antidot. As an upper bound, we take the limit of an infinitely thin antidot. Then, the orbit corresponding to the second focusing peak consists of two circles and the orbit length is a factor $\sqrt{2}$ larger than the one given above. Using equation 4.5, the level spacing is calculated to be

$$\Delta\epsilon(k_F) \approx 240 \mu\text{eV} \approx k_B \cdot 2.8 \text{ K}. \quad (4.11)$$

The characteristic temperature scale for the decay of the Aharonov-Bohm oscillations is therefore

$$k_{\text{B}}T_0 = \Delta\epsilon/2\pi^2 \approx 140 \text{ mK} . \quad (4.12)$$

Experimentally, the temperature scale can be extracted from the measured temperature dependence of the Aharonov-Bohm oscillations. We plot the oscillation amplitudes for different temperatures against the numerically computed temperature dependency as a function of the normalized Temperature T/T_0 in Figure 4.6. From this fit we can extract the characteristic temperature $T_0 \approx 85 \text{ mK}$. This is about 40% lower than the above theoretical estimate from the simple edge state model.

4.3.2 Phase dislocations

The separation of the conductance into a smooth and oscillatory contribution according to equation 4.1 allows us to follow the Aharonov-Bohm phase as a function of the side gate voltage V_{sg} and the magnetic field B in an illuminating way. One finds that at certain points in the (V_{sg}, B) -plane oscillations suddenly vanish. In Figure 4.7(a), obtained using similar but not identical gate voltages as in Figure 4.4, forklike dislocations in the interference signal occur at $B = 0.41 \text{ T}$, $V_{\text{sg}} = -0.83 \text{ V}$ and $B = 0.375 \text{ T}$, $V_{\text{sg}} = -0.81 \text{ V}$. These dislocations in the interference signal arise from abrupt phase changes. The phase dislocations have been interpreted as a sign of orbit bifurcations that arise from the interference between different electron orbits around the antidot. The effect has been reproduced by semiclassical [89] as well as quantum simulations [82]. Phase singularities arise in a variety of cases throughout physics, and they are usually connected with interesting topological aspects of the system [90]. The topological character is illustrated in the schematic drawing of Figure 4.7(b). One can move through the (α, β) -parameter space from position A to B following two paths (red and blue) on the left and right side of the phase singularity, respectively. The two paths have a phase difference of $\Delta\varphi = 2\pi$ because one path (red) sees an additional oscillation. The same behavior occurs when a vortex with ‘charge’ $m = 1$ is superimposed with a plane wave. Here, the ‘charge’ of the vortex is defined as $m = \Delta\varphi/2\pi$. A particular nice example of this effect has been recently reported for Bose-Einstein Condensates (BECs) [88, 91]. In this case the parameters space is just the real space, i.e. $(\alpha, \beta) = (x, y)$. If one of the condensates is in the ground state and the other one in a vortex state, the interference of the two condensates leads to the same kind of phase dislocation as observed in our system. Figure 4.7(b) and (c) show a simulation of the effect for the case of the BECs.⁵

⁵The interference period Δx in real space for the superposition of two BECs is given by $\Delta x = h/mv$, where v is the relative velocity between the two condensates, and m is the mass of the constituent particles [91].

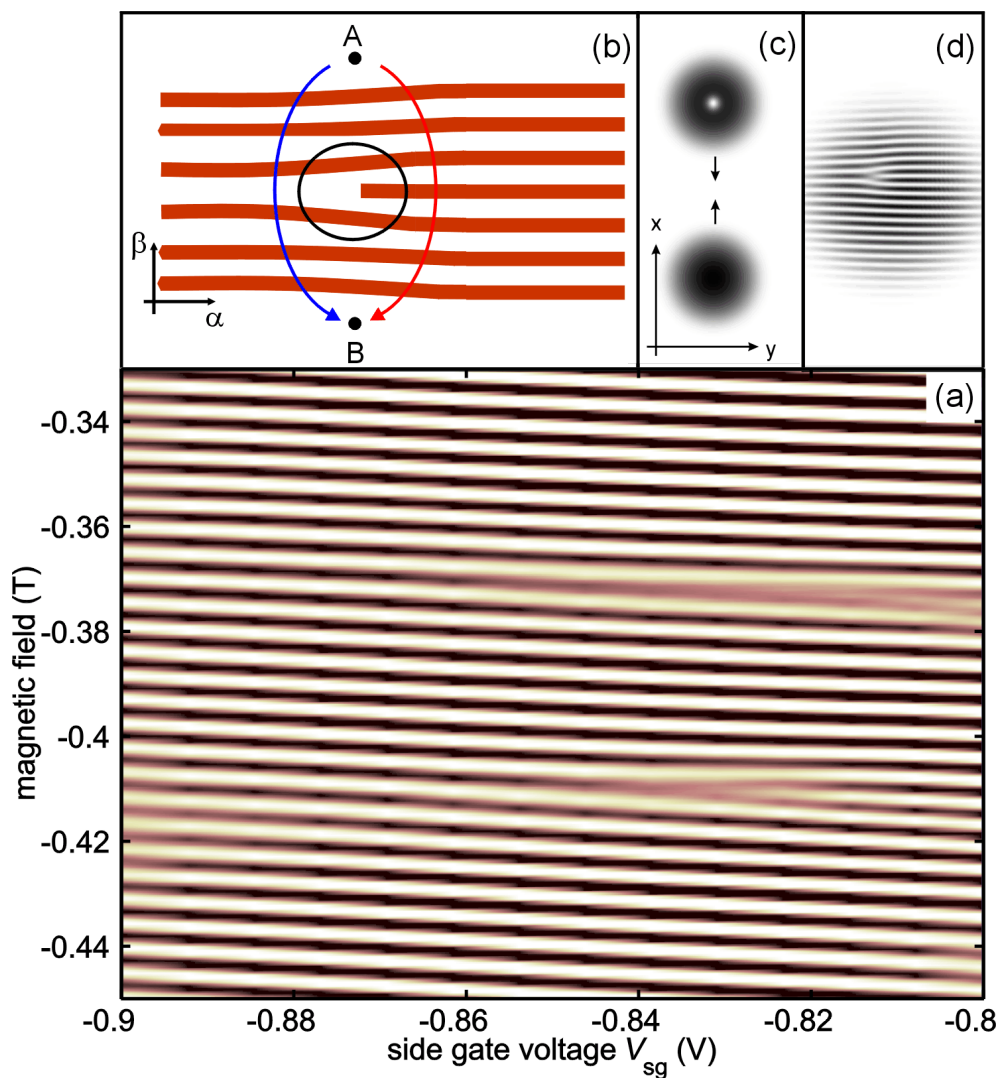


Figure 4.7: (a) Side gate voltage V_{sg} and magnetic field dependence of Aharonov-Bohm oscillations (peaks are light and minima dark colored). (b) Schematic drawing of a phase dislocation around a "vortex"(black circle). (c) Simulated density plot of two Bose-Einstein condensates (BECs) moving towards each other. One condensate (top) is in a $m = 1$ vortex state, the other one (bottom) is in the ground state [88]. (d) Simulated interference between the two BECs from (c) showing an interference dislocation [88].

Chapter 5

Correlated phases in the $N = 2$ Landau level

In this chapter, we present our experimental results on electronic transport in the regime of the correlated phases in the second excited Landau level ($N = 2$). Driven by the competition between repulsive and attractive components of the Coulomb interaction, long range ordered electron patterns form spontaneously within these phases. The Charge Density Wave (CDW) and the Electron Liquid Crystal (ELC) pictures, which describe the correlated phases, have already been introduced in sections 2.3.1 and 2.3.2, respectively. In the relevant Landau level, one distinguishes between the anisotropic stripe phase and the isotropic bubble and Wigner crystal phases.¹ In section 5.1, we briefly discuss resistance measurements which show features similar to those observed by other groups. Since the effects of anisotropic transport are more dramatic in the van-der-Pauw geometry, we employ it to obtain most of our results. Furthermore, we present data from a 'L'-shaped Hall-bar geometry. It allows us to measure both longitudinal resistivity components, ρ_{xx} and ρ_{yy} , simultaneously and offers a better defined current distribution within the sample. The main emphasis of this chapter will be on the differential resistance measurements presented in section 5.2. The data confirm the picture of the correlated phases in more detail and additionally reveal some completely unanticipated features.

5.1 Resistance around $\nu = 9/2$

The resistance measurements have been obtained with a conventional lock-in technique. An AC-current in the range $I_{AC} = 3 \text{ nA} \dots 10 \text{ nA}$ with a frequency of 13.31 Hz is injected into the sample at one ohmic contact and drained at a second one. The AC-voltage components are measured with a lock-in voltage amplifier that is in phase with the AC-current signal. The

¹To avoid confusion, we exclusively use the CDW terminology in this chapter. Still, we mention the importance of quantum fluctuations at the appropriate places.

magnitude of the excitation current has been chosen such that an optimal signal-to-noise ratio is obtained without inducing Joule heating effects by excessive currents.² Before a measurement is performed, the samples are illuminated at low temperatures with a red LED. The illumination procedure increases the density and the mobility of our samples. Even more important, it also enhances the transport effects inside the correlated phases substantially, probably because the illumination improves the overall homogeneity of the sample.

We would like to emphasize at this point that there can be quite large quantitative variations between results obtained on different samples, cooldowns or states of illumination. However, all our experimental results are confirmed to be generic features of electronic transport within the correlated phases of the $N = 2$ Landau level.

5.1.1 van-der-Pauw geometry

Most of the measurements have been obtained in a square van-der-Pauw (vdP) geometry. Our samples have lateral dimensions which are smaller by a factor of about 10-50 compared to samples from other groups. Additionally, we use lithographically defined ohmic contacts, instead of Indium contacts positioned by hand, to provide a well defined geometry. We mainly discuss square vdP samples fabricated from wafer VU4-97 with a size of $W = 90 \mu\text{m}$. The exact geometry and the fabrication process is described in appendix A. The mobility of the sample is around $\mu = 10 \cdot 10^6 \text{ cm}^2/\text{Vs}$ and the density around $n \approx 2.1 \cdot 10^{15} \text{ m}^{-3}$.³ In Figure 5.1(a), we show a measurement of the longitudinal resistance around filling factor $\nu = 9/2$, i.e. between $\nu = 4$ and $\nu = 5$. The blue curve depicts R_{xx} , i.e. the longitudinal resistance for the current flowing along the $[110]$ crystal axis ('easy-axis' configuration in Fig. 5.1(b)). The red trace is the longitudinal resistance R_{yy} for the current flowing in the perpendicular direction, that is along the $[1\bar{1}0]$ axis ('hard-axis' configuration Fig. 5.1(c)). Following the literature, we use the expressions 'hard-axis' and 'easy-axis' throughout this chapter as synonyms for the crystal axis $[1\bar{1}0]$ and $[110]$, respectively. Although used in the whole magnetic field range, the expressions are derived from the natural orientation of the stripes relative to the crystal axis in the stripe phase.

Stripe phase

The most striking difference between the two longitudinal resistance components is observed around the half filled topmost Landau level in the regime $0.38 < \nu_N < 0.62$ (highlighted with a yellow shade). Here, the resistance shows a huge anisotropy most pronounced exactly at $\nu_N = 1/2$, where $R_{yy}/R_{xx} \approx 40$. The anisotropy is consistent with the existence of a

²Since Joule heating effects depend on the current densities in the sample rather than the current itself, our samples are much more prone to heating than the much larger ones used by other groups. Therefore, we use comparatively smaller excitation currents.

³These quantities vary for different cool-downs and for different amounts of illumination.

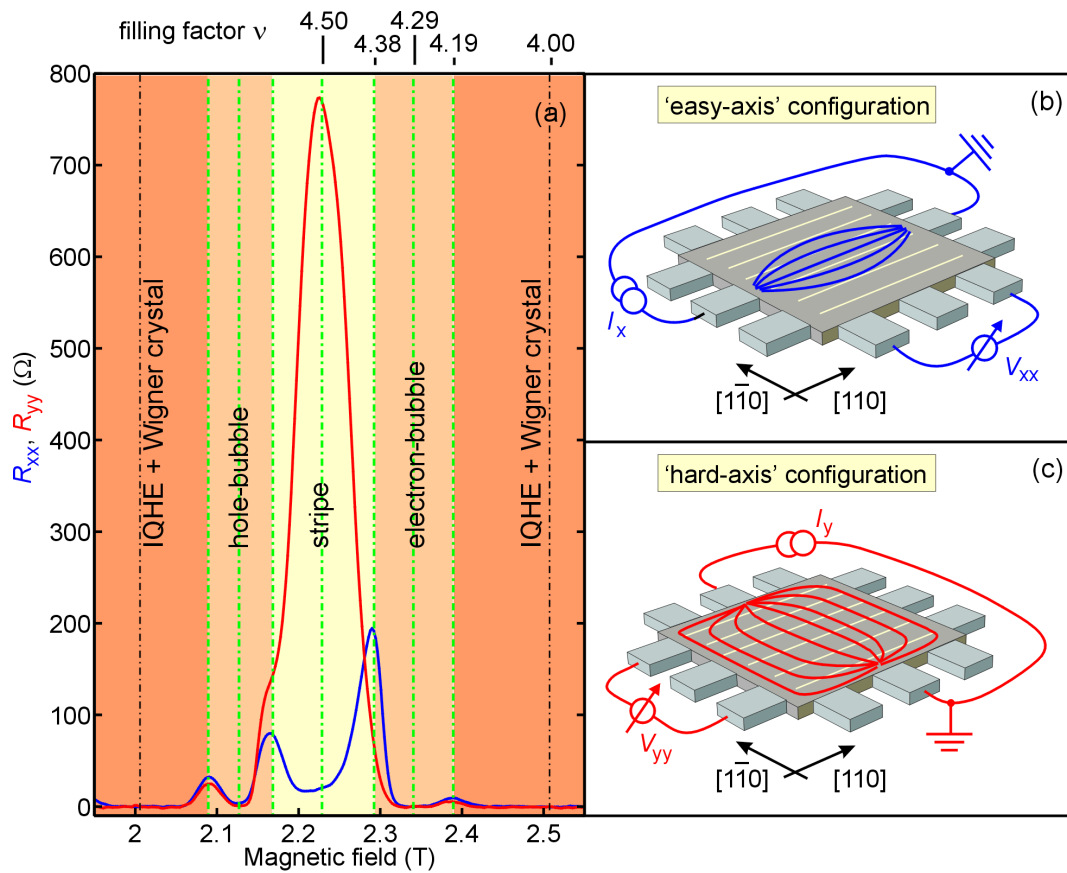


Figure 5.1: (a) Longitudinal resistance measurement in the van-der-Pauw geometry at $T = 40$ mK with the current directed along the natural stripe direction (blue curve) or perpendicular to it (red curve). On the right side, the two measurement configurations together with the resulting current distributions are shown schematically. In the 'easy-axis' configuration (b), R_{xx} is measured along the $[110]$ crystal axis, whereas in the 'hard-axis' configuration (c) R_{yy} is measured along the $[\bar{1}10]$ crystal axis. The yellow lines show the natural stripe direction, and the red and blues ones the current distribution within the sample in the stripe phase.

stripe phase in this regime. The current flow is 'easy' along the stripes whereas it is 'hard' across the stripes (yellow lines in Fig.5.1(b) and (c) indicate the natural stripe direction). The resistance anisotropy is strongly enhanced in square vdP geometries, since an anisotropy in the underlying resistivities ($\rho_{xx} < \rho_{yy}$) causes an inhomogeneous current density distribution in the sample [55]. When the current is directed along the stripes, it flows mainly near an imaginary line which directly connects the two current contacts. Hence, the current density near the voltage contacts will be low, further reducing the measured signal by Ohm's law $V_x \sim \rho_{xx} j_x$ (Fig.5.1(b)). On the other hand, the current will be distributed more evenly across the device

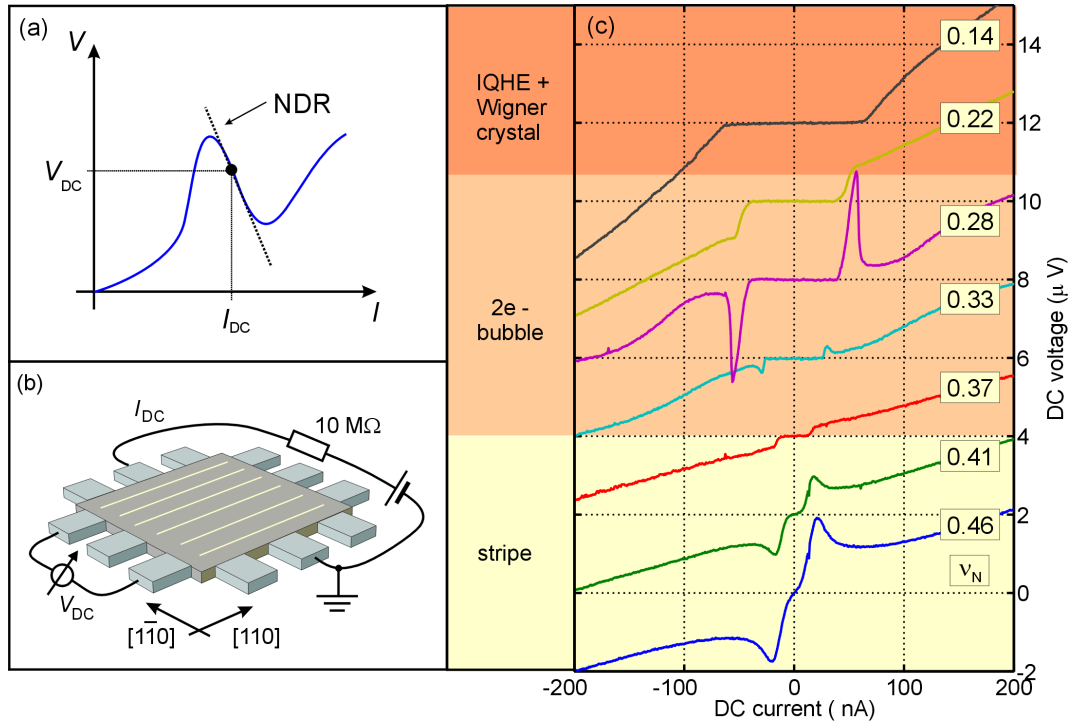


Figure 5.2: (a) Negative Differential Resistance (NDR) in a non-linear V-I measurement. (b) DC setup to directly measure the $V(I)$ dependence in the 'hard'-axis configuration. (c) Non-linear V-I characteristics for several filling factors ranging from the stripe phase (bottom trace) via the bubble phase to the IQHE (top trace). For clarity, the traces are vertically offset from each other by $2\mu\text{V}$. The color coding for the phases is the same as in Fig. 5.1.

for the perpendicular flow direction since the stripes tend to spread out the current in the $[110]$ crystal direction (Fig.5.1(c)). Within the stripe regime, the Hall-resistance is not quantized (see Fig. 5.9) confirming the compressible nature of this phase.

Bubble phase

Around filling factor $\nu_N = 0.29$ (and its particle-hole conjugate $\nu_N = 0.71$), the longitudinal resistance in both crystal directions completely vanishes at low enough temperatures. At the same time, the Hall-resistance is quantized to the value of the adjacent IQHE state (see Fig. 5.9). Vanishing longitudinal resistance and quantized Hall resistance are signs of an incompressible ground state in this regime. Since the quantized regime around filling factor $\nu_N = 0.29$ is isolated from the adjacent IQH-state by a non-zero resistance peak at $\nu_N = 0.19$, it is referred to as the Reentrant Integer Quantum Hall (RIQHE) state. This state is identified with the bubble phase and stabilized in the regime $0.20 < \nu_N < 0.38$ (as well as its particle hole conjugate $0.62 < \nu_N < 0.80$). This range of filling factors compares well with the theoretical predictions

for the 2-electron bubble phase ($0.25 < \nu_N^{\text{theo}} < 0.36$) [53].

Non-linear V-I characteristics

Resistance measurements, such as the ones described above, probe the linear response of the correlated phases for small excitation currents. However, complex electronic systems typically do not exhibit linear transport behavior, and it is therefore necessary to measure the full DC response. In Figure 5.2(c), we sweep the DC current between $I_{\text{DC}} = -200 \text{ nA} \dots 200 \text{ nA}$ by varying the voltage across a large resistor and measure the resulting DC voltage response⁴ in the 'hard-axis' configuration (see Fig. 5.1(b)). Clearly, the V-I response is highly non-linear in the regime of the correlated phases. Most striking is the observation of negative differential resistance (NDR) - schematically shown in Fig. 5.1(a) - seen in the center of the stripe (blue trace) and of the bubble phase (magenta trace). Especially in the bubble phase, the non-linear response is reminiscent of that of a resonant tunnel diode. We come back to this point in section 5.2 where we investigate the non-linearities within the correlated phases in detail.

5.1.2 Hall-bar geometry

Complementary to the measurements in the vdP geometry just presented, we employ a 'L'-shaped Hall-bar device (Fig. 5.3(b)) to measure the longitudinal resistivity components in both main crystal axis directions simultaneously and also provide a better defined current distribution. The Hall-bars have a width of $200 \mu\text{m}$ and are processed from wafer VU4-127. The mobility of the samples is around $\mu = 12 \cdot 10^6 \text{ cm}^2/\text{Vs}$, the density is $n = 3.1 \cdot 10^{15} \text{ m}^{-2}$.

Figure 5.3(a) shows a resistivity measurement on the 'L'-shaped Hall-bar with the current directed simultaneously along the $[\bar{1}\bar{1}0]$ (ρ_{yy}) and the $[110]$ (ρ_{xx}) crystal direction. The ρ_{xx} data is scaled down by a factor of 2 to match the ρ_{yy} data at magnetic fields below $B < 0.2 \text{ T}$ (Figure 5.3(c)).⁵ This way, we obtain very comparable resistances for the two directions also in the $N = 1$ Landau level, i.e. between $\nu = 2$ and $\nu = 4$. The scaling procedure accounts for an inherent, filling factor independent anisotropy in the resistances. Such an anisotropy is observed in many high mobility materials but its origin is unknown. It is not enhanced in vdP geometries, and therefore it is probably not related to a real anisotropy in the resistivities. So far, no connection has been established between this filling factor independent anisotropy and the preferred orientation within the correlated stripe phase.

At magnetic fields below $B = 1 \text{ T}$, the Shubnikov-deHaas oscillations show a pronounced even-odd filling factor asymmetry (Fig. 5.3(c)). For ρ_{yy} , the peaks on the high field side of an even filling factor are smaller than the ones on the low field side; for ρ_{xx} , the situation is just reversed. The origin of this even-odd asymmetry is probably related to the electron spin and the

⁴We use a 'Keithley 182 Sensitive Digital Voltmeter' with an input resistance $> 10 \text{ G}\Omega$ for the measurement of small DC voltages.

⁵Our choice to scale the ρ_{xx} data and not the ρ_{yy} data is arbitrary.

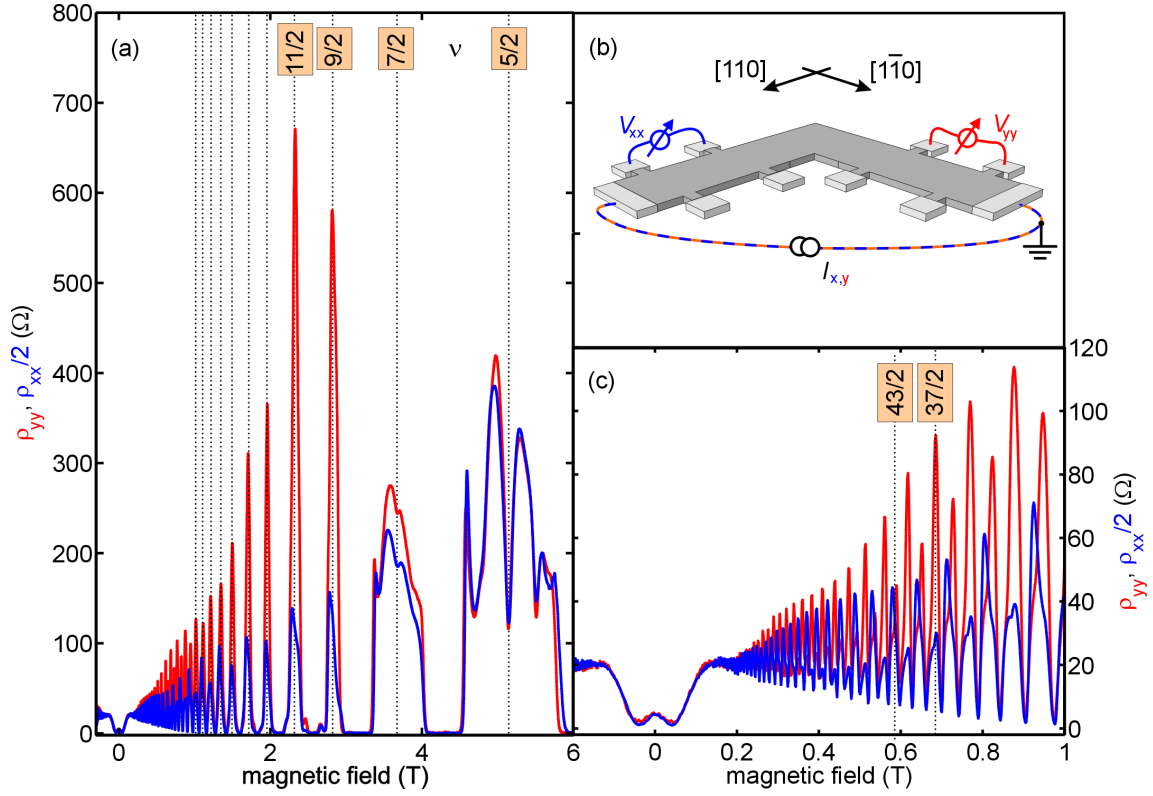


Figure 5.3: (a) Longitudinal resistance components ρ_{xx} (blue) and ρ_{yy} (red) measured simultaneously in the "L"-shaped Hall-bar shown schematically in (b). The curves have been normalized to each other at the lowest fields (see text). (c) An anisotropic even-odd behavior is observed in the low magnetic field regime.

reduced gap for odd filling factors. However, it is not clear why the asymmetry depends on the current direction and whether it is related to the origin of the preferred orientation of the stripes. We have not yet studied this effect systematically, but it deserves further attention because it might provide an additional clue to the question of the natural stripe orientation.

Around half filling of the higher Landau levels ($\nu = 9/2, 11/2, 13/2, \dots$), a pronounced anisotropy is seen induced by stripe formation along the $[110]$ crystal axis. The anisotropy is not as strong as in the vdP geometry and reaches factors of $\rho_{yy}/\rho_{xx} \approx 6$. The anisotropy persists up to high filling factors but its magnitude decreases in that direction. This agrees qualitatively with the behavior expected from the nematic stripe phase where the peak resistance should decrease as $\rho_{yy} \sim 1/\nu^2$.

Temperature dependence

Figure 5.4 shows the detailed temperature dependence of the longitudinal resistances in the Hall-bar below $T = 120$ mK. The measurements are shown for current flowing simultaneously

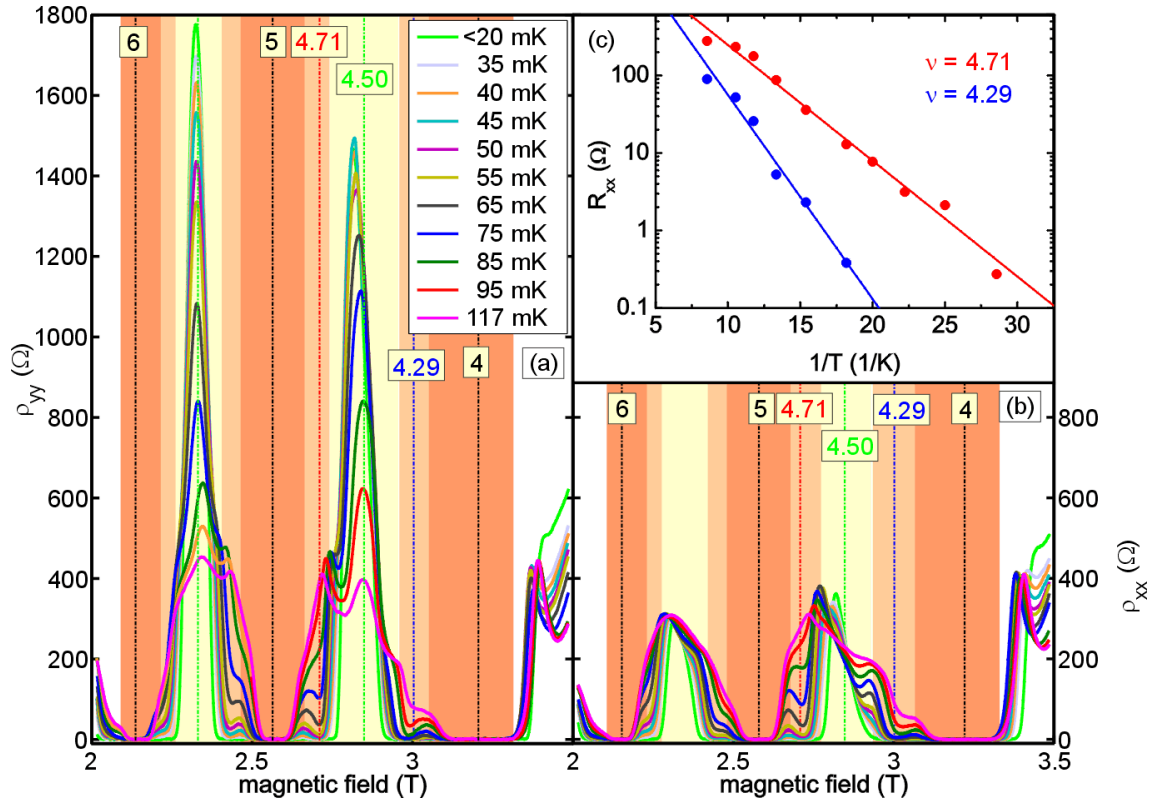


Figure 5.4: Temperature dependence in the "L"-bar geometry between filling factors $\nu = 4$ and $\nu = 6$. (a) Current in the $[1\bar{1}0]$ 'hard-axis' direction. (b) Current in the $[110]$ 'easy-axis' direction. (c) Arrhenius plot of the R_{xx} temperature dependence in the electron- and hole-bubble phases (blue near $\nu_N = 0.29$, $\Delta_e \approx 100 \mu\text{eV}$; red near $\nu_N = 0.71$, $\Delta_h \approx 60 \mu\text{eV}$). The evaluation of R_{yy} gives very similar values and is therefore not shown.

along the $[110]$ (5.4(a)) and the $[1\bar{1}0]$ direction (5.4(b)). Special care was taken in these experiments to keep the temperature stable to within $\Delta T = 1 \text{ mK}$ over the magnetic field range. The electron-bubble phase near the empty Landau level shows a less pronounced temperature dependence than the hole-bubble phase near the filled Landau level. This can be quantified when we analyze the activation energies Δ_e, Δ_h in the center of both phases (inset Fig. 5.4). The relation between longitudinal resistance and activation energies should be of the Arrhenius type

$$\rho_{xx} \propto \exp\left(-\frac{\Delta}{2kT}\right). \quad (5.1)$$

For the hole-bubble phase near $\nu_N = 0.71$, we obtain $\Delta_h \approx 60 \mu\text{eV}$, whereas for the electron-bubble phase near $\nu_N = 0.29$ we obtain $\Delta_e \approx 100 \mu\text{eV}$. The large difference in the activation energies is not consistent with particle-hole symmetry within the $N = 2$ Landau level. The effect has been observed by other groups but so far no explanation has been put forward. We return to

this point when we discuss our differential resistance results in the next section.

5.2 Differential resistance around $\nu = 9/2$

Virtually all resistance measurements on 2DES are performed in the linear regime, i.e. when the measured voltages scale linearly with the excitation currents. If signs of non-linearity are observed, they are usually attributed to Joule heating effects induced by too high excitation currents. We will show that, in the regime of the correlated phases in the $N = 2$ Landau level, the voltage-current (V-I) characteristics are inherently highly non-linear. The non-linear V-I

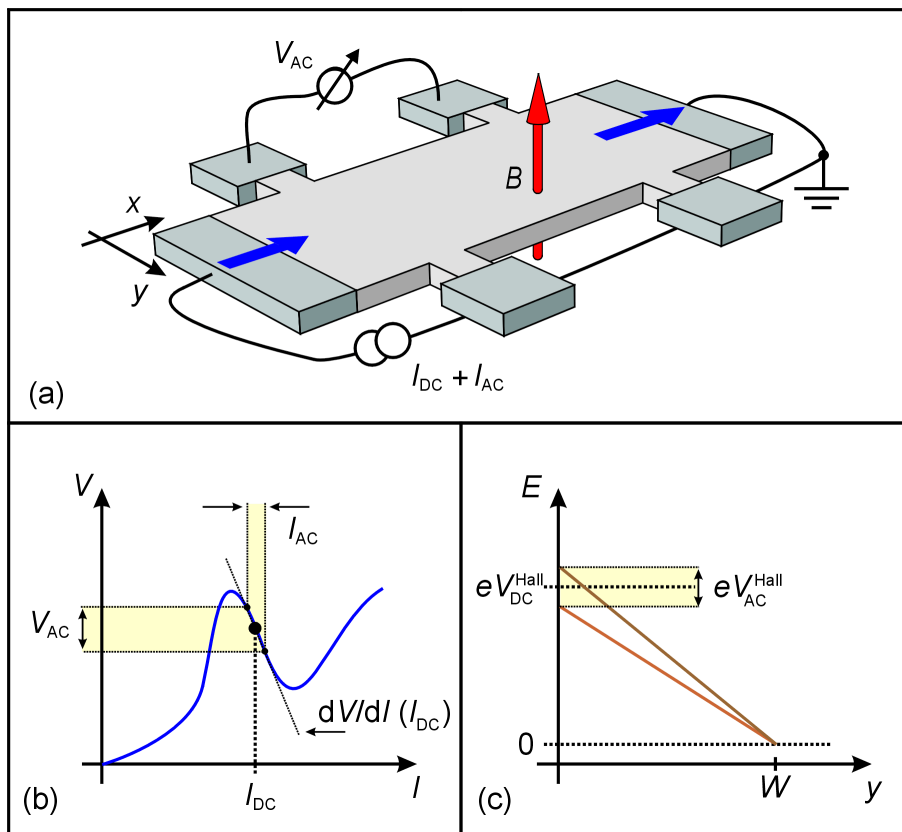


Figure 5.5: (a) Differential resistance measurement setup. A DC bias current I_{DC} is added to a small AC component I_{AC} . The voltage signal V_{AC} in phase with the AC current is detected via a standard lock-in technique. (b) From the in-phase voltage V_{AC} , induced by a current modulation I_{AC} around the working point I_{DC} , one obtains an approximation to the differential resistance $dV/dI(I_{DC})$. (c) Simple model for the effect of a combined AC and DC measurement. A DC Hall voltage V_{DC}^{Hall} drops over the width W of the sample and is modulated by a small AC Hall voltage V_{AC}^{Hall} .

curves can be measured directly (see Fig. 5.2), but in general, it is advantageous to measure the differential resistance (dV/dI). This way, one can take advantage of a lock-in technique to substantially increase the signal-to-noise ratio of the measurement. For this purpose, a DC bias current I_{DC} and a small AC excitation current I_{AC} are added (Fig. 5.5(a)). Only the voltage response in phase with the AC excitation is recorded. For sufficiently small AC current amplitudes, this results in an approximation to the local derivative of the V-I curve at the working point I_{DC} (Fig. 5.5(b))

$$dV/dI(I_{\text{DC}}) = \lim_{I_{\text{AC}} \rightarrow 0} \frac{V(I_{\text{DC}} + I_{\text{AC}}) - V(I_{\text{DC}} - I_{\text{AC}})}{2I_{\text{AC}}} \approx \frac{V_{\text{AC}}}{I_{\text{AC}}}(I_{\text{DC}}). \quad (5.2)$$

Adding a DC bias current produces a non-equilibrium situation inside the Hall-bar, and it is a priori not clear how this affects the transport properties. In the simplest picture, the DC bias current produces an additional Hall voltage, i.e. Hall electric field, perpendicular to the DC current across the sample. For a rough estimate of the Hall voltage, we neglect the modifications from the Quantum Hall Effect. Then, the DC Hall voltage is proportional to the DC current and the external magnetic field (Fig. 5.5(c))

$$V_{\text{DC}}^{\text{Hall}} = \frac{h}{e^2\nu} \cdot I_{\text{DC}}. \quad (5.3)$$

5.2.1 'easy-axis' configuration - AC/DC currents along [110]-axis

In the following, we discuss a differential resistance measurement between filling factor $\nu = 4$ and $\nu = 5$. The AC/DC currents are directed along the [110] crystal axis, i.e. the 'easy-axis' as far as the stripe phase is concerned. To obtain the results shown in Figure 5.6, the AC current is fixed to $I_{\text{AC}} = 3$ nA, and the DC current is increased stepwise in the range $I_{\text{DC}} = -180$ nA \dots 180 nA. For each particular value of the DC current, the magnetic field is swept between $B = 1.7$ T \dots 2.3 T. High differential resistance values are colored in red whereas low ones are shown in blue. For clarity, regions of negative differential resistance (NDR) are surrounded by a white contour. The resistance measurements presented in the previous section (see Fig. 5.1) correspond to measurements along the black horizontal line at $I_{\text{DC}} = 0$. For this particular cooldown and temperature ($T < 20$ mK), the results at vanishing DC current are not particularly illuminating. In most of the magnetic field range, the resistance vanishes completely. Only in the range $B = 1.9$ T \dots 2.0 T, one observes a small, non-zero resistance of a few Ohms. Much more information can be extracted by looking at the complete differential resistance scan. Around integer filling factors $\nu_{\text{N}} = 0$ and $\nu_{\text{N}} = 1$, i.e. within the IQHE phase, the resistance remains zero up to the highest DC currents shown. On the other hand, the zero resistance regime in the bubble phases and the low resistance regime in the stripe phase break down when the DC current reaches critical values. The critical DC currents increase roughly linearly from the boundary to the center of each phase. This gives rise to three diamond-shaped regions of low resistance, one for each phase, which are virtually symmetric around $I_{\text{DC}} = 0$.

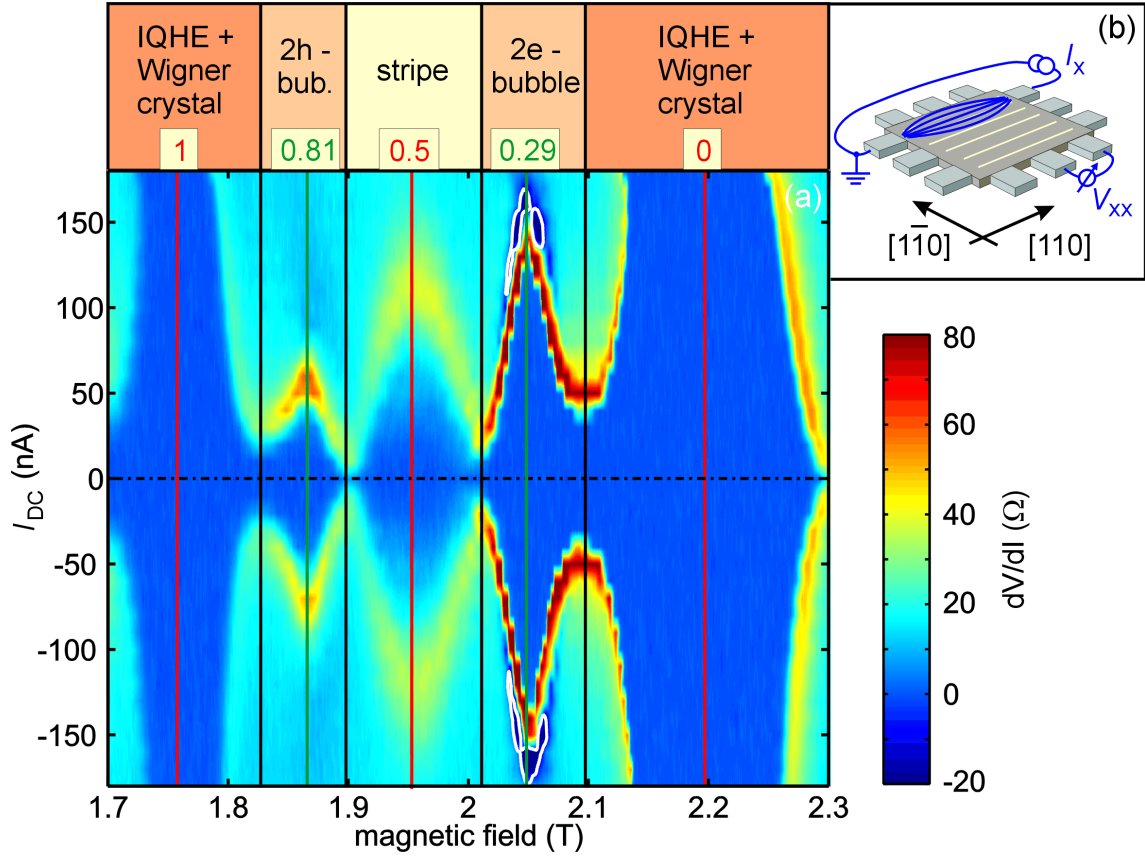


Figure 5.6: (a) Differential longitudinal resistance of a vdP sample in the 'easy-axis' configuration shown in inset (b) between $\nu = 4$ and $\nu = 5$, i.e. $\nu_N = 0$ and $\nu_N = 1$, at $T < 20$ mK. The AC/DC currents are directed along the [110] crystal axis. Three distinct regions are discernible. The stripe phase is centered directly around $\nu_N = 0.5$. In this regime, stripe formation along the [110] axis, i.e. parallel to the current direction, results in a resistance minimum. The stripe phase is bounded by bubble phase regions on either side, centered around $\nu_N = 0.29$ and $\nu_N = 0.81$. The phase boundaries (vertical black lines) above and below $\nu_N = 0.5$ are related to each other by particle-hole symmetry. The white contour surrounds areas of negative differential resistance (NDR).

Stripe phase

The stripe phase is centered around $\nu_N = 0.5$. In this regime, stripe formation along the [110] axis, i.e. parallel to the current direction, results in a resistance minimum. This minimum breaks down in a smooth way. In the center of the phase, the differential resistance starts to increase from its initial low value as the DC current reaches $I_{DC} \approx 50$ nA. After a maximum is reached in the range between 80 nA and 140 nA, it saturates to an intermediate value. Since this saturation value is quite similar to the one for the orthogonal current direction (see Fig. 5.7), we

believe that all remnants of an anisotropic stripe phase have disappeared at these high currents.

Bubble phase

At low currents, the electron-bubble phase around $\nu_N = 0.29$ is insulating, and accordingly, the longitudinal resistance vanishes inside this regime. Above a magnetic field dependent critical DC current, the bubble phase breaks down in a remarkable way. The breakdown current is highest in the middle of the phase where $\nu_N = 0.29$. At this point, the differential resistance abruptly increases followed by a strong decrease at only slightly higher currents. Strikingly, regions of negative differential resistance (NDR) occur (white contour in Fig. 5.6). Although not well resolved in Fig. 5.6, the breakdown of the hole-bubble phase near $\nu_N = 0.71$ is qualitatively similar to that of the electron-bubble phase. However, the breakdown currents are smaller and all features tend to be more smeared out indicating that this phase is more fragile. In similar measurements (not shown), we have observed NDR also in the hole-bubble phase.

Since positive and negative differential resistance features are sharp up to relatively high bias currents, the effects of an applied DC current can not be simply explained by an effective increase of the electron temperature (see section 5.2.4).

5.2.2 'hard-axis' configuration - AC/DC currents along $[1\bar{1}0]$ -axis

We turn to the differential resistance data for the 'hard-axis' configuration in which the current is directed along the $[1\bar{1}0]$ crystal axis (Fig. 5.7). The stripe and bubble phases are discussed separately. Then, we point out how these phases are reflected in the Hall resistance, and finally, we take a look on how the distance between current path and voltage contacts affects the results.

Stripe phase

As explained in section 5.1.1, a striking signature of the stripe phase is the huge resistance maximum close to $\nu_N = 0.5$ which appears when the current is directed orthogonal to the stripe direction (see also Fig. 5.1). This maximum shows up in Figure 5.7 as red colored region close to $I_{DC} = 0$. To allow for a better distinction, the highest values of the differential resistance ($dV/dI > 600 \Omega$) are surrounded by a cyan contour. In the stripe phase, a DC current of about $I_{DC} \approx 20$ nA is sufficient to completely eliminate the resistance maximum. Then, for a range of higher DC currents, a region of negative differential resistance (NDR) follows (surrounded by a white contour in Fig. 5.7). One finds the maximum of the differential resistance in the stripe phase for $I_{DC} = 0$ to occur not directly at $\nu_N = 0.5$ (vertical red line) but instead at slightly lower magnetic fields. As $\nu_N = 0.5$ is reached, the maximum splits into two maxima located at non-zero DC currents $I_{DC} \approx \pm 10$ nA. Therefore, as far as the maximum is concerned, a slight change in the filling factor can be compensated for by applying a small DC bias current.

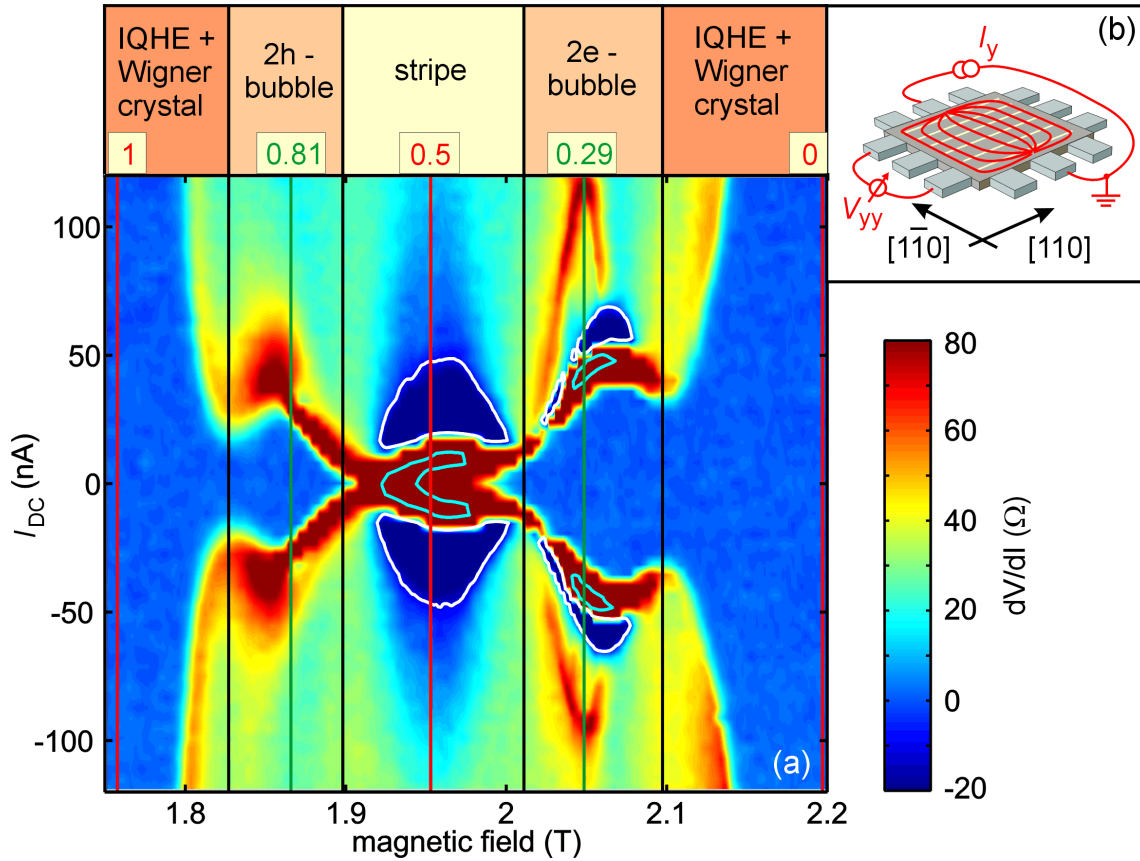


Figure 5.7: (a) Differential longitudinal resistance of a vdP sample in the 'hard-axis' configuration shown in inset (b) at $T < 20$ mK. AC/DC currents are directed along the $[1\bar{1}0]$ crystal axis. The white contour surround areas of negative differential resistance. The cyan contour highlights areas with the highest differential resistance ($dV/dI > 600 \Omega$). The phase boundaries (vertical black lines) are drawn at the same positions as in Figure 5.6.

Bubble phase

The breakdown of the bubble phase for the 'hard-axis' (Fig. 5.7) seems to be different from the one in the 'easy-axis' configuration (Fig. 5.6).⁶ Still there are similar features in Figures 5.7 and 5.6. The maximum of the differential resistance reaches similar values at the breakdown of the bubble phase and around zero DC current in the stripe phase. Together with the observations of NDR in both cases, this is a first indication of a closer, yet unknown connection between bubble and stripe phase. We return to this important finding in section 5.2.5 at the end of this chapter.

⁶However, we used different contact geometries for both measurements (see figures for details). The results for measurements along the two main crystal axis agree quite well in the bubble phase when the same geometry (only rotated) is used (compare Fig. 5.12 (a) and (d)). This is expected for an isotropic phase.

In the bubble phase, we observe additional differential resistance peaks at high DC currents ($I_{\text{DC}} \approx 100$ nA at $\nu_{\text{N}} = 0.29$). We are not sure whether these peaks are a generic feature because they only show up in a few measurements. Since they appear at a similar position as the pronounced features seen in Figure 5.6, they might indicate that the current is not flowing exactly in the $[1\bar{1}0]$ direction but instead has components along both crystal axes.

Hysteresis

Another interesting result appears when one compares the differential resistance at fixed magnetic field for different sweep directions of the DC current (Fig. 5.8). One finds clear hysteretic behavior near the breakdown of the bubble phase (upper two traces), whereas no hysteresis is found in the stripe phase (lower three traces). From this, one might infer that the bubble phase most likely breaks down via a first order phase transition whereas the stripe phase does so via a second order one. Apparently, our differential resistance measurements may open up the intriguing possibility to study the interplay between second and first order phase transitions in

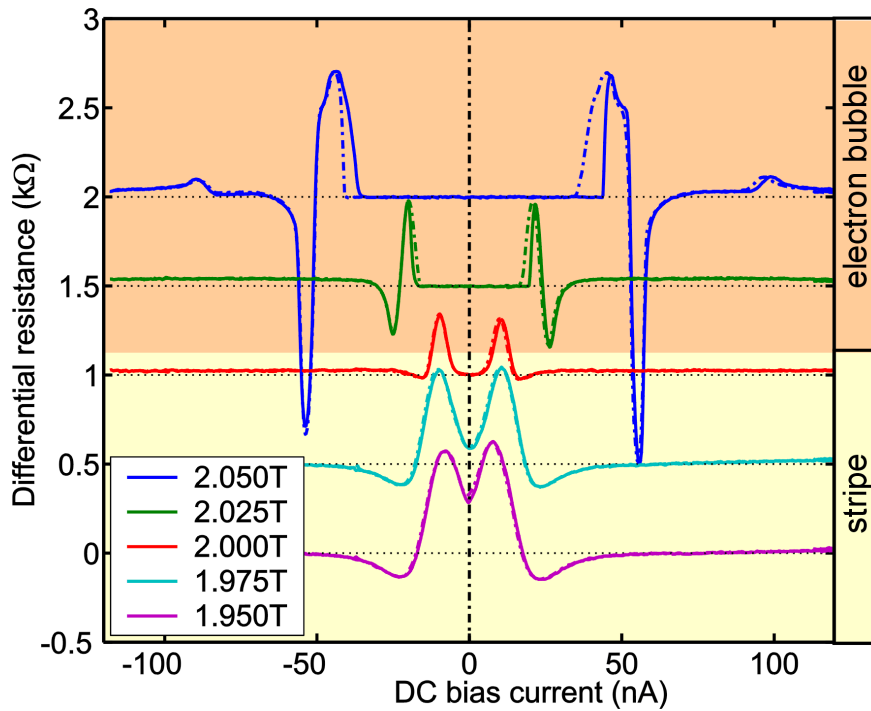


Figure 5.8: Differential resistance for several magnetic field values in the 'hard-axis' configuration (see Fig. 5.7) at $T < 20$ mK. The solid color lines correspond to the up-sweep and the dashed colored ones to the down-sweep of the DC current. The top trace (blue) is taken at the center of the bubble phase and the lowest one (magenta) in the stripe phase exactly at $\nu_{\text{N}} = 0.5$. The curves are vertically offset for clarity.

correlated quantum systems.

Hall resistance

Figure 5.9 shows the differential Hall resistance together with the differential longitudinal resistance in the 'hard-axis' configuration over a range of filling factors ($\nu = 4$ to $\nu = 6$) and DC currents⁷. For zero DC current (blue trace in (a)), the plateaus at the quantized resistance values h/ie^2 are broad, and the transition region near the half filled Landau level is relatively narrow. From the Hall resistance at $I_{\text{DC}} = 0$, it is not possible to determine whether the resistance quantization is caused by single particle localization (near integer filling factors) or rather by pinning of a correlated bubble phase (towards half filling). This issue is resolved at intermediate DC currents, where a small magnetic field region in which the Hall resistance is not quantized separates the IQHE (single particle) regime from the RIQHE (many-body) regime. This takes place around $I_{\text{DC}} = 16$ nA for the hole-bubble phase and around $I_{\text{DC}} = 40$ nA for the electron-bubble phase. Above $I_{\text{DC}} > 200$ nA (cyan trace), the quantized plateaus narrow down considerably. In this high current regime, the remaining width of a plateau presumably reflects localized single electron states only. The transition region between plateaus is broad and the Hall resistance almost follows the classical result. Since this resembles the behavior at sufficiently high temperatures ($T > 150$ mK), it probably indicates that electron correlations are destroyed at these high currents.

One of the few quantitative predictions for striped ELC phases concerns the Hall resistivity at $\nu_N = 0.5$ (see discussion of the smectic phase in sec. 2.3.2). Equation 2.53 predicts a value of $\rho_{xy} = 9/41 \cdot h/e^2$ exactly at $\nu = 9/2$, i.e. for the case $[\nu] = 4$ (included in Figure 5.9 as a black dashed horizontal line labelled McD. *et al.*). Experimentally, the Hall resistance takes on the theoretical value only at somewhat lower magnetic fields, exactly where the longitudinal resistance reaches its maximum (vertical black arrows in the figure). Instead, at $\nu_N = 0.5$ the Hall resistance is still very close to the value $\rho_{xy} = 1/4 \cdot h/e^2$ of the empty $N = 2$ Landau level.

An additional feature at intermediate DC bias currents deserves attention. For example, at $I_{\text{DC}} = 16$ nA and 40 nA, as one moves from the RIQHE regime (vertical red arrow) towards the stripe phase, the Hall resistance drops from its initial value of $0.25 h/e^2$ down below the line of the classical Hall resistance (white arrow). If the RIQHE would break down in a simple way, the Hall resistance should smoothly drop towards the classical value but not below it. It seems that for a narrow region of magnetic fields the Hall resistance starts to drop already to the value of $0.2 h/e^2$ which it normally reaches only in the stripe phase regime at substantially lower magnetic fields.

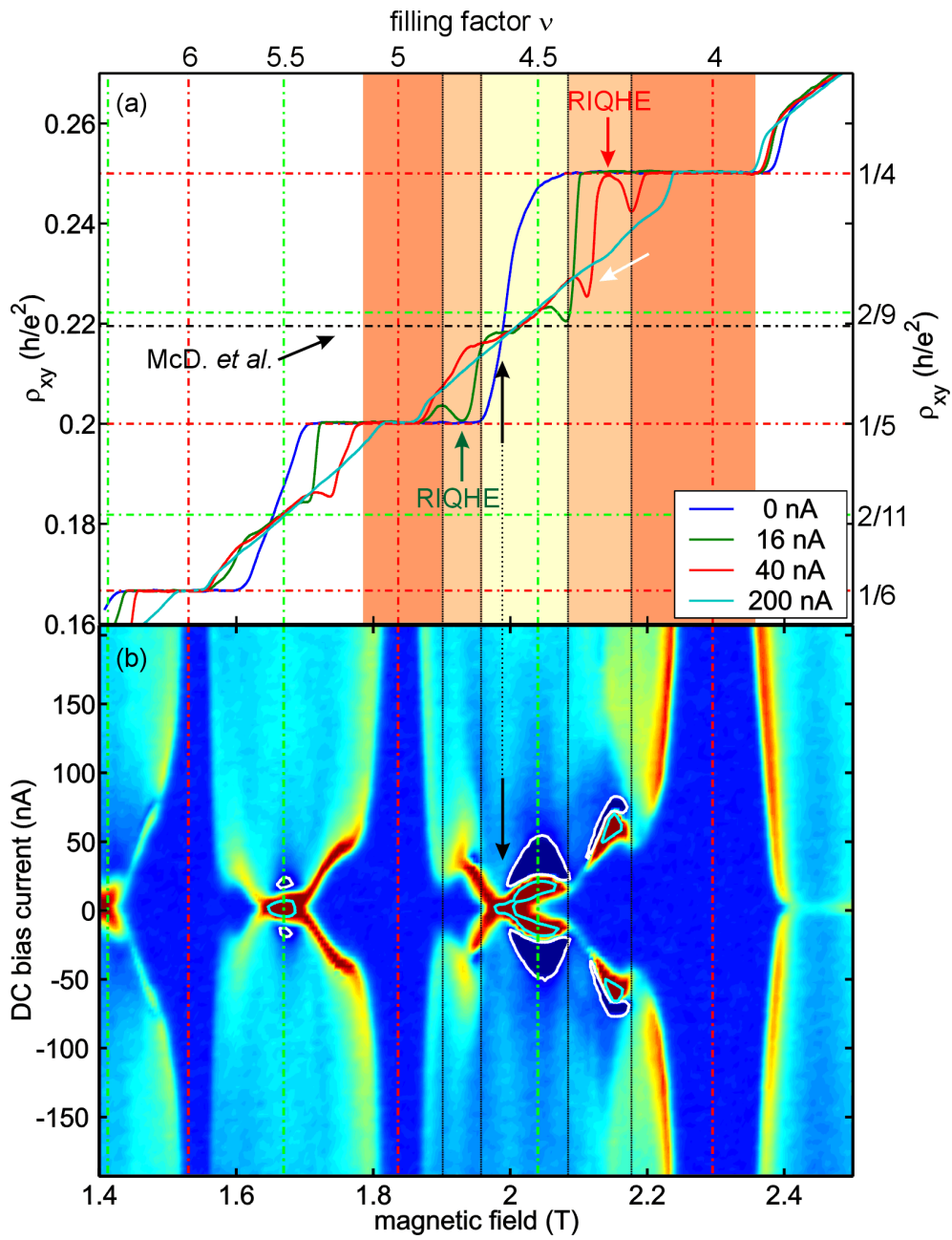


Figure 5.9: (a) Differential Hall resistance for a few selected DC currents. The reentrant quantization (RIQHE) in the center of the bubble phase is marked by colored arrows. The dashed black horizontal line shows the theoretical prediction for the Hall resistance in the center of the smectic phase (MacDonald *et. al* [67]). (b) Differential longitudinal resistance. At $I_{DC} = 0$, the maximum resistance occurs at a filling factor $\nu_N > 0.5$ (see text). The color coding, temperature and configuration are the same as in Fig. 5.7.

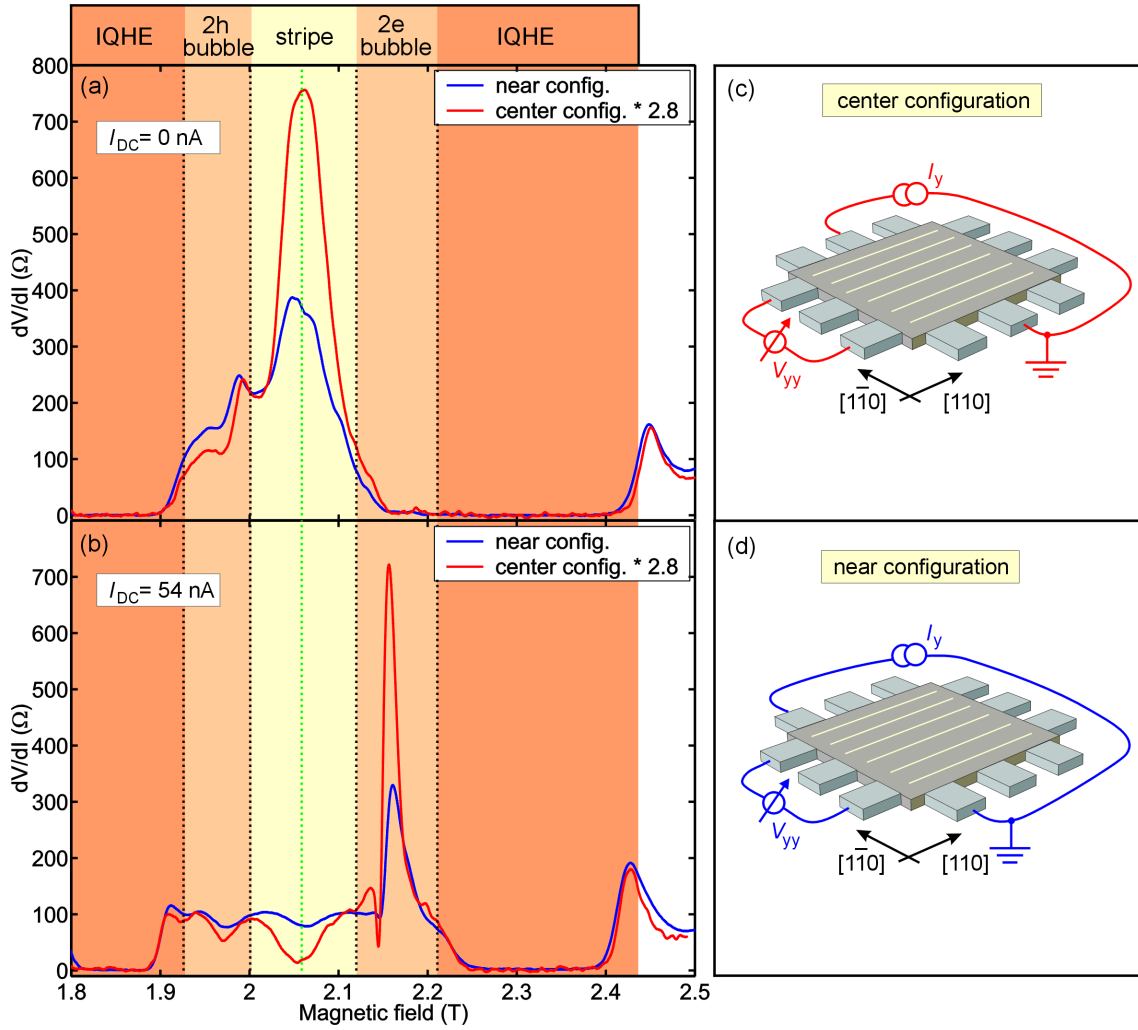


Figure 5.10: Differential resistance for (a) $I_{DC} = 0$ and (b) $I_{DC} = 54$ nA measured for two different 'hard-axis' contact configurations. The red trace is obtained in the 'center' configuration (c) and the blue trace in the 'near' configuration (d). The data for the red traces are scaled by a factor of 2.8 (see text).

Changing the distance between AC/DC current path and voltage contacts

In Figure 5.10, we compare data for two different contact configurations. In the 'center' configuration (c), the DC current path is further away from the voltage contacts than in the 'near' configuration (d). For an isotropic conductor, i.e. when $\rho_{xx} = \rho_{yy}$, the measured resistances fall off in a well defined way as the distance between current path and voltage contacts is increased [55]. The fall-off is determined solely by a geometry factor and is independent of the magnetic field. Therefore, the resistances obtained in the 'center' - configuration should be

⁷The corrections to the Hall resistivity by the longitudinal conductances can be neglected, since from eq. 2.53, $\sigma_{xx}\sigma_{yy}/\sigma_{xy}^2 \approx 1/81$.

scalable to the resistances from the 'near' - configuration with a field independent factor. Any deviation from this overall scaling factor in a range of magnetic fields is a clear indication for anisotropic transport ($\rho_{xx} \neq \rho_{yy}$) in this field range.⁸ Indeed at $I_{DC} = 0$, the 'center'-resistances, scaled by a factor of 2.8, resemble the 'near'-resistances to a good approximation except in the stripe phase regime (Fig 5.10(a)).⁹ After scaling, the 'center'-resistance in the stripe phase regime is larger than the 'near'-resistance by a factor of approximately 2. Thus, the measured resistance falls off much more slowly with the distance between voltage contacts and current path in the stripe phase than at all other magnetic fields. The intuitive picture for this observation is simple. Within the stripe phase, the current flows more easily along the stripes, i.e. in the [110]-direction, than perpendicular to them. Therefore, for the configurations in Figure 5.10, the current in the stripe phase is channeled towards the voltage contacts and a larger signal is measured there than without channeling. This effect is a strong evidence for anisotropic transport in the stripe phase. An equivalent argument is presented in reference [92].

Interestingly, a similar effect takes place in the bubble phase regime at nonzero DC currents. Figure 5.10(b) shows the resistances for the two configurations at $I_{DC} = 54$ nA, i.e. at the 'breakdown' of the bubble phase where the differential resistance is high. The 'center'-resistances are scaled with the same factor 2.8 as in (a). After scaling, an enhancement of the 'center'-resistance over the 'near'-resistance is now observed only in the bubble phase regime near $B = 2.15$ T. The enhancement is of the same magnitude as the enhancement in the stripe phase at $I_{DC} = 0$. In analogy to the situation in the stripe phase, we view this result as evidence for anisotropic transport in the bubble phase regime at sufficiently high DC currents. We return to this important point in the last section of this chapter.

At $I_{DC} = 54$ nA, in the stripe phase regime, the scaled 'center' resistances are suppressed below the 'near' resistances (Fig. 5.10 (b)). This is opposite to the behavior at $I_{DC} = 0$ and again indicates anisotropic transport behavior. One possible explanation would be that the DC current reorients the stripes parallel to it. However, this is in conflict with results of section 5.2.3 and therefore we favor another explanation. When an increasing amount of DC current is forced perpendicular to the stripes, it is reasonable to assume that the stripe order breaks down first along the shortest path between the two current contacts. The current density is highest between the two contacts and drops off quickly away from there. This spatial inhomogeneity in the $[1\bar{1}0]$ direction would produce just the behavior we observe.

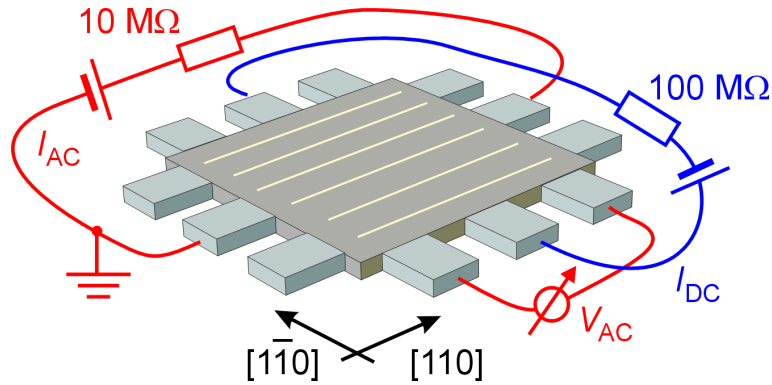


Figure 5.11: Generalized 'differential resistance' measurement setup. The DC bias current (blue) is independent from the AC probe current and AC voltage measurement (red). The setup has to be grounded at only a single point, and therefore the DC current loop is kept floating.

5.2.3 'mixed-axis' configuration - AC/DC currents along different axes

So far, we have applied AC and DC currents always at the same contacts. As described in the context of Figure 5.5, this corresponds to a measurement of the differential resistance. In general, one can apply the DC current at different contacts than the AC current (Fig. 5.11). This way, the AC and DC current directions may be chosen independently from each other. For simplicity, we still call the measured quantities 'differential resistances' keeping in mind that different directions are involved and the simple picture of Figure 5.5 does not hold anymore. For a better understanding, it is helpful to take on the following viewpoint: The AC current and corresponding AC voltage measurement are used to probe the system. Since the AC current is comparatively small, it does not disturb the system itself. The DC current on the other hand is used as a means to disturb the system and induce breakdown of the correlated phases or even phase transitions between them. From this viewpoint, it makes perfect sense, for example, to keep the DC current direction fixed and probe the resulting non-equilibrium system with an AC current applied in different directions.

In Figure 5.12 we show generalized 'differential resistance' scans for all different combinations of AC and DC current directions with respect to the $[110]$ crystal axis, i.e. the 'easy-axis' as far as the stripe phase is concerned. The DC current direction is fixed for each row and the resulting system is probed by the two possible AC current directions in the respective columns.

⁸The QHE also produces inhomogeneous current distributions. However, this effect should be negligible in the partially filled Landau level which hosts the correlated phases.

⁹We find approximately the same scaling factor for different samples and wafers of similar mobility, provided the geometry is unchanged. However, when the current is directed along the $[110]$ -axis, we find a different scaling factor. This points to an underlying, filling factor independent, anisotropy in the 2DES which is different from the stripe phase anisotropy discussed here (compare also section 5.1.2).

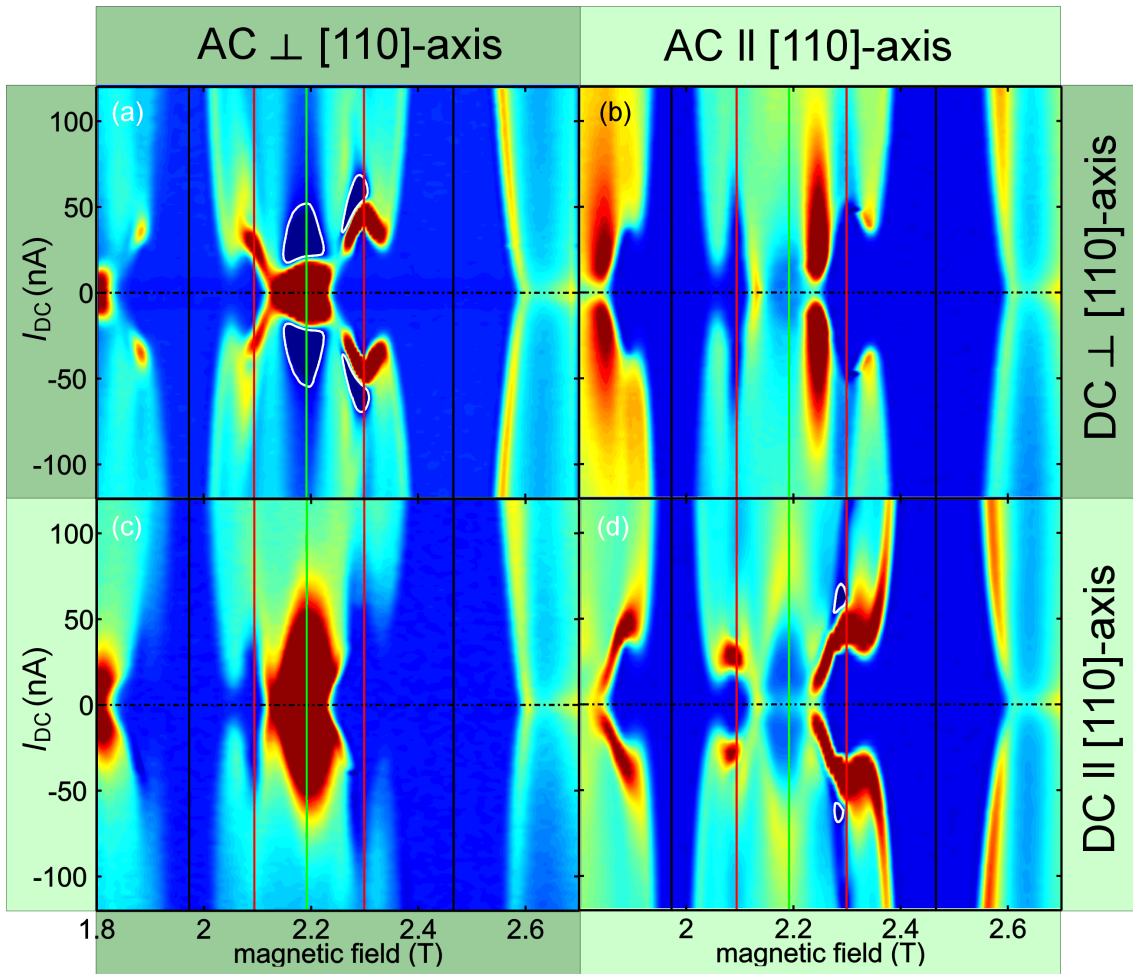


Figure 5.12: Generalized 'differential resistance' scans for all possible combinations of DC and AC current directions relative to the [110] crystal axis. In (a) and (d), DC and AC currents are parallel to each other, whereas they are perpendicular in (b) and (c). The green and red vertical lines highlight the center of the stripe and bubble phase, respectively. The measurements were taken at a temperature of $T < 20$ mK.

Therefore, in scans (a) and (d), the AC and DC currents are parallel. These are the 'hard-axis' and 'easy-axis' configurations, respectively, which we have extensively discussed in sections 5.2.2 and 5.2.1. The new results are depicted in (b) and (c) where AC and DC currents are perpendicular to each other. We evaluate the results for the two DC current directions separately.

top row - DC current along 'hard-axis' (perpendicular to [110]-axis)

The results in the stripe phase around $B = 2.2$ T (green vertical line) are consistent with the picture of an anisotropic phase with stripe formation along the [110]-axis. In (a), the AC current

probes the direction perpendicular to the stripes resulting in a resistance maximum whereas in (b) the AC current flows along the stripes resulting in a minimum. These extrema vanish at a DC current of about $I_{DC} \approx 20$ nA. The anisotropic stripe order breaks down at these currents. While NDR appears in (a), no equivalent feature is observed in (b), and thus, NDR seems to be connected with a nearby region of high differential resistance.

Now, for the bubble phase (around the red vertical line at $B = 2.3$ T) the results should be independent of the AC current direction reflecting the expected isotropy of this phase. However, this is only observed for small currents ($I_{DC} < 40$ nA), where the phase is an insulator and the longitudinal resistance therefore vanishes. Near breakdown of the bubble phase around $I_{DC} = 50$ nA, one observes intriguing anisotropic behavior. A huge resistance maximum and NDR occur in (a) whereas a minimum occurs in (b). This is very similar to the behavior of the stripe phase. The results suggest that the bubble phase breaks down via an intermediate anisotropic phase which has its 'easy'-axis directed parallel to the $[110]$ -axis in this configuration. However, we will show below that, unlike for the stripe phase, the 'easy'-axis direction depends on the DC current direction.

bottom row - DC current along 'easy-axis' (parallel to $[110]$ -axis)

The stripe phase data are qualitatively similar to those of the perpendicular DC current direction presented above. A resistance maximum appears in (c) and a minimum in (d). This is expected since the direction of the stripes is fixed to be parallel to the $[110]$ -axis. However, the extrema are observable up to considerably higher DC currents ($I_{DC} \leq 75$ nA) in this configuration. We conclude from this that the DC current stabilizes the stripe phase when it is directed along the stripes. In the introductory chapter 2.3.2, we noted that, in the realistic ELC scenario, the stripe phase consists of conducting stripes with shape fluctuations perpendicular to the stripe direction (see Fig. 2.15). Now, flowing current along the stripes seems to reduce the fluctuations and thereby stabilizes this particular correlated phase. In the context of conducting domain walls in high- T_c superconductors, an intuitive picture for a similar effect has been proposed [93]. If water (current) is pushed through an initially wavy garden hose (conducting stripe with shape fluctuations), it tends to straighten out the hose as the flow is increased. So far this scenario has not been addressed in the framework of the ELC phase picture. Nevertheless, it indicates the importance of considering fluctuations to fully describe the experimental observations.

The response near breakdown of the bubble phase is clearly anisotropic, similar to the case described above where the DC current is directed perpendicular to the $[110]$ -axis. A maximum and NDR occur near breakdown of the phase in (d), and a minimum is observed in (c). However, the respective extrema occur in the opposite AC current configuration than before. Hence, for this DC current direction, the anisotropic intermediate phase is now directed along the $[1\bar{1}0]$ -axis. We return to this intriguing observation in the discussion part of this chapter.

5.2.4 Temperature dependence

In the next two subsections, we discuss how the differential resistance measurements are affected by changes in the electron temperature. First, we present data for the Hall-bar and then for the van-der-Pauw (vdP) geometry.

Hall-bar geometry

Figure 5.13 shows the differential longitudinal resistance at different temperatures for the 'L'-shaped Hall-bar geometry introduced in section 5.1.2. The scans look qualitatively very similar to the results obtained at the lowest temperatures in the vdP geometry. Hence, the differential resistance effects discussed in the previous sections are not artifacts of the particular geometry chosen.

The breakdown currents in the Hall-bar geometry are considerably higher than in the vdP geometry. For example, the electron-bubble phase near $\nu_N = 0.29$ breaks down around $I_{DC} \approx 600$ nA instead of $I_{DC} \approx 100$ nA in the vdP geometry. The width of the Hall-bar is a factor of two larger than the size of the vdP square and the electron density is higher by 50%. Although we have not done a systematic study with samples of different densities, we believe that the breakdown currents are mostly affected by the sample size and not the electron density within the sample. This assumption also agrees with the high breakdown currents observed in much larger samples studied by other groups. The high differential resistance features are mainly weakened in intensity when the temperature is increased from $T < 20$ mK to $T = 75$ mK. Hence, applying a DC current bias is obviously not identical to increasing the temperature. Otherwise sharp features occurring at high DC currents can not be explained. This is an important point because it shows that differential resistance measurements are a powerful and independent tool to obtain information about the correlated phases. The dissipative regions at the boundary between the bubble phase and the IQHE phase (see red arrows in Fig.5.13) move towards lower DC currents when the temperature is increased. This behavior agrees with the picture that correlated states, which are pinned by disorder at low temperatures, whereas they delocalize and contribute to dissipative transport at higher temperatures.

van-der-Pauw geometry

The temperature dependence of the longitudinal differential resistance in the vdP geometry is depicted in Figure 5.14. The data has been obtained with a small in-plane magnetic field perpendicular to the [110] crystal direction.¹⁰ We focus on the behavior inside the bubble phase regime. The traces in (a) are taken in the center of the electron-bubble phase (see vertical red line near $B = 2.3$ T in (b)) for temperatures in the range $T = 40$ mK . . . 130 mK. Above

¹⁰This field stabilizes the correlated phases up to slightly higher temperatures and DC currents. We have checked that we get qualitatively the same behavior without in-plane magnetic field.

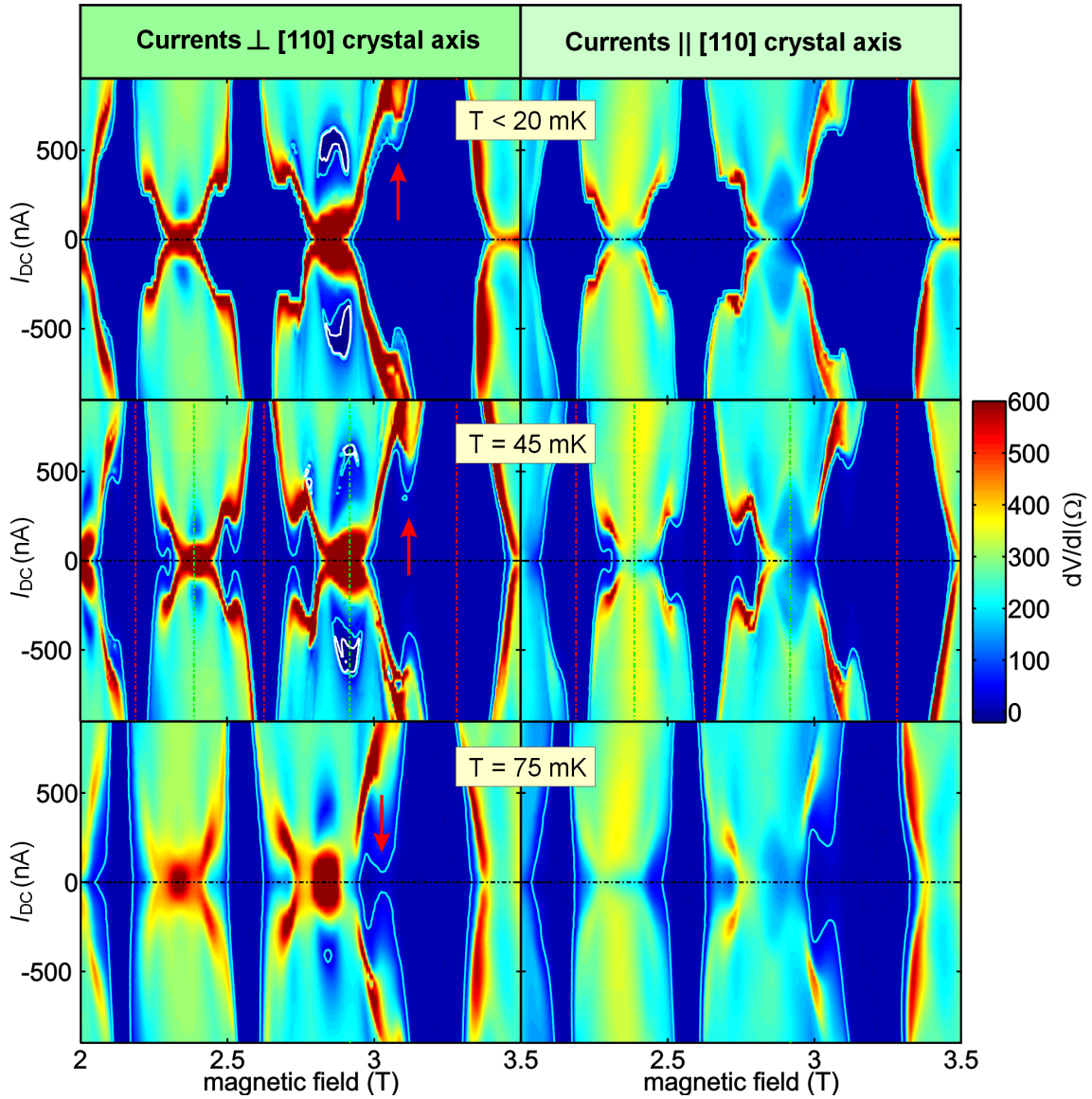


Figure 5.13: Temperature dependence of the differential resistance in the "L"-bar geometry (see Fig. 5.3) for the 'hard-axis' (left column) and 'easy-axis' current (right column) directions. The red vertical arrows indicate the position of the IQHE/bubble phase boundary. The white contour surrounds areas of NDR. The blue contour is plotted at 10Ω to highlight the breakdown of vanishing resistance. The sample density has slightly changed between the different measurements.

approximately $T = 180$ mK (not shown), the transport properties do not show any signature of the correlated phases. Below $T = 60$ mK (blue and green trace), the differential resistance vanishes for low DC currents and shows a huge peak near $I_{DC} \approx 40$ nA followed by NDR around $I_{DC} \approx 60$ nA. At $T = 80$ mK, the differential resistance still exhibits a minimum for

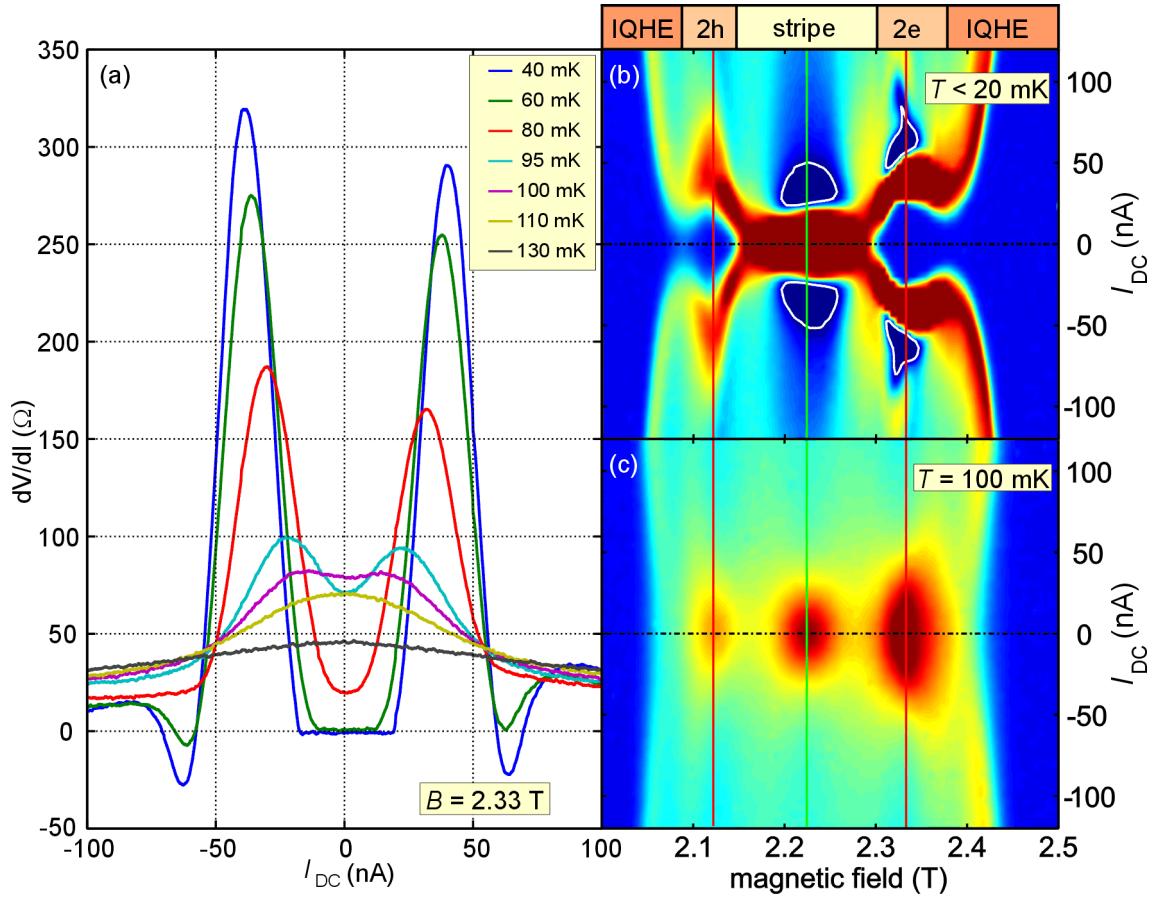


Figure 5.14: (a) Temperature dependence of the differential resistance in the vdP geometry at the center of the electron-bubble phase. (b) Differential resistance scan at $T < 20$ mK and (c) $T = 100$ mK. The red vertical line at $B = 2.33$ T indicates the center of the bubble phase. The data have been taken at a tilt angle of $\alpha = 20$.

low DC currents but it does not vanish anymore. Also, for intermediate currents, no NDR is observed above this temperature. We have verified (not shown) that both effects (NDR and zero resistance¹¹) vanish at about the same temperature.

As the temperature is increased, the differential resistance peaks which are initially centered around $|I_{DC}| \approx 40$ nA decrease in magnitude and approach each other until they merge into a single peak located at $I_{DC} = 0$. This happens at a temperature of $T \approx 110$ mK. The peak quickly fades away when the temperature is further increased. The overview in Figure 5.14(c) reveals that indeed, for a small temperature window around $T \approx 100$ mK, a resistance peak occurs at the center of the bubble phase similar to the one at the center of the stripe phase.

¹¹We define the resistance to be zero when the measured absolute resistance value is smaller than the resistance variation from the measurement noise.

Unlike the latter, however, the bubble phase peak is isotropic, i.e. it appears for both DC current directions (data not shown). Although the resistance peak in the bubble phase shows up in data published by other groups, it seems to have gone unnoticed so far. The temperature dependence in the stripe phase is not shown in detail. Here, the huge resistance peak at $I_{DC} = 0$ quickly reduces in magnitude as the temperature is increased and the NDR region becomes smaller and eventually vanishes. When comparing the stripe and the bubble phase, two observations should be noticed. The region of NDR in the stripe and bubble phase vanish at about the same temperature. Also, the differential resistance maxima in the bubble phase and in the stripe phase are very similar in magnitude at any temperature (data not shown).

5.2.5 Discussion

The presentation of our differential resistance data has revealed many interesting features. In this section, we want to summarize the main results of our experiments which help to understand the correlated phases in the $N = 2$ Landau level in greater detail.

Phase boundaries

The differential resistance measurements allow to determine the boundaries of the correlated phases on the magnetic field axis with good precision. The boundaries extracted from Figure 5.6 describe all our data from different samples, wafers and cool-downs very well. The filling factor range between $0.37 < \nu_N < 0.63$ is identified with the stripe phase. The stripe phase boundary $\nu_N = 0.37 \pm 0.01$ agrees well with numerical estimates ($\nu_N^{\text{theo}} = 0.36 \dots 0.4$ [53]). Next to the stripe phase, in the range $0.19 < \nu_N < 0.37$, we find the regime of the insulating electron-bubble phase. The phase boundaries agree roughly with the predictions for the 2-electron-bubble phase, although the boundary at $\nu_N = 0.19 \pm 0.01$ is significantly lower than predicted ($\nu_N^{\text{theo}} = 0.22 \dots 0.25$ [53]). At filling factors below $\nu_N = 0.19$, first the Wigner Crystal phase (see below) and then the IQHE phase are stabilized. The phase boundary at $\nu_N = 0.19$ is especially interesting, since it separates two insulating phases from each other. At the lowest temperatures (or DC currents), the longitudinal resistance vanishes not only within the insulating phases but also at their mutual boundary. Only at higher temperatures (or DC currents), a region of non-zero resistance between them allows for the clear identification of each phase. The highest critical breakdown current of the bubble phase usually is found at $\nu_N < 0.29$. However, some data (see Fig. 5.7) show a shift of this position towards lower filling factors.

In general, the positions of the phase boundaries obey very nicely the particle-hole symmetry which is expected around the half filled Landau level. This means that the electron-bubble phase $0.19 < \nu_N^e < 0.37$ has its particle-hole conjugate, the hole-bubble phase, at precisely $0.63 < \nu_N^h = 1 - \nu_N^e < 0.81$.

Particle-hole asymmetry

Because the Coulomb interaction treats positive and negative charges on an equal footing, each electron configuration for $\nu_N^e < 1/2$ should be transformable into an equivalent hole configuration with $\nu_N^h = 1 - \nu_N^e > 1/2$ by simply replacing electrons by holes and vice versa. Therefore, in the simplest picture, all transport properties within a given Landau level should be particle-hole symmetric around half filling. We just mentioned in the previous paragraph that the phase boundaries indeed obey this symmetry relation very well.

However, a clear particle-hole asymmetry reveals itself when we compare the breakdown currents of the electron- and the hole-bubble phases (see Fig. 5.6). The hole-bubble phase breaks down at considerably lower DC currents than the electron-bubble phase. From this behavior, we can infer that the former is much more fragile than latter. Earlier, we arrived at the same conclusion from activation energy measurements in both phases (see Fig. 5.4). The apparent particle-hole asymmetry is most likely related to differences in the coupling between the correlated phases in the bulk and edge states from lower Landau levels at the boundary of the sample. This coupling increases as one moves from the empty to the filled Landau level. The enhanced coupling tends to destabilize the bubble phase which appears closer to the filled Landau level, i.e. the hole-bubble phase (see the paragraph on breakdown below).

We now turn to the stripe phase (or smectic phase in the ELC picture to be precise). Particle-hole symmetry is incorporated into the ELC picture of the stripe phases by assuming that the scattering times τ_0, τ_1 across the empty ($\nu_N^{\text{loc}} = 0$) and filled ($\nu_N^{\text{loc}} = 1$) regions, respectively, depend only on the width of these regions (see sec. 2.3.2). Therefore, $\tau_0 = \tau_1$ has to hold exactly at $\nu_N = 1/2$ where empty and filled regions have equal widths. This leads to conductivities $\sigma_{xx}, \sigma_{yy}, \sigma_{xy}$ which are symmetric around the half filled Landau level. According to equation 2.53, one then expects the drop of ρ_{xy} and the maximum of ρ_{yy} to be shifted away from $\nu_N = 0.5$ towards slightly higher magnetic fields. However, the opposite is observed (see Figs. 5.7 and 5.9). The shift towards higher filling factors is a strong indication that particle-hole symmetry is also broken within the stripe phase itself. The observed particle-hole asymmetry can be reconciliated with the ELC picture if one assumes that scattering across a filled region is more likely than scattering across an empty one. Hence, $\tau_1 < \tau_0$ at $\nu_N = 0.5$. In order to obtain the theoretical predicted Hall resistance and the maximum in the longitudinal resistance, one has to move to lower magnetic fields where the width of the empty regions reduces at the expense of the filled regions. This will compensate for the inequality in the scattering times.

It is important to note that this shift of the resistance maximum is observed only at the lowest temperatures. Once the temperature exceeds $T = 40$ mK, the maximum is located exactly at $\nu_N = 0.5$ (see Fig. 5.1). Hence, it is unlikely that the symmetry is broken by spin effects, Landau level mixing or coupling between edge states and the bulk. Instead, probably subtle and yet unknown interaction effects play a role.

Negative differential resistance (NDR)

The V-I characteristics within the stripe and the bubble phases show regions of negative differential resistance above certain values of the DC current (see Figs. 5.2 and 5.7).¹² These NDR regions always appear in the vicinity of very high differential resistances. In the stripe phase, the high resistances appear only for transport along the 'hard-axis' and DC currents close to zero. On the other hand, in the bubble phase, strong dissipation appears for any DC current direction but only after critical DC currents are applied. Nevertheless, for both correlated phases, NDR indicates that a highly dissipative transport mechanism is strongly suppressed by a slight increase of the DC current.

We find NDR to occur only at the lowest temperatures $T < 60$ mK in both phases. Temperature dependent measurements in the bubble phase regime (see Fig. 5.14) indicate that NDR at high DC currents appears only as long as a RIQHE state develops at low currents in this phase, i.e. when a true resistance zero is observed near $I_{DC} = 0$. We speculate that the existence of incompressible regions is a requirement for NDR to develop. Maybe then, NDR in the stripe phase indicates tunneling between adjacent conducting stripes across incompressible regions. Once the temperature exceeds a critical value or tunneling becomes too large, the incompressible regions vanish and NDR is not observed anymore. In general, we propose that NDR is a signature of tunneling processes across incompressible regions which form within the correlated phases at the lowest temperatures. This might also explain why the magnitude of the NDR is much bigger in the bubble phase where the incompressible regions are much wider than in the stripe phase.

Wigner crystal

We mentioned in section 2.3.1 of the introductory chapter, that so far, there has been no evidence for Wigner crystal formation within the $N = 2$ Landau level in transport experiments. Here, we suggest that differential resistance measurements open up a new possibility to identify this phase.

Although the IQHE minima remain visible up to the highest DC currents we apply, their width on the magnetic field scale decreases with increasing DC currents. Strikingly, this decrease is much faster at low DC currents than at higher ones. This can be seen throughout our differential resistance data, especially around filling factor $\nu = 4$. We propose that the formation of a pinned Wigner crystal in the wings of the IQHE minima produces the additional broadening. Similar to the bubble phase, the Wigner crystal is stabilized only at low DC currents. With increasing currents, the long range order of the Wigner crystal is destroyed and the remaining width of the resistance minimum only reflects localization of single-electron IQHE-

¹²Especially within the bubble phase, the V-I curves are strongly reminiscent of the I-V curves of resonant tunneling diodes.

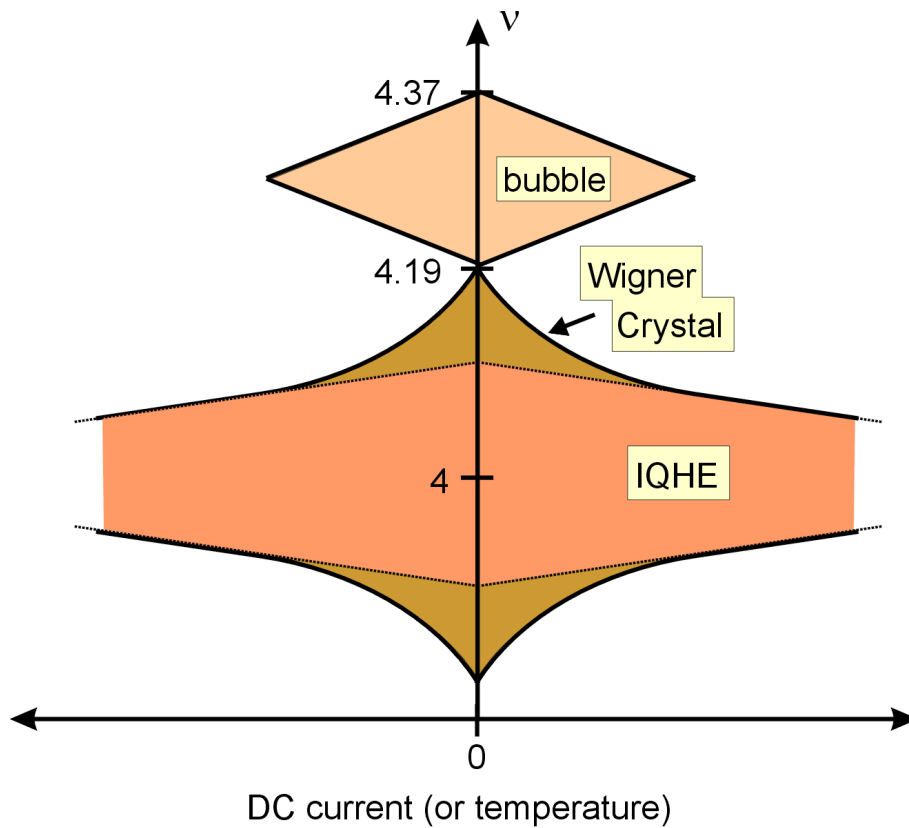


Figure 5.15: Schematic Wigner crystal phase diagram. The Wigner crystal can be identified in the wings of the IQHE resistance minima by an enhancement of the width of the minimum for small DC currents or temperatures. The Wigner crystal phase and the bubble phase are expected to break down at comparable DC currents.

states.¹³ Whereas the Wigner crystal regime is bounded by the bubble phase at $\nu_N = 0.19$, the position of the boundary towards the IQHE regime should depend on the sample quality. For a sample free of disorder, the Wigner crystal presumably is stable down to the empty Landau level, i.e. $\nu_N = 0$. Disorder breaks up the long range crystalline order starting at the lowest electron densities. Thus as the disorder increases, the boundary between Wigner crystal and IQHE will move from $\nu_N = 0$ towards $\nu_N = 0.19$.

Still, the important question remains why the IQHE phase smoothly transforms into a Wigner crystal, whereas Wigner crystal and bubble phase are separated by a region of non-zero resistance (at least in the highest mobility samples or at non-zero DC currents). Possibly, the Wigner crystal melts at the transition to the bubble phase, allowing electrons to rearrange

¹³Preliminary data around $\nu = 1, 2, 3$ show the same effect. This agrees with microwave resonance experiments, which find indications for Wigner crystallization in the wings of the IQHE minima in the lowest three Landau levels ($N \leq 2$) [62, 65, 66].

into clusters. At the melting point, long range crystalline order is destroyed and dissipative transport takes place. Instead, at the transition point between Wigner crystal and IQHE phase, the long range correlations between electrons give way to single electron localization without an intermediate dissipative regime.

Breakdown of correlated phases

What causes the correlated phases to break down when a DC current is applied? We already noted before that our data is inconsistent with a simple increase of the electron temperature within the sample induced by the DC current. Otherwise, one would mainly expect a broadening and a reduction of the differential resistance features at higher DC currents which is not observed. Also, the similarity of our differential resistance data for different samples, wafers and cooldowns makes it unlikely that the breakdown relies on sample inhomogeneities, impurities or other random effects. Instead, a generic mechanism must be responsible for it.

We propose that the phase breakdown is not directly triggered by the DC current or its density but rather by the induced DC Hall voltage which drops across the correlated phases

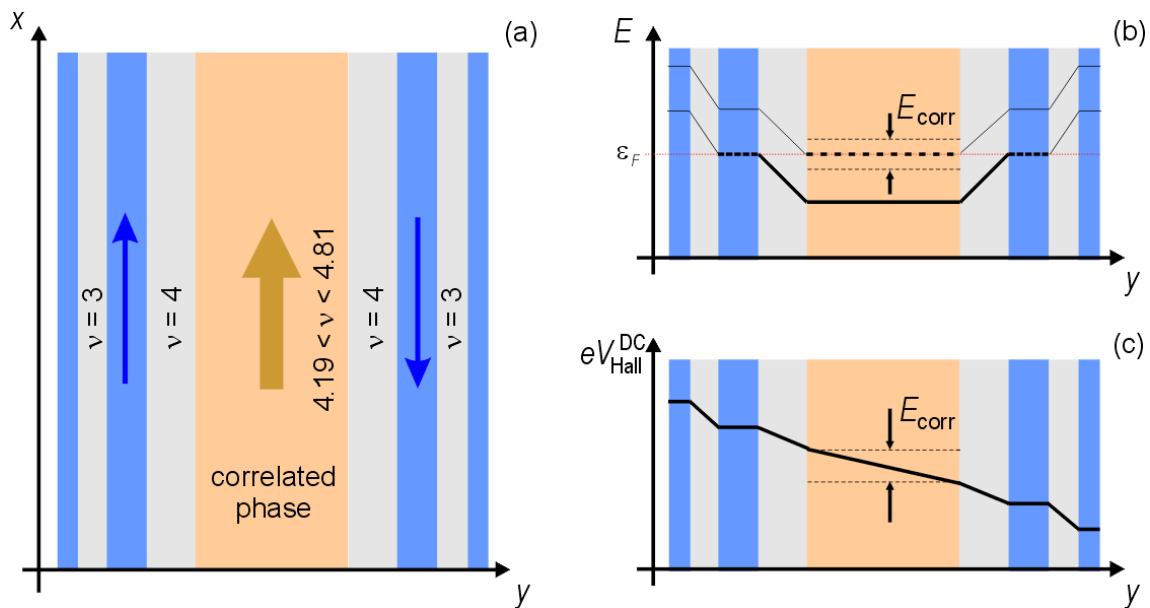


Figure 5.16: (a) The bulk correlated phase is separated from the conducting edge channels (blue) by an incompressible strip (gray). (b) Energy diagram in the correlated phase regime. In the topmost, partially filled Landau level, a (pseudo-)gap opens up in the bulk due to electron correlations. (c) DC Hall voltage across the sample. A considerable portion of it drops across the correlated phase in the bulk. Breakdown starts when the Hall voltage drop in the bulk is larger than the correlated phase (pseudo-)gap E_{corr} .

(Fig. 5.16(c)). In order to understand our argument, it is necessary to distinguish between two contributions of the DC current (Fig. 5.16(a)). One part of the current (probably the larger one) flows in the completely filled lower Landau levels. In the Büttiker picture, this portion of the current is distributed among conducting channels near the edges of the sample (sec. 2.1.4). The remaining part of the DC current flows through the correlated phase which forms within the bulk of the sample. As the magnetic field is changed, we expect only a smooth change of the edge current distribution. On the other hand, the bulk current distribution should strongly depend on the nature of the correlated phase that stabilizes at a particular magnetic field.

The breakdown current for a given correlated phase increases in accordance with the sample size.¹⁴ Hence, it would be reasonable to argue that a critical current density in the bulk triggers the breakdown. Implicitly one assumes here, however, that the current is equally distributed within the different bulk correlated phases. This is definitely not the case because, after all, the bubble phase is a true Quantum Hall state, i.e. incompressible, whereas the stripe phase is compressible. Consequently, one expects a large difference between the breakdown currents for these two types of phases.¹⁵ Such a difference is not observed. Instead, the maximum breakdown current decreases smoothly from the electron-bubble phase to the hole-bubble phase, i.e. from the empty to the filled Landau level, and it takes on very comparable values for the stripe phase (Fig. 5.6). Therefore, the bulk current density can not be responsible for the breakdown effect. On the other hand, the breakdown also can not be triggered by the edge currents in the lower Landau levels themselves, because this would contradict the strong sample size dependence of the breakdown currents. All observations can only be reconciled if we assume that the breakdown is triggered by the DC Hall electric field which is induced by the edge currents. This part of the Hall field is independent of the bulk current distribution and its magnitude depends on the sample size. Once the Hall electric field which drops across the correlated phase becomes larger than the (pseudo-)gap energy E_{corr} of this phase, the phase breaks down. The picture also explains the smooth decrease of the breakdown current from the electron-bubble to the hole-bubble phase. The width of the incompressible strip which separates the bulk from the innermost conducting edge channel decreases as one moves from the empty to the filled Landau level and the coupling between the edge channels and the bulk states smoothly increases accordingly. The ensuing hybridization between the innermost edge channel and the correlated phase in the bulk effectively destabilizes the phase and leads to a lower breakdown current for higher filling factors ν_N .

¹⁴Although we have not carried out a systematic study, we have confirmed this fact using larger samples as well as by comparing our data with those for large samples published by other groups.

¹⁵Additionally, in the stripe phase, the breakdown currents for the two main crystal axis directions should differ by a large amount because of current channeling (Fig. 5.1(b),(c)).

Similarities between stripe and bubble phase - anisotropy in the bubble phase regime

The incompressible bubble phase and the compressible stripe phase are always discussed separately throughout the literature. However, the differential resistance within those phases shows many striking similarities. These become most obvious in Figure 5.7. The differential resistance maxima in the two phases are of almost identical magnitude¹⁶ and they are both followed by a region of NDR towards higher DC currents. A closer look (see Fig. 5.8) reveals that the differential resistance maxima, signaling the breakdown of the bubble phase, smoothly approach each other as one moves towards the stripe phase regime. At the same time, the DC current range, in which a true resistance zero occurs in the bubble phase, decreases in size and gradually develops into a simple minimum inside the stripe phase. Our observations indicate a close connection between the bubble phase at intermediate DC currents and the stripe phase at low currents with a smooth transition between the two phases.

Even more strikingly, we find evidence for anisotropic behavior in the bubble phase regime at intermediate DC currents, i.e. near the breakdown of this phase. Figure 5.10 shows that the differential resistance maxima in the stripe and bubble phase depend in the same way on the distance between the current path and the voltage contacts. Current channeling which is a sign of anisotropic transport is observed in both cases. The strongest evidence for anisotropic transport, however, comes from our measurements using independent AC and DC current directions (Fig. 5.12). For a fixed DC current orientation, we find that the AC current direction determines whether a maximum or a minimum is observed in the differential resistance. This is clearly anisotropic behavior in the magnetic field regime of the bubble phase. However, unlike for the stripe phase, the preferred anisotropy axis in the bubble phase regime is independent of the underlying crystal axis orientation. Rather it is determined by the direction of the DC current itself. The low resistance direction is always perpendicular to the DC current, i.e. parallel to the DC Hall electric field. This is somewhat reminiscent of the preferred orientation of conventional liquid crystals parallel to an applied outside electric field [14]. Although in the stripe phase, the DC current direction does not determine the stripe orientation, we showed in section 5.2.3 that it stabilizes the stripes when it flows parallel to their preferred direction. This is opposite to the behavior we just described for the bubble phase regime. We believe that this discrepancy is noteworthy but not necessarily contradictory, because after all, the bubble phase is incompressible whereas the stripe phase is compressible. As we mentioned in the last paragraph, this has strong consequences for the DC current distribution within these phases, and it is likely to alter the impact of the DC current on each of these correlated phases.

The reason why transport anisotropies in the regime of the bubble phase have not been observed before is now obvious. If the AC current is directed parallel to the DC current, one will always probe the high-resistance direction of this anisotropic phase. Only our independent choice of the AC and DC current directions reveals the anisotropy. It is still an open question

¹⁶We find this statement to be true for any temperature at which the correlated phases exist.

whether the bubble phase itself is anisotropic (i.e. a stripe crystal - see section 2.3.2), or rather a new anisotropic phase is stabilized at intermediate DC currents.

Chapter 6

Conclusions

We now review the most important results of our experiments for each chapter separately. Subsequently, we give an outlook on possible future work based on our findings. The last section comments on the general relevance of our work.

Composite Fermion ballistic transport

At the beginning of chapter 3, we present conductance measurements through a Quantum Point Contact (QPC) constriction defined by metallic lateral surface gates. The quality of the QPC is reflected by the large number of conductance quantization steps at zero magnetic field as well as the observation of fractional edge state transport through the QPC around bulk filling factor $\nu = 1/2$. This gives us confidence in assembling two opposing QPCs into a device which is sensitive to straight ballistic transport of charge carriers. One QPC is used as the current injector and the second one as the voltage detector. In this way, we observe a clean signature of ballistic transport for electrons around zero magnetic field.

Using the same setup, we unequivocally demonstrate straight ballistic transport of Composite Fermions (CFs) at filling factor $\nu = 1/2$ as well as $\nu = 3/2$ over a distance of $1 \mu\text{m}$. Our results nicely verify particle-like motion of CFs around half filling of the lowest ($N = 0$) Landau level and indirectly the existence of an effective magnetic field for CFs (eq. 2.28). These central predictions of the Composite Fermion picture have been previously confirmed by other groups [43, 44].¹ However, our experiments are the first to address straight ballistic transport, i.e. transport in zero effective magnetic field. Furthermore, the clean signal and the tunability of the device allow us to perform several independent checks of the ballistic nature of CF transport. In particular, the (i) temperature dependence (sec. 3.3.2), (ii) gate voltage depen-

¹Because of the large width of the CF ballistic transport peak in our case, we find it unlikely that the narrow resistance features of reference [94] - often used as a textbook example - are a sign of ballistic CF transport. This speculation is supported by the strikingly different temperature dependence of the ballistic signal in both cases. We have observed similar features to those of [94] in very narrow constrictions which we relate to an interference effect.

dence (sec. 3.3.1), and (iii) configuration dependence (sec. 3.3.3) of the resistance feature near $\nu = 1/2$ or $\nu = 3/2$ all agree with the notion of straight ballistic transport of CFs. To our knowledge, there is no explanation for our experimental results outside the Composite Fermion framework.²

Apart from qualitative similarities between electron and CF ballistic transport, we have observed important differences which are, however, all in agreement with the CF picture. In some measurements, the CF ballistic resistance peak shifts towards lower external magnetic fields as the QPC constrictions are narrowed. We explain this by a reduced charge density within the constriction. The lower density deflects the CFs because it corresponds to a non-zero effective magnetic field. Along the same line of reasoning, we interpret the large width of the CF resistance peak as compared to the electronic resistance peak at zero external field. The smooth confinement potential of the QPCs leads to density variations within the constrictions. Therefore, CFs traversing the QPC experience slightly different effective magnetic fields depending on the local density they probe within the constriction. Accordingly, CFs will leave the QPC at slightly different angles producing the broad resistance peak. It would be interesting to test whether the line shape of the ballistic resistance peak can be described by simulations when a realistic confinement potential within the QPCs is assumed. The above observations further underline the duality between carrier density and external magnetic field for CFs according to equation 2.28.

The evidence of particle-like CF behavior shows the significance of the Composite Fermion picture beyond the explanation of the FQHE for which it had been originally proposed. In fact, it seems that CFs exist independently of the Quantum Hall Effect. For certain experiments, the notion of Composite Fermions is not just a dual way of understanding the observations, rather it seems that CF transport is the only way to interpret the results. Our experiments exemplify that one can devise sophisticated transport experiments for CFs by exploiting the analogy to electrons at low magnetic fields.

Another result from this chapter is somewhat hidden between the lines. It is possible to deposit metal gates defined by means of electron-beam lithography on the surface of a GaAs/AlGaAs heterostructure with negligible effects on the 2DES quality. This can be most clearly deduced from the low resistance at filling factor $\nu = 1/2$ and the many FQH oscillations nearby on these processed samples.

Interference effects in tunable antidot geometries

The results of chapter 4 have been obtained in a device in which a tunable antidot is located in the center of a constriction. In our case, the antidot is an elliptical surface gate which is contacted by means of a metallic air-bridge. This allows us to effectively create a hole inside

²After all, the classical cyclotron radius for electrons is below 10 nm at the high magnetic fields necessary to reach $\nu = 1/2$. Therefore, straight ballistic motion of electrons over distances of 1 μm is impossible.

the 2DES underneath the gate without disturbing the 2DES outside the contact area of the gate.

We observe resonances in the resistance whenever the magnetic field stabilizes a trapped classical orbit around the antidot. The dimensions of these orbits can be extracted from the positions of the resistance maxima on the magnetic field axis.

At low temperatures, quasi-periodic resistance oscillations with a high visibility ($\delta g \approx 0.5 e^2/h$) are a sign of electron Aharonov-Bohm like interference in this geometry. Electrons revolving around the antidot interfere with those that simply pass by. From the period of the oscillations, we extract the area enclosed by the electrons' path and find it to agree well with the dimensions obtained from the analysis of the classical orbits. By following the Aharonov-Bohm period with magnetic field, we observe a transition from cyclotron motion (orbit area determined by the external field) to edge state motion (area determined by antidot dimensions including depletion). We also analyze the temperature dependence of the interference oscillations and compare it with the predictions of a simple model. The experimentally determined characteristic temperature for the decay of the oscillations agrees well with the theoretical expectation. The results can be nicely explained by a strong coupling ($R = 0.81$) between the trapped orbits around the antidot and the traversing paths.

A special digital filtering technique allows us to separate the quasi-periodic oscillations from the more slowly varying background signal. The procedure enables us to study the influence of small changes in the gate voltages on the interference pattern. This way, we have observed phase dislocations where certain oscillations suddenly vanish as the parameters are changed. This has been interpreted as a sign of the influence of competing orbits. The phenomenon is quite general for complex interference patterns, and as another example, we show results from interfering Bose-Einstein condensates found in the literature.

The experimental results of this chapter show that the air-bridge gating technique for the electrical connection of the antidot minimizes the detrimental effects on the underlying 2DES. Although technologically challenging, such a technique has been demonstrated to be of great advantage for a variety of interference experiments. In Appendix A, we describe the lithography process for the reliable and reproducible fabrication of metallic air-bridges with footprints down to a size of 100×200 nm and bridging distances of about $1 \mu\text{m}$. This is an important tool for further interference experiments.

Transport in Electron Liquid Crystal phases

In chapter 5, we present transport measurements on the Electron Liquid Crystal (ELC) phases in the $N = 2$ Landau level. Most of our results are obtained on a small, lithographically defined van-der-Pauw geometry ($90 \times 90 \mu\text{m}$) where resistance anisotropies are most pronounced. In some cases, however, we employ a 'L'-shaped Hall-bar geometry for a simultaneous resistance measurement in both main crystal directions and a better defined current distribution.

Resistance measurements We find the anisotropic stripe phase in the filling factor range $4.37 < \nu < 4.63$ and the electron-bubble phase at $4.19 < \nu < 4.37$. The phase boundaries are independent of the sample details and nicely obey the expected particle-hole symmetry. In agreement with the literature, we find the stripes to be always oriented along the $[110]$ crystal direction in our samples. However, the mechanism that aligns the stripes along this axis is still elusive. In this respect, it is interesting to note that we observe a magnetic field-independent anisotropy for the resistance along the main crystal axes in the 'L'-geometry. Also, we find a similar field-independent anisotropy by studying the resistance drop as the distance between current path and voltage probes is increased in the vdP geometry. So far, it is an open question whether these field-independent anisotropies are caused by the same mechanism that leads to the preferred orientation in the stripe phase. In the vdP geometry, we find anisotropy factors of up to $R_{[1\bar{1}0]}/R_{[110]} \approx 40$ in the stripe phase. Factors as high as 3500 have been reported in the literature for large samples. Presumably, current channeling becomes even more effective when the sample size is large compared to the period of the stripe modulation λ_{CDW} . In the 'L'-shaped Hall-bar geometry, the anisotropy is reduced to a factor of $\rho_{[1\bar{1}0]}/\rho_{[110]} \approx 6$ because current channeling is negligible there.

The bubble phase and the adjacent IQHE have the same fingerprints, and in our sample, they can not be distinguished at the lowest temperatures. However, above $T \geq 40$ mK, a region of non-zero longitudinal resistance separates the two phases and makes them discernible. Similar to other groups, we extract a large difference in the activation energies for the electron- and the hole-bubble phase from temperature dependent measurements. The same asymmetry is also reflected in the different DC breakdown currents for these particle-hole conjugate phases. We explain the observations with a monotonic increase of the coupling between edge channels of the lower Landau levels and the correlated phase in the bulk with rising filling factor ν_N of the topmost Landau level.

Differential resistance measurements Rather small DC currents ($I_{\text{DC}} \approx 20 - 100$ nA) are sufficient to destroy the stripe and bubble phases in our vdP samples. These currents are smaller by a factor 5-10 as compared to the ones reported for the breakdown of the bubble phase in larger samples. For our small breakdown currents, we show that the results can not be explained by Joule heating effects. For the first time, we demonstrate that the breakdown of the stripe as well as the RIQHE of the bubble phase takes place in a well defined and reproducible way. We put forward the hypothesis that breakdown is induced as soon as the portion of the DC Hall electric field which drops across the bulk correlated phases becomes larger than the (pseudo-)gap E_{corr} of these phases.

Within the stripe phase, a shift of the resistance maximum away from $\nu = 9/2$ to higher fillings is observed which occurs only at the lowest temperatures ($T < 40$ mK). We have no explanation for this particle-hole asymmetry, but the strong temperature dependence suggest subtle interaction effects to be involved. The experiments only agree with the theoretical pre-

dictions for coupled Luttinger liquids if we assume unequal scattering times across filled and empty stripe regions exactly at $\nu_N = 1/2$.

We also observe strong negative differential resistance (NDR) signals at the breakdown of the stripe as well as the bubble phase which have not been reported in the literature before. These features appear only at low temperatures $T \leq 60$ mK for which the longitudinal resistance in the bubble phase still remains zero. We infer from this that NDR presumably is a signature of tunneling across incompressible regions within the bulk of the sample. This also explains why the NDR signal is much larger in the electron-bubble phase than in the stripe phase, since in the former the incompressible regions are simply wider than in the latter.

Throughout our measurements, we find strong similarities between the differential resistance data in the stripe and the bubble phase which have gone unnoticed so far. In particular, we observe

- a comparable magnitude of the dV/dI peak in both phases (Fig. 5.7),
- a continuous evolution of the stripe dV/dI peak at zero DC current into the bubble peak at intermediate DC current as a function of the magnetic field (Fig. 5.8),
- regions of negative differential resistance (NDR) in both phases for a range of DC currents close to the dV/dI peak (Fig. 5.7),
- very similar dependence of dV/dI peak values in both phases on the distance between current path and voltage contacts (Fig. 5.10).

We interpret our findings as evidence for anisotropic transport in the magnetic field regime of the bubble phase. This is corroborated by clear anisotropy seen in experiments in which the DC current direction is fixed while the AC probe current direction is varied. Unlike in the stripe phase, the anisotropy in the bubble phase regime appears only at intermediate DC currents, and even more important, it is not related to the underlying crystal axis. The 'easy'-resistance axis of the bubble regime anisotropy is always perpendicular to the DC current, i.e. parallel to the Hall electric field.

Finally, we interpret the additional broadening of the IQHE minimum at low DC currents as evidence for Wigner crystal formation in the wings of these minima. The correlated nature of this phase renders it more susceptible to DC currents as the much more robust IQHE phase. Preliminary measurements in lower Landau levels support this idea.

Outlook

Combining the experiments on Composite Fermion transport of chapter 3 with the interference experiments of chapter 4 opens up the fascinating possibility to search for interference effects of Composite Fermions. If observed, such effects would underline the predictive power of the

CF concept and would also allow to study interference effects in strongly interacting systems from a new viewpoint. The duality between external magnetic field and charge carrier density for CFs holds the prospect of observing an Aharonov-Bohm effect driven exclusively by the carrier density. However, we find a few remaining obstacles towards the goal of CF interference experiments. So far, we observe ballistic Composite Fermion transport only in illuminated samples. Unfortunately, illumination leads to persistent charge fluctuations in the sample which are known to inhibit interference effects. Therefore, a necessary prerequisite for the proposed experiments is to find samples with high mobility even without illumination. At the same time, the samples must show a steep confinement potential at QPC constrictions which minimizes the deflection of Composite Fermions as they pass through the QPC.

An important question arises from our observations in the correlated ELC phases. Is the anisotropy we find in the regime of the bubble phase a sign of a new phase which forms only at intermediate DC currents or does it reflect an inherent anisotropy of the bubble phase itself? A detailed non-equilibrium theoretical description which treats stripe and bubble phase on an equal footing is missing. In order to find out exactly how the DC current induces a breakdown of the correlated phases, it will be important to compare the breakdown behavior in samples of various sizes and also to determine how the DC Hall voltage drops across the sample in the different phases. An important unsolved question is why the stripes always tend to align along a certain crystal axis. Maybe a systematic study of the magnetic field-independent anisotropies that we find and their relation to the preferred stripe direction is a starting point for resolving this enigma. With respect to the Wigner crystal formation in the wings of the IQHE minima, it would be interesting to determine how the size of the additional broadening of the minima at low DC currents depends on the sample quality. All experiments performed in the regime of the correlated phases so far have only indirectly inferred their properties. Ultimately, it would be fascinating to resolve the spatial variation of the charge density within the ELC phases with the help of a local probe, e.g. a scanning tunneling microscope (STM).

Final comments

We have learned in the introductory chapter that a well-defined mathematical operation transforms a strongly interacting system of electrons into a weakly interacting one of Composite Fermions. Is the existence of such a transformation just a lucky coincidence for strongly interacting electrons living in a 2-dimensional plane? According to the holographic principle, first introduced in 1993 by Gerard't Hooft, any 3-dimensional physical system can be completely described by a theory operating solely on its 2-dimensional boundary [95]. Therefore, in principle, Composite Fermions and the more general concept of statistical transmutation, i.e. the change of particle statistics by a mathematical transformation, may well have an impact on our understanding of systems in higher dimensions. Even more generally, modern quantum field theories, in particular string and M-brane theory, seem to indicate that every strongly interacting

system has a dual weakly interacting one with equivalent physical properties [96]. The difficult part is to find the duality transformation for a particular case. Therefore, it seems to be a matter of our viewpoint how complicated a physical system looks like. We hope that further research on the detailed properties of Composite Fermions will deepen the understanding of strongly interacting systems even outside the realm of the 2DES.

The Electron Liquid Crystal phases are a beautiful example of self organization in systems with competing ranges and types of interactions. Unlike their classical counterparts, the properties of ELC phases are modified by quantum fluctuations in ways which still remain poorly understood. It has been proposed that very similar phenomena play a role in the formation of high- T_c superconductivity. We hope that further investigations of the non-equilibrium transport properties of ELC phases will ultimately benefit the understanding of quantum phase transitions and dynamical ordering in general.

Deutsche Zusammenfassung

Seit der Entdeckung des ganzzahligen Quanten-Hall Effekts (IQHE) durch K. von Klitzing *et al.* im Jahre 1980 [1] sind 2-dimensionale Elektronensysteme (2DES) in Halbleiterstrukturen eine faszinierende Spielwiese für die experimentelle sowie theoretische Festkörperphysik.

Der experimentelle Fortschritt wurde vornehmlich durch eine kontinuierliche Verbesserung der Probenqualität erzielt. In den besten zur Zeit verfügbaren Proben bewegen sich Elektronen über Entfernungen von etwa $200 \mu\text{m}$ fort, ohne gestreut zu werden. Dies entspricht einer Steigerung um etwa drei Größenordnungen verglichen mit den Proben der frühen Experimente. Die stark verbesserte Probenqualität, sowie die Fähigkeit empfindliche elektronische Messungen bei hohen magnetischen Feldern ($B \approx 10 \text{ T}$) und immer tieferen Temperaturen ($T \approx 10 \text{ mK}$) auszuführen, haben innerhalb der letzten 24 Jahre zu einer Palette aufregender Entdeckungen auf dem Gebiet der 2DES geführt.

Diese Entdeckungen haben intensive theoretische Anstrengungen ausgelöst mit dem Ziel, die zugrunde liegenden fundamentalen Prozesse und Prinzipien zu verstehen. In den frühen Jahren der Forschung an 2DES waren nicht-wechselwirkende Einteilchen-Modelle vielfach ausreichend, um die beobachteten Phänomene zu beschreiben. Allerdings rückte die Entdeckung des gebrochenzahligen Quanten-Hall Effekts (FQHE) im Jahre 1982 durch Tsui *et al.* [2] und seine Erklärung durch Laughlin [3] die Bedeutung von Elektron-Elektron Korrelationseffekten in den Fokus. Schnell wurde auch klar, dass tiefe Einsichten in die Feinheiten der Quantenfeldtheorie notwendig sind, um unser Verständnis der Physik auf dem Gebiet zu verbessern. So trug zum Beispiel Laughlin der präzisen Quantisierung des Widerstands im IQHE Rechnung, indem er ein Eichinvarianz Argument verwendete [4].

Bis heute bleiben die komplizierten kollektiven Phänomene, die durch elektronische Korrelationen hervorgerufen werden, eine Herausforderung für die Forschung. Diese Arbeit befasst sich hauptsächlich mit zwei wichtigen Korrelationsphänomenen innerhalb von 2DES: Verbundfermionen und elektronischen Flüssigkristallen. Wir werden diese Effekte in den nächsten zwei Abschnitten kurz einführen.

Im Jahre 1989, bei einem Versuch in intuitiver Weise die experimentell beobachteten FQH-Zustände zu erklären, führte J. Jain das Konzept der Verbundfermionen ein [5]. Hierbei handelt

es sich um Quasiteilchen, die jeweils aus einem Elektron und zwei elementaren magnetischen Flussquanten zusammengesetzt sind. Innerhalb dieser Beschreibung lässt sich der FQHE in natürlicher Weise als der IQHE von Verbundfermionen verstehen. Von Halperin, Lee und Read wurde in 1993 gezeigt, dass Verbundfermionen unabhängig vom IQHE existieren. Sie verhalten sich wie schwach wechselwirkende Teilchen, die einem effektiven magnetischen Feld ausgesetzt sind, welches deutlich kleiner als das externe magnetische Feld ist [6].

Ausgehend von der Analogie zu Elektronensystemen bei kleinen magnetischen Feldern, kann man sich mesoskopische Experimente für Verbundfermionen ausdenken. Dabei scheint es unmöglich die Resultate solcher Experimente vorauszusagen, ohne sich des Konzepts der Verbundfermionen zu bedienen. Verbundfermionen sind auch von einem allgemeine feldtheoretischen Blickwinkel aus faszinierend. Mit Hilfe einer wohldefinierten mathematischen Transformation kann ein stark korreliertes System in ein schwach wechselwirkendes umgeformt werden. Das transformierte System lässt sich wesentlich einfacher quantitativ behandeln und macht es auch intuitiv leichter zugänglich.

In unserer Arbeit untersuchen wir hauptsächlich das teilchenartige Verhalten von Verbundfermionen in wohldefinierten und einstellbaren Geometrien. Diese Experimente sollen die Grenzen des Verbundfermion Bildes beleuchten. Letztendlich stellt sich aber die faszinierende Frage, ob es möglich ist, wellenartige Eigenschaften von Verbundfermionen nachzuweisen. Als ein wichtiger erster Schritt in Richtung dieses Zieles untersuchen wir spezielle Proben, die starke Interferenzeffekte für Elektronen bei kleinen magnetischen Feldern zeigen. Die ungelösten Schwierigkeiten, die bisher noch einer Beobachtung von Interferenzeffekten von Verbundfermionen im Wege stehen, betrachten wir kurz am Ende dieser Zusammenfassung.

Bei mittleren magnetischen Feldern, unterhalb der Felder bei denen der FQHE beobachtet wird, führen elektronische Korrelationen zu qualitativ ganz neuem Verhalten. In diesem Bereich beobachtet man anisotropen Transport und einen wieder-eintretenden IQHE (RIQHE). Diese Phänomene wurden erst im Jahre 1999, mit der Verfügbarkeit von Proben extrem hoher Qualität, unabhängig voneinander von Lilly *et al.* und Du *et al.* entdeckt [7, 8].

Die Effekte können qualitativ durch ein Modell beschrieben werden, das schon 1996, also noch vor der experimentellen Entdeckung, von Koulakov *et al.* und auch von Moessner und Chalker [10, 9] vorgeschlagen worden ist. Diese Gruppen sagten unabhängig voneinander eine Instabilität des 2DES voraus, die zu einer spontanen räumlichen Modulation der Elektronendichte mit einer langreichweitigen Ordnung führt. Die Modulation wird durch den Wettbewerb zwischen abstoßenden und anziehenden Wechselwirkungskomponenten ausgelöst. Sie hat starke Ähnlichkeit mit der Modulation in konventionellen Ladungsträger-Dichte-Wellen (CDW) Leitern [11]. Abhängig von der jeweiligen Symmetrie der Modulation des 2DES unterscheidet man zwischen anisotropen Streifen-Phasen und isotropen Blasen-Phasen. Übergänge zwischen den verschiedenen Phasentypen können einfach herbeigeführt werden, indem das angelegte senkrechte Magnetfeld leicht verändert wird. Die Blasen-Phase ähnelt dem wohlbekannten Wigner Kristall [12]. Bei dem letzteren bilden einzelne Elektronen durch ihre gegenseitige ab-

stoßende Coulomb Wechselwirkung ein Gitter mit dreieckiger Elementarzelle. In der Blasen Phase wird stattdessen jeder Gitterplatz von zwei oder mehr Elektronen besetzt.

Ein anspruchsvolleres Modell wurde von Fradkin und Kivelson eingeführt [13]. Sie erkannten die Bedeutung von Quantenfluktuationen für eine realistische Beschreibung der korrelierten Phasen. Das resultierende Phasendiagramm ist dem der klassischen molekularen Flüssigkristalle sehr ähnlich [14]. Deswegen ist das Modell bekannt als das elektronischer Flüssigkristalle (ELC). Ähnliche langreichweitige Phasen treten in einer Vielzahl von chemischen und physikalischen Systemen auf, wie zum Beispiel bei dünnen magnetischen Filmen und Ferrofluiden [15]. In allen Fällen können die Phasen auf konkurrierende abstoßende und anziehende Wechselwirkungen zurückgeführt werden. Im Falle der Coulomb Wechselwirkung wird das ELC Bild auch im Zusammenhang mit Hochtemperatur-Supraleitern diskutiert [16].

In unseren eigenen Untersuchungen der ELC Phasen in 2DES hoher Qualität benutzen wir Gleichströme um eine Nicht-Gleichgewichts Situations in der Probe herbeizuführen und die korrelierten Phasen in einer kontrollierten Art und Weise zu destabilisieren. Wir erhalten so einen weiteren Parameter, den wir dazu verwenden die ELC Phasen im Detail zu untersuchen. Am Ende dieser Zusammenfassung werden wir darstellen, welche neue Einblicke wir in die ELC Phasen gewinnen konnten und welche interessanten neuen Fragestellungen sich daraus ergeben.

Im Folgenden fassen wir unsere Arbeit nach Kapiteln geordnet zusammen:

Grundlagen (Kapitel 2)

Im Kapitel 2 dieser Arbeit diskutieren wir die grundlegenden Konzepte, die notwendig sind um unsere eigenen experimentellen Ergebnisse in den späteren Kapiteln zu verstehen. Zuerst führen wir 2-dimensionale Elektronensysteme, den ganz- und den gebrochenzahligen Quanten Hall Effekt und den Aharonov-Bohm Effekt ein. Ein weiterer Abschnitt beschäftigt sich mit Verbundfermionen, ihrem teilchenartigen Charakter und ihrer Rolle für das Verständnis des FQHE. Am Ende dieses Kapitels widmen wir uns den korrelierten Phasen, die bei mittleren Magnetfeldern auftreten, und diskutieren das CDW sowie das ELC Bild.

Ballistischer Transport von Verbundfermionen (Kapitel 3)

Am Anfang von Kapitel 3 präsentieren wir Messungen der Leitfähigkeit an einem Quantenpunktkontakt (QPC), einer Verengung des 2DES, die durch eine negative Spannung an metallischen Oberflächenelektroden definiert werden. Die Qualität des QPC wird durch die große Zahl von Quantisierungsstufen in der Leitfähigkeit bei verschwindendem Magnetfeld und der Beobachtung von gebrochenzahligem Randkanaltransport durch den QPC unterstrichen. Dies bestärkt uns darin, zwei gegenüberliegende QPCs so zusammenzuschalten, dass die Schaltung empfindlich für geraden ballistischen Transport von Ladungsträgern ist. Einer der QPCs wird

als Strominjektor benutzt, während der zweite als Spannungsdetektor fungiert. Auf diese Weise beobachten wir ein klares Zeichen von ballistischem Transport von Elektronen bei verschwindendem Magnetfeld.

Mit dem gleichen Aufbau demonstrieren wir unzweifelhaft geraden ballistischen Transport von Verbundfermionen nahe Füllfaktor $\nu = 1/2$ sowie $\nu = 3/2$ über eine Distanz von $1 \mu\text{m}$. Unsere Ergebnisse bestätigen sehr schön die teilchenartige Bewegung von Verbundfermionen in der Nähe des halbgefüllten untersten Landau Niveaus ($N = 0$) und indirekt auch die Existenz eines effektiven magnetischen Feldes für Verbundfermionen. Diese zentralen Voraussagen des Verbundfermion Bildes wurden zwar schon vorher von anderen Gruppen bestätigt, allerdings sind unsere Experimente die ersten die geraden ballistischen Transport adressieren, d.h. Transport bei verschwindendem effektiven Magnetfeld. Weiterhin erlaubt das klare Signal und die Einstellbarkeit der Probe, dass wir einige unabhängige Test durchführen können, die den ballistischen Charakter des Verbundfermion-Transports verifizieren. Insbesondere die (i) Temperaturabhängigkeit (Abschnitt 3.3.2), (ii) Abhängigkeit von der Elektrodenspannung (Abschnitt 3.3.1) und die (iii) Konfigurationsabhängigkeit (Abschnitt 3.3.3) des Widerstandsextremums nahe $\nu = 1/2$ sowie $\nu = 3/2$ stimmen alle mit der Idee von geradem ballistischem Transport von Verbundfermionen überein. Unseres Wissen gibt es keine Erklärung der experimentellen Ergebnisse außerhalb des Verbundfermion Bildes.³

Abgesehen von den qualitativen Ähnlichkeiten zwischen ballistischem Transport für Elektronen und für Verbundfermionen haben wir wichtige Unterschiede festgestellt, die allerdings alle mit dem Verbundfermion Bild übereinstimmen. In einigen Messungen verschiebt sich das ballistische Maximum der Verbundfermionen hin zu kleineren externen Magnetfeldern wenn die QPC Verengung verkleinert wird. Wir erklären diesen Effekt mit einer verringerten Ladungsträgerdichte innerhalb des QPCs. Die reduzierte Dichte lenkt die Verbundfermionen ab, weil sie einem nicht verschwindenden effektiven Magnetfeld entspricht. Auf eine ähnliche Art und Weise erklären wir die große Breite des Verbundfermion Maximums im Vergleich mit dem Elektronen Maximum bei verschwindendem externen Magnetfeld. Unsere Beobachtungen unterstreichen die Dualität zwischen Ladungsträgerdichte und äußerem Magnetfeld für Verbundfermionen wie sie in Gleichung 2.28 zum Ausdruck kommt.

Die Beweise für den teilchenartigen Charakter der Verbundfermionen betont den Wert des Verbundfermion Bildes über die Erklärung des FQHE hinaus, für den es ursprünglich eingeführt worden ist. Es scheint ganz so, als ob Verbundfermionen unabhängig vom Quanten-Hall Effekt existieren. Für bestimmte Experimente sind Verbundfermionen nicht nur eine weitere, duale Art die Resultate zu erklären, sondern sie scheinen der einzige Weg zu sein, dies zu tun. Unsere Experimente zeigen beispielhaft, dass es möglich ist, sich komplexe Transportexperimente für Verbundfermionen auszudenken, in dem man die Analogie zu Elektronen bei niedrigen Ma-

³Tatsächlich ist der klassische Zyklotronradius für Elektronen bei den hohen magnetischen Feldern, die notwendig sind um $\nu = 1/2$ zu erreichen, kleiner als 10 nm . Deswegen ist gerader ballistischer Transport von Elektronen über Distanzen von $1 \mu\text{m}$ nicht möglich.

gnetfeldern ausnutzt.

Ein letztes Ergebnis des Kapitels steckt ein wenig verborgen zwischen den Zeilen. Wir haben gezeigt, dass es möglich ist, metallische Elektroden mit Hilfe der Elektronenstrahl-Lithographie auf die Oberfläche einer GaAs/AlGaAs Heterostruktur aufzubringen, ohne dass die Qualität des 2DES merklich reduziert wird. Das kann man am einfachsten an dem niedrigen Widerstand bei $\nu = 1/2$ und den vielen FQHE Oszillationen in der Nähe erkennen, die selbst bei bearbeiteten Proben beobachtet werden können.

Interferenzeffekte in einstellbaren Antidot Geometrien (Kapitel 4)

Die Ergebnisse des 4. Kapitels wurden mit einer Struktur gewonnen, in der sich ein einstellbarer Antidot in der Mitte einer Verengung im 2DES befindet. Eine elliptische Oberflächenelektrode, die mit Hilfe einer metallischen Luftbrücke kontaktiert ist, erlaubt es uns, ein Loch innerhalb des 2DES (den Antidot) unterhalb der Elektrode zu erzeugen, ohne das 2DES an den anderen Stellen zu beeinflussen.

Wir beobachten immer dann Resonanzen im Widerstand, wenn das magnetische Feld einen geschlossenen, klassischen Elektronenorbit um den Antidot stabilisiert. Die Ausdehnung des Orbits kann man aus der Position des Widerstandsmaximums auf der Magnetfeldachse ermitteln.

Bei tiefen Temperaturen deuten quasi-periodische Widerstandoszillationen mit einer großen Amplitude ($\delta g \approx 0.5 e^2/h$) auf einen Aharonov-Bohm-artigen Interferenzeffekt in dieser Geometrie hin. Elektronen, die den Antidot umkreisen interferieren mit solchen, die ihn einfach nur passieren. Die Fläche, die von den Elektronenorbits eingeschlossen wird, extrahieren wir aus der Periode der Quantenoszillationen und stellen fest, dass sie sehr gut mit den Dimensionen übereinstimmt, die wir aus der Analyse der klassischen Orbits erhalten hatten. Wir können einen Übergang von einer Zyklotron-Bewegung zu einer Randkanal Bewegung beobachten, indem wir die Veränderung der Aharonov-Bohm Periode mit dem Magnetfeld betrachten. Im ersten Fall wird die Fläche der Orbits durch das angelegte Magnetfeld bestimmt, während dafür im zweiten Fall im Wesentlichen die Fläche des Antidots verantwortlich ist. Wir analysieren auch die Temperaturabhängigkeit der Interferenzoszillationen und vergleichen sie mit den Vorhersagen eines einfachen Modells. Die experimentell gewonnene charakteristische Temperatur für den Abfall der Oszillationen stimmt recht gut mit der theoretischen Abschätzung überein. Die Ergebnisse können erklärt werden, wenn man eine starke Koppelung ($R \approx 0.81$) zwischen geschlossenen Orbits um den Antidots und durchquerenden Bahnen annimmt.

Eine spezielle digitale Filtertechnik erlaubt es uns, die quasi-periodischen Oszillationen von dem langsamer variierenden Hintergrund zu trennen. Durch dieses Verfahren gelingt es uns, den Einfluss kleiner Änderungen der Elektrodenspannungen zu untersuchen. So beobachten wir Phasensprünge, bei denen durch leichte Veränderung der Parameter bestimmte Oszillationen plötzlich verschwinden. Diese Phasensprünge werden als ein Zeichen für das Wechselspiel zwischen miteinander im Wettbewerb stehender Orbits gewertet. Sie sind ein generelles Phä-

nomen, das bei komplexen Interferenzmustern auftritt. Als ein weiteres Beispiel zeigen wir Ergebnisse von interferierenden Bose-Einstein Kondensaten, wie sie in der Literatur zu finden sind.

Die experimentellen Ergebnisse dieses Kapitels zeigen, dass die Luftbrücken-Verbindungstechnik für den elektrischen Anschluss des Antidots einen vernachlässigbaren Einfluss auf das darunter liegende 2DES hat. Diese Technik hat sich schon in einer Anzahl von Interferenzexperimenten bewährt, obwohl sie technologisch herausfordernd ist. Im Anhang A beschreiben wir den Lithographieprozess für eine reproduzierbare Herstellung metallischer Luftbrücken mit Fußabdrücken bis hinunter zu einer Größe von 100×200 nm und einer Überbrückungsdistanz von etwa $1 \mu\text{m}$. Diese Brücken werden für weitere Interferenzexperimente ein wichtiges Werkzeug sein.

Transport in elektronischen Flüssigkristallen (Kapitel 5)

In Kapitel 5 präsentieren wir Transportexperimente an elektronischen Flüssigkristall (ELC) Phasen im $N = 2$ Landau Niveau. Die meisten unserer experimentellen Ergebnisse haben wir an kleinen, lithographisch definierten, van-der-Pauw Geometrien ($90 \times 90 \mu\text{m}$) erhalten, in denen Widerstandsanisotropien am deutlichsten hervortreten. Allerdings benutzen wir in manchen Fällen auch eine 'L'-förmige Hall-bar Geometrie, um den Widerstand simultan in beiden Kristallrichtungen zu messen und gleichzeitig eine besser definierte Stromverteilung zu gewährleisten.

Widerstandsmessungen Wir bestimmen den Füllfaktorbereich für die anisotrope Streifen-Phase zu $4.37 < \nu < 4.63$ und für die Elektronen-Blasen-Phase zu $4.19 < \nu < 4.37$. Die Phasengrenzen sind unabhängig von den Details der Probe und gehorchen sehr gut der erwarteten Teilchen-Loch Symmetrie. In Übereinstimmung mit der Literatur finden wir, dass die Streifen in unseren Proben immer entlang der $[110]$ Kristallrichtung orientiert sind. Der Mechanismus, der die Streifen entlang dieser Richtung orientiert ist allerdings weiterhin ungeklärt. Interessanterweise stellen wir eine ausgeprägte Anisotropie des Widerstands entlang der Haupt-Kristallachsen in der 'L'-Geometrie fest, die unabhängig vom angelegten senkrechten Magnetfeld ist. Zusätzlich beobachten wir eine magnetfeldunabhängige Anisotropie im Abfall des Widerstands, der entsteht wenn wir die Distanz zwischen Strompfad und Spannungskontakten in der vdP Geometrie vergrößern. Es bleibt eine offene Frage, ob diese magnetfeldunabhängigen Anisotropien durch den gleichen Mechanismus hervorgerufen werden, der auch die Vorzugsrichtung in der Streifen-Phase festlegt. In der vdP Geometrie finden wir in der Streifen-Phase Anisotropiefaktoren von bis zu $R_{[1\bar{1}0]}/R_{[110]} \approx 40$. Faktoren bis zu 3500 sind für grosse Proben in der Literatur berichtet worden. Dies kann durch den Effekt der Strombündelung erklärt werden, der umso stärker ausgeprägt ist, je größer die Probe gegenüber der Periode der Streifenmodulation λ_{CDW} ist. In der 'L'-förmigen Hall-bar Geometrie ist die Anisotropie auf einen Wert von $\rho_{[1\bar{1}0]}/\rho_{[110]} \approx 6$ reduziert, weil dort die Strombündelung vernachlässigbar ist.

Die Blasen-Phase und der benachbarte IQHE haben die gleiche Signatur im Widerstand und sie können in unseren Proben bei den tiefsten Temperaturen nicht unterschieden werden. Allerdings trennt oberhalb von $T \geq 40$ mK ein Bereich von nicht-verschwindendem Widerstand die Gebiete beider Phasen und macht sie so unterscheidbar. Wie auch schon andere Gruppen vor uns extrahieren wir aus temperaturabhängigen Messungen einen großen Unterschied in den Aktivierungsenergien für die Elektronen- und Loch-Blasen-Phase. Die gleiche Asymmetrie zeigt sich auch in den unterschiedlichen DC Strömen, die zu einem Zusammenbruch diese beiden Teilchen-Loch konjugierten Phasen führen. Wir erklären diese Beobachtungen mit einer Veränderung in der Kopplung zwischen den Randkanälen der untersten Landau Niveaus und der jeweiligen korrelierten Phase im Bulk. Die Kopplung steigt kontinuierlich, mit steigendem Füllfaktor ν_N des obersten Landau Niveaus, an.

differentielle Widerstandsmessung Recht kleine DC Ströme ($I_{DC} \approx 20 - 100$ nA) sind ausreichend, um die Streifen- und Blasen-Phasen in unseren vdP Proben zu zerstören. Diese Ströme sind um einen Faktor 5-10 geringer als diejenigen, die für größere Proben in der Literatur genannt wurden. Für unseren kleinen DC Ströme zeigen wir, dass die Ergebnisse nicht einfach durch eine Joule'sche Erwärmung des Elektronensystems erklärt werden können. Wir zeigen, dass in unseren kleinen Proben der Zusammenbruch der Streifen- und auch der Blasen-Phase in einer wohldefinierten und reproduzierbaren Art und Weise stattfindet. Wir stellen die Hypothese auf, dass der Zusammenbruch eintritt sobald der Teil des DC Hall-Feldes, der über der korrelierten Phase im Bulk abfällt, größer wird als die (Pseudo-) Energielücke E_{corr} dieser Phase.

Wir stellen innerhalb der Streifen-Phase eine Verschiebung des Widerstands Maximums von $\nu = 9/2$ zu höheren Füllfaktoren fest, die allerdings nur bei den tiefsten Temperaturen ($T < 40$ mK) auftritt. Wir haben keine Erklärung für diese unbekannte Teilchen-Loch Asymmetrie aber die starke Temperaturabhängigkeit suggeriert, dass subtile Wechselwirkungseffekte beteiligt sein müssen. Die Experimente stehen nicht im Widerspruch zur Theorie gekoppelter Luttinger Flüssigkeiten, falls wir für die Streuung über gefüllte oder leere Regionen ungleiche Streuzeiten annehmen.

Wir beobachten auch einen starken negativen differentiellen Widerstand (NDR) beim Zusammenbruch der Streifen- sowie der Blasen-Phase. Dieser Effekt wurde bisher noch nicht in der Literatur beobachtet und tritt nur bei tiefen Temperaturen $T \leq 60$ mK auf, solange der longitudinale Widerstand in der Blasen-Phase noch verschwindet. Der NDR ist wahrscheinlich ein Zeichen von Tunnelprozessen durch inkompressibele Regionen im Bulk der Probe. So erklärt sich auch, warum das NDR Signal in der Elektronen-Blasen-Phase viel größer ist als in der Streifen-Phase; in der ersteren sind die inkompressibelen Regionen schlichtweg breiter sind als in der zweiten.

In allen unseren Messungen finden wir starke Ähnlichkeiten zwischen dem differentiellen Widerstand in der Streifen- und Blasen-Phase, die bisher nicht beobachtet worden sind. Insbe-

sondere beobachten wir

- eine vergleichbare Größe der dV/dI Maxima in beiden Phasen (Bild 5.7),
- eine kontinuierliche Veränderung des dV/dI Maximums der Streifen-Phase in das der Blasen-Phase als Funktion des Magnetfeldes (Bild 5.8),
- Regionen mit negativem differentiellen Widerstand (NDR) nahe der dV/dI Maxima (Bild 5.7),
- eine sehr ähnliche Abhängigkeit der dV/dI Maxima in beiden Phasen von der Entfernung zwischen Strompfad und Spannungskontakten (Bild 5.10).

Wir interpretieren diese Ergebnisse als Beweis für anisotropen Transport im magnetischen Feldbereich der Blasen-Phase, der durch Anlegen eines DC Stromes induziert wird. Diese These wird unterstützt durch Experimente, bei denen die DC Strom Richtung festgelegt und nur die AC Strom Richtung variiert wird. Hierbei ist eine Anisotropie im Bereich der Blasen-Phase deutlich sichtbar, die allerdings im Unterschied zum Fall der Streifen-Phase nur bei mittleren DC Strömen auftritt. Außerdem hängt die Richtung der Anisotropie nicht mit der zugrundeliegenden Kristallrichtung zusammen. Die Achse des niedrigen Widerstands steht hier immer senkrecht zum DC Strom, d.h. parallel zum elektrischen Hall-Feld.

Schließlich interpretieren wir eine zusätzliche Verbreiterung des IQHE Minimums bei kleinen DC Strömen als einen Beweis für die Bildung eines Wigner Kristalls in den Flanken dieser Minima. Diese korrelierte Phase ist empfindlicher gegenüber DC Strömen als die wesentlich robustere IQHE Phase. Vorläufige Messungen in niedrigeren Landau Niveaus unterstützen diese Idee.

Ausblick

Gelingt es die Experimente mit Verbundfermionen aus Kapitel 3 mit den Interferenzexperimenten aus Kapitel 4 zu kombinieren, eröffnet sich die faszinierende Möglichkeit, nach Interferenzeffekten von Verbundfermionen Ausschau zu halten. Solche Effekte würden die Vorhersagekraft des Verbundfermion-Konzepts unterstreichen und es gleichzeitig erlauben, Interferenzeffekte in stark wechselwirkenden Systemen von einem neuen Blickwinkel aus zu betrachten. Die Dualität zwischen externem magnetischen Feld und Ladungsträgerdichte, wie sie für Verbundfermionen herrscht, birgt zusätzlich die Möglichkeiten einen Aharonov-Bohm Effekt zu beobachten, der ausschließlich durch eine Änderung der Ladungsträgerdichte gesteuert wird. Wir stellen ein paar verbleibende Hindernisse auf dem Weg zu Interferenzexperimenten mit Verbundfermionen fest. Bis jetzt beobachten wir ballistischen Transport von Verbundfermionen nur in beleuchteten Proben. Unglücklicherweise ruft die Beleuchtung der Probe langanhaltende Ladungsträgerfluktuationen hervor, die Interferenzeffekte unterdrücken. Deswegen ist es eine

entscheidende Voraussetzung für die vorgeschlagenen Experimente, dass Proben gefunden werden, die auch ohne Beleuchtung eine hohe Mobilität besitzen. Gleichzeitig müssen diese Proben ein steiles Einschlusspotenzial an der QPC Verengung aufweisen, so dass die Ablenkung der Verbundfermionen minimiert wird wenn sie den QPC durchqueren.

Eine wichtige Frage stellt sich im Zusammenhang mit unseren Beobachtungen in den korrelierten ELC Phasen. Ist die Anisotropie im Bereich der Blasen-Phase ein Zeichen einer neuen Phase, die nur bei mittleren DC Strömen auftritt, oder ist sie ein Zeichen für eine inhärenten Anisotropie der Blasen Phase selbst? Eine detaillierte theoretische Nicht-Gleichgewichts Beschreibung, die Streifen- und Blasen-Phase gleichwertig behandelt, fehlt. Um herauszufinden wie genau der DC Strom zum Zusammenbruch der korrelierten Phasen führt, wird es wichtig sein, den Zusammenbruch in Proben unterschiedlicher Größe zu betrachten und außerdem festzustellen, wie die DC Hall Spannung über der Probe innerhalb der unterschiedlichen Phasen abfällt. Eine wichtige offene Frage ist, warum die Streifen-Phase sich immer entlang einer bestimmten Kristallrichtung ausrichtet. Vielleicht kann eine systematische Untersuchung der von uns gefundenen magnetfeldunabhängigen Anisotropien einen Ansatzpunkt für die Lösung dieses Problems darstellen. Im Zusammenhang mit der Formation von Wigner Kristallen in den Flanken der IQHE wäre es interessant zu bestimmen, wie die Größe der zusätzlichen Verbreiterung bei kleinen DC Strömen von der Qualität der Probe abhängt. Alle Experimente im Bereich der korrelierten Phasen haben bisher deren Existenz nur indirekt bestätigt. Letztendlich wäre es faszinierend direkt die räumliche Variation der Ladungsträgerdichte innerhalb der ELC Phasen direkt mit der Hilfe einer lokalen Methode, z.B. eines Rastertunnelmikroskops, zu beobachten.

Abschlusskommentar

Wir haben in der Einführung gelernt, dass eine wohldefinierte mathematische Operation ein stark korreliertes Elektronensystem in ein schwach wechselwirkendes aus Verbundfermionen transformiert. Ist die Existenz einer solchen Transformation nur ein glücklicher Zufall für korrelierte Elektronen in zwei Dimensionen? Nach dem holografischen Prinzip, das erstmals 1993 von Gerard 't Hooft eingeführt wurde, kann jedes 3-dimensionale physikalische System durch eine Theorie, die ausschließlich auf dessen 2-dimensionaler Begrenzung operiert, vollständig beschrieben werden [95]. Deswegen könnten im Prinzip Verbundfermionen und insbesondere das allgemeinere Konzept der statistischen Transmutation, d.h. der Änderung der Statistik eines Teilchens durch eine mathematische Transformation, auch einen Einfluss auf unser Verständnis von Systemen in höheren Dimensionen haben. Noch allgemeiner betrachtet scheinen moderne Quantenfeldtheorien, insbesondere die String und M-brane Theorie, zu zeigen, dass jedes stark wechselwirkende System eine duales schwach wechselwirkendes mit äquivalenten physikalischen Eigenschaften hat [96]. Die schwierige Aufgabe ist es, im einem bestimmten Fall die Dualitätstransformation zu finden. Es scheint also, als ob es auf unsere Sichtweise ankommt, wie kompliziert ein physikalisches System aussieht. Wir hoffen, dass eine weitere Erforschung der detaillierten Eigenschaften der Verbundfermionen unser Verständnis von stark

wechselwirkenden Systemen auch außerhalb des Bereichs der 2DES vertieft werden wird.

Die elektronischen Flüssigkristall Phasen sind ein wunderschönes Beispiel von Selbstorganisation in Systemen, bei denen unterschiedliche Typen und Reichweiten von Wechselwirkungen im Wettbewerb sind. Anders als ihre klassischen Gegenstücke werden die Eigenschaften von ELC Phasen durch Quantenfluktuationen auf eine Art und Weise modifiziert, die nur unzureichend verstanden ist. Es wurde vorgeschlagen, dass sehr ähnliche Phänomene für das Auftreten der Hochtemperatur-Supraleitung verantwortlich sein könnten. Wir hoffen, dass weitere Untersuchungen der Nicht-Gleichgewichts Transporteigenschaften der ELC Phasen letztendlich zum Verständnis von Quanten-Phasenübergängen und von dynamischer Ordnung im Allgemeinen beitragen werden.

Appendix A

Sample fabrication

A.1 Heterostructures

The GaAs/AlGaAs-heterostructures, which we used for the experiments presented in the chapters 3 and 5, were grown by Vladimir Umansky from the Weizmann Institute of Science, Rehovot, Israel. The most valuable wafer, VU4-97, combined high electron mobility after illumination with very good surface Schottky-gate behavior (i.e. low leakage current, small influence on the sample quality). There has been no systematic study as to why the gate behavior differs greatly between heterostructures. A large distance of the 2DES from the surface is certainly beneficial in this respect. Unfortunately, there is a major drawback of using deep 2DES. When defining small structures in the 2DES with surface gates, one loses spatial resolution because the electrostatic potential of the gates gradually smears out with the distance from the surface.

wafer number	spacer thickness	2DES depth	density	mobility
VU4-97	67 nm	149 nm	$2.1 \cdot 10^{15} \text{ m}^{-2}$	$10 \cdot 10^6 \text{ cm}^2/\text{Vs}$
VU4-127	55 nm	220 nm	$3.1 \cdot 10^{15} \text{ m}^{-2}$	$12 \cdot 10^6 \text{ cm}^2/\text{Vs}$

A.2 Optical lithography

With the help of optical lithography, predefined patterns are transferred from a Cr-coated glass mask onto a piece of the sample (Fig. A.1). In this way, certain areas of the sample are selected (the mesa), ohmic contacts are defined and subsequently diffused into the 2DES, and provisions for bonding and the following electron-beam (e-beam) lithography steps are made. A completely processed sample is shown in Figure A.3.

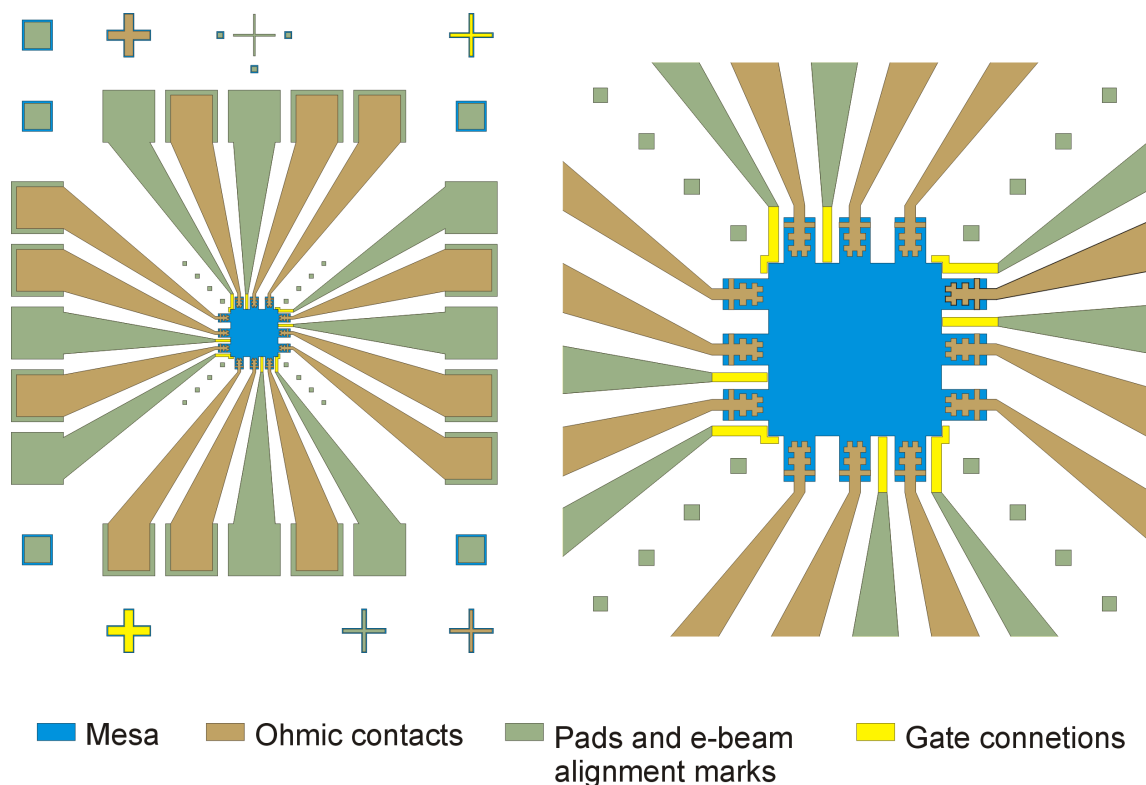


Figure A.1: (left) Mask with various layers (see color code) used for the optical lithography steps. (right) Zoom into the central region around the mesa. The gate connections (yellow) are only partially visible because they are covered mostly by the pads (green) for protective reasons. The size of the square mesa (blue) without arms is $90 \mu\text{m} \times 90 \mu\text{m}$.

A.2.1 Mesa etch

In this step, the top of the heterostructure is etched away everywhere except in a region referred to as the mesa. This leaves the 2DES intact only inside the mesa area, and it provides a well defined geometry for later measurements. There are two different types of etching procedures. Either one only etches down through the Si-dopant layer¹ (shallow etch) or all the way through the 2DES (deep etch). We have used shallow etching because we tried to minimize the step height needed to be climbed by the thin e-beam gates (see below) when they run onto the mesa. To further minimize the chance that the e-beam gate metallization is interrupted at the mesa edge, we have used a special etchant that produces equally tilted etch facets in both the $[110]$ and the $[1\bar{1}1]$ crystal directions (Fig. A.2) [97].

¹To fully deplete the 2DES, it is not even necessary to etch away the dopant layer. Most charge carriers provided by the dopants will be trapped in immobile surface states instead of contributing to the 2DES.

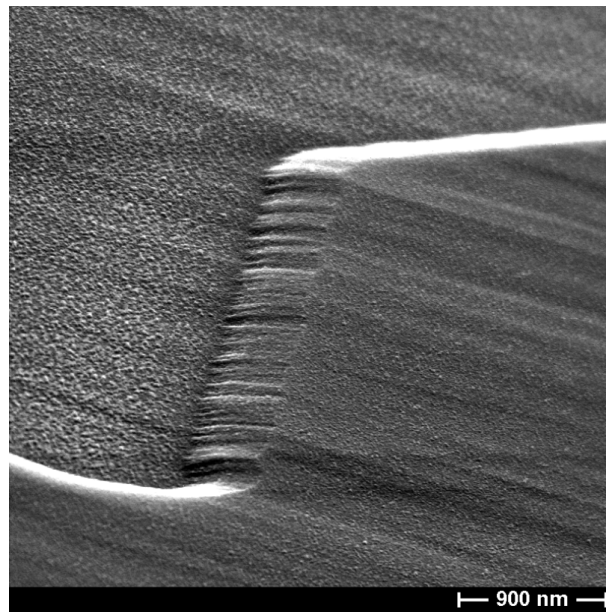


Figure A.2: Mesa edge after etching with the recipe described in the text. The edges in both main crystal directions (only one is shown) have a sufficiently small slope so that metal, evaporated in later steps, can climb up the mesa border without tearing at the step.

Process

1. Clean

- (a) Immerse sample in acetone and put into ultra-sonic basin for 2 min
- (b) Immerse sample in three consecutive acetone baths for a decreasing amount of time (30 s, 10 s, 2 s)
- (c) Splash with acetone
- (d) Immerse sample in propanol, do not let the acetone dry on the sample as it will leave a residue

2. Coat with photoresist S1805

- (a) Use spin-coater 1001S/St146 (Convac)
- (b) Adjust sample on platter and blow dry with nitrogen
- (c) Apply a few drops of Shipley Microposit resist S1805 onto the sample and spin at 4500 min^{-1} for 30 s
- (d) Bake for 2 s on hotplate at 90°C

3. Expose photoresist

- (a) Use Karl Süss MJB3 mask aligner (300 - 400 nm UV-light)
- (b) Expose sample for 7s with the MESA part of the mask (Figure A.1)

4. Develop photoresist

- (a) Shake sample for 35 s in AZ 726 developer to remove exposed areas of the photoresist
- (b) Rinse sample with DI-water to remove developer
- (c) Blow dry sample with nitrogen

5. Etch with tilted facets

- (a) Mix $\text{H}_2\text{O} : \text{H}_2\text{O}_2(31\%) : \text{H}_3\text{PO}_4(35\%)$ at a ratio of 50:1:50
- (b) Cool etching solution to room temperature in water bath (otherwise it will etch much faster)
- (c) Etch sample in the mixture at a rate of approximately 250 nm/min (check with a test sample first!)
- (d) Rinse sample thoroughly with DI-water to completely remove the viscous etching solution
- (e) Blow dry sample with nitrogen

A.2.2 Ohmic contacts

Making ohmic contacts to the 2DES is an art by itself. One strives for a low contact resistance combined with a linear, ohmic I-V characteristic. We have benefited from earlier work in which recipes have been varied and the vast parameter space has been searched through [98]. We have exclusively used the recipe given below.² The contacts tended to show not only excellent ohmic behavior, but they were also homogenous on the μm -scale. This turned out to be an important prerequisite because in our case the overlap area between the contacts and the 2DES had to be small. The quality of the ohmic contacts depends on the orientation of the interface between the contacts and the 2DES with respect to the crystal axis. For this reason, a Christmas-tree like shape has been chosen for the contacts. In this way, interfaces in both main crystal axis directions occur (see Fig. A.1).

²Sometimes, problems during liftoff occurred because of bad adhesion of the Au layer on the substrate. This was most likely triggered by too fast metal evaporation.

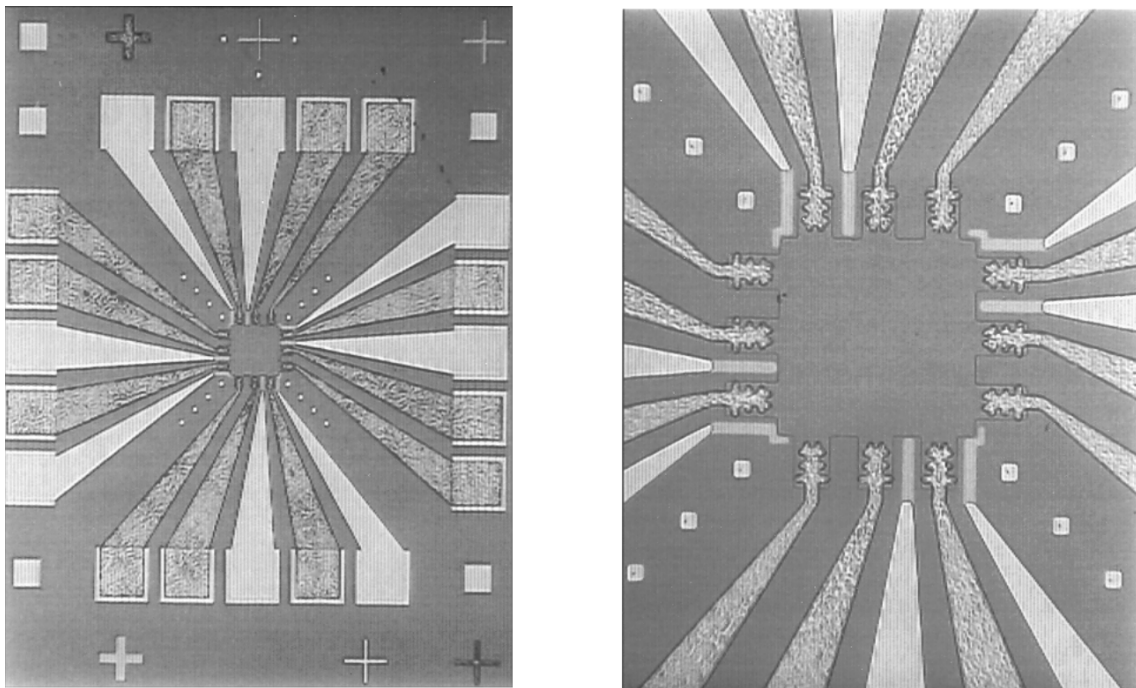


Figure A.3: Image of a fully processed sample taken with an optical microscope. Compare with the mask design (Fig. A.1) to identify the different parts. The size of the square mesa without arms is $90\ \mu\text{m} \times 90\ \mu\text{m}$.

Process

1. Clean
2. Prebake 5 min on hotplate at $120\ ^\circ\text{C}$
3. Coat with AZ 5214E photoresist
 - (a) Use spin-coater 1001S/St146 (Convac)
 - (b) Adjust sample on platter and blow dry with nitrogen
 - (c) Apply a few drops of AZ 5214E to the sample and spin at $6000\ \text{min}^{-1}$ for 30 s
 - (d) Bake for 4 s on hotplate at $90\ ^\circ\text{C}$
4. Expose photoresist and create undercut (inverted process³)
 - (a) Use MJB3 mask aligner
 - (b) Expose sample for 6 s with the OHMIC CONTACTS part of the mask (Figure A.1)
 - (c) Postbake for 60 s on hotplate at $120\ ^\circ$

³After this process, the resist will be removed at all places where it was *not* exposed to light.

- (d) Flood exposure for 70 s without mask
5. Develop photoresist with AZ 726 for 40 s
6. Prepare sample surface for ohmic contact evaporation
 - (a) Process sample in an O₂-plasma (30 s, pressure 0.3 torr, power 200 W in a 100-EPLASMA SYSTEM from Technics Plasma GmbH)
 - (b) Immerse sample in 'Semico Clean' for 2 min
 - (c) Dip sample in DI-water for 5 s
 - (d) Dip sample in HCl (30%) for 2 s
 - (e) Dip sample in DI-water for 1 s
 - (f) Put sample into evaporator within 5 min after HCl-Dip
7. Deposit ohmic contact metallization
 - (a) Use Leybold Heraeus Univex 450 evaporator with thermal sources
 - (b) evaporate 3200 nm of Au at a rate of ≈ 0.2 nm/s
 - (c) evaporate 1600 nm of Ge at a rate of ≈ 0.2 nm/s
 - (d) evaporate 1200 nm of Ni at a rate of ≈ 0.1 nm/s
8. Liftoff
 - (a) Immerse sample into acetone, wait for the photoresist to dissolve, metal will only stick at the predefined areas
 - (b) Immerse sample into propanol
 - (c) Blow dry with nitrogen
9. Alloy ohmic contacts
 - (a) Use annealing oven AZ500 from MBE-Komponenten GmbH with forming gas
 - (b) 370 °C for 120 s, forming gas pressure 0.3 bar, no gas flow
 - (c) 440 °C for 120 s, forming gas pressure 0.3 bar, no gas flow
 - (d) rapid cool down, forming gas flow

A.2.3 Gate connections

The gate connections provide access to the surface gates defined on the mesa by e-beam lithography at a later stage (see Sec. A.3). The gate connections are relatively thin (30 nm) so that they can be climbed by the e-beam gates. Most of the area of the gate connections is covered by the pads (next section) to minimize the probability of damage to them.

Process

1. Clean
2. Coat with photoresist
3. Expose photoresist and create undercut (inverted process)
4. Develop photoresist
5. Deposit gate metallization
 - (a) evaporate 30 nm of Pd/Au at a rate of ≈ 0.2 nm/s
6. Liftoff

A.2.4 Pads and e-beam alignment marks

This layer has two functions. The pads facilitate wire-bonding to the sample and protect the fragile gate connections. Additionally, the alignment marks provide a reference frame for later e-beam lithography steps. The edges of the marks should be very straight to obtain optimal alignment precision. Also, the marks should consist of a relatively thick layer of metal, because this improves the contrast when looked at with an electron microscope. Thereby, manual and automatic detection of the alignment marks is facilitated. For this high precision layer, the resist buildup ('edge bead') at the edges of the sample has to be removed manually. This increases the surface flatness of the resist and allows to press the glass mask evenly against the sample for a homogenous exposure during the optical lithography process. Although the resist removal is a rather cumbersome procedure, it greatly improves the quality of the alignment marks.

Process

1. Clean
2. Coat with photoresist
3. Manually remove resist from sample edges with acetone
4. Expose photoresist and create undercut (inverse process)
5. Develop photoresist
6. Deposit metallization
 - (a) 20 nm of Cr at a rate of ≈ 0.1 nm/s
 - (b) 120 nm of Au at a rate of ≈ 0.2 nm/s
7. Liftoff

A.3 Electron-beam lithography

The technique of electron-beam lithography is used to define the surface gate structures as well as the airbridge structures on the mesa. To reliably obtain complicated devices with a high yield, a lot of expertise in the lithography equipment is required. Most of our devices were written by Ulrike Waizmann from the Max-Planck-Institut, Stuttgart, Germany, specialized in e-beam lithography. Against common claims, we found it to be possible to process high mobility wafers with e-beam lithography with virtually no sign of degradation of the samples in terms of the electron mobility.

A.3.1 Surface gates

The surface gates are used to tailor predefined regions and constrictions of the 2DES within the mesa. Mostly, we have patterned Quantum Point Contacts (section 3.1) and connections to airbridge gates (section A.3.2) out of surface gates.

Process

1. Clean

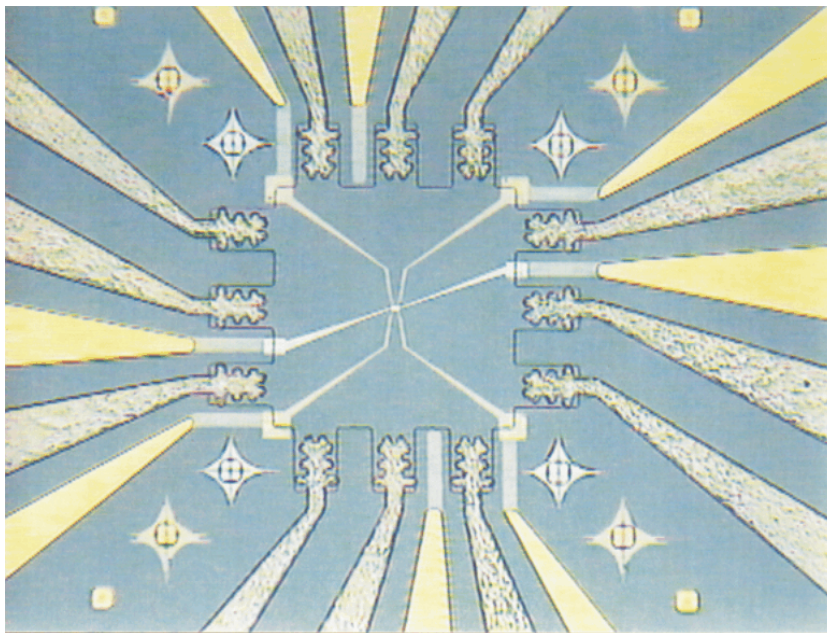


Figure A.4: Optical microscope image of a sample after two consecutive e-beam lithography steps. The star-like shape of the inner two groups of alignment marks comes from the automatic alignment procedure of the e-beam machine. Up to two or four e-beam steps would be possible with this layout.

2. Coat with double layer e-beam resist (≈ 200 nm)
 - (a) Spin PMMA 200K 3.5% (from Allresist GmbH) for 5 s at 3000 min^{-1} , then 30 s at 8000 min^{-1}
 - (b) Bake in oven at 160°C for 60 min
 - (c) Spin PMMA 950K 1.5% as above
 - (d) Bake as above
3. Expose resist with Leica EBL 100-03
 - (a) Set acceleration voltage 50 kV, beam current 30 pA, area dose $625 \mu\text{C}/\text{cm}^2$
 - (b) Expose gate structures
4. Develop resist
 - (a) Develop in Methyl Isobutyl Ketone (MIBK):Propanol with mixing ratio 1:3 for 30 s/100 nm resist, add 30 s
 - (b) Stop development in Propanol
 - (c) Process sample in an O_2 plasma (10 s, pressure 0.3 torr, power 200 W)
5. Deposit metallization
 - (a) 15 nm of AuPd at a rate of $\approx 0.1 \text{ nm/s}$
 - (b) 15 nm of Au at a rate of $\approx 0.1 \text{ nm/s}$
6. Liftoff
 - (a) Immerse for 90 min in AZ Remover at 55°C
 - (b) Acetone/Propanol bath

A.3.2 Air-bridge gates

Building metallic air-bridges, i.e. gates that do not touch the surface of the sample for some distance, on the sub-micron scale is a difficult task. We have used a process developed at the Weizmann Institute of Science, Rehovot, Israel (courtesy of Diana Mahalu) and modified it for our purposes and electron-beam equipment. Important tasks are to ensure the stability of the bridge to obtain sufficient yield and alignment precision of the bridge with respect to gates defined in a previous e-beam step. We have managed to reliably build air-bridges with a footprint of $100 \text{ nm} \times 200 \text{ nm}$ with an alignment precision of better than 20 nm.

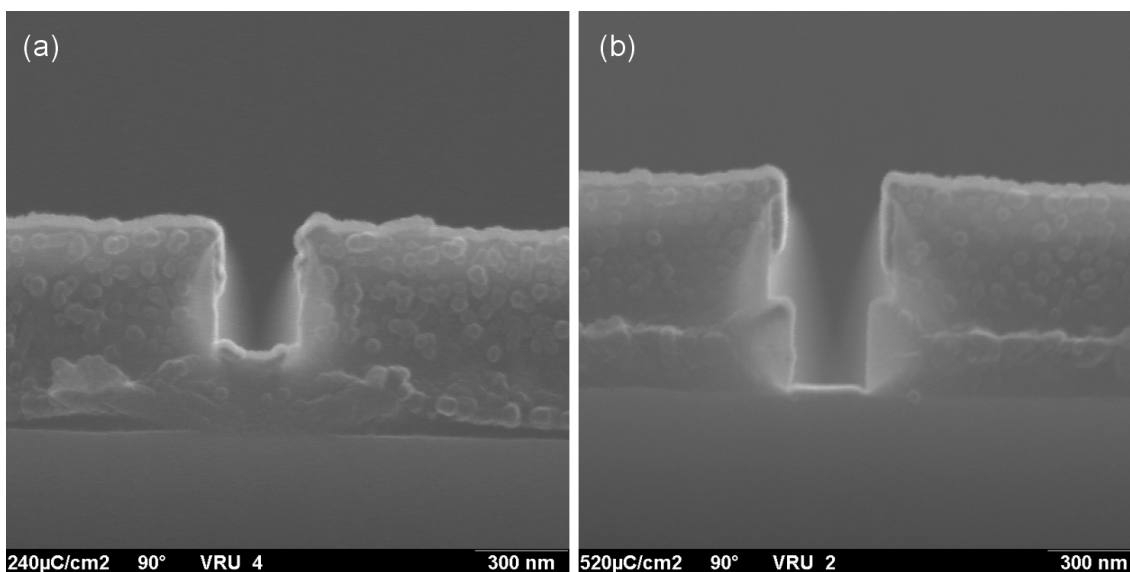


Figure A.5: The electron micrographs show a cross section through the triple layer resist used for the air-bridge process. The thin top resist layer is only barely visible. (a) With a dose of $\approx 240 \mu\text{C}/\text{cm}^2$ only the first two resist layers are developed. (b) With a dose of $\approx 520 \mu\text{C}/\text{cm}^2$ all three layers are developed. The second dose is used for the footprint and the bridge base, whereas the first one is used for the free-standing part of the bridge.

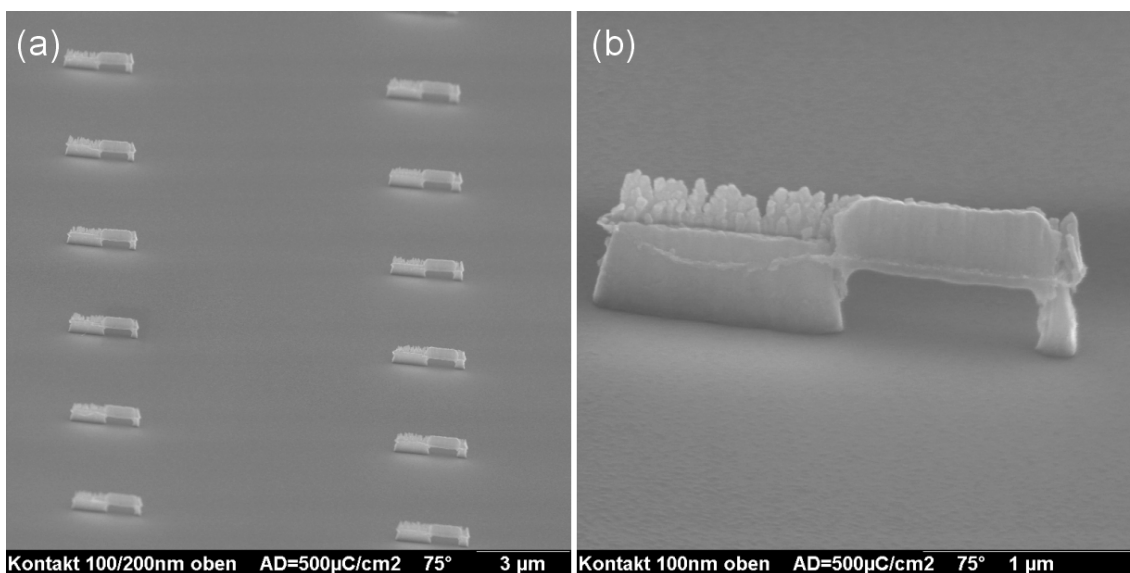


Figure A.6: Electron micrograph showing (a) the high yield of the air-bridge process and (b) an individual bridge with a footprint of $100 \text{ nm} \times 200 \text{ nm}$.

Process

1. Clean
2. Coat with e-beam resist (≈ 700 nm)
 - (a) Spin PMMA 950K A5 for 60 s at 5000 min^{-1}
 - (b) Bake in oven at 180°C for 60 min
 - (c) Spin MMA(17.5%) - MAA EL9 as above
 - (d) Bake as above
 - (e) Spin PMMA 200K A3 as above
 - (f) Bake as above
3. Expose resist with Leica EBL 100-03
 - (a) Set acceleration voltage 50 kV, beam current 30 pA, area dose for bridge footprint $510 \mu\text{C}/\text{cm}^2$, area dose for free-standing bridge section $270 \mu\text{C}/\text{cm}^2$
 - (b) Expose air-bridge structures with the two area doses from above
4. Develop resist
5. Deposit metallization
 - (a) 25 nm of AuPd at a rate of ≈ 0.1 nm/s
 - (b) 300 nm of Au at a rate of ≈ 0.3 nm/s
6. Liftoff

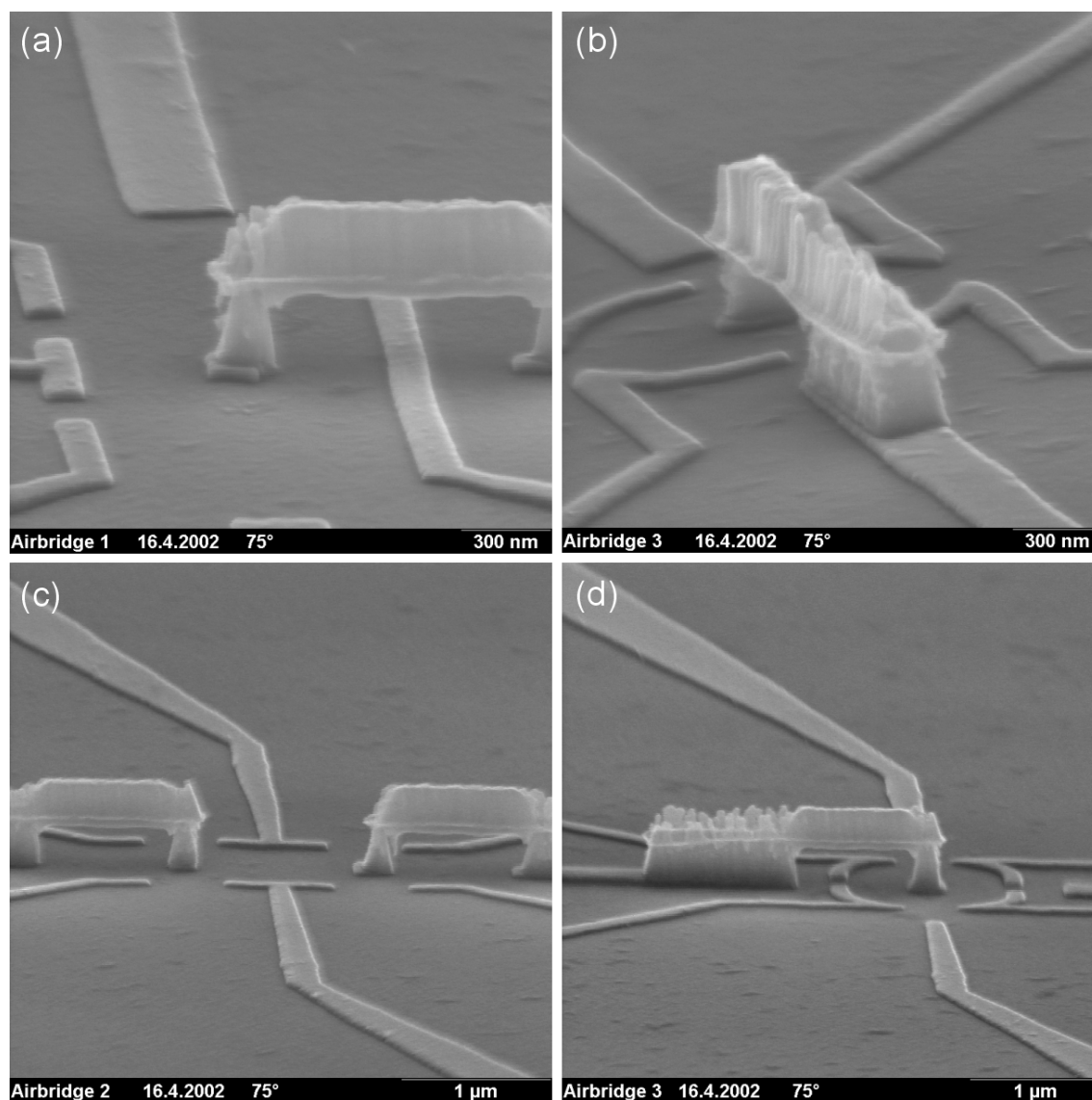


Figure A.7: Electron micrographs showing complete devices including the surface gate and the air-bridge gate layer. The alignment precision of the two consecutive electron-beam steps is better than 20 nm. This can be seen best from the overlap of the bridge footprint with the surface gate underneath. The alignment is extraordinary if one takes into account that the sample has been removed from the e-beam machine and has been processed further by optical lithography between e-beam steps.

Appendix B

Ultra-low temperature probe

The base temperature T_{base} of our Kelvinox TLM He₃/He₄ dilution refrigerator is 10 mK.¹ The relevant temperature T_{2DES} for the experiments is that of the 2DES in the samples. Without any special precautions, one usually finds that $T_{\text{2DES}} > T_{\text{base}}$, and often the electron temperature saturates around $T_{\text{2DES}} \approx 60$ mK even though the base temperature is considerably lower. In our dilution refrigerator, the sample sits directly in the He₃/He₄ mixture, and therefore, one would assume that the sample temperature should equilibrate with that of the mixture. Whereas this is likely true for the GaAs and AlGaAs crystals, the assumption is not valid for the electrons in the 2DES.

B.1 Cooling of the 2DES

The electrons from the 2DES are cooled mainly via two processes. The most effective one at higher temperatures is that of electron-phonon scattering with a cooling power estimated from [99]

$$P_{\text{el-ph}}(W) \approx 3.3 \times 10^6 \frac{A}{\sqrt{n}} (T_{\text{2DES}}^5 - T_{\text{GaAs}}^5). \quad (\text{B.1})$$

All quantities in this expression should be given in SI-units. $T_{\text{GaAs}} \approx T_{\text{base}}$ is the temperature of the phonons in the GaAs host lattice. The electron-phonon cooling power depends directly on the area A of the 2DES. Therefore, large samples are favored for experiments at low temperatures. Because of the strong temperature dependence of phonon-electron cooling, a different mechanism dominates electron cooling at the lowest temperatures. At those temperatures, electrons mainly cool by diffusion of hot electrons from the 2DES into the leads and diffusion of cold electrons in the opposite direction. The cooling power of this process can be determined

¹This temperature has been determined by measuring the angular distribution of the γ -decay of a Co⁶⁰ source that has been mounted instead of the sample.

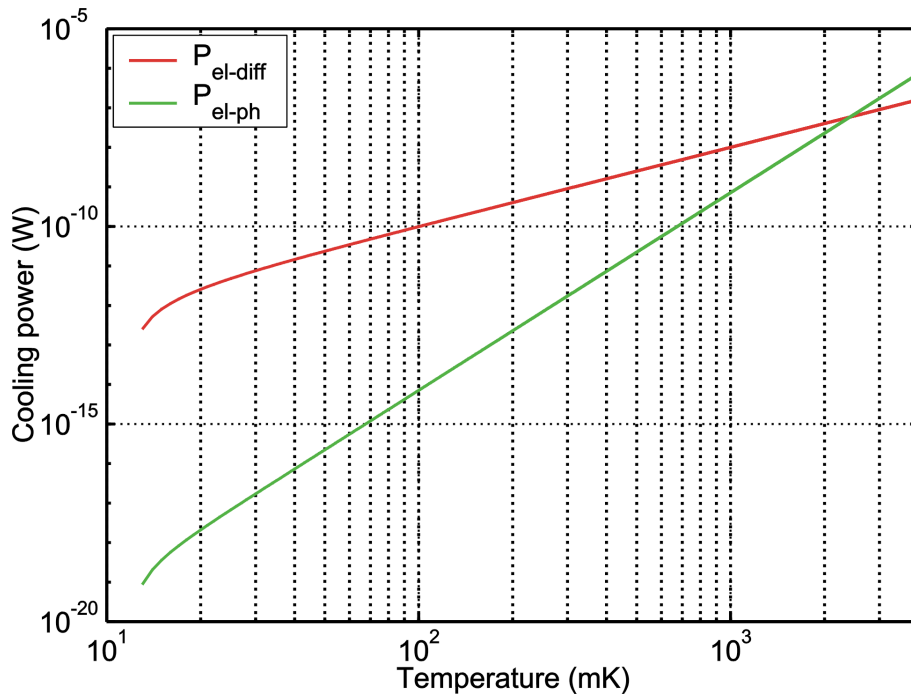


Figure B.1: Simulated cooling power for electrons in a GaAs/AlGaAs 2DES as a function of the temperature. The sample area is $A = 1 \cdot 10^{-8} \text{ m}^2$, its resistance per square is 10Ω , and the lattice temperature is $T = 12 \text{ mK}$.

from the Wiedemann-Franz law to be [99]

$$P_{\text{el-diff}}(W) \approx \frac{10^{-7}}{R} (T_{\text{2DES}}^2 - T_{\text{leads}}^2), \quad (\text{B.2})$$

where T_{leads} is the temperature of electrons in the leads. For our 2DES parameters, we find that below $T = 2 \text{ K}$ the total cooling power is mainly determined by electron diffusion rather than electron-phonon scattering (Fig. B.1). At the lowest temperatures, the diffusive cooling power is a mere $P_{\text{el-diff}} \approx 1 \text{ pW}$, whereas cooling from electron-phonon scattering is completely negligible. Therefore, even tiny amounts of energy deposited into the system will lead to heating effects.² Also, it is important that electrons entering into the sample via the leads have the same temperature as the He_3/He_4 mixture in order to ensure optimal cooling of the 2DES. For this reason, we cool the leads via heat exchangers made from sintered Ag-powder (see section B.4).

²We observe Joule heating effects at roughly 10 nA excitation current. With a characteristic sample resistance of $R = 10 \text{ k}\Omega$ one obtains a heating power on the order of $P = 1 \text{ pW}$.

B.2 RF-heating

A small cooling power of electrons in the 2DES means a long equilibration time between the temperature of the 2DES and that of the host lattice. One generally finds the electron temperature to saturate well above the base temperature of the fridge suggesting that the electron system is heated. High frequency electromagnetic radiation is the main candidate for the heating effect [100]. Small amounts of radio, microwave or thermal radiation couple into the system either directly or via the many wires that run down into the fridge. This way, the power deposited into the 2DES may exceed its cooling power, and hence, it becomes necessary to filter the wires at various stages outside and inside the dilution refrigerator. To avoid direct incidence of electromagnetic radiation onto the sample, we enclosed it with a Faraday cage.

B.3 RF-filter

Three sets of high frequency filters have been mounted into the ultra-low temperature probe.

B.3.1 Room temperature π -filter

The π -filters for intermediate frequencies (100 MHz - 10 GHz) are mounted at room temperature at the top of the probe. They must be far away from the magnet since they rely on ferrites for their inductances, and hence, stray magnetic fields degrade their performance. Because the π -filters do not contain resistances, mounting them at room temperature does not add Johnson noise to the system. We have mounted π -filtered miniature connectors (Spectrum Control Inc., Series 700, 4000 pF). For optimal performance, the filters are mounted into a grounding plate

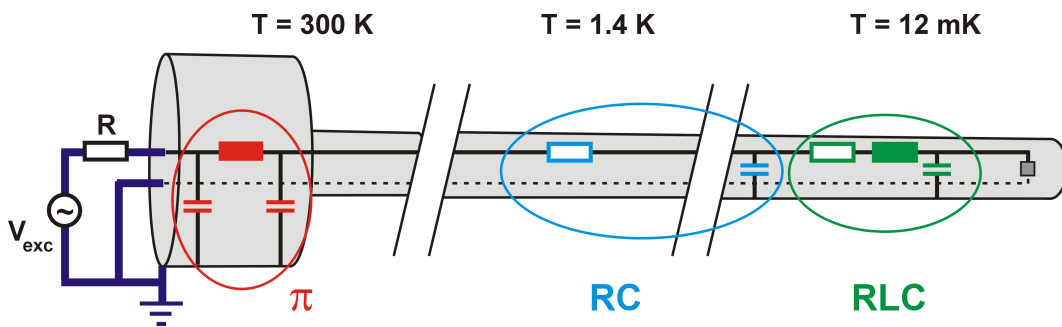


Figure B.2: Schematic drawing of the ultra-low temperature probe wiring. The sample (dark gray square) is current biased with an excitation voltage V_{exc} and a resistance R connected to the probe with coaxial cables (dark blue). The RF-filters (colored) are mounted at various stages of the probe which are at different temperatures. For simplicity, the filters are shown only for one line.

that hermetically seals the input from the output side of the filter. Because it is necessary to pump on the probe top, two waveguide openings are left in the grounding plane. The waveguide nature of the openings, with a length of $l = 3$ cm and a diameter of $d = 3$ mm, ensures that radiation below 50 GHz will be strongly attenuated. From the specifications, we know that the performance of the π -filters starts to decrease beyond 10 GHz.

B.3.2 RC-filter at 1K-Pot

To minimize the contribution from Johnson (Nyquist) noise [101], RC-filters, used to efficiently filter in the lower frequency range, are mounted at the 1K-pot. Mounting the filters at still lower temperatures is not advised, since Joule heating of the filters may exceed the cooling power at the mixing chamber. At the 1K-pot, the cooling power is much higher so that heat from the filters can be easily removed. The RC-filters use a resistance of $R = 1000 \Omega$ and a capacitance of $C = 2$ nF. Then the characteristic cutoff frequency is around $f = 1/2\pi RC \approx 80$ kHz (Fig. B.4).

B.3.3 Strip-line filter at base temperature

For the highest frequencies, $f > 1$ GHz, we have employed a special filter design referred to as a micro-strip-line filter [100, 102]. The basic idea behind this filter design is that of a lossy (resistive) coax cable with small diameter which acts as a distributed RLC-filter [103]. For each line, the filter is made up of 50 cm of insulated $50 \mu\text{m}$ -diameter Manganin wire with a resistance

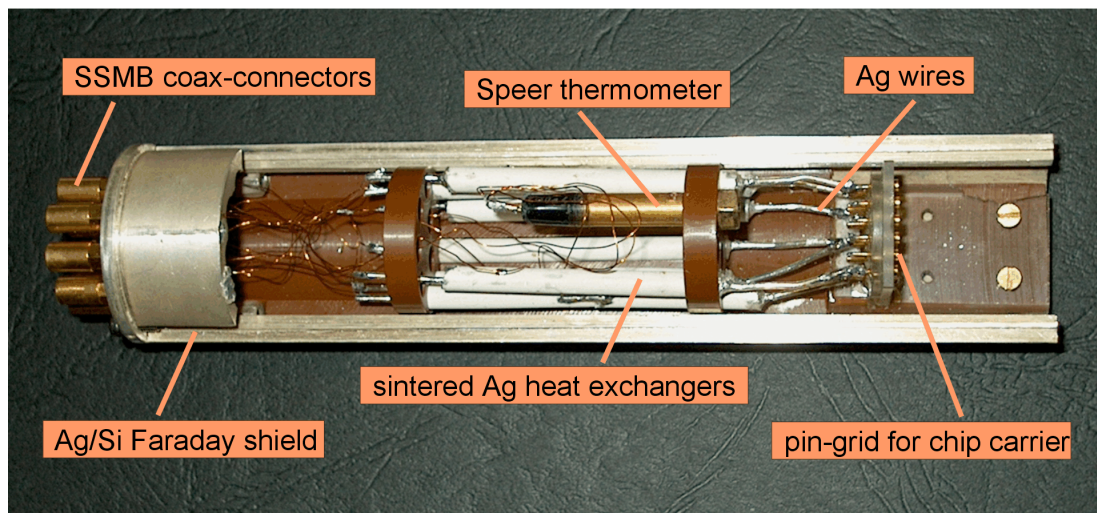


Figure B.3: Photograph of the sample enclosure at the bottom of the ultra-low temperature probe. The top part of the enclosure has been removed to allow a view into the inside.

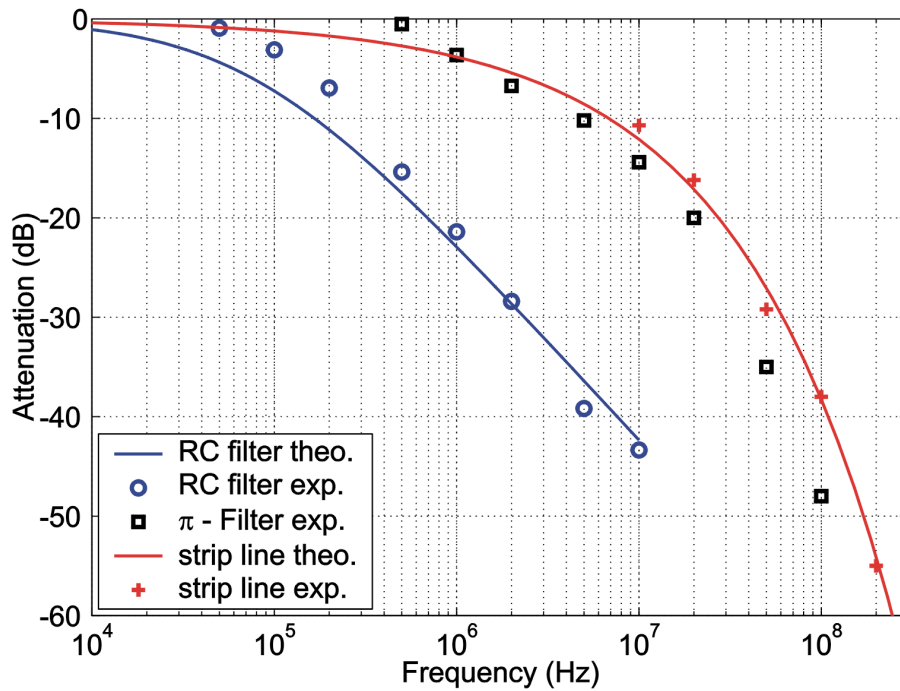


Figure B.4: Performance of the RF-filters mounted at various points in the ultra-low temperature probe.

of $218 \Omega/\text{m}$ wound around a rod and covered with silver epoxy. The wire acts as the central conductor, the epoxy is the outer shield, and the thin wire insulation serves as the dielectric. For optimal performance, the silver epoxy outer shield must be well grounded to the dilution refrigerator that serves as the main ground. The performance of the filter has been simulated and the results are shown in figure B.4. The performance up to 200 MHz has been verified. In principle, the strip-line filter should behave well up to 9 THz where TM- and TE- modes start to propagate down the wire [102].

B.3.4 Ag/Si Faraday-shield

To minimize the effect of stray electromagnetic radiation onto the sample, we have surrounded it with a metallic enclosure acting as a Faraday cage (see Fig. B.3). The only openings of the enclosure are SSMB coaxial connectors for the wire feed-throughs and waveguide openings. The enclosure can be pumped through the waveguide openings, and also the He_3/He_4 mixture enters the enclosure through them. We used Ag as the enclosure material because of its small nuclear magnetic moment. About 1.5% Si is added to the Ag to increase the residual resistance at low temperatures, and hence, to minimize eddy current heating when the magnetic field is

swept.³

B.4 Sintered Ag-heat exchangers

As described above, at temperatures below $T < 1$ K, the 2DES is mainly cooled via electron diffusion from the leads. For efficient cooling, one has to make sure that electrons in the metallic leads are well equilibrated with the He₃/He₄ mixture. Since the wires run directly through the mixture, one expects them to be at the temperature of the mixture. One has to keep in mind, though, that the heat transfer between a liquid (the mixture) and a solid (the wires) is very inefficient, mainly because of the large differences in the speed of sound in both media [104]. The thermal resistance between two media is referred to as the Kapitza resistance

$$R_K = \frac{A\Delta T}{\dot{Q}}, \quad (\text{B.3})$$

where A is the contact area, ΔT the temperature difference between the media and \dot{Q} the heat flux. Usually, the leads are made from 30 cm long CuNi wires with a diameter of $d = 200 \mu\text{m}$. The heat transfer between mixture and wires is very low because of the small surface area $A = 1.88 \cdot 10^{-4} \text{ m}^2$ of the wires (see table ??). In our design, we use leads made out of 1 g of sintered Ag powder with a nominal particle diameter of $d = 700 \text{ \AA}$.⁴ The Kapitza resistance at 10 mK is a factor of 16 higher than for the CuNi wires, but the surface area $A \approx 1 \text{ m}^2$ is much larger resulting in an increase of the heat flux by a factor of 300 (table B.1). The wire parts made from sintered Ag should be close to the sample and no solder points should be in between (see Fig. B.3). Solder points become superconducting at low temperatures and thus very effectively inhibit heat transfer along the wire. If solder points are necessary, they should be covered with conductive silver paste to ensure good thermal contact [106].

³This alloy composition was suggested to us by Christian Probst and colleagues from the Walter-Meissner Institute, Munich, Germany, and the alloy was produced by Kessel Feinguß GmbH, Niefern-Öschelbronn, Germany.

⁴The Ag powder (70nm, 4N, Ulvac GmbH, Germany) is sintered under mechanical pressure in vacuum at 150 °C for 60 min (see also [101]).

material	Kapitza resistance R_K (K m^2/W)	heat transfer \dot{Q} (W)
30 cm CuNi wire (200 μm)	$1.9 \cdot 10^4$	$20 \cdot 10^{-12}$
1g Ag-sinter (700 \AA)	$1.6 \cdot 10^5$	$6.25 \cdot 10^{-9}$

Table B.1: Kapitza resistance at $T = 10$ mK and heat transfer for $\Delta T = 1$ mK for CuNi [104] wires and sintered Ag [105] leads.

Bibliography

- [1] K. v. Klitzing, G. Dorda, and M. Pepper, Phys. Rev. Lett. **45**, 494 (1980).
- [2] D. C. Tsui, H. L. Störmer, and A. C. Gossard, Phys. Rev. Lett. **48**, 1559 (1982).
- [3] R. B. Laughlin, Phys. Rev. Lett. **50**, 1395 (1983).
- [4] R. B. Laughlin, Phys. Rev. B **23**, 5632 (1981).
- [5] J. K. Jain, Phys. Rev. Lett. **63**, 199 (1989).
- [6] B.I. Halperin, P.A. Lee, and N. Read, Phys. Rev. B **47**, 7312 (1993).
- [7] M.P. Lilly, K.B. Cooper, J.P. Eisenstein, L.N. Pfeiffer, and K.W. West, Phys. Rev. Lett. **82**, 394 (1999).
- [8] R.R. Du, D.C. Tsui, H.L. Stormer, L.N. Pfeiffer, K.W. Baldwin, and K.W. West, Sol. Stat. Comm. **109**, 389 (1999).
- [9] R. Moessner and J. Chalker, Phys. Rev. B **54**, 5006 (1996).
- [10] A.A. Koulakov, M.M. Fogler, and B.I. Shklovskii, Phys. Rev. Lett. **76**, 499 (1996).
- [11] G. Grüner, Rev. Mod. Phys. **60**, 1129 (1988).
- [12] E.P. Wigner, Phys. Rev. **46**, 1002 (1934).
- [13] E. Fradkin and S. Kivelson, Phys. Rev. B **59**, 8065 (1999).
- [14] P.G. de Gennes and J. Prost, *The Physics of Liquid Crystals*, (Oxford University Press, New York, 1995).
- [15] M. Seul and D. Andelman, Science **267**, 476 (1995).
- [16] S.A. Kivelson, E. Fradkin, and V.J. Emery, Nature **393**, 550 (1998).
- [17] T. Ando, A.B. Fowler, and F. Stern, Rev. Mod. Phys. **54**, 437 (1982).
- [18] H.L. Störmer, Surf. Science **132**, 519 (1983).

- [19] L.L. Chang and K. Ploog (eds.), *Molecular Beam Epitaxy and Heterostructures*, (Martinus Nijhoff Publishers, Dordrecht, 1985).
- [20] P. Drude, *Ann. Phys.* **3**, 369 (1900).
- [21] H. Aoki, *J. Phys. C* **10**, 2583 (1977).
- [22] R.J. Nicholas, R.J. Haug, and K. von Klitzing, *Phys. Rev. B* **37**, 1294 (1988).
- [23] L. Shubnikov and W.J. de Haas, *Leiden Comm.* **207a,c,d,210a**, (1930).
- [24] K. v. Klitzing, *Rev. Mod. Phys.* **58**, 519 (1986).
- [25] B.N. Taylor and T.J. Witt, *Metrologia* **26**, 47 (1989).
- [26] M. Büttiker, *Phys. Rev. B* **38**, 9375 (1988).
- [27] R. Landauer, *Z. Phys. B* **68**, 217 (1987).
- [28] H. L. Störmer, *Rev. Mod. Phys.* **71**, 875 (1999).
- [29] D. C. Tsui, *Rev. Mod. Phys.* **71**, 891 (1999).
- [30] R. B. Laughlin, *Rev. Mod. Phys.* **71**, 863 (1999).
- [31] S.M. Girvin, *Phys. Rev. B* **29**, 6012 (1984).
- [32] F.D.M. Haldane, *Phys. Rev. Lett.* **51**, 605 (1983).
- [33] B.I. Halperin, *Helv. Phys. Acta* **56**, 75 (1983).
- [34] R. Willett, J.P. Eisenstein, H.L. Störmer, D.C. Tsui, A.C. Gossard, and J.H. English, *Phys. Rev. Lett.* **59**, 1776 (1987).
- [35] W. Pan, J.-S. Xia, V. Shvarts, D. E. Adams, H. L. Stormer, D. C. Tsui, L. N. Pfeiffer, K. W. Baldwin, and K. W. West, *Phys. Rev. Lett.* **83**, 3530 (1999).
- [36] F.D.M. Haldane and E.H. Rezayi, *Phys. Rev. Lett.* **60**, 956,1886 (E) (1988).
- [37] J.P. Eisenstein, R. Willett, H.L. Störmer, D.C. Tsui, A.C. Gossard, and J.H. English, *Phys. Rev. Lett.* **61**, 997 (1988).
- [38] Y. Aharonov and D. Bohm, *Phys. Rev.* **115**, 485 (1959).
- [39] F. Wilczek, *Fractional Statistics and Anyon Superconductivity*, (World Scientific, Singapore, 1990).
- [40] F. Wilcek, *Sci. Am.* **264**, 24 (1991).

- [41] D. Arovas, J.R. Schrieffer, and F. Wilczek, Phys. Rev. Lett. **55**, 722 (1984).
- [42] R.L. Willett, R.R. Ruel, K.W. West, and L.N. Pfeiffer, Phys. Rev. Lett. **71**, 3846 (1993).
- [43] W. Kang, S. He, H.L. Störmer and L.N. Pfeiffer, K.W. Baldwin, and K.W. West, Phys. Rev. Lett. **75**, 4106 (1995).
- [44] J.H. Smet, D. Weiss, R.H. Blick, G. Lütjering, K. von Klitzing, R. Fleischmann, T. Geisel, and G. Weimann, Phys. Rev. Lett. **77**, 2272 (1996).
- [45] I.V. Kukushkin, J.H. Smet, K. von Klitzing, and W. Wegscheider, Nature **415**, 412 (2002).
- [46] J.K. Jain, Physics Today **53**, 39 (2000).
- [47] R.E. Prange and S.M. Girvin, eds. *The Quantum Hall Effect*, (Springer-Verlag, New York, 1987).
- [48] N. Read, Semicond. Sci. Technol. **9**, 1859 (1994).
- [49] A. Stern, B.I. Halperin, F. von Oppen, and S.H. Simon, Phys. Rev. B **59**, 12547 (1999).
- [50] V.C. Karavolas and G.P. Triberis, Phys. Rev. B **63**, 035313 (2001).
- [51] N. Read, Physica B **298**, 121 (2001).
- [52] H. Fukuyama, P.M. Platzman, and P.W. Anderson, Phys. Rev. B **19**, 5211 (1979).
- [53] N. Shibata and D. Yoshioka, Phys. Rev. Lett. **86**, 5755 (2001).
- [54] K.B. Cooper, M.P. Lilly, J.P. Eisenstein, L.N. Pfeiffer, and K.W. West, Phys. Rev. B **60**, R11285 (1999).
- [55] S.H. Simon, Phys. Rev. Lett. **83**, 4223 (1999).
- [56] M.P. Lilly, K.B. Cooper, J.P. Eisenstein, L.N. Pfeiffer, and K.W. West, Phys. Rev. Lett. **83**, 824 (1999).
- [57] K.B. Cooper, M.P. Lilly, J.P. Eisenstein, T. Jungwirth, L.N. Pfeiffer, and K.W. West, Solid State Commun. **119**, 89 (2001).
- [58] J. Zhu, W. Pan, H.L. Stormer, L.N. Pfeiffer, and K.W. West, Phys. Rev. Lett. **88**, 116803 (2002).
- [59] W. Pan, R.R. Du, H.L. Stormer, D.C. Tsui, L.N. Pfeiffer, K.W. Baldwin, and K.W. West, Phys. Rev. Lett. **83**, 820 (1999).

- [60] T. Jungwirth, A.H. MacDonald, L. Smrcka, and S.M. Girvin, *Phys. Rev. B* **60**, 15574 (1999).
- [61] K.B. Cooper, J.P. Eisenstein, L.N. Pfeiffer, and K.W. West, *Phys. Rev. Lett.* **90**, 226803 (2003).
- [62] R.M. Lewis, P.D. Ye, L.W. Engel, D.C. Tsui, L.N. Pfeiffer, and K.W. West, *Phys. Rev. Lett.* **89**, 136804 (2002).
- [63] *Perspectives in Quantum Hall Effects*, eds. S. Das Sarma and A. Pinczuk, (John Wiley & Sons, New York, 1997).
- [64] Y. Chen, R.M. Lewis, L.W. Engel, D.C. Tsui, P.D. Ye, L.N. Pfeiffer, and K.W. West, *Phys. Rev. Lett.* **91**, 016801 (2003).
- [65] R.M. Lewis, Y. Chen, L.W. Engel, D.C. Tsui, P.D. Ye, L.N. Pfeiffer, and K.W. West, *cond-mat/ 0307182* (2003).
- [66] R.M. Lewis, Y. Chen, L.W. Engel, D.C. Tsui, P.D. Ye, L.N. Pfeiffer, and K.W. West, *cond-mat/ 0401462* (2004).
- [67] A.H. MacDonald and M.P.A. Fisher, *Phys. Rev. B* **61**, 5724 (2000).
- [68] F. von Oppen, B.I. Halperin, and Ady Stern, *Phys. Rev. Lett.* **84**, 2937 (2000).
- [69] E. Fradkin, S.A. Kivelson, E. Manousakis, and K. Nho, *Phys. Rev. Lett.* **84**, 1982 (2000).
- [70] K.B. Cooper, M.P. Lilly, J.P. Eisenstein, L.N. Pfeiffer, and K.W. West, *Phys. Rev. B* **65**, 241313 (2002).
- [71] C.W.J. Beenakker and H. van Houten, *Quantum Transport in Semiconductor Nanostructures, Solid State Physics* **44**, (Academic Press, San Diego, 1991).
- [72] M. Büttiker, *The Quantum Hall Effect in Open Conductors, Semiconductors and Semimetals* **35**, (Academic Press, San Diego, 1992).
- [73] C.W.J. Beenakker, *Phys. Rev. Lett.* **64**, 216 (1990).
- [74] P.L. McEuen, B.W. Alphenaar, R.G. Wheeler, and R.N. Sacks, *Surf. Sci.* **229**, 312 (1990).
- [75] L.W. Molenkamp, A.A.M. Staring, C.W.J. Beenakker, R. Eppenga, C.E. Timmering, J.G. Williamson, C.J.P.M. Harmans, and C.T. Foxon, *Phys. Rev. B* **41**, 1274 (1990).
- [76] G. Müller, D. Weiss, K. von Klitzing, K. Ploog, H. Nickel, W. Schlapp, and R. Lösch, *Phys. Rev. B* **46**, 4336 (1992).

- [77] Th. Schäpers, M. Krüger, J. Appenzeller, A. Förster, B. Lengeler, and H. Lüth, *Appl. Phys. Lett.* **66**, 3603 (1995).
- [78] G.F. Giuliani and J.J. Quinn, *Phys. Rev. B* **26**, 4421 (1982).
- [79] Y. Feng, A.S. Sachrajda, P. Zawadzki, S. Kolind, M. Buchanan, J.H. Smet, J. Lapointe, and P.A. Marshall, *J. Vac. Sci. Technol. A* **18**, 730 (2000).
- [80] H. van Houten, C.W.J. Beenakker, P.H.M. van Loosdrecht, T.J. Thornton, H. Ahmed, M. Pepper, C.T. Foxon, and J.J. Harris, *Phys. Rev. B* **37**, 8534 (1988).
- [81] C. Gould, A.S. Sachrajda, Y. Feng, A. Delage, P.J. Kelly, K. Leung, and P.T. Coleridge, *Phys. Rev. B* **51**, 11213 (1995).
- [82] G. Kirczenow, B.L. Johnson, P.J. Kelly, C. Gould, A.S. Sachrajda, Y. Feng, and A. Delage, *Phys. Rev. B* **56**, 7503 (1997).
- [83] W.H. Press and S.A. Teukolsky and W.T. Vetterling and B.P. Flannery, *Numerical Recipes in C: The Art of Scientific Computing*, (Cambridge University Press, Cambridge, 1988).
- [84] A. Yacoby, U. Sivan, C.P. Umbach, and J.M. Hong, *Phys. Rev. Lett.* **66**, 1938 (1991).
- [85] M.R. Geller and D. Loss, *Phys. Rev. B* **56**, 9692 (1997).
- [86] S. Datta, *Electronic transport in mesoscopic systems*, (Cambridge University Press, Cambridge, 1995).
- [87] C. de C. Chamon, D.E. Freed, S.A. Kivelson, S.L. Sondhi, and X.G. Wen, *Phys. Rev. B* **55**, 2331 (1997).
- [88] E.L. Bolda and D.F. Walls, *Phys. Rev. Lett.* **81**, 5477 (1998).
- [89] J. Blaschke and M. Brack, *Europhys. Lett.* **50**, 293 (2000).
- [90] M Berry, *Physics of Defects, Les Houches, Session XXXV, 1980*, ed. R. Balian, (North Holland Publishing Company, Amsterdam, 1981).
- [91] S. Inouye, S. Gupta, T. Rosenband, A.P. Chikkatur, A. Görlitz, T.L. Gustavson, A.E. Leanhardt, D.E. Pritchard, and W. Ketterle, *Phys. Rev. Lett.* **87**, 080402 (2001).
- [92] R.L. Willett, K.W. West, and L.N. Pfeiffer, *Phys. Rev. Lett.* **87**, 196805 (2001).
- [93] C. Nayak and F. Wilczek, *Phys. Rev. Lett.* **78**, 2465 (1997).
- [94] V.J. Goldman, B. Su, and J.K. Jain, *Phys. Rev. Lett.* **72**, 2065 (1994).
- [95] L. Susskind, *J. Math. Phys.* **36**, 6377 (1995).

- [96] E. Witten, *Physics Today* **50**, 28 (1997).
- [97] H.P. Meier, R.F. Broom, P.W. Epperlein, E. van Gieson, Ch. Harder, H. Jäckel, W. Walter, and D.J. Webb, *J. Vac. Sci. Technol. B* **6**, 692 (1988).
- [98] U. Graumann, unpublished .
- [99] A. Mittal, R.G. Wheeler, M.W. Keller, D.E. Prober, and R.N. Sacks, *Surf. Sci.* **361/362**, 537 (1996).
- [100] D. Vion, P.F. Orfila, P. Joyez, D. Esteve, and M.H. Devoret, *J. Appl. Phys.* **77**, 2519 (1995).
- [101] R.C. Robertson, E.N. Smith, *Experimental Techniques in Condensed Matter Physics at Low Temperatures*, (Addison-Wesley, Redwood City, 1988).
- [102] H. Courtois, O. Buisson, J. Chaussy, and B. Pannetier, *Rev. Sci. Instrum.* **66**, 3465 (1995).
- [103] A.B. Zorin, *Rev. Sci. Instrum.* **66**, 4296 (1995).
- [104] O.V. Lounasmaa, *Experimental principles and methods below 1K*, (Academic Press, London, 1974).
- [105] C. Enss, S. Hunklinger, *Tieftemperaturphysik*, (Springer, Berlin, 2000).
- [106] G. Frossati, private communication .

Acknowledgements

At this point, I would like to thank everybody who has contributed to this work directly or indirectly. Without support, such an endeavor would not have been possible. In particular, I am indebted to

- my advisor Prof. Klaus v. Klitzing who welcomed me in his group to work on this interesting topic. With his critical questions and comments and his financial support, he contributed strongly to the results of this thesis. His enthusiasm for "his" Quantum Hall Effect is exemplary.
- Prof. T. Pfau who kindly agreed to co-advise this thesis. I truly hope that he finds the topics also interesting in respect to his own research field of photonics as I had promised them to be.
- my direct supervisor Dr. habil. Jurgen Smet for introducing me to the topic of Composite Fermions, his numerous helpful suggestions during the course of this work, giving me the chance to work independently, supporting all my equipment wishes and my stays abroad, and last but not least his critical reading of the manuscript.
- Prof. M. Heiblum (Weizmann Institute of Science, Israel) for making possible my extended stays in Israel. These visits were fascinating and inspiring not only scientifically.
- my supervisor and collaborator in Israel Prof. A. Yacoby (Weizmann) for his ideas and critical comments that have influenced this work strongly and for welcoming me in his nice group.
- Diana Mahalu (Weizmann) for her expert e-beam lithography work during my stay in Israel. From Diana, I have learned the challenging air-bridge fabrication process which hopefully will also be useful in future experiments in Stuttgart.
- V. Umansky (Weizmann) for providing his wonderful heterostructures which are the most important ingredient for high mobility experiments and for illuminating discussions on world politics.

- Prof. A. Sachrajda (NRC, Canada) for his collaboration and his stimulating ideas in respect to the antidot work. Y. Feng (then also NRC) for his expert e-beam lithography of the antidot samples.
- U. Waizmann for her expertise regarding the electron-beam-lithography equipment. Her careful and reliable e-beam fabrication steps on the precious high-mobility material were a key to the success of the ballistic transport experiments.
- the cleanroom team for providing excellent facilities.
- our ingenious technician M. Schmid for the CAD-design and machining of the low-temperature probe. The late J. Behring for this help in constructing the probe head and for the wiring. Sadly, he could not see his work come into use anymore.
- U. Wilhelm for implementing the measkern software which tremendously facilitates complex automated measurements.
- O. Stern for proof-reading the manuscript, many interesting discussions, being a constant source of good spirit, introducing me to his astonishing theory of the soccer game as being a perfect representation of real life and most of all for becoming a really good friend.
- my colleagues in the group for creating a nice atmosphere and for distracting conversations during lunch and tea-time.
- our secretary H. Ludwig for keeping things running smoothly and bringing a family feeling to the group
- the low temperature service group for continuously and reliably providing large amounts of liquid Helium and Nitrogen for our cryostats.
- Prof. G. Frosatti (University of Leiden, Netherlands) for letting me tap his profound knowledge of low temperature physics which greatly helped me in the design of the low-temperature probe.
- H. M. Strassner (hms-Elektronik) for several very helpful discussions on grounding and shielding of the experimental setup. He brought the superior performance of shielded Hifi-cables and Balun filters to my attention which increased the sensitivity of our electronic setup.
- Prof. M.A. Kastner (MIT, USA) and Prof. D. Goldhaber-Gordon (now Stanford University, USA) for introducing me to the fascinating physics of low-dimensional systems and in particular Single-Electron-Transistors. Being a proud member of Prof. Kastner's group at MIT has been an inspiring experience, both personally and scientifically.

- Prof. J. Budnick and Prof. D. Pease (University of Connecticut, Storrs, USA) for introducing me to the joy and hardships of experimental physics. I will always admire Prof. Budnick's enthusiasm and his gift to motivate.
- my friends for letting me not forget that there are other important themes in life besides physics and for objecting when I spent too much time in the lab. I would have never finished this long journey without the strong personal support and understanding of some of you.
- Sanela for her love, support and understanding and for giving birth to our son Remis who has brought a completely new meaning to my life.
- my parents and my brother for supporting me morally throughout the extend of this thesis and for not stopping to believe that I would eventually finish.

Curriculum Vitae

Persönliche Daten

Name Jörn Göres
Geburtstag 12. März 1971
Geburtsort Hilden

Ausbildung

09/81 - 06/90	Annette-von-Droste-Hülshoff Gymnasium Allgemeine Hochschulreife	Düsseldorf
07/90 - 07/91	Wehrdienst bei der Luftwaffe	Eckernförde
10/91 - 09/93	Heinrich-Heine-Universität Vordiplom in Physik	Düsseldorf
09/94 - 05/95	University of Connecticut Master of Science in Physik, Fulbright Stipendium <i>X-ray Absorption Spectroscopy for Trace Analysis of Chemical Phase and Composition</i>	Storrs, USA
10/93 - 08/97	Ruprecht-Karls-Universität Diplom in Physik <i>Der chirale Phasenübergang bei endlicher Dichte in einer $1/N_c$-Entwicklung des NJL Modells</i>	Heidelberg
09/97 - 01/99	Massachusetts Institute of Technology wissenschaftlicher Mitarbeiter bei Prof. M. A. Kastner Stipendium der NEC Electronics, Inc. <i>The Kondo- and the Fano-effect in Single-Electron-Transistors (SETs)</i>	Cambridge, USA
seit 02/99	Max-Planck-Institut für Festkörperforschung Promotion in Physik bei Prof. Klaus v. Klitzing	Stuttgart